Degree-Per-Hour Mode-Matched Micromachined Silicon Vibratory Gyroscopes

A Dissertation
Presented to
The Academic Faculty

By

Mohammad Faisal Zaman

In Partial Fulfillment
Of the Requirements for the Degree
Doctor of Philosophy in the
School of Electrical and Computer Engineering

Georgia Institute of Technology
April 2008

Degree-Per-Hour Mode-Matched Silicon Micromachined

Vibratory Gyroscopes

Approved by:

Professor Farrokh Ayazi, Advisor
School of Electrical and Computer
Engineering
Georgia Institute of Technology

Professor Thomas Michaels
School of Electrical and Computer
Engineering
Georgia Institute of Technology

Professor Oliver Brand
School of Electrical and Computer
Engineering
Georgia Institute of Technology

Professor Paul Kohl
School of Chemical and
Biomolecular Engineering
Georgia Institute of Technology

Professor Mark Allen
School of Electrical and Computer
Engineering
Georgia Institute of Technology

Date Approved: 3/26/2008

I dedicate this dissertation to my loving parents for all their support, encouragement, patience, and wisdom

ACKNOWLEDGEMENTS

TABLE OF CONTENTS

LIST OF TABLES

LIST OF FIGURES

SUMMARY

Silicon micromachined gyroscopes have been incorporated into several practical automotive and consumer electronics sub-systems owing to their small size, low power and relatively inexpensive production and maintenance costs. However, anti-skid or traction control systems in automobiles, and image stabilization in digital cameras represent applications where resolution and precision are not critical. Silicon micromachined gyroscopes have yet to satisfy the navigation-grade requirements needed for high-precision applications such as inertial measurement units for GPS augmented navigation, unmanned surveillance vehicles, and aircraft and personal heading references.

Vibratory gyroscopes rely on the transfer of energy from one structural vibration mode to another in response to rotation-induced Coriolis acceleration. The objective of this research dissertation is to develop two novel micromachined silicon vibratory gyroscopes, which attempt to incorporate all the necessary attributes of sub-deg/hr noise performance requirements in a single framework: large resonant mass, high drive-mode oscillation amplitudes, large device capacitance coupled with optimized electronics, and high-Q resonant mode-matched operation. Mode-matching leverages the high-Q of the operating modes of the gyroscope and offers significant improvements in mechanical and electronic noise floor, sensitivity, and bias stability.

The first micromachined silicon vibratory gyroscope presented in this work is the resonating star gyroscope (RSG): a novel Class-II shell-type structure which utilizes degenerate flexural modes. The RSG offers improved mass and capacitance area over its circular analogue of similar dimensions. After an iterative cycle of

design optimization, an RSG with 2.7mm radial diameter was implemented using a multiple-shell approach on 40μm-thick (111) SOI substrate. Multiple-shells enable a higher operating frequency and larger resonant mass, essential components for reducing the mechanical noise floor of the sensor. Experimental data of an (111) single-crystalline silicon multiple-shell prototype indicates sub-5 deg/hr/√Hz Brownian noise floor, with a measured Allan deviation bias drift of 3.5 deg/hr, operating under a mode-matched operating Q of 30,000 at 23ºC. The RSG exhibits an open-loop rate sensitivity of 16.7 mV/deg/s in vacuum.

The second micromachined silicon vibratory gyroscope presented in this work is the mode-matched tuning fork gyroscope (M^2-TFG): a novel Class-I tuning fork device which utilizes in-plane non-degenerate resonant flexural modes. Operated under vacuum, it offers the highest Qs reported for flexural operating modes (facilitated by TED analysis of suspension springs). The M^2-TFG represents the first reported high-Q perfectly mode-matched operation in Class-I vibratory microgyroscope. This implementation has been made possible by the development of quadrature minimization electrode scheme. Experimental results of device implemented on 60μm-thick SOI substrate with 5μm drive-mode deflections, demonstrate an effective mode-matched quality factor (Q_{EFF}) of 36,000 with a measured open-loop scale-factor of 88mV/deg/s in vacuum. The device displayed a measured ARW and bias drift of 0.0083deg/hr and 0.32deg/hr respectively at 23ºC. This represents an order of magnitude better noise performance than any commercial gyroscope currently in production or reported in literature.

In an effort to increase capacitive aspect ratio, a new fabrication technology was developed that involved the selective deposition of doped-polysilicon inside the capacitive sensing gaps (SPD Process). By preserving the structural

composition integrity of the flexural springs, it is possible to generate operating-modes at the correct frequencies while maintaining high-Q operation. The M^2-TFG devices implemented on 80μm-thick SOI substrate with 3μm sensing gaps demonstrated mode-matched operation (Q_{EFF} = 4,000) and enhanced bandwidth. The device displayed a rate sensitivity of approximately 12mV/deg/s and a measured Allan deviation bias instability of 1.8deg/hr at 23°C.

M^2-TFG devices fabricated on 100μm-thick single-crystalline substrate using the Silicon-on-Glass fabrication technology were successfully vacuum-packaged (at University of Michigan under DARPA HERMIT program). The M^2-TFG devices demonstrated high-Q mode-matched operation (Q_{EFF} = 55,000) and displayed a rate sensitivity of approximately 92mV/deg/s and a measured Allan deviation bias instability of 0.7deg/hr at 23°C.

CHAPTER I

INTRODUCTION

The word *gyroscope* was coined by the French scientist Leon Foucault and is derived from the Greek words "Gyros" meaning *rotation*, and "Skopien" meaning *to view*. By definition, a gyroscope is a sensor that measures the angle or rate of rotation. Micromachined gyroscopes constitute one of the fastest growing segments of the microsensor market. The application domain of these devices is rapidly expanding from automotive to consumer electronics and personal navigation systems. Small form-factor, light weight, and low-power consumption make micromachined gyroscopes ideal for use in handheld applications, many of which require multi-axis sensitivity. Gaming consoles, image stabilization in digital cameras and roll-over detection and traction control systems in automobiles represent applications which demand angular rate resolution on the order of 0.1deg/s [1]. Micromachined gyroscopes however have yet to break into the high-precision market that requires sub-deg/hr resolution and bias stability. Applications in this area include inertial navigation and platform stabilization. The aim of this dissertation is the research and development of high-performance mode-matched vibratory microgyroscopes that have the potential to achieve near or better than sub-deg/hr resolution and bias stability.

It had been mentioned that although microgyroscopes have been utilized for an array of specialized applications that involve motion detection, they have yet to be utilized for the solitary purpose that their predecessors were initially

developed for, i.e. inertial navigation. The application space of microgyroscopes may be broadly divided, based upon performance requirements into two key categories – (a) Rate-Grade applications, and (b) Navigation-Grade applications. A summary of the requirements for each classification is shown in Table 1.1. The various gyroscope performance parameters (in relationship to micromachined vibratory gyroscopes) will be explained in detail in Chapter II.

Table 1.1: Performance requirements for rate-grade and navigation-grade gyroscopes.

Parameter	Rate-Grade	Navigation-Grade
Angle Random Walk	> 0.5 °/√hr	< 0.1 °/√hr
Bias Stability	10 – 100 °/hr	< 1 °/hr
Scale Factor Accuracy	1 – 10 %	0.1 – 1 %
Full Scale Range	100 – 1000 °/s	500 °/s
Bandwidth	> 50-100 Hz	1 – 100 Hz

Over the past few years, much of the efforts in development of micromachined silicon gyroscope have concentrated on rate-grade devices driven by investments from the automotive and consumer electronics industry. These applications typically require a resolution of 0.1deg/s in a 50Hz bandwidth. However navigation-grade performance levels required for inertial navigation systems (INS) or inertial measurement units (IMU) have eluded micromachined gyroscopes. In this chapter, a quantitative and qualitative analysis of the importance of a gyroscope performance in relation to two high-precision gyroscope application is discussed.

1.1 Inertial Navigation

Inertial navigation is a self-contained navigation technique in which measurements provided by accelerometers and gyroscopes are used to track the position and orientation of an object relative to a known starting point, orientation and velocity. It is not subject to the line-of-sight problem inherent in many radio navigation systems, and is not affected by external jamming or spoofing. This non-radiating property of inertial navigation has led to the revolutionary development in technology to produce navigation systems for military and aerospace applications. These include guidance system for ballistic missiles, submarines, and space vehicles. The development of digital computers and micro-miniaturization of electronics systems arose largely from continuing requirements of inertial navigation systems for aerospace applications, for more accuracy, higher reliability, smaller size, and lower weight [2-4]. An inertial measurement unit typically comprises of three orthogonally-positioned rate-gyroscopes, and three orthogonally-positioned accelerometers, measuring the angular velocity and linear acceleration components along each axis respectively. The fundamental principle of inertial navigation is simple, i.e. to measure the components of the vehicle's acceleration along precisely defined axes. However, the accuracy which must be achieved, and the inherent sources of error, makes practical systems inevitably complex. All IMUs fall into one of two categories. The classification is based on the frame of reference in which the rate-gyroscopes and accelerometers operate. During the course of this chapter, the navigation system's frame of reference will be referred to as the body-frame

(represented by 'b'), while the inertial reference frame (in which guidance occurs) will be referred to as the global-frame (represented by 'g'). This is schematically shown in Figure 1.1.
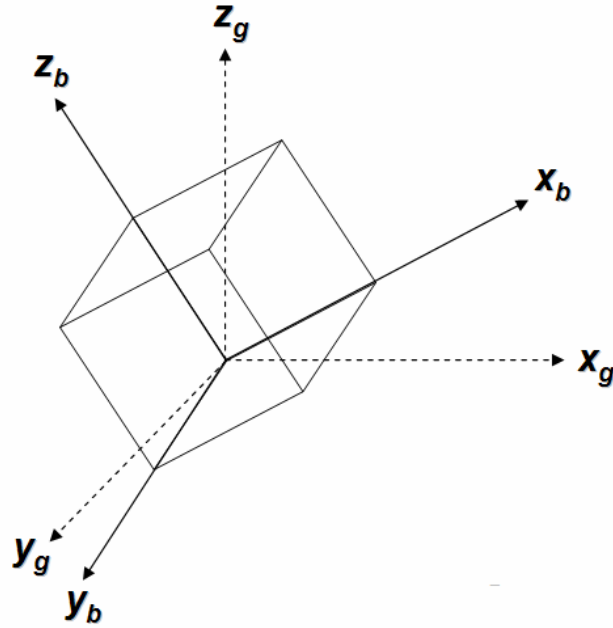
Figure 1.1: The body (b) and global (g) frames of reference.

1.1.1 Stabilized Platform Systems

In stabilized platform systems, the inertial sensors are mounted on a platform which is isolated from any external rotational motion. The platform is held in alignment with the global frame. This is achieved by mounting the platform using gimbals/frames which allow the platform freedom in all three axes. An example of such a system is illustrated in Figure 1.2 (as deployed in the Apollo series of lunar space vehicles [5]). The platform mounted gyroscopes detect any platform rotations. These signals are consequently fed back to torque motors which rotate the gimbals in order to cancel out rotations, hence keeping the platform aligned with the global frame.
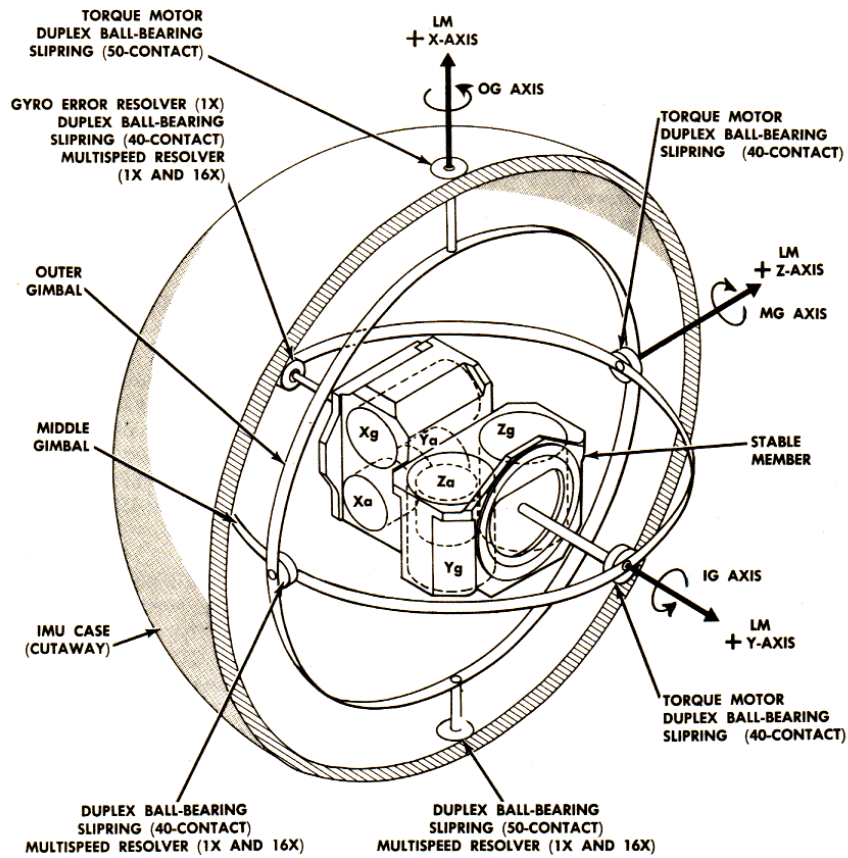
Figure 1.2: A stabilized platform IMU system [5].

Angle-pickoff readings are used to track the orientation of the device the angles between adjacent gimbals. To calculate the position of the device the signals from the platform mounted accelerometers are integrated twice. To obtain the actual acceleration experienced by the system, it is necessary to subtract the components of acceleration due to gravity. The gravitational components are evaluated from the measurements made by the on-board gyroscopes. A simplified version of the stabilized platform inertial navigation algorithm is outlined in Figure 1.3 [6].
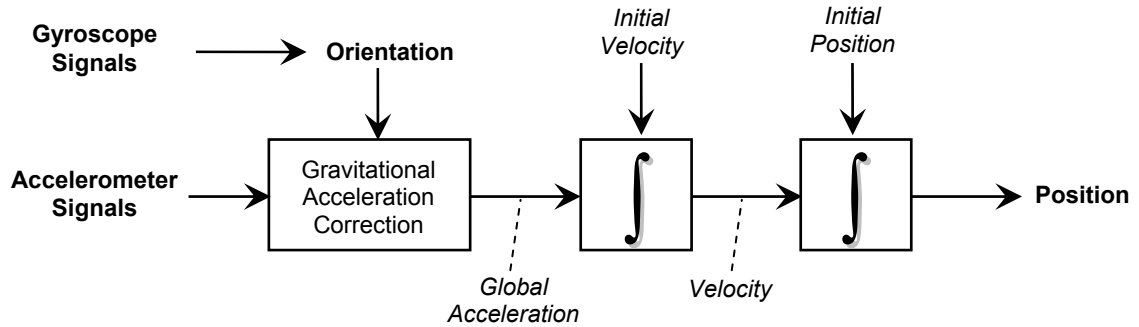
Figure 1.3: Stabilized platform inertial navigation algorithm [6].

1.1.2 Strapdown Systems

In strapdown systems the inertial sensors are mounted onto the device undergoing motion, and therefore output quantities are measured in reference to the body-frame (rather than the global-frame). To extract orientation, the angular-rate information extracted from the gyroscopes is integrated (as will be described in the following section). To track the position, the three accelerometer signals are resolved into the global coordinates using the orientation information extracted from the rate gyroscopes. An outline of a conventional strapdown inertial measurement unit is shown in Figure 1.4 [4]. In general, most strapdown IMU are integrated with global positioning system (GPS) and internal navigation correction software to correct for errors accumulated by the drift of the inertial sensors [2]. Both stabilized platform and strapdown systems are based upon the same underlying principles. Strapdown systems have reduced mechanical complexity and tend to be physically smaller than stable platform systems. These benefits are achieved at the cost of increased computational complexity. However, as the cost of computation has decreased

exponentially, strapdown systems have become the dominant type of INS. Hence, in this chapter inertial navigation system analysis will be developed using strapdown inertial technology.
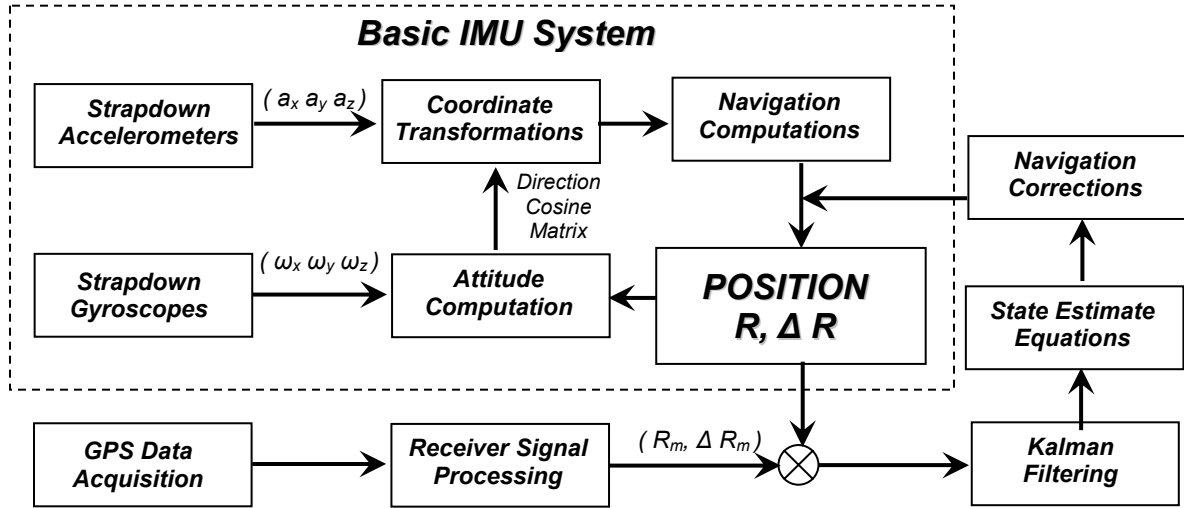
Figure 1.4: Basic block-diagram of a strapdown IMU system.

1.2 Strapdown Inertial Navigation Algorithm

A simplified version of the strapdown navigation algorithm is shown in Figure 1.5 [6]. A brief overview of the algorithm and an outline of error propagation through the algorithm is presented in this section.
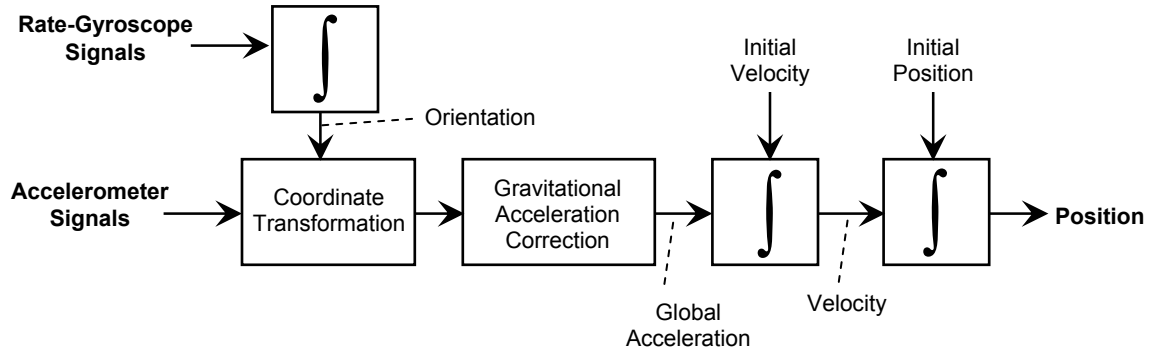
Figure 1.5: Strapdown inertial navigation algorithm [6].

1.2.1 Tracking Orientation

The orientation, or attitude, of an INS relative to the global reference frame is tracked by 'integrating' the angular velocity signal obtained from the system's rate-gyroscopes. In order to specify the orientation of an INS, direction cosines are used derive the attitude. In the direction cosines representation the attitude of the body frame relative to the global frame is specified by a 3×3 rotation matrix 'C' [6], in which each column is a unit vector along one of the body axes specified in terms of the global axes. Any vector quantity 'r_b' is expressed as in the global refernce frame as follows:

$$r_g = Cr_b \tag{1.1}$$

The inverse transformation is expressed as:

$$r_b = C^T r_g \tag{1.2}$$

To track the attitude of the INS, the component 'C' must be tracked through time. If the attitude at time 't' is given by 'C(t)', then the rate of change of 'C' is expressed as follows:

$$\frac{dC(t)}{dt} = \lim_{\partial t \to 0} \frac{C(t + \partial t) - C(t)}{\partial t} \tag{1.3}$$

In Eq. 1.3, C (t+δt) may be written as the product of two matrices in Eq. 1.4. A(t) is the rotation matrix which relates the body-frame at time 't' to the body frame at time 't+δt'.

$$C(t + \partial t) = C(t)A(t) \tag{1.4}$$

8

If δΦ, δθ, and δΨ represent small rotations (along x,y, and z-axes respectively) through which the body frame has rotated in the time interval 'δt', then using small angle approximation A(t) may be expressed as following [6]:

$$A(t) = I + \delta\Theta \tag{1.5}$$

$$\delta\Theta = \begin{pmatrix} 0 & -\partial\psi & \partial\theta \\ \partial\psi & 0 & -\partial\phi \\ -\partial\theta & \partial\phi & 0 \end{pmatrix} \tag{1.6}$$

Therefore, by substituting Eq. 1.4-1.6 in Eq. 1.3:

$$\frac{dC(t)}{dt} = \lim_{\partial t \to 0} \frac{C(t)A(t) - C(t)}{\partial t} \tag{1.7}$$

$$\frac{dC(t)}{dt} = \lim_{\partial t \to 0} \frac{C(t)(I + \partial\Theta) - C(t)}{\partial t} \tag{1.8}$$

$$\frac{dC(t)}{dt} = C(t) \lim_{\partial t \to 0} \frac{\delta\Theta}{\delta t} \tag{1.9}$$

$$\lim_{\partial t \to 0} \frac{\delta\Theta}{\delta t} = \Omega(t) \tag{1.10}$$

$$\Omega(t) = \begin{pmatrix} 0 & -\omega_{bz}(t) & \omega_{by}(t) \\ \omega_{bz}(t) & 0 & -\omega_{bx}(t) \\ -\omega_{by}(t) & \omega_{bx}(t) & 0 \end{pmatrix} \tag{1.11}$$

In Eq. 1.11, $\Omega(t)$ represents the skew-symmetric form of the angular rate vector $\omega_b(t)$. Therefore in orientation information is extracted from the attitude algorithm through the following differential equation solutions:

$$\frac{dC(t)}{dt} = C(t)\Omega(t) \tag{1.12}$$

The solution of Eq. 1.12 is as follows, where C(0) is the initial attitude of the device.

$$C(t) = C(0)\exp\left(\int_0^t \Omega(t)dt\right)$$

(1.13)

However, in conventional INS the continuous signal $\omega_b(t)$ generated from the strapdown gyroscopes, is actually sampled data of the angular velocity (at a fixed sampling frequency). Hence, an integration scheme is typically used to integrate the sampled signal. A rectangular rule solution presented adroitly in [6], will be used in this discussion. Let the period between successive angular velocity samples be δt. For a single period $[t, t + \delta t]$ the solution to Equation 1.12 may be written as:

$$C(t + \delta t) = C(t)\exp\left(\int_t^{t+\partial t} \Omega(t)dt\right)$$

(1.14)

$$\int_t^{t+\partial t} \Omega(t)dt = B$$

(1.15)

$$B = \begin{pmatrix} 0 & -\omega_{bz}(t)\partial t & \omega_{by}(t)\partial t \\ \omega_{bz}(t)\partial t & 0 & -\omega_{bx}(t)\partial t \\ -\omega_{by}(t)\partial t & \omega_{bx}(t)\partial t & 0 \end{pmatrix}$$

(1.16)

By letting $\sigma = |\omega_b \delta t|$, and substituting Eq. 1.15 in Eq. 1.12:

$$C(t + \delta t) = C(t)\left(1 + B + \frac{B^2}{2!} + \frac{B^3}{3!} + \frac{B^4}{4!} + \ldots\right)$$

(1.17)

$$C(t + \delta t) = C(t)\left(1 + B + \frac{B^2}{2!} + \frac{\sigma^2 B}{3!} + \frac{\sigma^2 B^2}{4!} + \ldots\right)$$

(1.18)

$$C(t + \delta t) = C(t)\left(I + \frac{\sin\sigma}{\sigma}B + \frac{1 - \cos\sigma}{\sigma^2}B^2\right)$$

(1.19)

Eq. 1.19 represents the attitude update equation used to update 'C' at the arrival of a new measurement sample. The angular velocity signals obtained from the gyroscopes are 'integrated' by the standard INS attitude algorithm; therefore errors in the gyroscope signals propagate through to the calculated orientation (as seen in Figure 1.5). For micromachined vibratory gyroscopes white noise and uncorrected bias errors are the main causes of an error in the orientation. White noise causes an angle random walk whose standard deviation grows proportionally to the square root of time [6]. An uncorrected bias causes an error in orientation which grows linearly with time. Quantization errors also arise in the calculated attitude due to the quantization of the angular velocity samples and due to the integration scheme used to update C. An examination of the various gyroscope errors present in the prototype designs examined in this dissertation were performed using Allan variance analysis [7], and have been summarized in Chapter VI.

1.2.2 Tracking Position

To track the position (which is the ultimate objective of an inertial navigation system) the acceleration signal '$a_b(t)$', obtained from the accelerometers is projected into the global frame of reference:

$$a_g = C(t)a_b \tag{1.20}$$

Acceleration components due to gravity are consequently eliminated and the residual acceleration component (true device acceleration) is integrated once to obtain velocity, and then successively repeated to obtain the displacement:

$$v_g(t) = v_g(0) + \int_0^t \left(a_g(t) - g_g \right) dt \qquad\qquad (1.21)$$

$$x_g(t) = x_g(0) + \int_0^t v_g(t) dt \qquad\qquad (1.22)$$

In Eq. 1.21 and Eq. 1.22, '$v_g(0)$' and '$x_g(0)$' represent the initial velocity and initial displacement of the device respectively and is the initial displacement and 'g_g' is the acceleration due to gravity in the global reference frame. As with attitude algorithm, the rectangular rule of integration was adopted to integrate each measurement sample of the accelerometer [6].

$$v_g(t + \partial t) = v_g(t) + \partial t \left(a_g(t + \partial t) - g_g \right) \qquad\qquad (1.23)$$

$$x_g(t + \partial t) = x_g(t) + \partial t \left(v_g(t + \partial t) \right) \qquad\qquad (1.24)$$

Errors which arise in the accelerometers propagate through the double integration and attributes to the drift in tracked position. However, the errors in the angular velocity signals are the major contributor to drift in the calculated position. The rotation matrix 'C' obtained from the attitude algorithm is used to project the acceleration signals into global coordinates. Therefore, an error in orientation causes an incorrect projection of the acceleration signals onto the global axes. This leads to integration of the device acceleration along the wrong directions as the gravitational components of acceleration are no longer evaluated correctly. A tilt error '$\delta\theta$' (evaluated from the gyroscope output) will cause a component of the acceleration due to gravity with magnitude 'g sin($\delta\theta$)' to be projected onto the accelerometer horizontal axes. This causes a residual bias due to gravity with magnitude 'g sin($\delta\theta$)' to remain in the globally

horizontal acceleration signals. Similarly, there will also be a residual bias of magnitude 'g (1-cos(δθ))' in globally vertical axis. However this is much less severe since for small δθ, using small-angle approximation, cos(δθ) → 1 and sin(δθ) → δθ. Hence the error in position caused by a residual tilt error bias will mainly be projected along the global horizontal-plane. It can be inferred that the propagation of gyroscope errors through to the calculated position is the critical error path in nearly all INS systems [2-4, 6]. In many applications the magnitude of g is much greater than the mean absolute acceleration of the IMU in motion. In such cases the component of the acceleration due to gravity is projected onto the globally horizontal axes. This residual bias causes an error in the horizontal position which consequently grows quadratically and makes integration with GPS essential.

1.3 Gyrocompassing: Platform Alignment

Inertial navigation can only be as accurate as the initial conditions which are set in. When an INS is started, a sequence of operation is performed to align the system to specific coordinates before it is operational. In terrestrial surveillance vehicles self-alignment is typically performed using only the sensors of the INS. The two basic references used to align an INS are the Earth's gravitational vector and its rotation vector. The local vertical is determined through the gravity vector and the earth's spin provides the reference for north. The process occurs in two consecutive steps called leveling and gyrocompassing (or north-alignment). During leveling, the platform is maneuvered such that the horizontal accelerometers do not measure a component of gravity.

13
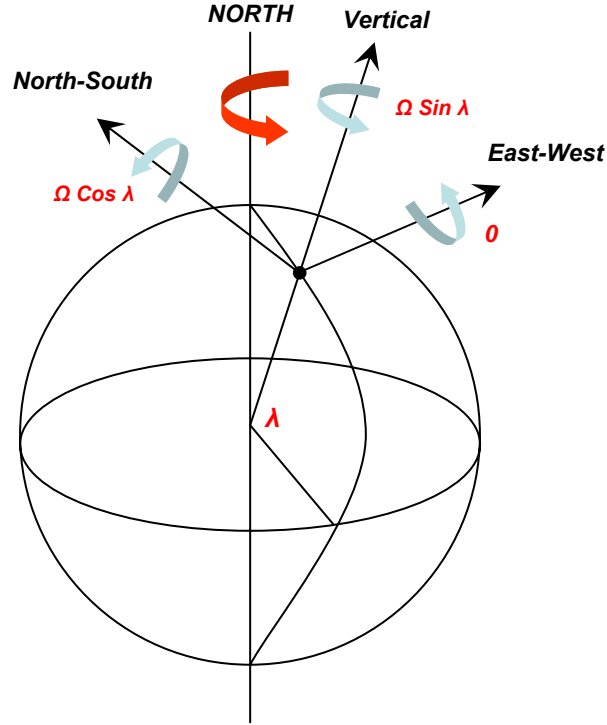
Figure 1.6: Illustration of gyrocompassing (with three isolated gyroscopes)

At this point, the vertical accelerometer is aligned along the local vertical (and the platform is level). Gyrocompassing is accomplished by rotating the level platform about the vertical until the gyroscope defining the east axis senses zero component of the Earth's rotation. A coarse azimuth alignment with respect to true north is initially made to within a few degrees by using a magnetic compass reference [2, 3]. The components of the Earth's rate of rotation, Ω, about the north-south, east-west, and vertical axes at latitude 'λ' are shown in Figure 1.6.

If the platform axes are misaligned in the horizontal plane by an amount $\Delta\Psi$, from true north, then the east-west (x-axis) gyroscope measures a rate '$\Omega\cos(\lambda)\sin(\Delta\Psi)$', which reduces to '$\Omega\cos(\lambda)\Delta\Psi$' for small-angle approximation. Assuming that y-axis and z-axis gyroscopes are being supplied with feedback signals to compensate for '$\Omega\cos(\lambda)$' and '$\Omega\sin(\lambda)$' respectively, then in the

absence of an erection and gyrocompassing loops, the "north" or y-axis accelerometer will be titled from the horizontal at a rate of 'Ωcos(λ)ΔΨ'. A closed-loop system may be formulated [3] whereby the y-axis accelerometer output is constantly fed into the azimuth (z-axis) gyroscope as well as into the x-gyroscope, the x-axis accelerometer being coupled into the y-axis gyroscope. In steady state (assuming perfect gyroscope operation), ΔΨ must come to zero, and there is no tilt.

The gyrocompassing step is often complicated by the low signal-to-noise ratios encountered when measuring the relatively small earth rate. Systematic gyroscope drift must also be eliminated for the technique to be practical. The allowable drift of the x-axis gyroscope can be determined from the accuracy required from the azimuth alignment. If an accuracy of 0.1˚ is required for a latitude location of 45˚, then the component of the Earth's rate, sensed at this latitude with a misalignment of 0.1˚ is equal to 0.017 deg/hr.

$$\left(\frac{0.1}{360/2\pi}\times 15\sin 45°\right)\deg/hr \tag{1.25}$$

It can be naturally inferred that the magnitude of the component of earth's rate to be sensed decreases with increasing latitude, so that the gyrocompassing is effectively restricted to the latitudes below 80˚ [3].

1.4 Current High-Precision Gyroscope Solutions

As illustrated in Figure 1.7 [1], the performance specifications of navigation-grade gyroscopes compatible with inertial navigation and platform stabilization are currently only met by bulk-mechanical gyroscopes and optical gyroscopes.

15

MEMS gyroscopes, referred as rate/integrating gyros in Figure 1.7, do not occupy any application space beyond 15 deg/hr. In this section, a brief analysis of the conventional gyroscope will be provided highlighting the inherent drawbacks of current navigation-grade solutions.
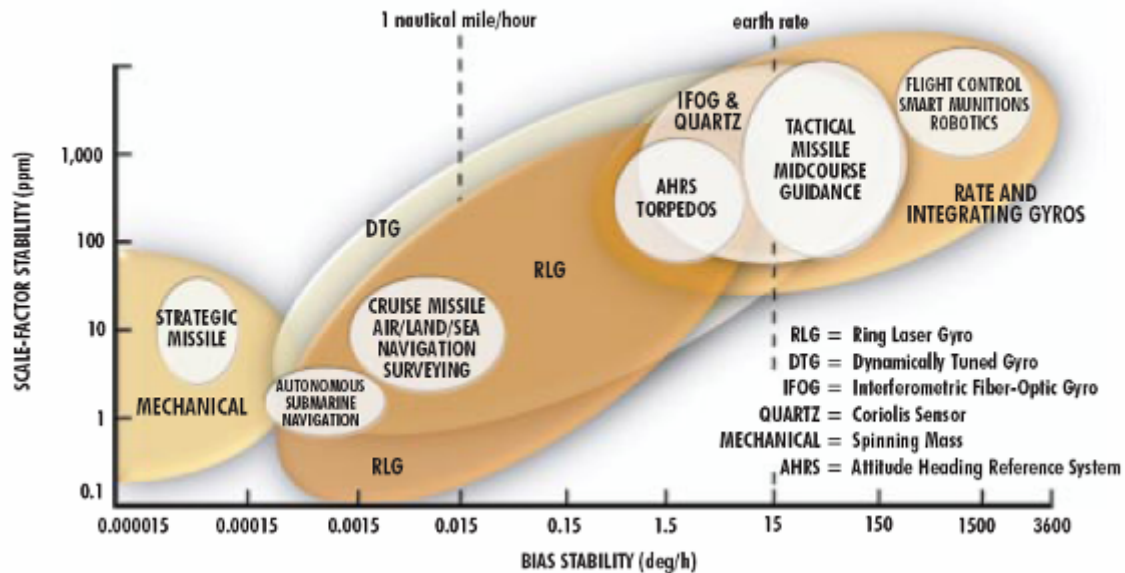
Figure 1.7: Current gyroscope technology application space [1].

1.4.1 Mechanical Gyroscopes

Mechanical gyroscopes are comprised of a spinning wheel mounted on two gimbals which allow rotation along all three axes as shown in Figure 1.8. Due to conservation of angular momentum, the spinning wheel will resist change in orientation. Hence when a mechanical gyroscope is subjected to a rotation, the wheel will remain at a constant global orientation and the angles between the adjacent gimbals will change. To measure the orientation of the device, the angles between the adjacent gimbals is read using angle pick-offs.

16
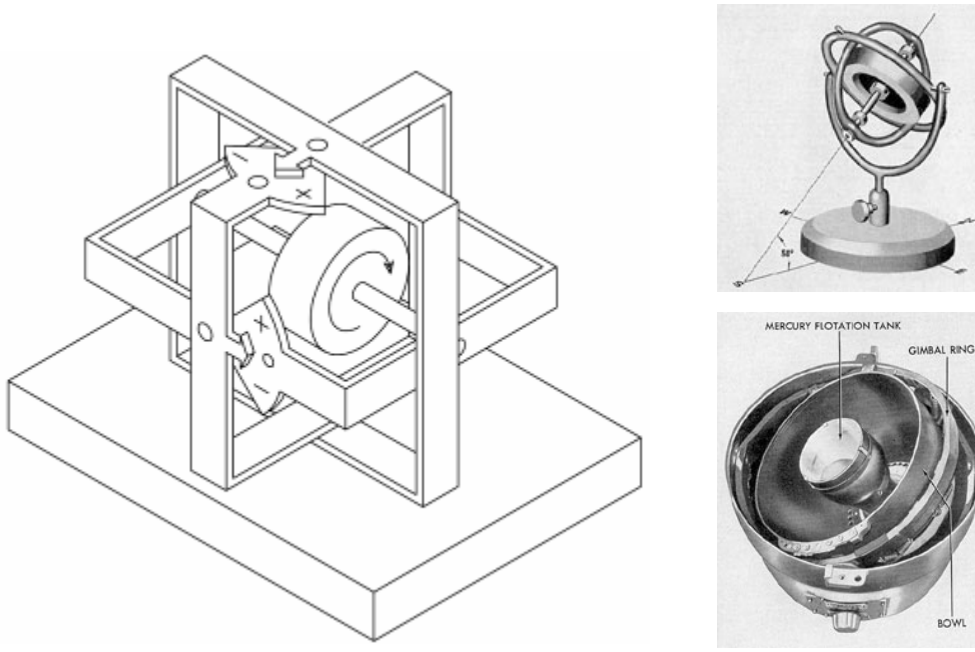
Figure 1.8: Conventional mechanical gyroscopes [6, 9].

It must be noted that a mechanical gyroscope measures orientation directly. Optical and vibratory gyroscopes (which are the subject-matter of this dissertation) are rate gyroscopes, which measures angular velocity. The main disadvantage of the mechanical gyroscopes is that they comprise of moving/spinning parts, which lead to friction. This eventually causes drift over time. To minimize the frictional effects, high-precision bearings and special lubricants are required, thereby adding to the overall cost to the manufacture and maintenance of the device. Mechanical gyroscopes also require warm-up time, which is not ideal for many applications [3, 8].

1.4.2 Optical Gyroscopes

A fiber optic gyroscope (FOG) uses the interference of light to measure angular velocity. A FOG consists of a large coil of optical fiber. Two beams of light are introduced into the optical coil along opposite directions. When the FOG

17

undergoes rotation, the beam of light travelling along the direction of rotation will experience a longer path-length than its counter-part (travelling along the other direction). This phenomenon illustrated in Figure 1.9 is referred to as the Sagnac effect and constitutes the working principle of all optical gyroscopes.
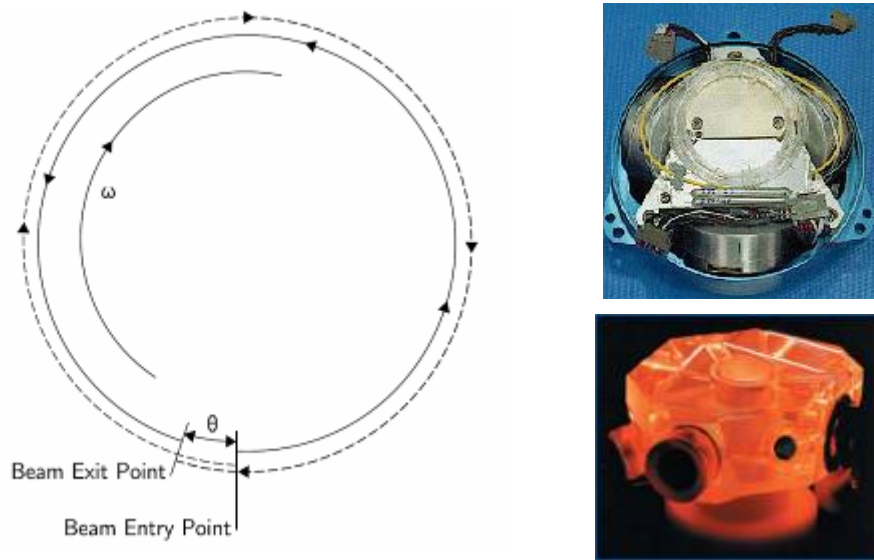
Figure 1.9: Illustration of the Sagnac effect utilized in optical gyroscopes [6, 9]. (Top-Right) An example of IFOG. (Bottom-Right) An example of RLG.

The phase-shift introduced between the opposite beams due to the Sagnac effect causes interference patterns, and the resulting intensity is a function of the angular velocity. Ring laser gyroscopes (RLG) are also based on the Sagnac effect and rely on laser beams being directed around a closed path using mirrors rather than optical fiber. Unlike mechanical gyroscopes, optical gyroscopes contain no moving parts and require only a few seconds to start-up. However, the accuracy of an optical gyro is largely dependent on the length of the light transmission path (larger is better), which is constrained by the size of the device. Also optical gyroscopes rely on the complicated assembly of several

external components such as laser-sources, and power-intensive detection mechanisms which make unite cost quite prohibitive in several applications. Figure 1.10 depicts two common IMU solutions implemented using optical gyroscopes [10, 11] and it is evident that despite sub-deg/hr performance demonstration, size-constraints, assembly and power requirements represent a major drawback in comparison to a MEMS solution.
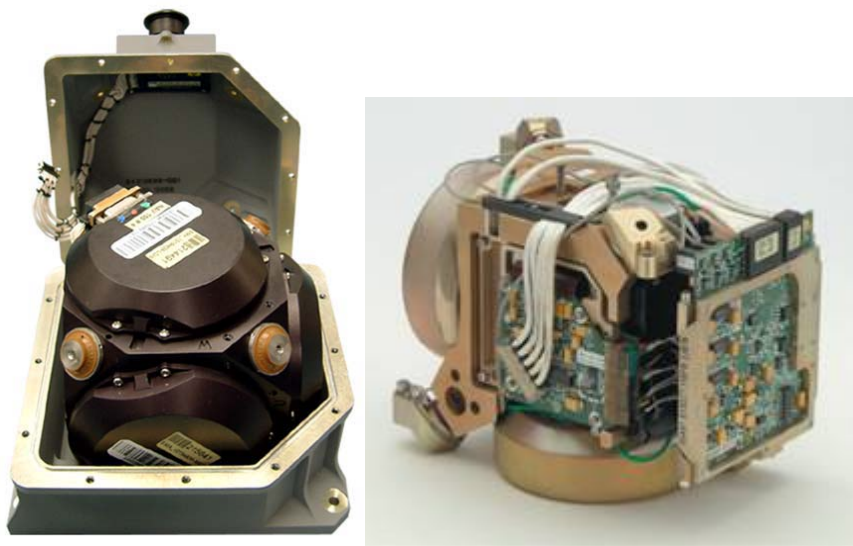
Figure 1.10: (Left) Honeywell HG-9900 RLG-based IMU [10]. (Right) Northrop Grumman LN260 IFOG-based IMU [11].

1.4.3 Quartz-Based Vibratory Gyroscopes

The final class of high-performance gyroscope with navigation-grade performance capabilities is the hemispherical resonator gyroscope (HRG). The HRG sensor is comprised of three machined-parts – a high-Q vibrating hemispherical resonator, and inner and outer shells (which support the resonator within). The quartz construction of the HRG is inherently stable, impervious to aging effects and naturally radiation-hard [12]. Operating in a completely

evacuated hermetically sealed case, the HRG sensor is immune to wear-out making it the ideal-gyroscope for space applications. The IMU based upon the HRG, commonly referred to as Space Inertial Reference Unit (SIRU), is shown in Figure 1.11. The SIRU has been reported to demonstrate bias stability of 0.0003 deg/hr and a resolution of 0.00006 deg/hr/$\sqrt{Hz}$. However, the SIRU unit consumes power in excess of 10W, and weighs more than 10lbs (occupying a large footprint). The HRG is an example of a vibratory gyroscope, operating based upon the Coriolis principle, and offers realistic potential for MEMS gyroscope to achieve sub-deg/hr performance in the near future.

Figure 1.11: The quartz-core of the HRG. (Left) An SIRU unit based upon the HRG [13]

1.5 Motivation

Silicon micromachined gyroscopes have yet to break into the high-precision market currently dominated by bulk-mechanical and optical gyroscopes. A survey of Table 1.2 demonstrates the disparity between two classes of devices manufactured by Honeywell. The GG1320AN [14] represents the most

inexpensive RLG in production, while the GG5300 [15] is the most accurate MEMS

gyroscope in production.

Table 1.2: Performance comparison between Honeywell's RLG and MEMS Gyroscopes.

Parameter	GG1320AN (RLG)	GG5300 (MEMS)
Size (Weight)	88mm x 55mm x 30mm (454g)	50mm x 50mm x 30mm (136g)
Start-Up Time	< 4s	< 1s
Power	15V, 1.6W	5V, <500mW
Operating Bandwidth	1000 Hz	100 Hz
Angle Random Walk	0.0035 °/√hr	0.2 °/√hr
Bias Stability	0.0035 °/hr	70 °/hr

Even the most accurate MEMS gyroscope in production (at Honeywell) is a few

orders of magnitude away from the mid-performance RLG in terms of the device

resolution and bias stability, two parameters critical for high-precision

applications such as inertial navigation and gyrocompassing. The goal of this

research topic is to identify the shortcomings of the existing MEMS gyroscope

through the detailed evaluation of the device parameters pertaining to Coriolis-

based vibratory gyroscopes. Two distinct structures, the resonating star

gyroscope and the mode-matched tuning fork gyroscope, are developed

during the course of this dissertation that will enable performance approaching

sub-deg/hr resolution and bias stability.

1.6 Dissertation Organization

The remainder of this dissertation is organized in the following manner:

Chapter II discusses the salient features of the micromachined vibratory

gyroscopes. The advantage of mode-matching is highlighted in reference to the

gyroscope performance metrics, and a few design rules are developed to

implement prototype gyroscope designs capable of demonstrating sub-deg/hr resolution and bias stabilities. The chapter concludes with a historical overview of micromachined gyroscopes presented in literature and also summarizes a list of commercially available MEMS gyroscopes. *Chapter III* introduces the design, implementation, and characterization of a novel shell-type Class-II vibratory microgyroscope, the resonating star gyroscope (RSG). A novel Class-I vibratory microgyroscope is the subject of *Chapter IV*. The concept and design of the mode-matched tuning fork gyroscope (M^2-TFG) is discussed. Both chapters also explore and identify the contribution of thermo-elastic damping as the dominant energy loss mechanisms present in vibratory gyroscopes operated using flexural vibration modes of the structure. The control system of the M^2-TFG is discussed in *Chapter V*. The chapter begins with an examination of trans-impedance amplifiers as front-end interfacing for motional current detection. Following a discussion of the sense and drive-channels of the operating system, the chapter ends with a closer look at quadrature error and means of eliminating it to ensure perfect mode matching (i.e. 0Hz frequency split between operating modes). *Chapter VI* presents the characterization results of the M^2-TFG. A detailed account of the sensitivity and bias stability measurements of the device is made during the course of this chapter. A novel bulk-micromachining fabrication technology developed for enhancing the capacitive aspect ratio of the M^2-TFG is the topic of *Chapter VII*. This chapter also presents the preliminary characterization results of vacuum packaged M^2-TFG prototypes. Finally, *Chapter VIII* provides an overview of the contributions of this research and possible future directions in the area of device performance optimization.

CHAPTER II

MICROMACHINED VIBRATORY GYROSCOPES

Despite years of development, mechanical and optical gyroscopes still have high part counts and a requirement for components with high-precision tolerances and complicated assembly techniques. As a result they remain exceedingly expensive. In contrast MEMS gyroscopes built using silicon micromachining technology have low part counts and are relatively cheap to manufacture in commercial quantities. In this chapter, we discuss the most popular class of MEMS gyroscopes, the Coriolis-based vibratory gyroscopes and give an overview of the performance parameters that define their performance.

2.1 Coriolis Vibratory Gyroscopes

Coriolis-based micromachined vibratory gyroscopes use vibrating mechanical elements to sense rotation. They have no rotating parts that require bearings and can be easily miniaturized and batch fabricated using conventional silicon micromachining techniques. Vibratory gyroscopes are based on the transfer of energy between two vibration modes of a structure caused by Coriolis acceleration. Coriolis acceleration, named after the French scientist and engineer Gaspard Gustave de Coriolis (1792-1843), is an apparent acceleration that arises in a rotating reference frame and is proportional to the rate of rotation [16]. The Coriolis Effect may be illustrated by an example of a flying object as viewed through the eyes of an observer located on a rotating reference frame as seen in Figure 2.1.

23
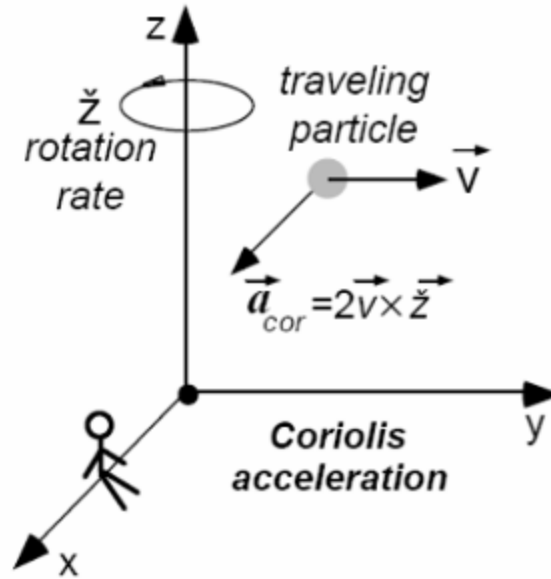
Figure 2.1: Visualization of the Coriolis Effect.

The observer located along the x-axis of the xyz coordinate system is viewing an object traveling above him in space with a certain velocity 'v'. If the observer's reference frame rotates normally (about the z-axis) by an angular velocity 'ž', to the observer the object appears to move towards the x-axis with an acceleration equivalent to '2v X ž'. Although no real force has been exerted on the flying object, to the observer located on the rotating reference frame, an apparent force has resulted which is directly proportional to the rate of rotation.

2.1.1 Coriolis Acceleration

To better understand Coriolis acceleration it is often helpful to study it analytically. In Figure 2.2, Frames A and B are the inertial and rotating reference frames respectively. The component 'r_A' and 'r_B' are position vectors relative to the inertial and rotating frames. Finally, θ and R refer to the orientation and position of the rotating frame B.
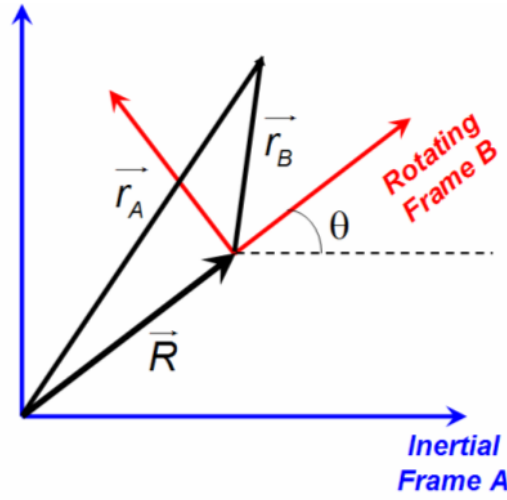
Figure 2.2: Illustration of the coordinate reference frames.

The time derivative of any vector 'r', which is defined in frames A and B, is indicated by the transport theorem as [17]:

$$\frac{d}{dt}r_A(t) = \frac{d}{dt}r_B(t) + \frac{d}{dt}\theta \times r_B(t)$$

(2.1)

Taking the second time derivative of the position vector, the acceleration of a body moving with the rotating reference frame may be calculated as:

$$r_A(t) = R(t) + r_B(t)$$

(2.2)

$$\frac{d}{dt}r_A(t) = \frac{d}{dt}R(t) + \frac{d}{dt}r_B(t) + \frac{d}{dt}\theta \times r_B(t)$$

(2.3)

$$\frac{d^2}{dt^2}r_A(t) = \frac{d^2}{dt^2}R(t) + \frac{d^2}{dt^2}r_B(t) + \frac{d}{dt}\theta \times \frac{d}{dt}r_B(t) + \frac{d}{dt}\theta \times \left(\frac{d}{dt}\theta \times r_B(t)\right) + \frac{d^2}{dt^2}\theta \times r_B(t) + \frac{d}{dt}\theta \times r_B(t)$$

(2.4)

By replacing the first and second time derivatives of the references frames with velocity and acceleration components, the acceleration expression reduces to:

$$a_A = A + a_B + \Omega \times r_B + \Omega \times (\Omega \times r_B) + 2\Omega \times v_B$$

(2.5)

25
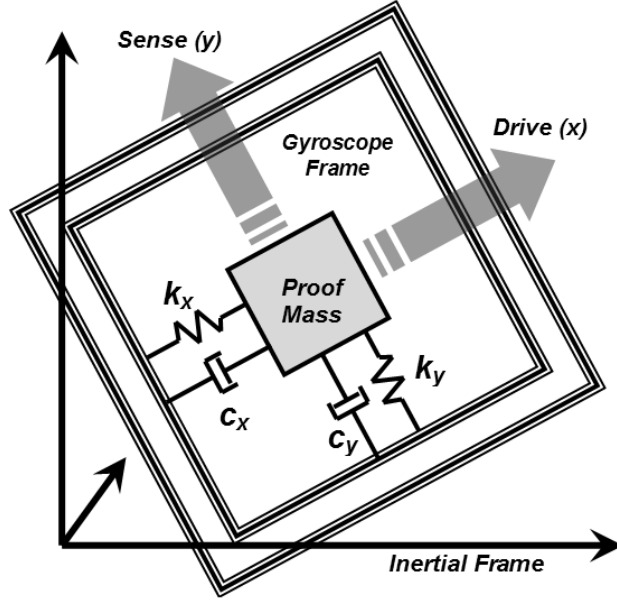
Figure 2.3: Illustration of a single proof-mass vibratory gyroscope.

2.1.2 Vibratory Gyroscope Dynamics

In Eq. 2.5, '$2\Omega \times v_B$' is the Coriolis term. The vibratory rate gyroscope can essentially be viewed as an accelerometer measuring the Coriolis acceleration to determine the rotation rate. Figure 2.3 will be used to examine the equations of motion of a typical vibratory gyroscope (based on a single-proof mass) subjected to rotation about an inertial reference frame. In order to analyze the dynamics of the 2-DOF gyroscope, Lagrange's equation is used to derive the equations of motion [18].

When the proof-mass motion is decomposed along its two principal vibratory axes, the two equations of motions are expressed as:

$$M\frac{d^2}{dt^2}x + c_x\frac{d}{dt}x + k_x x - M\Omega_z^2 x - y\frac{d}{dt}\Omega_z = 2M\Omega_z\frac{d}{dt}y \tag{2.6}$$

$$M\frac{d^2}{dt^2}y + c_y\frac{d}{dt}y + k_y y - M\Omega_z^2 y - x\frac{d}{dt}\Omega_z = 2M\Omega_z\frac{d}{dt}x \tag{2.7}$$

26

The linear acceleration components of Eq. 2.5 may be large, but is ignored. This is because the Coriolis acceleration signal is modulated by the vibration signal which is typically at large frequencies (much higher than linear acceleration signals). The linear acceleration is consequently filtered out. By neglecting the minimal contributions of the second derivative components of off-axes angular acceleration (because typically $\omega \gg \Omega$), the simplified 2-DOF equations of motion for the gyroscope proof-mass may be expressed as follows:

$$M\frac{d^2}{dt^2}x + c_x\frac{d}{dt}x + k_x x = 2M\Omega_z\frac{d}{dt}y \qquad (2.8)$$

$$M\frac{d^2}{dt^2}y + c_y\frac{d}{dt}y + k_y y = 2M\Omega_z\frac{d}{dt}x \qquad (2.9)$$

The two final terms '$2M\Omega_z\frac{d}{dt}x$' and '$2M\Omega_z\frac{d}{dt}y$' are rotation induced Coriolis-force components and cause dynamic coupling between the vibratory axes. They are utilized for angular rate measurements in a vibratory gyroscope. From Eq. 2.8-2.9, it is evident that it is necessary to devise a mechanism to excite the mass into its reference vibration mode. A second mechanism must be implemented to pick-off the Coriolis induced signal. A number of schemes have been used to implement the drive and pick-off mechanisms for Coriolis-based vibratory microgyroscopes. The reference drive excitation can be achieved using piezoelectric, capacitive electrostatic or electromagnetic actuation schemes. Similarly, the Coriolis signal can be picked-off using piezo-resistive or capacitive means. The subject matter of this dissertation refers mainly to the case of capacitive, silicon-based vibratory microgyroscopes.

A better understanding of the dynamics of a single proof-mass 2-DOF vibratory gyroscope system (shown in Figure 2.3) can be acquired by starting with the assumption that the system is driven open-loop. A driving force 'F_d' applies a constant driving amplitude 'x' along the drive axis at the drive-mode resonant frequency 'ω_{drive}'. The equations of motion expressed in Eq. 2.8-2.9 may be expressed as follows:

$$M\frac{d^2}{dt^2}x + c_x\frac{d}{dt}x + k_xx = F_{drive}\sin\left(\omega_{drive}t\right)$$ (2.10)

$$M\frac{d^2}{dt^2}y + c_y\frac{d}{dt}y + k_yy = 2M\Omega_z\frac{d}{dt}x$$ (2.11)

The system has two independent resonant frequencies: the drive-mode resonant frequency (along the x-axis) which is '$\omega_x = \sqrt{k_x/M}$' and the sense-mode resonant frequency (along the y-axis) which is '$\omega_y = \sqrt{k_y/M}$'. When the stiffness values in the drive and sense directions are the same (i.e. $k_x = k_y$), then the two resonant modes will be matched (i.e. $\omega_x = \omega_y$).

As seen in Eq. 2.10, in the ideal case, the drive-mode is not influenced by the sense-mode and can be well-controlled. Also it is known that:

$$Q = \frac{M\omega_0}{c}$$ (2.12)

$$\omega_0 = \sqrt{\frac{k}{M}}$$ (2.13)

In Eq. 2.12, 2.13 'Q' and 'ω_0' represent the quality-factor and resonance frequency respectively. Assuming that the drive mode is operated in a sinusoidal fashion, the expression for displacement along the drive-mode is as follows:

$$x(t) = \frac{F_{drive}}{k_x} \frac{1}{\sqrt{\left(1 - \left(\frac{\omega_{drive}}{\omega_x}\right)\right)^2 + \left(\frac{\omega_{drive}}{Q_x\omega_x}\right)^2}} \sin\left(\omega_{drive}t - \phi_x\right) \qquad (2.14)$$

It is evident that when the driving frequency is equal to the drive-mode resonance frequency, i.e. $\omega_d = \omega_x$, there is a Q_x enhancement in the drive-mode displacement as seen in Eq. 2.15

$$x(t) = \frac{F_{drive}}{k_x} Q_x \sin\left(\omega_x t - \phi_x\right) \qquad (2.15)$$

Now the expression for the sense-mode deflection in response to rotation-induce Coriolis acceleration (along the normal z-axis) may be expressed as follows:

$$y(t) = \frac{2Q_x\omega_x F_{drive}\Omega_z}{k_x\omega_y^2} \frac{1}{\sqrt{\left(1 - \left(\frac{\omega_{drive}}{\omega_y}\right)\right)^2 + \left(\frac{\omega_{drive}}{Q_y\omega_y}\right)^2}} \sin\left(\omega_{drive}t - \phi_y\right) \qquad (2.16)$$

It is clear from Eq. 2.16, that when the sense-mode is equal to the drive-mode frequency, i.e. $\omega_d = \omega_y$, there is a Q_y enhancement in the sense-mode displacement. Also it can be inferred from Eq. 2.16, that when the device is operated at mode-matched resonance, $\omega_0 = \omega_y = \omega_x$, there is a Q-factor enhancement in both drive-amplitude and consequent sense-mode deflection.

$$y(t) = \frac{2Q_x Q_x F_{drive}\Omega_z}{k_x\omega_0} \sin\left(\omega_0 t - \phi_y\right) \qquad (2.17)$$

The ratio between the drive-mode and sense-mode deflections is:

$$\frac{y}{x} = \frac{2\Omega_z Q_y M\omega_0}{k_y} = \frac{2\Omega_z Q_y}{\omega_0} \quad \left(Mode - Matched\ Operation\right) \qquad (2.18)$$

The phase difference between the drive and sense-mode deflections is:

$$\phi = \phi_{drive} - \phi_y = \tan^{-1}\left(\frac{\omega_{drive}/\omega_y}{Q_y\left(1-\omega_{drive}/\omega_y\right)^2}\right) - 90° \qquad (2.19)$$

2.2 Vibratory Gyroscope Performance Specifications

Several specifications exist for vibratory gyroscope which determines performance. In this section, a partial set of the more important parameters have been discussed. A complete list of vibratory gyroscope parameters can be found in the published IEEE standard for inertial sensor technology [19].

2.2.1 Resolution

The resolution of a gyroscope represents the minimum detectable rotation rate that can be distinguished from the noise floor of the system per square-root of the bandwidth of detection. Resolution is typically expressed in units of deg/hr/√Hz or deg/s/√Hz. The overall resolution of a vibratory gyroscope (total noise equivalent rotation - TNEΩ) is determined by two uncorrelated components: the mechanical (or Brownian) noise equivalent rotation (MNEΩ) and the electronic noise equivalent rotation (ENEΩ).

$$TNE\Omega = \sqrt{MNE\Omega^2 + ENE\Omega^2} \qquad (2.20)$$

Brownian motion of the structure caused by molecular collisions from surrounding medium represents the mechanical noise component of any vibratory gyroscope [20]. The Brownian noise displacement for a second order mass-spring system undergoing harmonic motion is expressed as:

$$\left|y_{Brownian}\right| = \sqrt{4k_BTR}\, \frac{1\!\!/k_y}{\sqrt{\left(1-\left(\dfrac{\omega}{\omega_y}\right)^2\right)^2 + \left(\dfrac{\omega}{Q_y\omega_y}\right)^2}} \qquad (2.21)$$

In Eq. 2.21, the mechanical resistance is expressed as:

$$R = \frac{k_y}{Q_{EFF}\omega_0} = \frac{M\omega_0}{Q_{EFF}} \qquad (2.22)$$

Hence at resonance, the Brownian displacement is as follows:

$$\left|y_{Brownian}\right| = \sqrt{\frac{4k_BTQ_{EFF}}{M\omega_0^3}} \qquad (2.23)$$

By equating the displacement caused by Brownian motion to the displacement induced by Coriolis acceleration (as shown in Eq. 2.17) one may derive the mechanical resolution of a vibratory microgyroscope. This expression (for matched-mode operation) is shown in Eq. 2.24.

$$MNE\Omega \propto \frac{1}{x_{drive}} \sqrt{\frac{4k_BT}{\omega_0 MQ_{EFF}}} \sqrt{BW} \qquad (2.24)$$

In Eq. 2.24, the quantities 'k_B', 'T', and 'BW' represent the Boltzmann's constant (1.38e-23 Joules/K), operating temperature (K) and measurement bandwidth (Hz) respectively. 'Q_{EFF}' represents the effective mode-matched quality factor of the system. Mode-matching offers a $\sqrt{Q_{EFF}}$ factor enhancement in the mechanical resolution of the device.

The electronic noise floor is dependent on the input referred noise of the front-end electronics interface. This dissertation will focus on transimpedance based

front-end electronics, and the electronic noise floor for vibratory gyroscope in such an implementation is expressed as [21]:

$$ENE\Omega \propto \frac{d_{s0}}{2V_P C_{s0} Q_{EFF} x_{drive}} I_{N-Total} \sqrt{BW} \qquad (2.25)$$

In Eq. 2.25, 'V_P' and '$I_{N-total}$' represent the polarization voltage applied to the structure, and the total noise equivalent input noise current respectively. 'C_{s0}' and 'd_{s0}' are the sense rest capacitance and initial sense gap respectively.

It is evident from Eq. 2.24-2.25 that the drive amplitude 'x_{drive}', resonant mass 'M', sense gap, and the effective quality factor all play a key role in determining the overall noise floor. The impact of mode-matching can be highlighted by a set of MATLAB simulations carried out in varying degrees of mode-matched operation for a vibratory gyroscope's mechanical resolution as a function of the drive-mode displacement. Three different vibratory gyroscope prototypes were investigated: A surface micromachined gyroscope with an average resonant mass of 5µg, a 40-60µm thick bulk-micromachined vibratory gyroscope prototype (with a 1mm² device footprint), and a through-wafer 400µm-thick bulk-micromachined gyroscope (with a 4mm² device footprint). In each simulation, the operating resonant frequency was set at 15kHz.

Figure 2.4 depicts the case of split-mode operation. In this scenario, the prototype gyroscopes operate with a mechanical Q-factor amplification of 1. It is evident that sub-deg/hr resolution is not possible, even with drive amplitudes approaching 10-15µm and using a large resonant proof-mass (~500µg). In Figure 2.5, which simulates a low-Q mode-matched operation (Q_{EFF} = 1000), it is

observed that sub-deg/hr resolution is possible but for large-drive displacement amplitudes and large resonant mass (M~500µg). However, this solution is not practical since the required operating voltages will be increasingly large to enable large deflections on such heavy resonant mass.
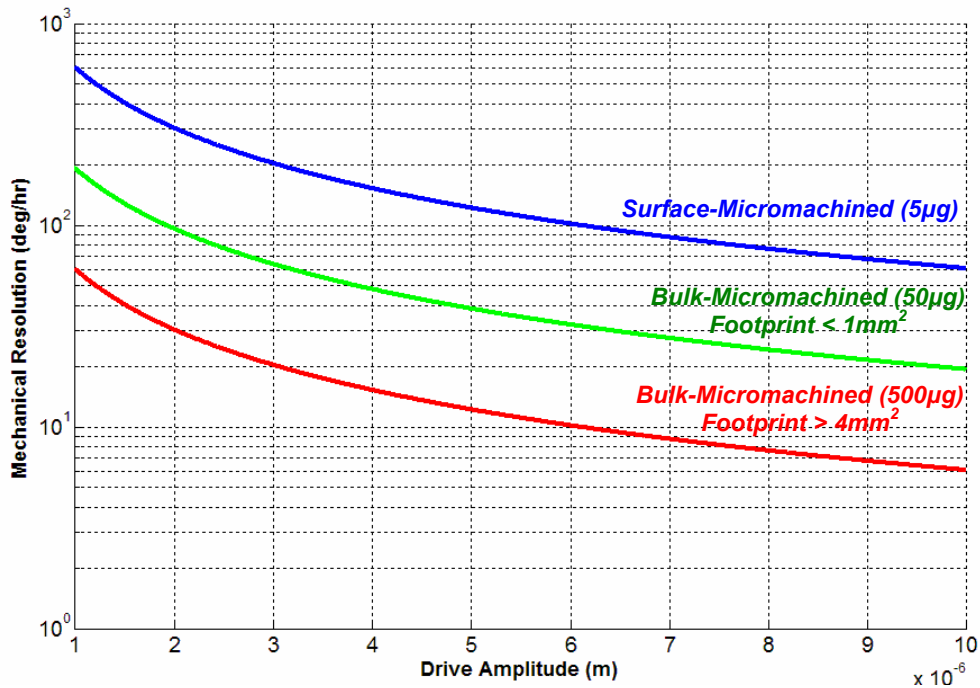
Figure 2.4: Mechanical resolution as a function of drive-amplitude for the split-mode operation (when Q_{EFF} = 1).

Finally, Figure 2.6 shows the case where the prototype vibratory gyroscopes operate under high-Q mode-matched operation (Q_{EFF} = 50,000). It is apparent that sub-deg/hr mechanical resolution is enabled in such cases for all the varying vibratory gyroscope prototypes. Hence in this dissertation, prototype gyroscopes will be developed to operate in mode-matched operation to enable enhancement in device sensitivity, resolution, and bias stability. A blue-shaded region in Figure 2.6 highlights the design space for the M²-TFG.
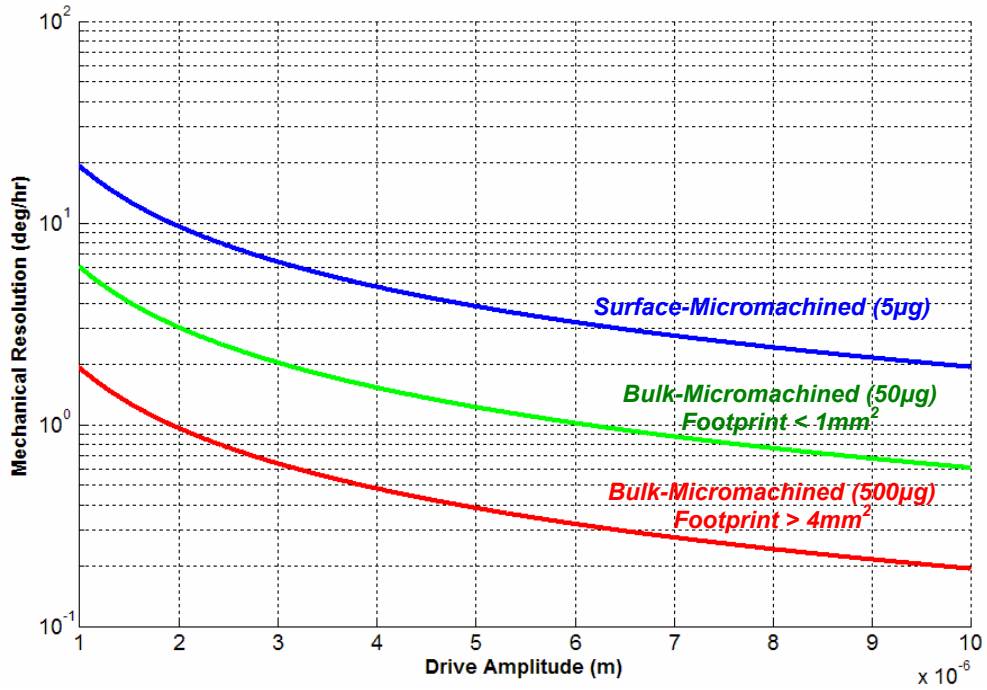
Figure 2.5: Mechanical resolution as a function of drive-amplitude for the low-Q mode-matched operation (when Q_{EFF} = 1000).
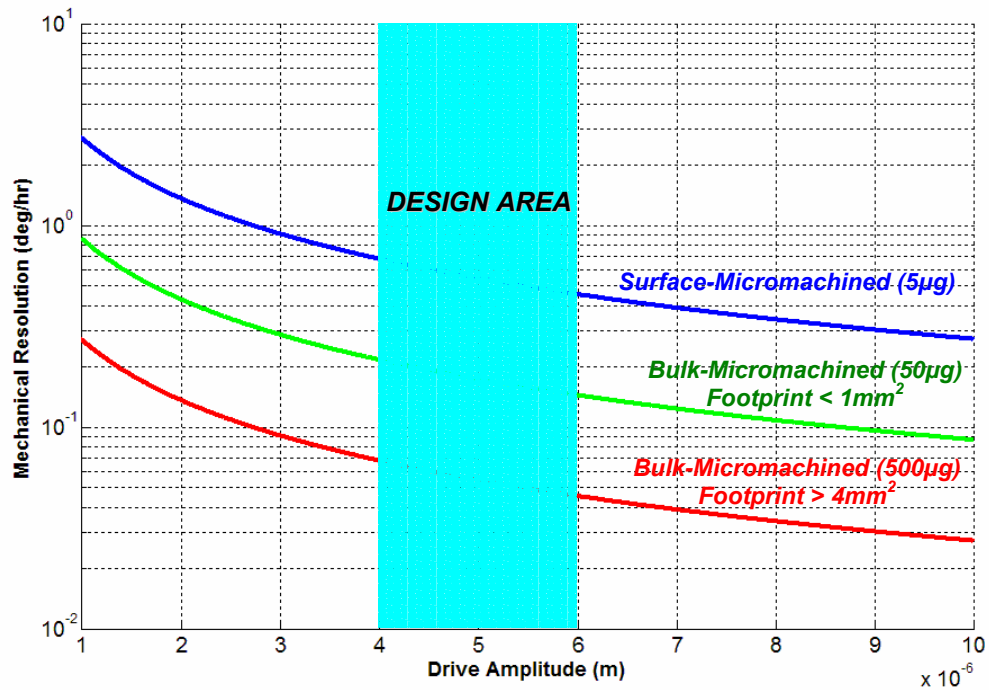
Figure 2.6: Mechanical resolution as a function of drive-amplitude for high-Q mode-matched operation (when Q_{EFF} = 50,000).

34

2.2.2 Scale-Factor

Coriolis-induced sense mode vibrations are detected through change in capacitance at the sense electrodes. The scale factor of vibratory gyroscopes is the ratio of change in the measured output to a change in the input rotation signal. Scale factor is generally evaluated as the slope of the straight line that can be fit by the method of least squares to input-output data [19] and is most commonly expressed in units of V/deg/s.

As expressed in Eq. 2.18, in a typical vibratory gyroscope, the sense mode deflections are proportional to the effective quality factor and the resonant drive amplitude. The Coriolis-induced current at the sense electrode (for a transimpedance-based front-end detection system as reported in Chapter V) is expressed as:

$$I_{Coriolis} = \frac{2V_P C_{s0} Q_{EFF} x_{drive}}{d_{s0}} \Omega \tag{2.26}$$

In Eq. 2.26, 'Ω' represents the input rotation rate, and the factor 'C_{s0}/d_{s0}' clearly demonstrates the need for high-aspect ratio sensing gaps for enhanced device sensitivity. The dynamic range of a vibratory gyroscope refers to the range of input values over which the output is detectable. It is typically computed as the ratio between the maximum input rotation rate (full-scale rate) and the system noise floor. Linearity of the dynamic range refers to the parameter that measures the extent of deviation from the norm from an idealized linear relationship between the output and the input. Parallel-plate capacitive sensing mechanism is the most popular means of detecting sense-mode deflections in vibratory

gyroscopes, and will be utilized in the two gyroscope designs reported in this dissertation. The linearity of this detection mechanism however is restricted to $1/10^{th}$ of the sensing gaps. As displayed in Eq. 2.18, a large Q_{EFF} will cause the gyroscope to approach non-linearity in a more rapid fashion, thereby reducing the linear dynamic range of the device. By operating the mode in closed-loop condition, it is possible to improve the linear dynamic range of the device.

2.2.3 Bias Stability

The bias of a vibratory gyroscope is the average output recorded from the gyroscope when it is not undergoing any rotation. It is often referred to as the Zero Rate Output (ZRO) and is typically expressed in units of deg/hr or deg/s. Bias stability measurement describes how the bias of the gyroscope may change over a specific period of time under fixed conditions (i.e. constant temperature and pressure). Bias stability is expressed in units of deg/hr or deg/s, and is most commonly evaluated using the root Allan variance of the output over fixed time intervals. A detailed discussion of the bias stability is provided in Chapter VI in this dissertation.

2.2.4 Bandwidth

The bandwidth of a vibratory gyroscope represents the range of input frequencies for which the output-input relationship is preserved. The bandwidth determines the response time of the system. The response time, often referred to as the settling time, is the time required for the output to settle within a certain

range of the expected value for an input step function. The bandwidth is expressed as:

$$BW = \omega_0 / Q_{EFF} \qquad\qquad (2.27)$$

It is evident from Eq. 2.27, that although a high-Q_{EFF} is beneficial for a large sensitivity and improved mechanical resolution, and bias stability, it places limitations on the device bandwidth. The bandwidth of a high-Q_{EFF} vibratory gyroscope may be improved by operating the device in a closed-loop (force-to-rebalance mode) configuration [22, 23]. In this mode of operation, the sense-mode displacement is continuously monitored and driven to zero by applying the appropriate forces along the sense axis. Since there is no effective buildup of amplitude along the sense axis over time, the bandwidth of the sensor can be increased to values approaching the resonance frequency of the closed-loop electronics. However, increased bandwidth comes with its own set of penalties, in this case the increase in signal-to-noise ratio as expressed in Eq. 2.24, 2.25.

2.2.5 Quadrature Signal or Mode-Coupling

The sense-mode deflection in a vibratory gyroscope, even under mode-matched operation is comparatively small compared to the drive-mode oscillations. Hence even a small amount of mechanical or drive force asymmetry will make the coupled drive motion overwhelm the sense signal. This is called quadrature error. Under mode-matched operation, both these signals have roughly the same frequency, and can only be distinguished using phase-detection techniques. As will be explained in depth in Chapter V, force balancing is needed to compensate the mode-coupling and thus null /reduce

the quadrature error. The quadrature error is in phase with the drive-mode displacement amplitude while the Coriolis-induced sense-mode deflection (based upon Eq. 2.5) is in phase with the drive-mode displacement velocity. This leads to the 90˚ phase-shift between quadrature signal and rotation-rate signal. However, high-Q_{EFF} mode-matched operation adds significant challenges to the phase detection scheme as highlighted in Eq. 2.19. A slight deviation of the driving frequency from the sense-mode frequency will cause significant variation in the phase-change. Hence even phase-selective detection will be unable to distinguish between quadrature and Coriolis signal. This will result in degraded noise floor, and bias drift of the vibratory gyroscope.

2.3 Classification of Vibratory Gyroscopes

Vibratory gyroscopes are based on Coriolis-induced transfer of energy between two vibration modes of a structure and can operate in either matched-mode or split-mode condition. Under matched-mode condition, the sense mode is designed to have the same (or nearly the same) resonant frequency as the drive mode. Hence, the rotation-induced Coriolis signal is amplified by the mechanical quality factor of the sense mode. In split-mode condition, the drive and sense modes are separated in resonant frequency. The sense mode is then a controlled mode that operates similar to an accelerometer and measures the Coriolis acceleration [24-26]. Due to mechanical Q-factor amplification, gyroscopes operated under matched-mode configuration offer higher sensitivity and consequently better resolution. Resonant matched devices are themselves broadly classified into two types depending upon the nature of their operating

38

modes. Class-I devices rely on non-degenerate vibration modes for driving and sensing. Tuning fork and frame gyroscopes are examples of Class-I gyroscopes [27-29]. Class-II devices on the other hand function with degenerate vibration modes and are invariably easier to match and operate under matched condition. Shell type gyroscopes are examples of Class-II gyroscopes [30, 31].

2.3.1 History of Silicon Vibratory Microgyroscopes

The first batch fabricated silicon micromachined vibratory gyroscope was demonstrated by the Charles Stark Draper Laboratory in 1991. This p-doped silicon bulk mechanical device was a double-gimbal vibratory gyroscope supported by torsional flexures [32]. In this design, an outer gimbal was electrostatically excited at constant amplitude using drive electrodes. This oscillatory motion was transferred to the inner gimbal along the stiff axis of the inner flexures. When exposed to a rotation input normal to the plane of the device, Coriolis force caused the inner gimbal to oscillate about its sensitive axis. A rotation rate resolution of 4deg/s was realized using this structure. Two years later, in 1993, the Charles Stark Draper Laboratory reported a silicon-on-glass tuning fork gyroscope [24] fabricated through the dissolved wafer process [33]. This gyroscope, shown in Figure 2.7, was electrostatically vibrated in its plane using a set of comb drive actuator to achieve drive amplitudes as large as 10μm. Any rotation signal normal to the drive mode would then excite the out-of-plane rocking mode of the structure which was capacitively monitored. The noise equivalent rate observed by this structure was 0.1deg/s in a 60 Hz bandwidth operated at split-mode condition).
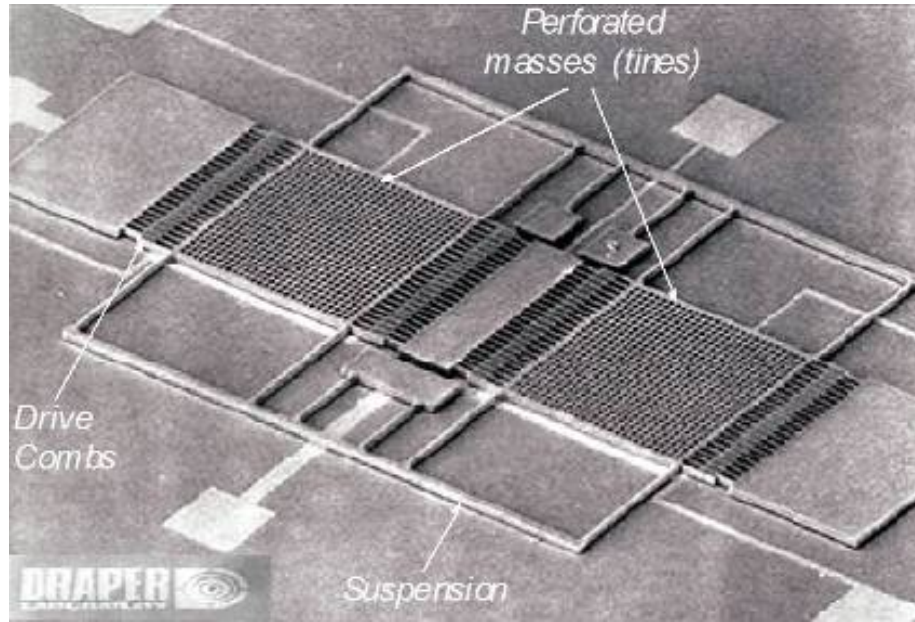
Figure 2.7: SEM image of Draper's silicon-on-glass tuning fork gyroscope [24].

Since 1993, there has been a whole host of silicon micromachined vibratory reported which employed a diverse set of silicon micromachining fabrication technology (surface-micromachining, bulk-micromachining, and mixed-mode micromachining) and implemented several architectures (single proof-mass, frame, tuning fork and shell structures). A partial list of some of the different silicon micromachined vibratory gyroscopes (based on capacitive detection) reported in literature chronologically over the years, have been summarized in Table 2.1.

Table 2.1: A Summary of MEMS vibratory gyroscopes reported in literature.

Year	Author	Sensitive Axis	Vacuum	Structure	Resolution Scale Factor	Fabrication Technology
1994 [34]	M. Putty (Univ. Michigan)	z-axis	Yes	Shell-Type	0.05 deg/s/√Hz 15 mV/deg/s	Electroformed Nickel
1996 [35]	W. Clark (U.C. Berkeley)	z-axis	Yes	Frame	1 deg/s/√Hz 0.1 mV/deg/s	Surface-micro. 2µm thick polysilicon
1997 [36]	I. Hopkins (BAE Systems)	z-axis	No	Shell-Type	0.05 deg/s/√Hz 20 mV/deg/s	Bulk-micro. single crystal silicon
1997 [37]	T. Juneau (U.C. Berkeley)	x-y axis	Yes	Suspended Disk	0.24 deg/s/√Hz 2 mV/deg/s	Surface-micro. 2µm thick polysilicon

1997 [38]	M. Lutz (R. Bosch)	z-axis	No	Dual-Mass Approach	0.05 deg/s/√Hz 18 mV/deg/s	Surface-micro. 12μm thick polysilicon
1998 [39]	A. Kourepenis (Draper Labs)	x-axis	Yes	Tuning Fork	0.24 deg/s/√Hz 2 mV/deg/s	Surface-micro. 12μm thick polysilicon
2000 [40]	Y. Mochida (Murata)	x-axis	Yes	Frame	0.022 deg/s/√Hz 0.13 mV/deg/s	Bulk-micro. 50μm thick single crystal silicon
2000 [30]	F. Ayazi (Univ. Michigan)	z-axis	Yes	Shell-Type	0.24 deg/s/√Hz 2 mV/deg/s	Mixed-mode 80μm LPCVD polysilicon
2000 [41]	H. Song (Samsung)	x-axis	Yes	Frame	0.013 deg/s/√Hz 0.67 mV/deg/s	Bulk-micro. 40μm thick single crystal silicon
2002 [42]	W. Geiger (HSG-IMIT)	x-axis	Yes	Frame	25 deg/hr/√Hz 10 mV/deg/s	Surface-micro. 10μm thick polysilicon
2002 [43]	Bae (JPL)	z-axis	Yes	Coupled-Masses	6 deg/hr/√Hz 24 mV/deg/s	Bulk-micro metal post with silicon base-plate
2002 [44]	G. He (Univ. Michigan)	z-axis	Yes	Shell-Type	10.4 deg/hr/√Hz 132 mV/deg/s	Bulk-micro 150μm thick single crystal silicon
2004 [45]	H. Xie (CMU)	x-z axis	No	Frame	0.01 deg/s/√Hz 0.4 mV/deg/s	55μm Silicon DRIE on CMOS wafers
2007 [46]	R. Neul (Bosch)	z axis	Yes	Coupled-Masses	0.12 deg/hr/√Hz NA	Surface-micro. 11μm thick polysilicon

Surface micromachined devices dominated initial MEMS gyroscope research primarily due to the ability to integrate with the interface electronics. However, they suffer from thin-film residual stress, squeeze-film damping and other problems associated with low mass [45]. The 'low-mass' problem also implied that sub-deg/hr resolution levels was not feasible. The need to address the low mass inadequacies of surface micromachined gyroscopes has directly led to research in bulk-micromachined gyroscopes. The issues that plagued bulk micromachining such as high aspect ratio trench etching, wafer bonding, and vacuum packaging have been addressed in recent years with advancement in micromachining tools and technology. Another trend in bulk micromachined gyroscope that is gaining popularity is the utilization of SOI wafers. The thick single crystalline silicon device layer of SOI wafers provide the necessary substrates for

large-mass mechanical structures and improved sensing area, which are both critical to gyroscope performance.

2.3.2 Commercial Silicon Vibratory Microgyroscopes

The consumer electronics and automotive industries were quick to exploit the advent of such practical miniature devices and this has consequently led to the rise of several successful commercial MEMS gyroscopes. A partial list of the commercial MEMS gyroscopes have been summarized in Table 2.2.

Table 2.2: A Summary of commercial MEMS gyroscopes

Ref.	Authors	Sensitive Axis	Resolution	Bias Stability	Scale Factor
[47]	Analog Devices (ADXRS614)	z-axis	0.022 deg/s/√Hz	21.6 deg/hr	25mV/deg/s
[48]	Bosch (SMG061)	z-axis	2 deg/s/√Hz	NA	25mV/deg/s
[49]	Silicon Sensing (SiRRS01)	z-axis	12 deg/hr/√Hz	3 deg/hr	20mV/deg/s
[50]	InvenSense (IDG-1004)	x-y axis	0.014 deg/s/√Hz	N/A	4mV/deg/s
[51]	N. Grumman (MAG-16)	z-axis	0.03 deg/s/√Hz	10.1 deg/hr	36mV/deg/s

A quick overview of Tables 2.1-2.2 reveals that no MEMS gyroscope to date has been able to approach the sub-deg/hr resolution and bias stability specifications required to satisfy navigation-grade applications. To achieve this performance level, based upon Eq. 2.18, 2.24-2.26 and the observations from MATLAB simulation displayed in Figure 2.6, a micromachined silicon vibratory gyroscope must possess all the following minimum specifications in a single framework:

1. A stable drive amplitude exceeding 5µm.

2. A high-Q_{EFF} ($Q\sim$ 30,000-50,000) mode-matched operation.

3. A resonant mass exceeding 50µg.

4. A large device capacitance facilitated by large electrode overlap area and high-aspect ratio sensing gaps.

The remainder of this dissertation reports on the design and implementation of two vibratory microgyroscope structures developed as means of incorporating the requirements outlined above.

CHAPTER III

THE RESONATING STAR GYROSCOPE

The focus of the dissertation switches to the first of two silicon microgyroscopes investigated during the course of this research work. This chapter describes the design and implementation of the Resonating Star Gyroscope (RSG), a novel Class-II shell-type vibratory gyroscope.

3.1 Concept and Design

The Resonating Star Gyroscope may be visualized as a merged superposition of two identical square shells that are spatially 45° apart (observed in Figure.3.1). The schematic diagram of the resonating star gyroscope (RSG) as seen in Figure 3.2 shows the structure is composed of an eight-folded star-shape outer shell, which is anchored to the central post by means of eight flexural springs. Symmetry considerations require eight optimally designed springs to generate a balanced device with two identical normal modes that have equal natural frequencies and are 45° apart from each other [23].
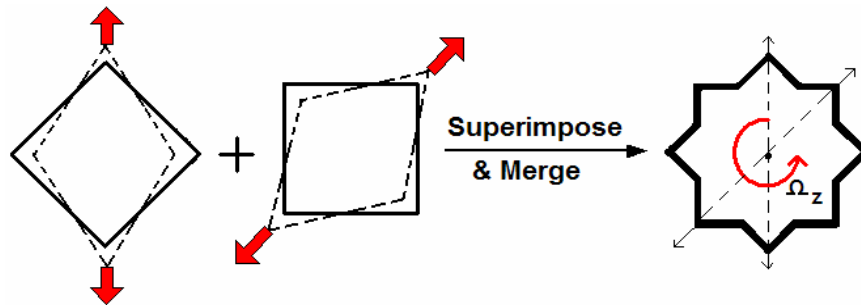
Figure 3.1: Concept illustration of the Resonating Star Gyroscope.
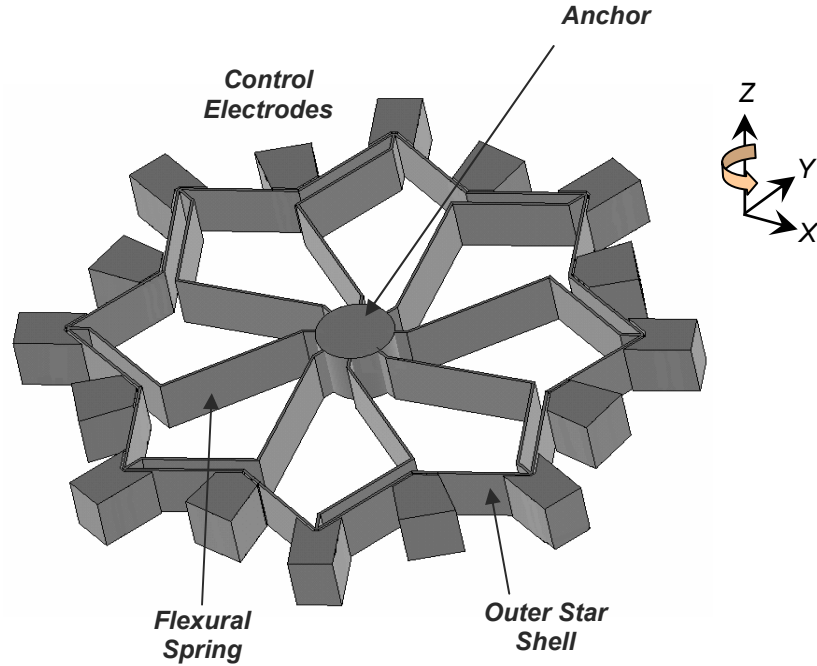
Figure 3.2: Schematic diagram of the Resonating Star Gyroscope.

The degenerate primary flexural modes of the RSG are shown in Figure 3.3. They are analogous to the elliptical mode shapes observed in the vibrating ring gyroscope [30, 34]. It is evident that the nodes of each mode are located at the anti-nodes of its degenerate counterpart. Sixteen capacitive electrodes are distributed along the periphery of the RSG structure at intervals of 22.5˚. These electrodes are used to drive, sense, and balance the shell-structure. The RSG structure is electrostatically vibrated into the primary flexural mode with a fixed drive amplitude (x_{drive}). When subjected to rotation around its normal axis, Coriolis force causes energy to be transferred from the primary mode to the secondary flexural mode (of the degenerate pair), which is located 45˚ apart. This causes displacement amplitude to build up proportionally in the latter mode; this build-up is capacitively monitored. It has been shown in [20] that in the open-loop

mode of operation, the amplitude of the second mode (x_{sense}) is proportional to the rotation rate and is expressed as:

$$x_{sense} = 4A_g \frac{Q_{EFF}}{\omega_0} x_{drive} \Omega \tag{3.1}$$

In Eq. 3.1, A_g is the angular gain and is equivalent to 0.37 (similar to VRG [30, 34]). Q_{EFF} represents the mode-matched effective quality factor of the mechanical structure, ω_0 is the angular flexural resonance frequency and Ω is the rotation rate being applied normal to the structure.
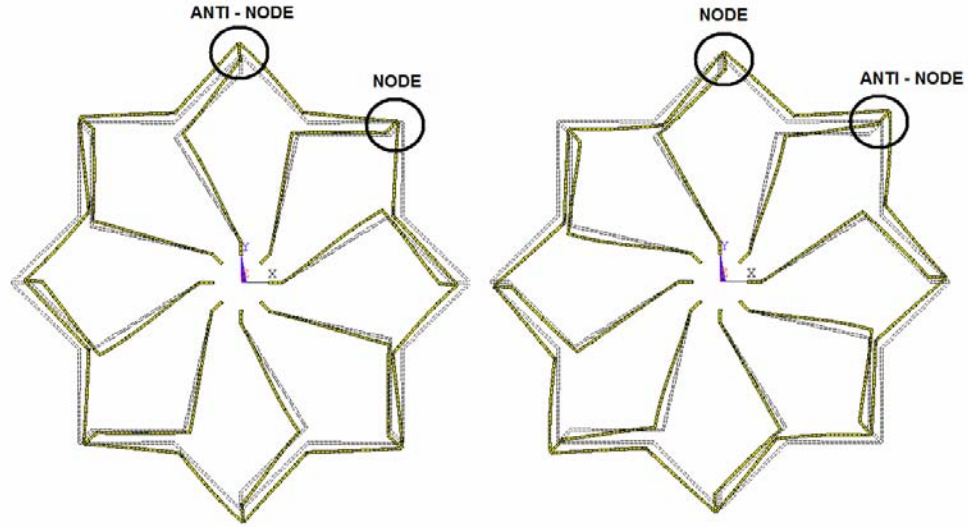
Figure 3.3: Flexural Vibration Modes (2-Node Lines) as simulated in ANSYS. The displacement of the shell-structure has been exaggerated for clarity.

3.2 Advantages of the RSG Geometry

The M^2-TFG structure (as will be discussed in a later section) relies on non-degenerate resonant modes, and hence to obtain two orthogonal modes in close proximity requires precise control of the device geometry and processing conditions. However, in the RSG structure, as long as the structural component is

isotropic in crystalline orientation, it is possible to generate two identical flexural modes of the structure with nominally equal resonant frequencies. Control electrodes are distributed around the periphery of the shell-structure that enables mode-matching (compensation of device non-idealities) and thereby Q-factor enhancements. The RSG shares all the benefits of its circular analogue – the vibrating ring gyroscope (VRG). It has a balanced symmetrical structure that is less sensitive to spurious vibrations. Symmetry also provides immunity to temperature variations, since both modes are equally affected. In addition the RSG structure incorporates two unique optimization schemes which make it a preferred option over the shell-structure.

3.2.1 Increased Electrode Area and Mass

The rotation rate sensitivity of the RSG is a direct function of the electrode sense area. By increasing the sensing area, it is also possible to improve device resolution and reduce operating voltages. Figure 3.4 compares the electrode parameters for the two shell-type structure of equivalent radial diameter. For a 20˚ electrode span, a 1mm VRG would provide an effective area of (140 × Thickness) μm^2. Its RSG counterpart with a 1mm radial diameter would provide an effective electrode area of (205 × Thickness) μm^2. This represents a 40% increase in the electrode area. Similarly the mass of the outer shell structure is also increased in the case of the RSG, which results in improved Brownian noise floor for a specified space constraint.
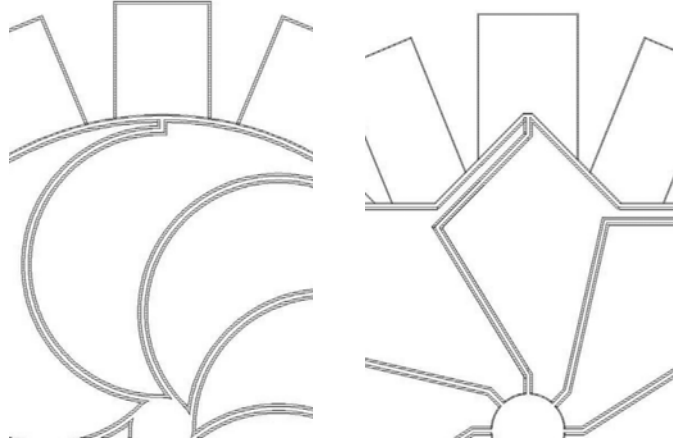
Figure 3.4: Electrode area comparison of the VRG and the RSG.

3.2.2 Increased Drive Amplitude

Shell-type structures such as the VRG and the RSG rely on parallel plate actuation, since comb-drive structures affects the degeneracy of the vibratory modes. Parallel-plate actuation schemes have limited drive amplitude due to pull-in. The drive amplitude affects the device sensitivity as well as the noise floor, and hence is a critical parameter of vibratory gyroscope performance. The electrode shape of the RSG enables greater drive amplitude (before pull-in) in comparison to the VRG as shown in Figure 3.5.
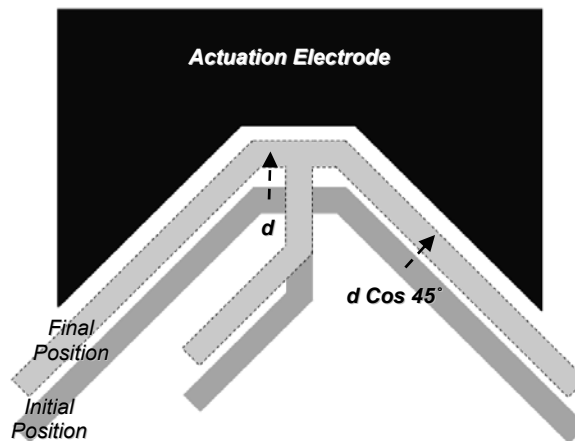
Figure 3.5: Illustration of increased displacement amplitude for RSG actuation electrode.

While the RSG structure undergoes flexural deformation in the primary degenerate mode, the area of the electrode that is susceptible to pull-in only undergoes 70% of the radial displacement.

3.3 HARPSS Polysilicon RSG Prototype

The first prototypes of the RSG were implemented with trench-refilled LPCVD polysilicon as the structural material using the HARPSS process [52]. In this fabrication technology, the mechanical structures are created by refilling trenches with polysilicon deposited over a sacrificial oxide layer, similar to the flow outlined in [31]. The structural polysilicon layer is doped to make it conductive. SEM pictures of fabricated 1mm diameter, 65μm thick HARPSS RSG can be viewed in Figure 3.7.
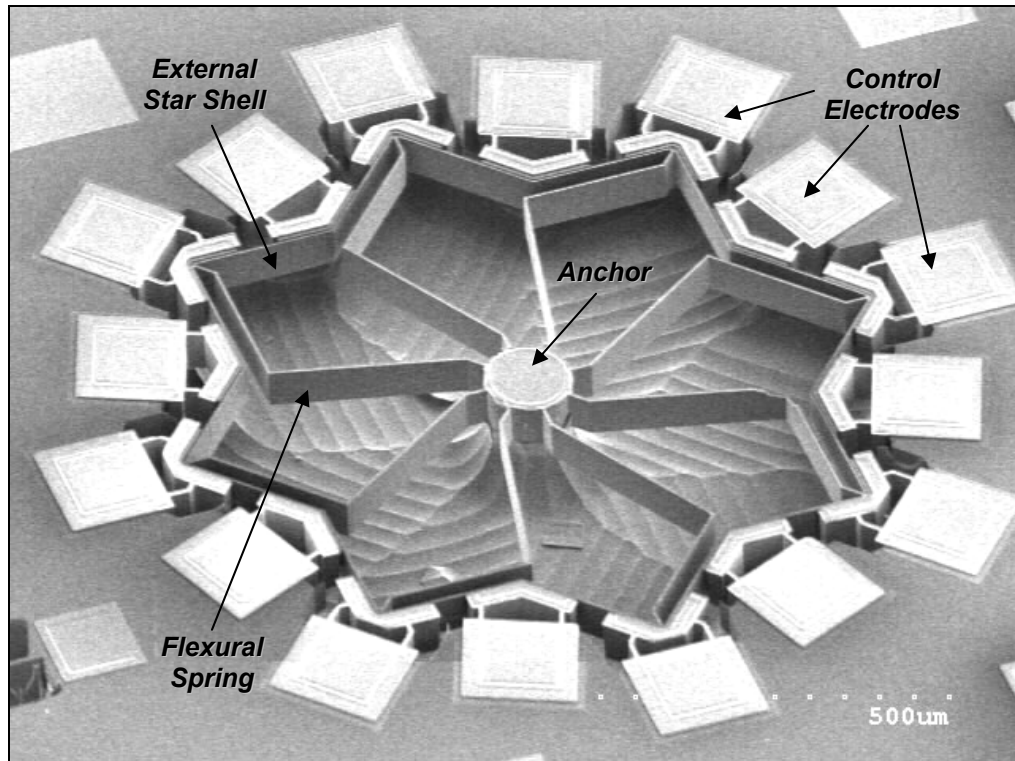
Figure 3.6: SEM of a HARPSS 1mm diameter 65 μm thick polysilicon RSG.

High aspect ratio capacitive gaps are shown in Figure 3.7. The process flow of the HARPSS RSG has been outlined in Appendix A. These small capacitive gaps (~1μm) enable low voltage operation of the gyroscope. Frequency split of 400Hz were compensated using tuning voltages of less than ± 10V.
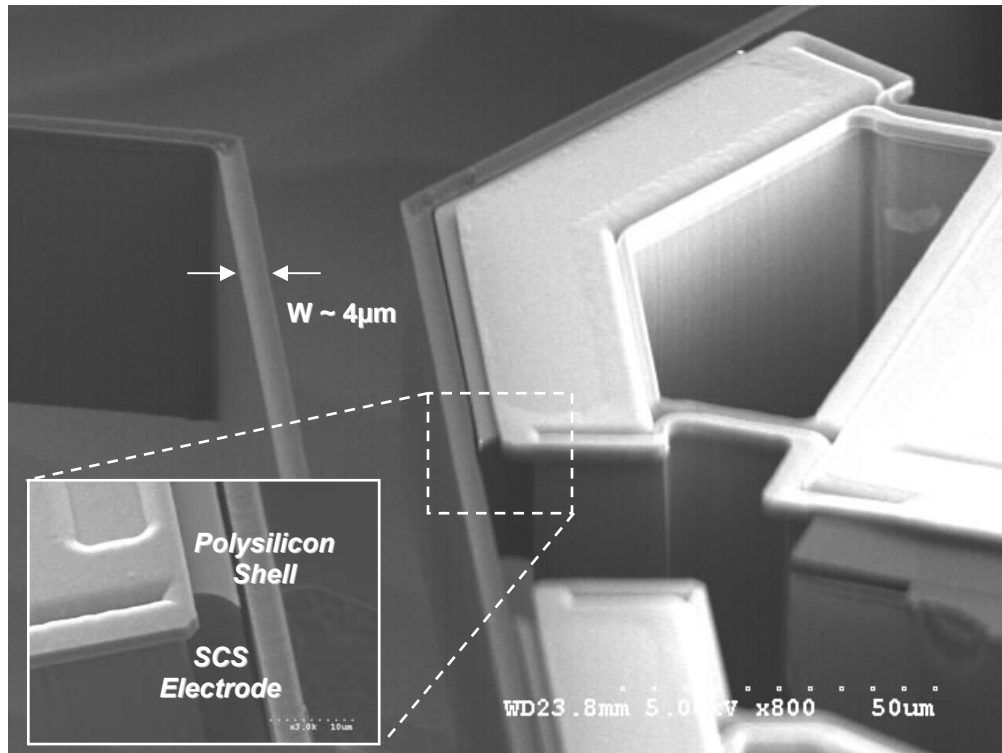
Figure 3.7: A close-up of the electrode area highlighting the high-aspect ratio (>60:1) capacitive gaps.

3.3.1 Device Modal Analysis

Mode shape functions for the resonating star gyroscope have been obtained using the finite element modeling software ANSYS. The FEM model was constructed using the SOLID45 element – ideal for investigating isotropic high-aspect ratio structures. A list of the first ten resonant mode-shapes of the RSG implemented in HARPSS using 4μm-wide, 65μm-thick LPCVD polysilicon structural material is summarized in Table 3.1.

Table 3.1: Summary of finite element analysis of HARPSS RSG

Mode Description	Frequency (kHz)	Figure #
Torsional	10.875	Figure 7.8
x- Translational	28.865	Figure 7.9
y - Translational	28.865	Figure 7.9
Primary Flexural (2 Node Lines)	42.350	Figure 7.3
Primary Flexural (2 Node Lines)	42.350	Figure 7.3
Out of Plane (2 Node Lines)	47.340	Figure 7.10
Out of Plane (2 Node Lines)	47.340	Figure 7.10
Higher-Order Flexural (3 Node Lines)	57.430	Figure 7.11
Higher-Order Flexural (3 Node Lines)	57.430	Figure 7.11
Out of Plane z- Translational	71.440	Figure 7.12

The first mode of the structure shown in Figure 3.8 is a torsional mode in which the shell remains rigid and rotates about its center support. The second and third modes as shown in Figures 3.9 are the translational modes in which the entire shell is displaced along the x and y axis. The stiffness along these translation modes determines the pull-in stiffness of the device [23]. The fourth and fifth modes (shown in Figure 3.3) are the flexural modes that are used to sense rotation. These modes are degenerate as verified by their identical natural frequencies. Out-of-plane vibration modes (shown in Figure 3.10) occur at frequencies higher than 30 kHz where the contribution of common environmental noise is rare and negligible. Higher-order degenerate flexural modes are illustrated in Figure 3.11.
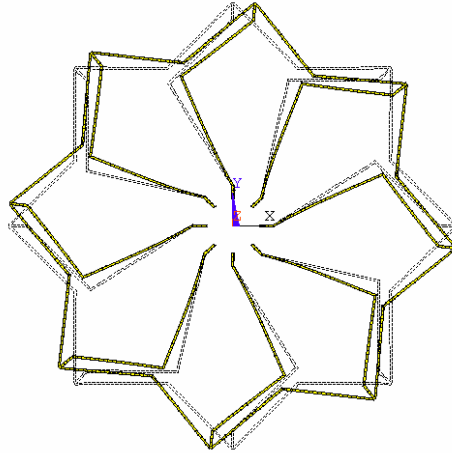
Figure 3.8: Torsional mode of the RSG as simulated in ANSYS. The displacement of the shell-structure has been exaggerated for clarity.
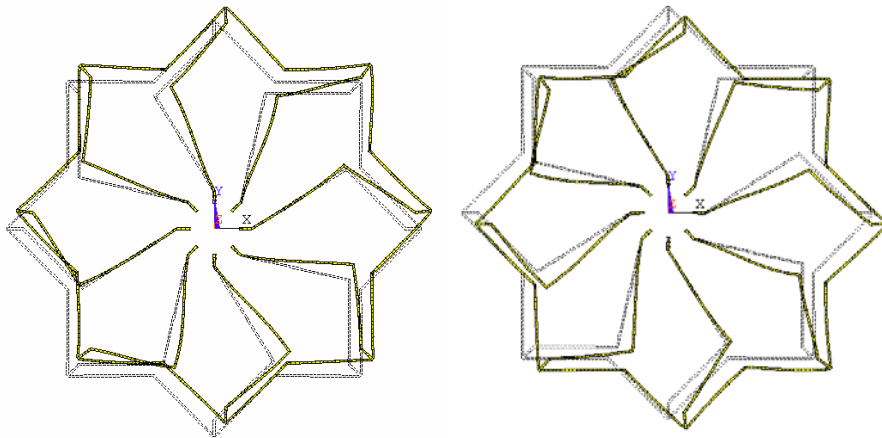
Figure 3.9: Translational vibration modes of the RSG as simulated in ANSYS. The displacement of the shell-structure has been exaggerated for clarity.
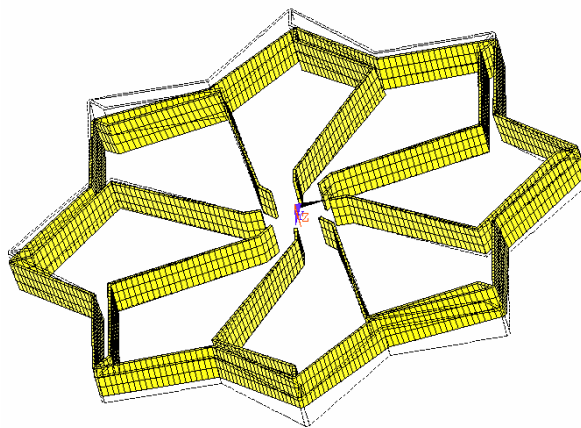
Figure 3.10: Out-of-plane vibration mode (2-nodes) of the RSG as simulated in ANSYS. The displacement of the shell-structure has been exaggerated for clarity.
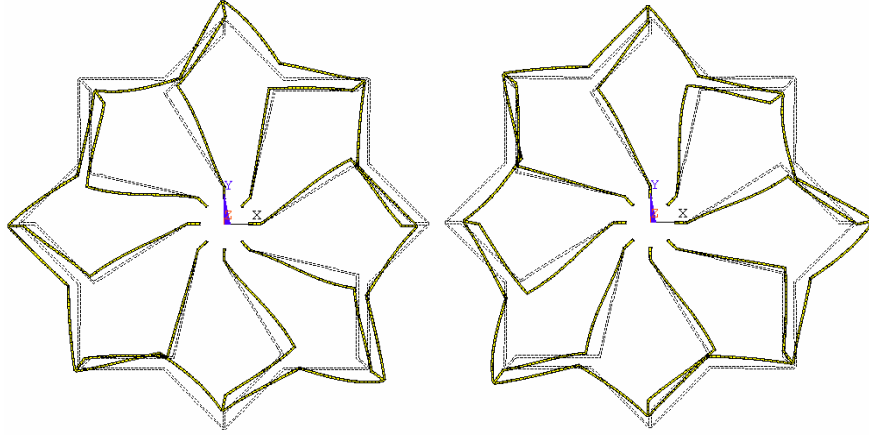
Figure 3.11: Flexural Vibration Modes (3-Node Lines) as simulated in ANSYS. The displacement of the shell-structure has been exaggerated for clarity.
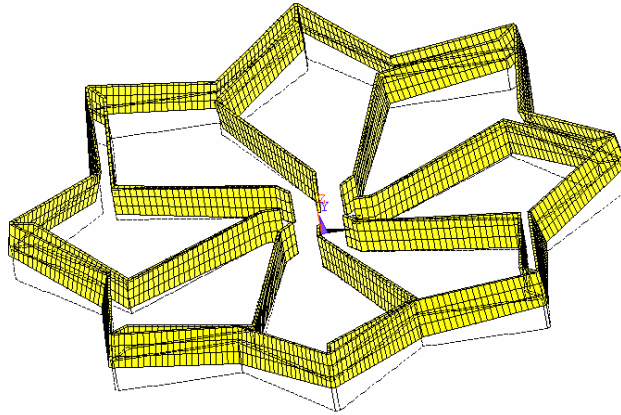
Figure 3.12: Out-of-plane mode (z-translational) of the RSG as simulated in ANSYS. The displacement of the shell-structure has been exaggerated for clarity.

3.3.2 HARPSS RSG Device Characterization

Preliminary open-loop characterization of the RSG is performed using dedicated analog front-end electronics (AFE) implemented by means of discrete amplifiers (similar to the M²-TFG setup). The RSG die is mounted on the AFE board and wire-bonded to pads that interface them to transimpedance amplifiers. This AFE board is then placed in the vacuum chamber and the device characterization is performed. The devices were characterized in 1mTorr vacuum and an Agilent 4395A network analyzer was used to measure the frequency response. The

measured primary-flexural mode Q-factor for a typical 65μm thick HARPSS RSG is shown in Figure 3.13.
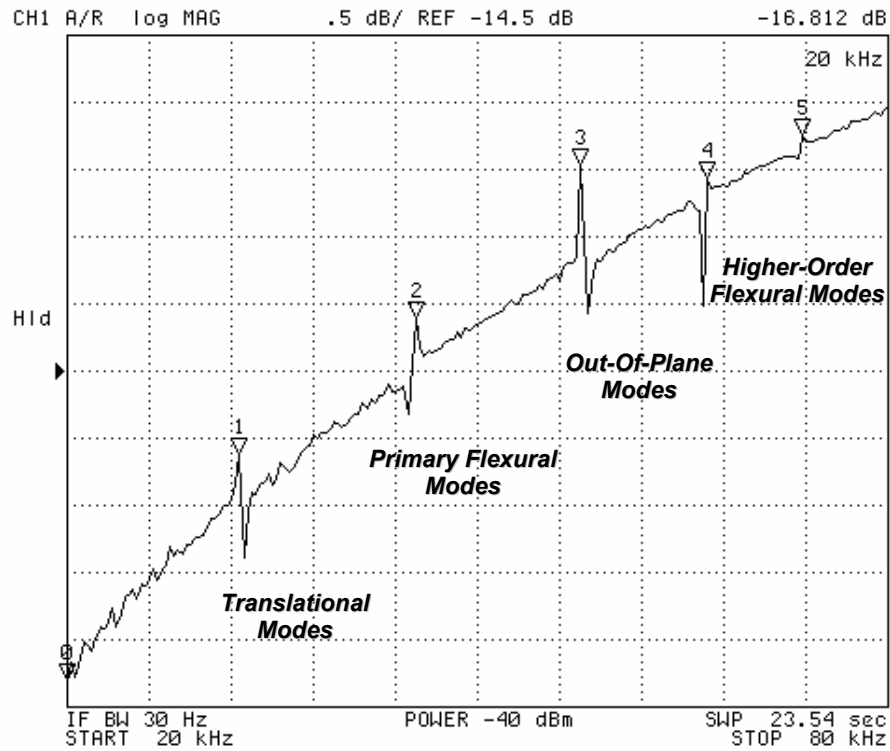
Figure 3.13: Frequency response of the RSG device illustrating all the various resonant modes of the device.
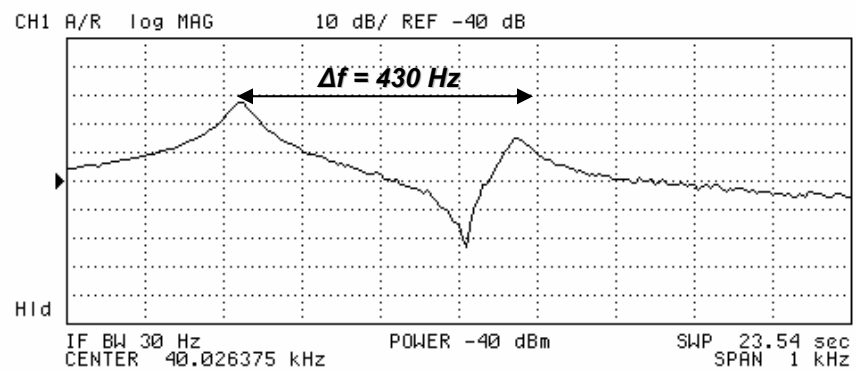
Figure 3.14: Initial separation of the primary flexural modes is approximately 400Hz.

In this particular device the primary flexural modes occur at approximately 40kHz and are initially 430Hz apart and the resonant Q-factor is approximately 1,500. The frequencies of the two degenerate flexural modes can be different due to imperfection in the fabrication process and/or device structure as well as electrostatic stiffening effect of bias voltages applied to the surrounding electrodes. The importance of matched-mode operation is paramount to achieving high performance of the gyroscope – by means of leveraging the mechanical gain of the system. Quality factors of the resonant flexural operating modes not only guarantee low operating voltages and improved drive amplitude but provide a significant improvement in device resolution and bias stability. Electronic tuning is performed to compensate the frequency mismatch between the degenerate primary flexural modes.
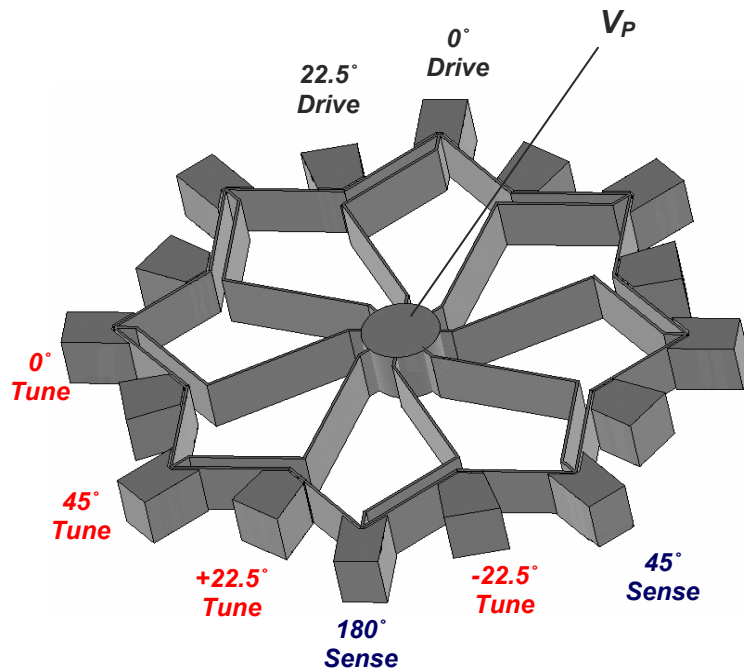
Figure 3.15: Electrode configuration of the RSG. The unutilized electrodes are all connected to either V_P or are grounded.

Balancing the RSG has been done by applying DC voltages to two pairs of electrodes and the process of mode-alignment is similar to the one implemented in VRG [23, 30]. All the surrounding electrodes except the 0° sense and 45° sense electrodes were connected to the polarization voltage (V_P) and the balancing voltages were applied to a pair of balancing electrodes located at 22.5° and – 22.5° and to another pair located at 0° and 45° angles. The balancing electrode configuration is shown in Figure 3.15. The mode-matched resonant peak of the HARPSS RSG is shown in Figure 3.17.
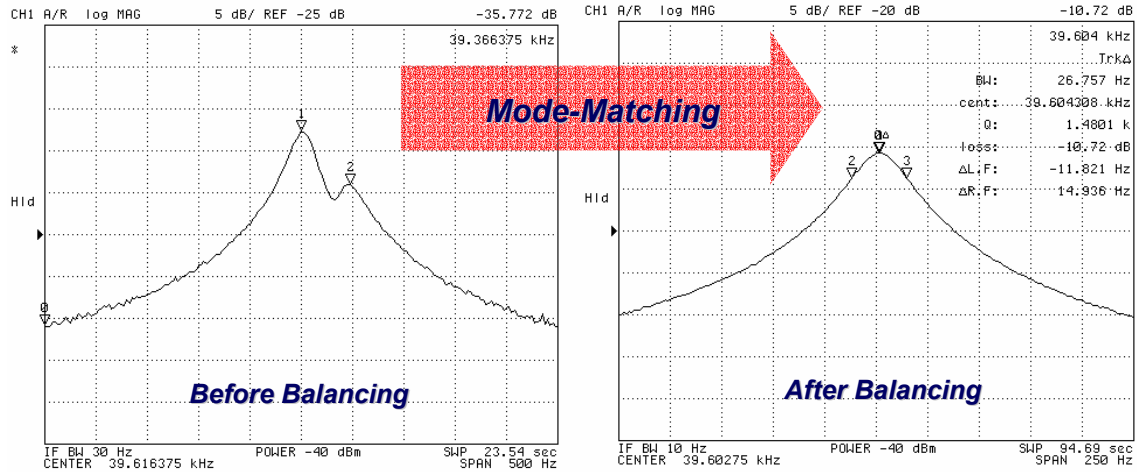
Figure 3.16: (Left) *Before balancing*, the two flexural modes have different frequencies. (Right) *After balancing*, the two peaks merge and the effective quality factor is 1,500.

High aspect ratio capacitive gaps (1μm) shown in Figure 3.7 enable low voltage operation of the gyroscope. Frequency split of 300Hz were compensated using tuning voltages of less than ± 10V. To understand the significance of this value, one must take into consideration examples of tuning voltages in other shell-type structures fabricated using alternate technologies. The first generation nickel vibratory ring gyroscope [23], a 40 Hz frequency mismatch was compensated using in excess of 15 Volts of tuning voltages. In the last reported version of the

56

vibrating ring gyroscope [44] implemented on single crystal silicon using DRIE, 100 Hz of frequency split was accounted for using in excess of 50 Volts of tuning voltage. In both case the limiting factor was the capacitive gap.

3.3.3 HARPSS RSG Sensitivity Analysis

In addition to the balancing stage, in order to extract the rotation rate information from the sense electrodes a certain amount of signal processing is required. The signal processing circuitry shown in Figure 3.17 has been implemented using discrete electronic components and consists of two main blocks: (1) Drive loop to maintain resonance in the drive mode, and (2) Sense channel that extracts the rotation rate from the output at the sense electrode.
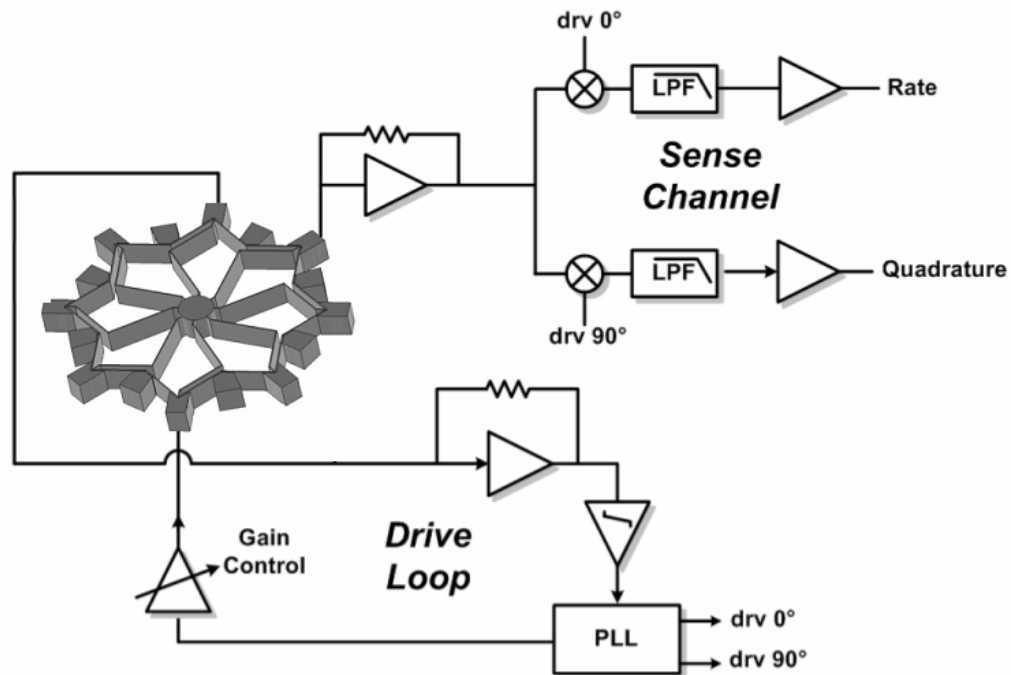
Figure 3.17: Schematic of the interface circuitry for the RSG

The drive loop uses a digital PLL to lock to the drive resonant frequency, and supplies the actuation voltage to the drive electrodes. The variable gain amplifier (VGA) maintains constant drive amplitude and prevents over-driving the sensor. The front-end of the RSG sense-channel is comprised of discrete transimpedance amplifier. The sense channel further consists of a synchronous demodulator to extract the rate signal from the sensor output. The PLL generates a signal that is proportional to the drive velocity. This square wave is used in a synchronous demodulator to chop the incoming signal from the sensor and subsequently low passed filtered to obtain the rate signal. A synchronous demodulator maintains inherent phase information while demodulating the AM signal. This phase relationship is used to distinguish between the rotation rate and quadrature signal.

The scale factor plot of the HARPSS RSG (measured in 1mTorr vacuum) is shown in Figure 3.18. The low flexural-mode quality factor restricts the device performance of the HARPSS implementation of the RSG. This has been attributed to thermo-elastic damping (TED) losses associated with trench-refilled polysilicon structural material. This matter will be investigated in the following section. A summary of the HARPSS polysilicon RSG prototype parameters are shown in Table 3.2.
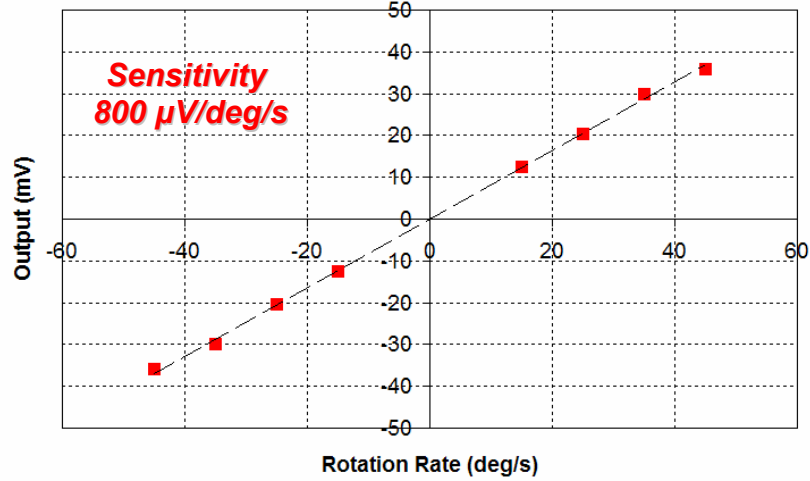
Figure 3.18: Scale-factor plot of the HARPSS polysilicon RSG prototype.

Table 3.2: Device parameter summary of the HARPSS polysilicon RSG prototype

Device Parameter	RSG Value
Radial Diameter	1mm
Mode-Matched Quality Factor	1,500
Sense Electrode Gap Spacing	1.5 µm
Star-Shell and Spring Width	4 µm
Height of Device Structure	65 µm
Drive Amplitude	100 nm
Resonant Frequency	39.6 kHz
Theoretical Brownian Noise Floor	0.03 ˚/s/√Hz
Rate sensitivity	800 µV/˚/s

3.4 TED in Trench-Refilled Polysilicon RSG

The flexural resonant mode shapes of the RSG represent simultaneous extension or compression of a thermo-elastic solid. The mechanism responsible for thermo-elastic damping in solids is the lack of thermal equilibrium between various parts of the vibrating solid. In order for the equilibrium to be re-instated, irreversible heat flow driven by the temperature gradient occurs, also referred to as thermal relaxation. The irreversibility of such a relaxation process is associated with energy

59

dissipation or damping. The void generated from the polysilicon deposition process causes a discontinuity in the thermal path across the width of the vibrating structure. An SEM image of the void in the polysilicon structural material is shown in Figure 3.19.
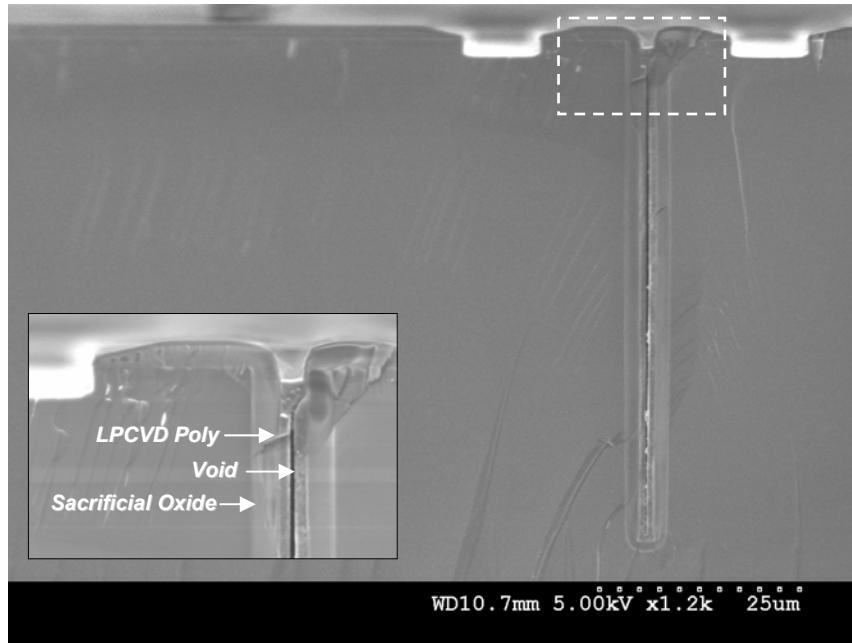
Figure 3.19: An SEM view of typical thermal-path void in LPCVD polysilicon refilled trench.

Figure 3.20 shows the two thermal paths associated with trench-refilled flexures. 'P1' represents the thermal path across the thickness of the beam wall, while 'P2' represents the thermal path around the void. Table 3.3 summarizes the material constants of p-doped polysilicon that will used to derive the Q_{TED} function.
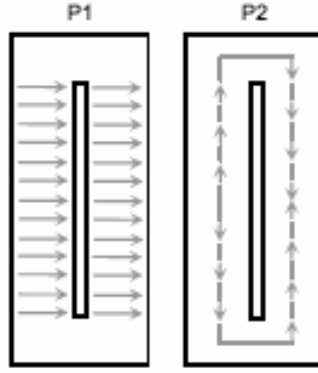
Figure 3.20: Thermal paths around the trench-refilled polysilicon flexures (cross-section).

Table 3.3: Summary of material constants for p-doped polysilicon structural material [53].

Parameter	Symbol	Value
Young's Modulus	E	150 GPa
Thermal Conductivity	κ	40 W/mK
Density	ρ	2330 kg/m^3
Specific Heat Capacity	C_P	713 J/kgK
Thermal Expansion Coefficient	α	2.6 x 10^{-6} /K

The overall frequency-dependent thermo-elastic dissipation in a trench-refilled polysilicon flexure was derived in [53]:

$$Q_{TED} = \left(\Delta \frac{\omega \tau_{TH1}}{1 + \left(\omega \tau_{TH1} \right)^2} + \Delta \frac{\omega \tau_{TH2}}{1 + \left(\omega \tau_{TH2} \right)^2} \right)^{-1} \tag{3.2}$$

In this equation the relaxation strength 'Δ' and the thermal relaxation time constants 'τ_{TH}' are expressed as:

$$\Delta = \frac{E \alpha^2 T}{\rho C_P} \tag{3.3}$$

$$\tau_{TH1} = \frac{\rho C_P \left(\frac{w}{2} \right)^2}{\kappa \pi^2} \quad , \quad \tau_{TH2} = \frac{\rho C_P \left(h \right)^2}{\kappa \pi^2} \tag{3.4}$$

Figure 3.21 simulates the projected Q_{TED} values for RSG implemented with and without a void (with identical flexural width). The device with a void displays local minima in the vicinity of the operating frequency range of the RSG which is between 30 kHz – 100 kHz (shaded region). The absence of the void, and consequently the elimination of the second thermal path imply that there is only one distinct minima value. A plot of a device without the void indicates a much higher-Q_{TED} in the same operating frequency regime. In the proceeding section we shall implement a polycrystalline version of the RSG without a thermal void to verify improvement in the quality factor.
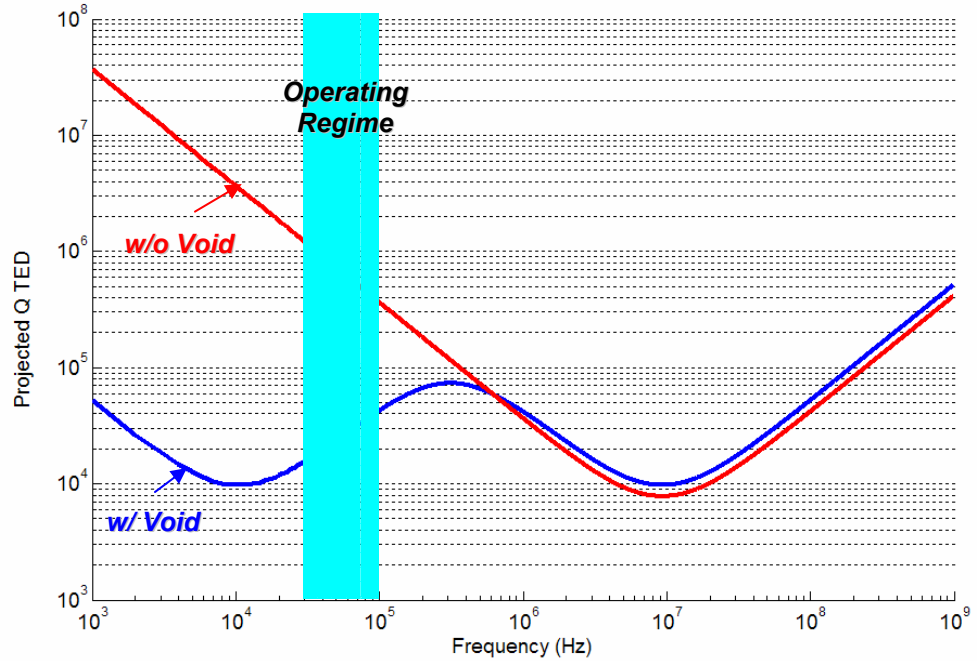
Figure 3.21: Comparison of projected Q_{TED} between RSG implemented with (blue) and without (red) a void in the isotropic structural material.

3.5 Epitaxial Polysilicon RSG Prototype

In an effort to confirm TED as the primary cause of low-Q resonant modes in the HARPSS implementation, RSG prototypes were constructed using an alternate isotropic silicon structural material – low-resistivity epitaxial polysilicon developed by ST Microelectronics for the THELMA process [54]. The device was defined through anisotropic silicon etching of the epitaxial structural material, which lies electrically isolated from the underlying silicon substrate through a buried oxide layer (as seen in Figure 3.22).
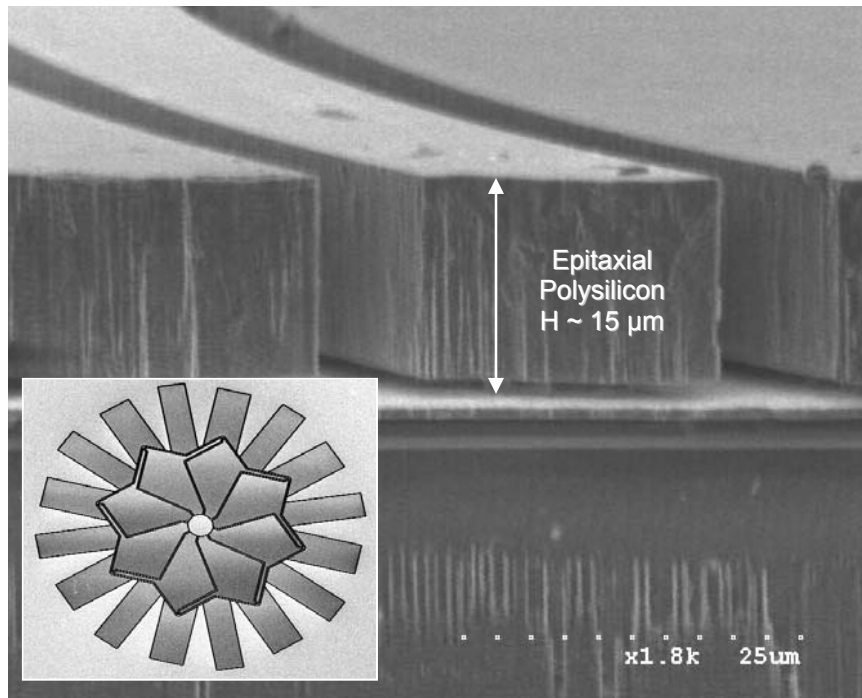
Figure 3.22: SEM images of an RSG implemented on 15μm thick epitaxial polysilicon substrate. (Inset) An overview of the RSG.

As anticipated device characterization on a 15μm thick epitaxial polysilicon structure with flexural and shell width of 5μm displayed high-Q resonant flexural modes. The device was electronically tuned and yielded a matched-mode quality factor of approximately 60,000 (displayed in Figure 3.23). This represents a

significant improvement from the LPCVD polysilicon HARPSS implementation. The rotation rate scale factor plot of an epitaxial polysilicon RSG prototype is displayed in Figure 3.24. A summary of the epitaxial-polysilicon RSG prototype parameters are listed in Table 3.4.
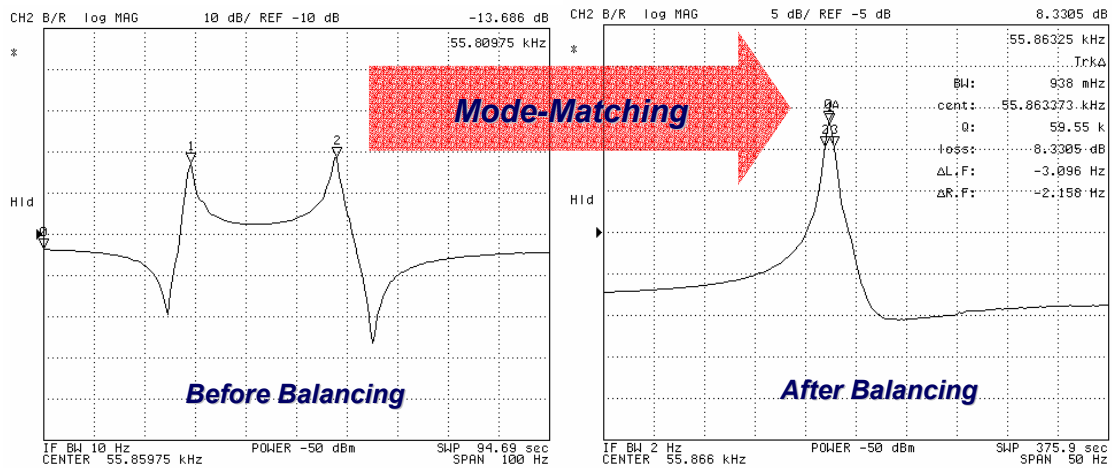
Figure 3.23: (Left*) Before balancing*, the two flexural modes have different frequencies. (Right) *After balancing*, the two peaks merge and the effective quality factor is 60,000.
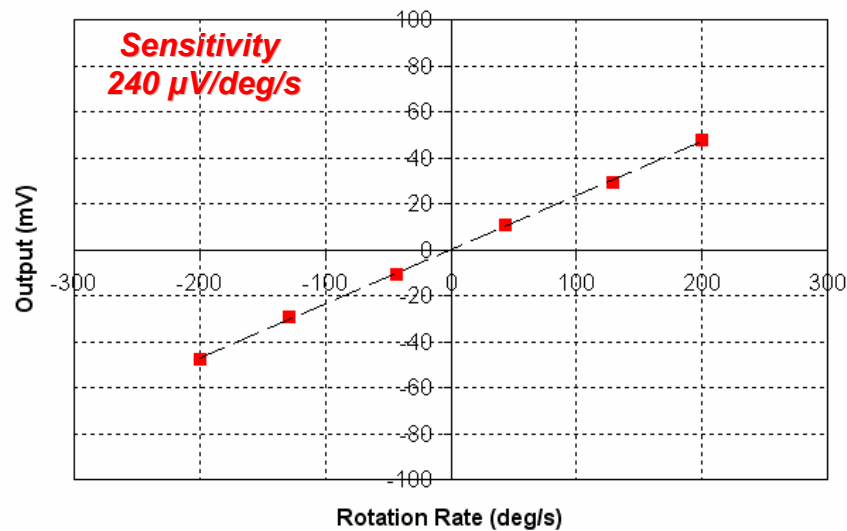
Figure 3.24: Scale-factor plot of the RSG prototype implemented on epitaxial polysilicon.

Table 3.4: Device parameter summary of the epitaxial polysilicon RSG prototype

Device Parameter	RSG Value
Radial Diameter	1mm
Mode-Matched Quality Factor (Q)	60,000
Sense Electrode Gap Spacing	5 µm
Star-Shell and Spring Width	4 µm
Height of Device Structure	15 µm
Drive Amplitude	300 nm
Resonant Frequency	55.9 kHz
Theoretical Brownian Noise Floor	0.05 °/s/√Hz
Rate sensitivity	240 µV/°/s

3.6 Multiple-Shell (111) Single Crystal Silicon Implementation of RSG

In the previous sections, the limitations of using polycrystalline silicon were described. Trench-refilled LPCVD polysilicon yielded low-Q factors due to increased TED loss, while the epitaxial polysilicon device performance is limited by the thickness of the structure (low resonant mass, reduced sensitivity, and susceptibility to out-of-plane modes). The possible solution of implementing the RSG in a single crystalline silicon substrate was explored as means of addressing these issues. By choosing (111) single crystalline silicon substrate (SCS) –which has uniform and homogenous Young's modulus along all directions in its plane [55, 56], a multiple shell RSG design was implemented. By connecting three concentric star-shaped shells of width 20µm, it was possible to generate a larger mass, while ensuring operation at the region of high-Q at an elevated frequency regime [57]. Mode shape functions for the multiple-shell resonating star gyroscope have been obtained using the finite element modeling software ANSYS. A list of the relevant resonant mode-shapes of the multiple-shell RSG

implemented in (111) single crystalline silicon using 20μm-wide, 40μm-thick structural material is summarized in Table 3.5. A review of the primary flexural mode shapes of the (111) SCS multiple-shell RSG displays two resonant vibration modes that are spatially 45° apart (as illustrated in Figure 3.25).

Table 3.5: Summary of finite element analysis of (111) SCS Multiple-Shell RSG.

Mode Description	Frequency (kHz)
Torsional	10.559
x- Translational	28.549
y - Translational	28.549
Out of Plane (2 Node Lines)	77.570
Out of Plane (2 Node Lines)	77.570
Primary Flexural (2 Node Lines)	90.455
Primary Flexural (2 Node Lines)	90.455
Higher-Order Flexural (3 Node Lines)	160.289
Higher-Order Flexural (3 Node Lines)	160.289
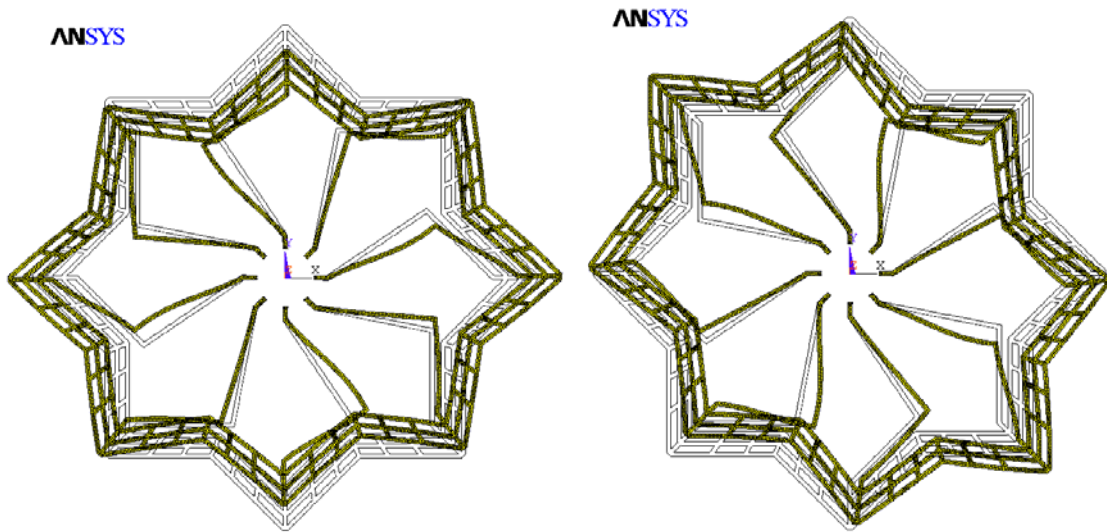
Figure 3.25: Primary Flexural Vibration Modes as simulated in ANSYS. The displacement of the shell-structure has been exaggerated for clarity.

3.6.1 Multiple-Shell (111) SCS RSG Device Characterization

An implementation of the RSG on 40µm thick (111) SOI substrate is shown in the SEM image (Figure 3.26). The RSG devices are fabricated using a simple two mask approach and eliminates the complexities of previous high-performance (111) single crystalline shell-structure implementation reported in [44].
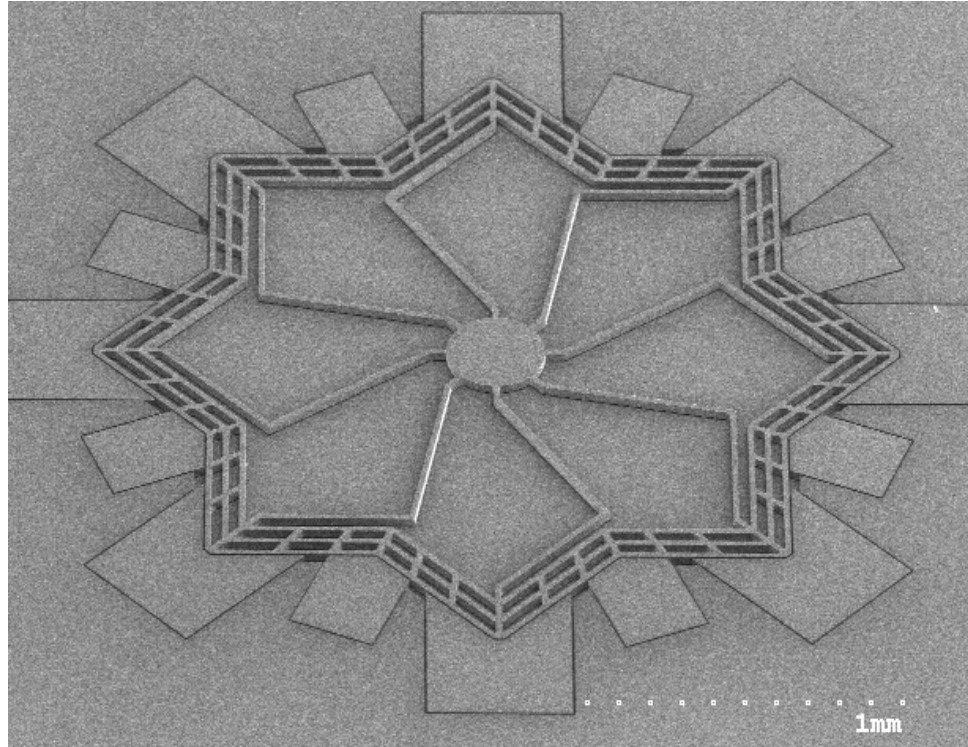
Figure 3.26: SEM image of a 40µm thick multiple-shell RSG with 2.7mm radial diameter implemented on (111) SCS SOI substrate.

The capacitive actuation and sensing gaps of the fabricated device are 4µm. The aspect ratio was restricted by the limitations of the DRIE tool, and leads to significantly larger voltage operation for the gyroscope (in comparison to the HARPSS implementation). A list of device parameter improvements and changes has been highlighted in Table 3.7. The multiple-shell implementation of the RSG

offers almost two order of magnitude improvement in the theoretical Brownian noise floor over its HARPSS predecessor.
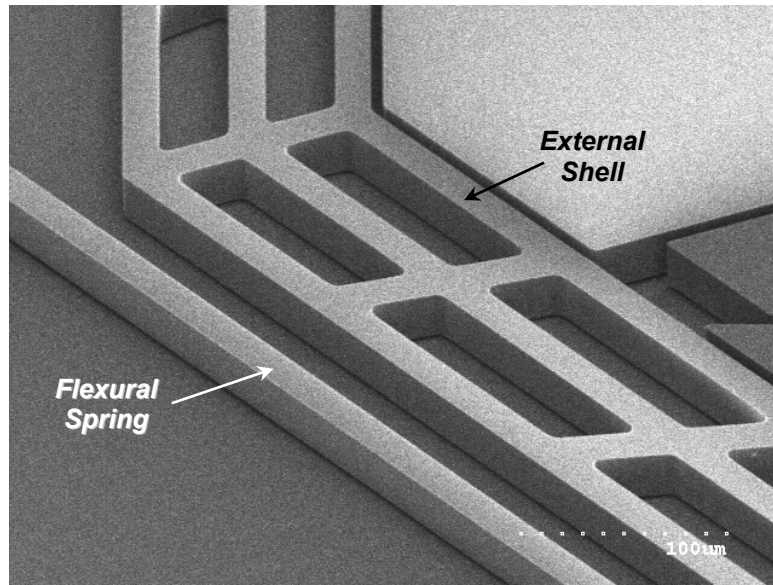
Figure 3.27: Close-up of the multiple-shell approach of the (111) SCS RSG prototype.

Table 3.6: Parameter comparison of RSG improvements

Device Parameter	HARPSS Polysilicon	(111) SOI SCS
Radial Diameter	1mm	2.5mm
Device Thickness	65µm	40µm
Number of Shells	1	3
Flexural Width	4µm	20µm
Resonant mass	5µg	50µg
Operating Frequency	40kHz	90kHz
Operating Q-Factors	~ 1500	~ 30,000
Drive amplitude	100nm	400nm
Sense gap (aspect ratio)	1.5 µm (~44:1)	4 µm (~10:1)
Brownian noise floor	108 °/hr/√Hz	2.3 °/hr/√Hz

Figure 3.28 shows the two flexural resonance peaks of the prototype multiple-shell RSG showing a split of 100Hz. The resonant Q-factor of each flexural mode measured at 25ºC and under 1mTorr pressure is approximately 30,000. Frequency split of 100Hz was compensated using tuning voltages of approximately ± 50V.

This has been shown in Figure 3.29. A comparison of the operating voltages of the HARPSS implementation and the multiple-shell RSG device formed using regular DRIE silicon etching is highlighted in Table 3.7.
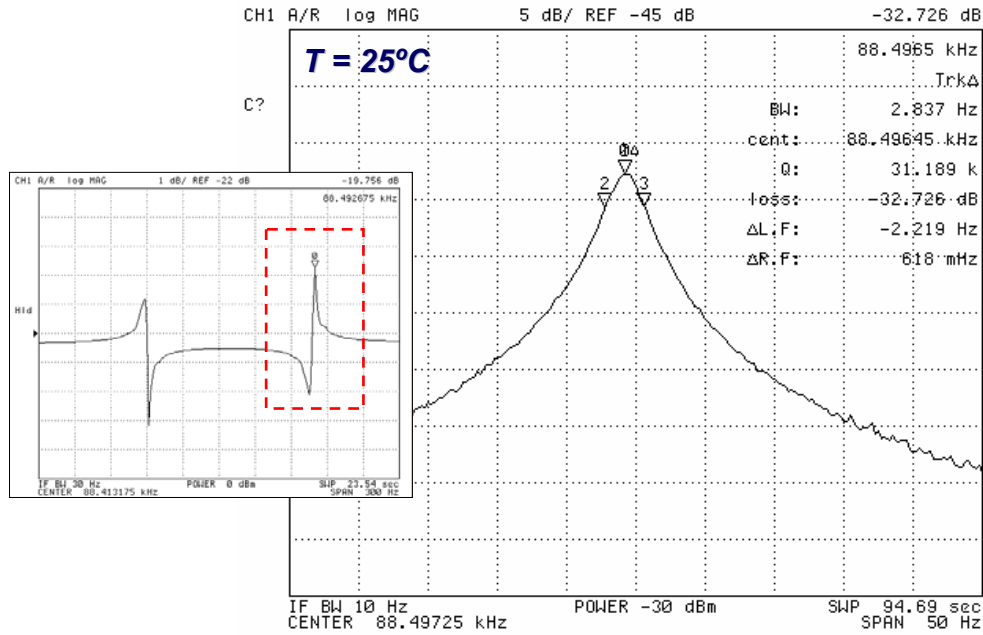
Figure 3.28: Primary flexural-mode resonant peak of the (111) multiple-shell RSG. (Inset) The typical initial frequency split of 100Hz.
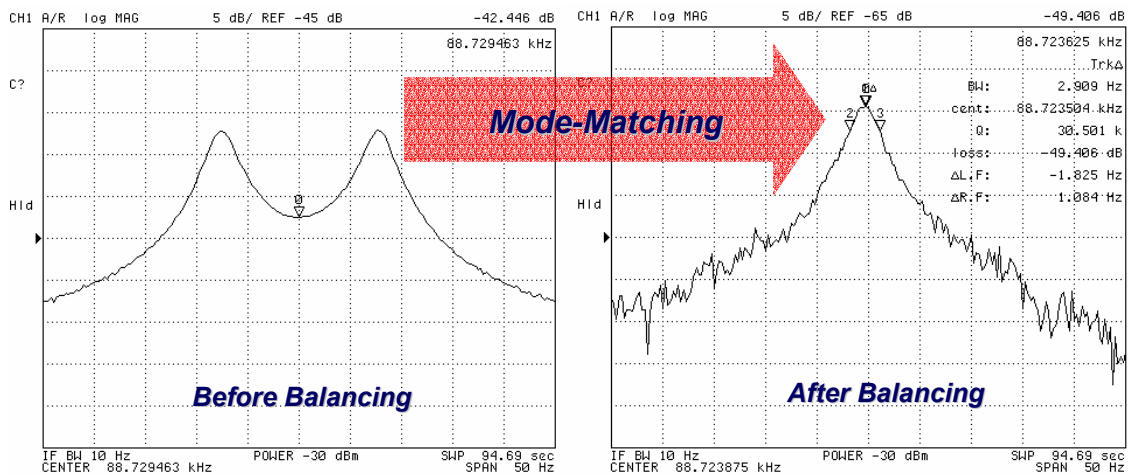
Figure 3.29: (Left*) Before balancing*, the two flexural modes have different frequencies. (Right) *After balancing*, the two peaks merge and the effective quality factor is 30,500.

Device Parameter	HARPSS Polysilicon	(111) SOI SCS
Frequency Separation	430 Hz	120 Hz
Polarization Voltage	4.8 V	45 V
0° Balancing	- 7.6 V	0 V
45° Balancing	11.1 V	48 V
+22.5° Balancing	0 V	-2.5 V
-22.5° Balancing	2.3 V	20 V

Figure 3.30 shows the Zero Rate Output of multiple-shell RSG after balancing. The bottom trace is the 45° sense signal and the top trace is the 0° sense signal while the device is driven at 0° drive. The quadrature phase difference can be verified in this picture.
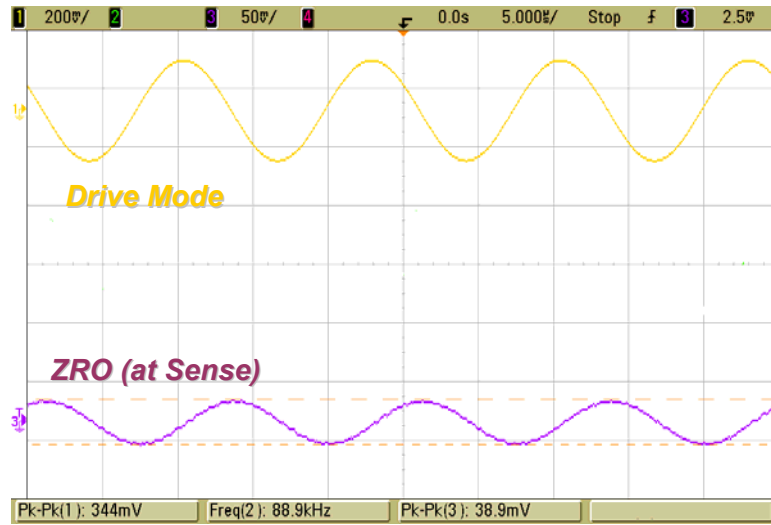
Figure 3.30: ZRO of the multiple-shell RSG after balancing (quadrature nulling)

3.6.2 Multiple-Shell (111) SCS RSG Performance Analysis

The rotation rate sensitivity response of a 40µm-thick multiple-shell RSG under mode-matched operation is presented in Figure 3.31. The RSG device with Q_{EFF} of 30,000 exhibits a rate sensitivity of 16mV/deg/s (at room temperature). This output

is obtained after a post-demodulation gain stage. Figure 3.32 shows the response of the multiple-shell (111) SCS RSG to a sinusoidal input rotation signal. The scale factor of the RSG is a direct function of the mode-matched Q and its stability over time. It was experimentally verified that the measured Q_{EFF} remained constant at the initial value of 30,000 over an extended period of time (under constant temperature and vacuum). The ZRO of a balanced RSG was sampled every 100ms for a period of 6 hours.
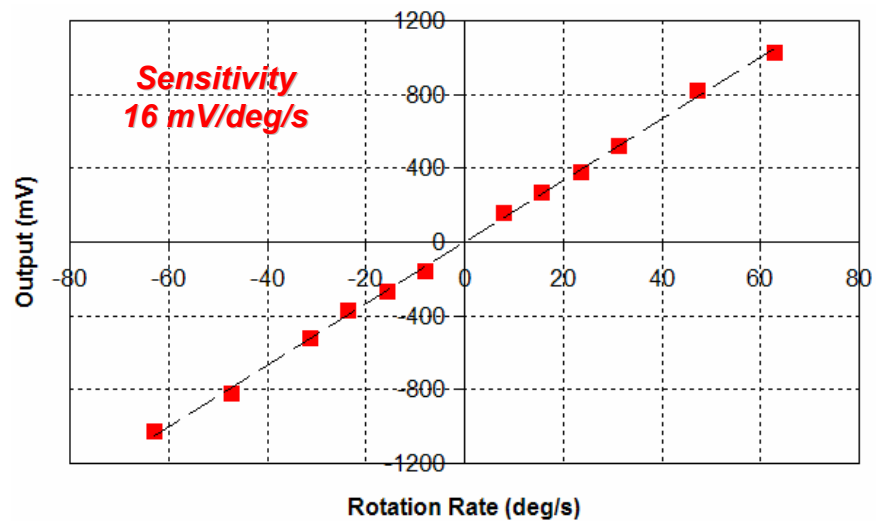
Figure 3.31: Scale-factor plot of the (111) SCS multiple-shell RSG prototype.
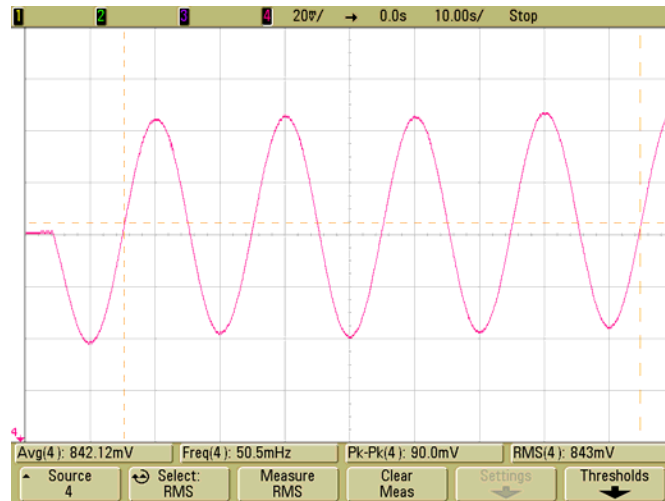
Figure 3.32: Output of the (111) SCS multiple-shell RSG to a sinusoidal input rotation signal.
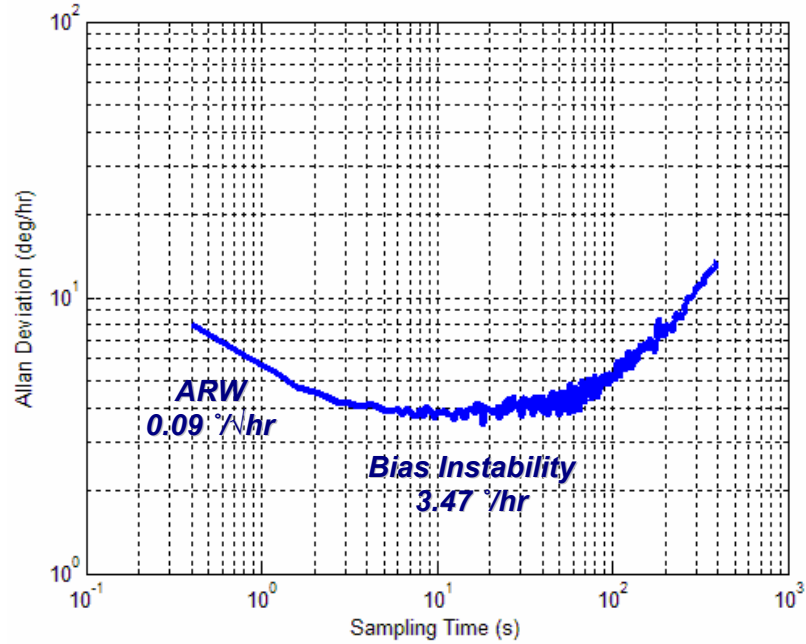
Figure 3.33: Root Allan Variance plot of the (111) SCS multiple-shell RSG at 25ºC.

The root Allan variance plot of the RSG is shown in Figure 3.33. From this graph, the estimated angle random walk (ARW) is determined to be 0.09deg/√hr while the measured bias instability of the system is 3.5deg/hr. A summary of the muliple-shell RSG device parameters are summarized in Table 3.8.

Table 3.8: Device parameter summary of the multiple-shell (111) SCS RSG prototype

Device Parameter	RSG Value
Radial Diameter	2.7mm
Mode-Matched Quality Factor	30,000
Sense Electrode Gap Spacing	4 µm
Star-Shell and Spring Width	20 µm
Height of Device Structure	40 µm
Drive Amplitude	400 nm
Resonant Frequency	88.8 kHz
Theoretical Brownian Noise Floor	2.3 ˚/hr/√Hz
Rate sensitivity	16 mV/˚/s
Angle Random Walk	0.09 °/√hr
Bias Drift	3.47 °/hr

3.6.3 Multiple-Shell (111) SCS RSG Temperature Characterization

In order to ensure high-performance, it is essential that mode-matching is maintained over temperature. The RSG was tested under both matched and split-mode conditions to accurately determine the effects of temperature on the operating modes. A summary of the device mode characterization in temperature may be found in Table 3.9. It is observed that the modes track with temperature. There is an observed Q-factor degradation to individual operating resonant modes at increased temperatures (shown in Figure 3.34). This is attributed to increased Q_{TED} at elevated temperatures.

Table 3.9: Measured operating mode Q-factor with temperature

Device Parameter	-5°C	25°C	50°C
Drive Frequency	88.750 kHz	88.722 kHz	88.691 kHz
Drive Q-Factor	40,306	30,017	24,080
Sense Frequency	88.765 kHz	88.737 kHz	88.706 kHz
Sense Q-Factor	40,329	29,011	23,966
Frequency Split	15 Hz	15 Hz	15 Hz
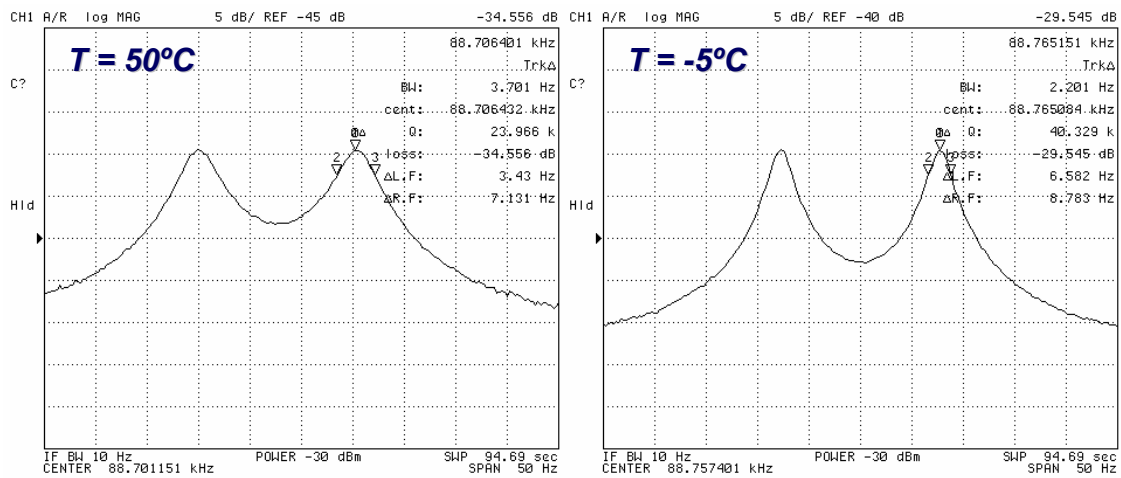
Figure 3.34: (Left) Measured primary flexural mode Q of 24,000 at 50°C. (Right) Measured primary flexural mode Q of 40,000 at -5°C.

Scale-factor measurements were made at three different temperature settings at matched-mode conditions and the sensitivity plot is displayed in Figure 3.35. As expected, with an increase in temperature the device operating-Q decreases, and consequently the sensitivity degrades.

Temp (°C)	Q_{EFF}	Output (mV/°/s)
-5	40,300	22.5
25	30,500	17.7
50	22,000	14.3
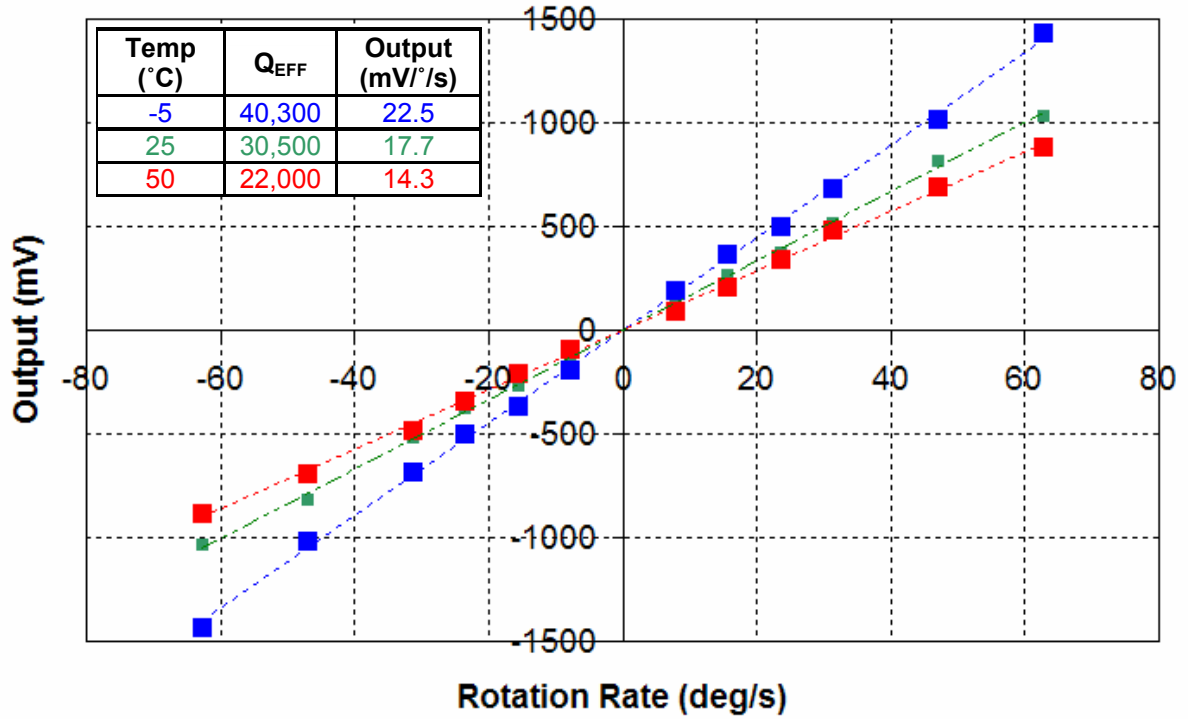
Figure 3.35: The rate sensitivity plot of the multiple-shell (111) SCS RSG device under mode-matched operation and at three different temperature settings.

Allan variance analysis was performed with ZRO data collected over a period of 6 hours, and at three constant temperature settings. In each case, the 40μm-thick multiple-shell (111) SCS RSG prototype was operated under mode-matched operation. As observed in Figure 3.36, the device has a bias instability of 3.47deg/hr at room temperature (25°C). The bias instability degraded at 50°C, which is primarily caused by the sensitivity of the device quality factor to

74

temperature variations. However at -5°C, the multiple-shell RSG prototype displayed an enhanced bias instability of 2.55deg/hr.

Temp (˚C)	ARW (deg/√hr)	Bias Drift (deg/hr)
-5	0.07	2.55
25	0.09	3.47
50	0.11	4.28
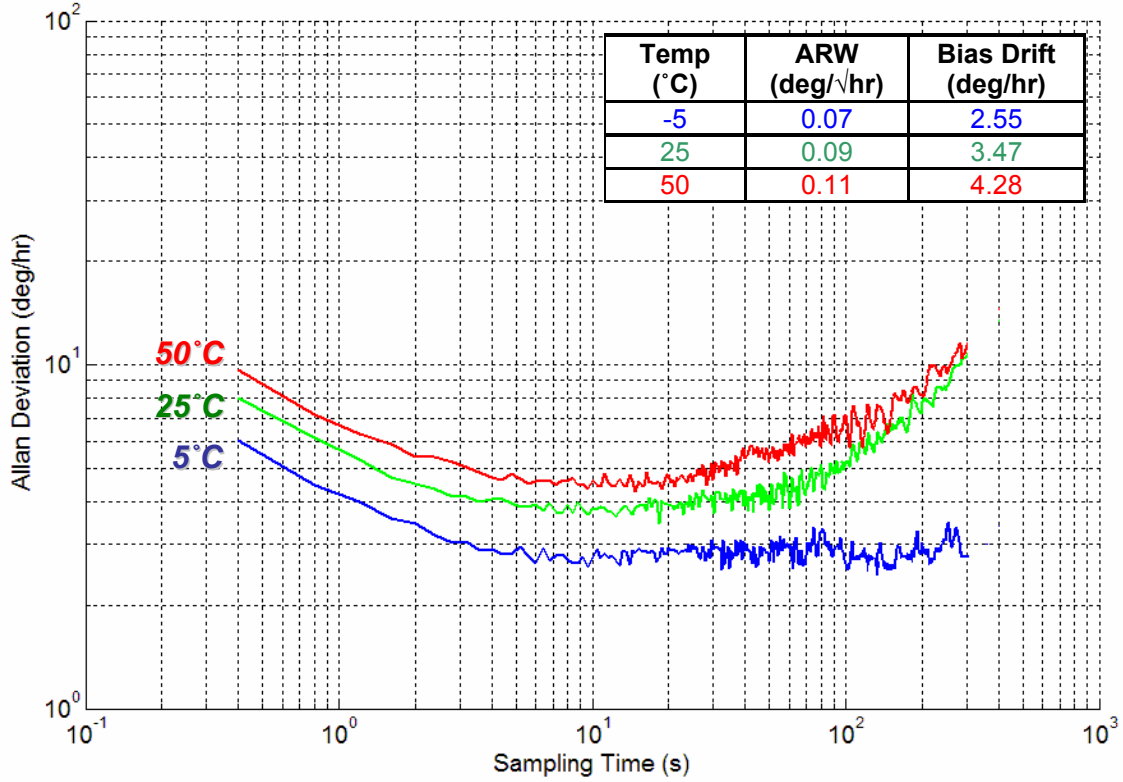
Figure 3.36: Root Allan variance plot of the multiple-shell (111) SCS RSG device under mode-matched operation and at three different temperature settings.

3.7 Summary

This chapter presented the design, implementation and characterization of a novel shell-type Class-II microgyroscope. The resonating star gyroscope is formed as a merged superposition of two square shells, yielding in-plane flexural modes that are utilized to sense rotation along the normal axis (yaw-rate). The first prototypes of the RSG implemented using a single-shell approach was fabricated using the HARPSS process. While the operating voltages were low, the device performance suffered as a result of low-Q operating modes. This low-Q is

attributed to the void-formation in trench-refilled polysilicon. To alleviate this problem and to ensure larger resonant mass, a multiple-shell RSG was implemented in a 40µm-thick (111) SOI substrate. The multiple-shell design has the required attributes for a high-precision gyroscope – a large resonant mass, and high-Q resonant modes through optimized flexural design. The optimized version of the RSG design implemented in 40µm (111) SOI substrate displayed Allan Variance bias instability of 3.47deg/hr. The current limitations of aspect ratio and device thickness can be addressed with the advancements in the field of DRIE silicon etching [58]. This will permit the RSG structure to approach sub-1 deg/hr bias stability values in the near future. The RSG structure will always be limited by the restrictions of the drive-mode amplitude. The mode-matched tuning fork gyroscope (M^2-TFG), the subject of the proceeding chapters addresses this concern while incorporating high-Q_{EFF} mode-matched operation.

CHAPTER IV

THE MODE-MATCHED TUNING FORK GYROSCOPE

In this chapter the concept and design of a novel Class-I mode-matched vibratory microgyroscope is discussed. In order to attain sub-deg/hr noise performance a vibratory gyroscope must attain high-Q mode-matched operation, large resonant proof-mass and large drive amplitude (the primary limiting factor in the RSG). The mode-matched tuning fork gyroscope (M^2-TFG) introduced in this chapter incorporates all the above specifications within a single framework.

4.1 Concept and Design

The mode-matched tuning fork gyroscope, as illustrated in the Figure 4.1, is comprised of two proof-masses, supported by a network of flexural springs and anchored at a central post. A collection of capacitive control electrodes are symmetrically distributed around the proof-masses. The operating principle is based upon a standard tuning fork's response to rotation. The two proof-masses are analogous to tines and driven in-plane into resonance along the x-axis using comb-drive electrodes. An input rotation signal normal to the device-plane (along z-axis) causes a Coriolis-induced transfer of energy to the sense vibration mode. The resulting in-plane displacement is sensed at sense electrodes located along the y-axis. The operating mode-shapes of the M^2-TFG may be viewed in Figure 4.2.
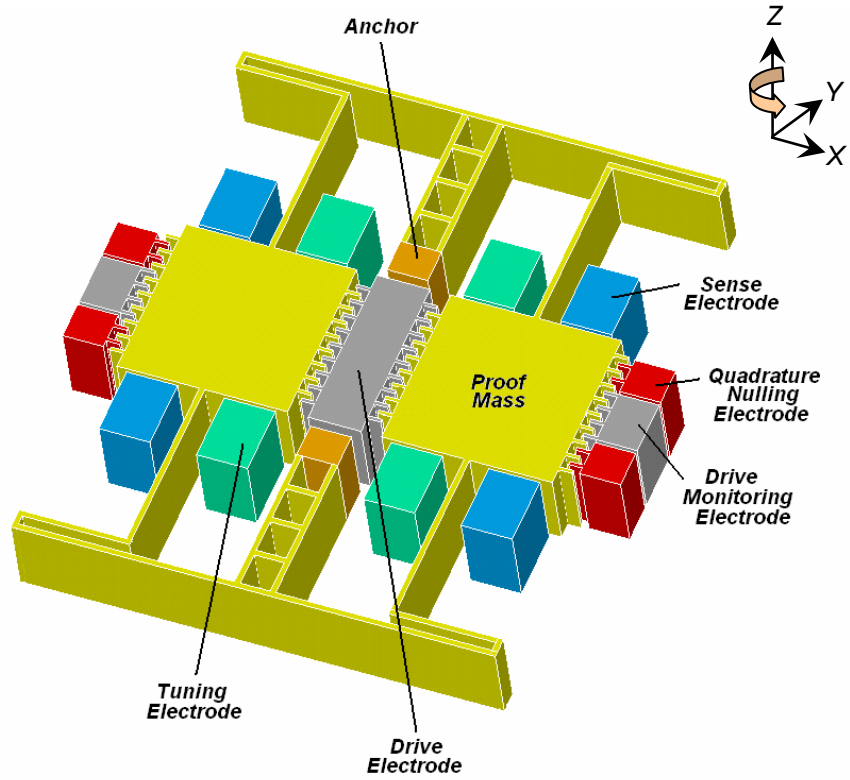
Figure 4.1: Schematic diagram of the Mode-Matched Tuning Fork Gyroscope
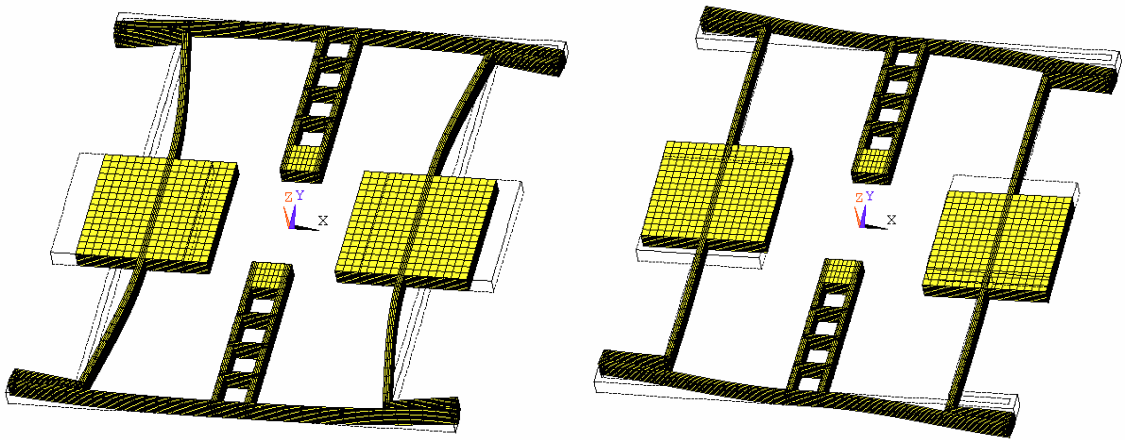
Figure 4.2: In-plane operating flexural modes. (Left) Drive resonant mode along the x-axis. (Right) Sense resonant mode along the y-axis.

An advantage in utilizing symmetric tuning fork architecture is the inherent differential nature of the sense-mode. As a result, linear acceleration is rejected as common mode signal without the need for complex electronics. The anchor

design of the M²-TFG satisfies two critical properties: mechanical coupling and resonant mode isolation. The mechanical coupling, promoted by the central ladder-shape anchor structure, allows synchronization of the phases of the proof-masses even in the presence of minor fabrication imperfections. The second important function enabled by the anchor, is the isolation of the in-plane operating modes from the two other existing in-plane resonant modes. These are the pseudo-drive mode (both proof-masses vibrate along the drive-axis in same direction) and the pseudo-sense mode (both proof-masses vibrate along the sense-axis in same direction). These two modes correspond to the symmetric and anti-symmetric modes of a tuning-fork structure and are also influenced by Coriolis acceleration. The pseudo-operating modes may be viewed in Figure 4.3. In the current M²-TFG design, these modes occur at least 200 Hz away from the operating modes of interest.
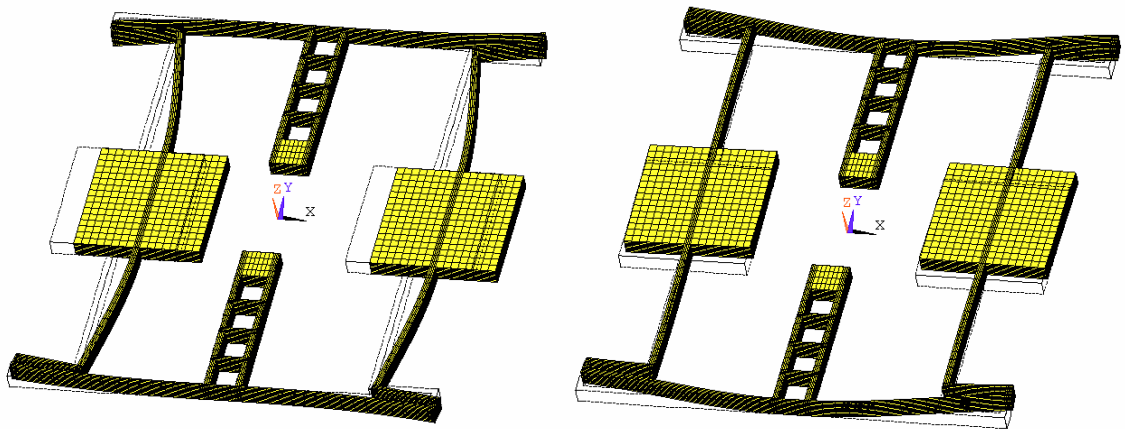
Figure 4.3: In-plane pseudo-operating flexural modes. (Left) Pseudo-drive resonant mode along the x-axis. (Right) Pseudo-sense resonant mode along the y-axis.

The flexural spring design must satisfy a host of critical properties. The ideal spring design must ensure large mobility along both axes. To this effect, a fish-hook

architecture was adopted which ensures that the mode shapes have two-directional flexibility [59]. The current spring structure enables 4-6μm drive mode displacements. The second important criterion is to ensure that the two operating mode frequencies lie in close proximity of one another while remaining isolated from the out-of-plane resonant modes.

4.1.1 Modal Analysis of the M²-TFG Geometry

Detailed modal analysis of the flexural springs and anchor were performed in ANSYS to optimize the dimensions to allow the sense mode to occur 50–200Hz higher than the drive mode. The FEM model was constructed using the SOLID64 element – ideal for investigating anisotropic high-aspect ratio structures. Upon fabrication, the sense mode frequency is electrostatically tuned to match the drive mode frequency. A summary of the first seven mode-shapes simulated in ANSYS for a prototype M²-TFG implemented on 50μm thick (100) single crystalline SOI device layer with 400μm square-proof-masses and 20μm wide flexural beam suspensions is displayed in Table 4.1.

Table 4.1: ANSYS summary of the flexural resonant modes of a prototype M²-TFG

Resonant Mode	Frequency (kHz)	Figure #
Rocking	14.447	Figure 4.4
Pseudo-Drive	15.863	Figure 4.3 (Left)
Drive	16.121	Figure 4.2 (Left)
Sense	16.269	Figure 4.2 (Right)
Pseudo-Sense	16.491	Figure 4.3 (Left)
Out of Plane	22.625	Figure 4.5
Tilt	42.455	Figure 4.6
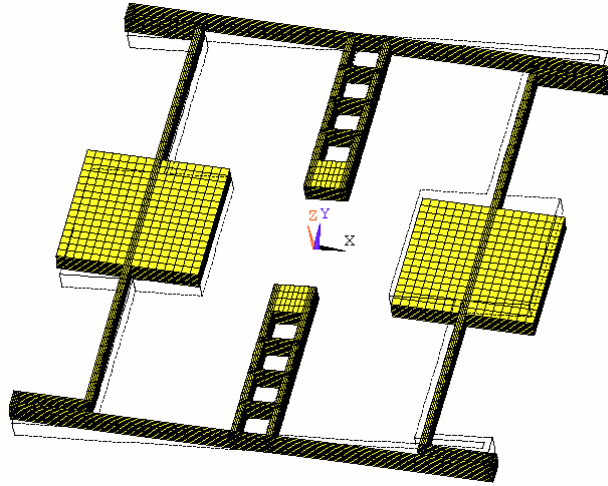
Figure 4.4: Out-of-plane rocking flexural resonant mode
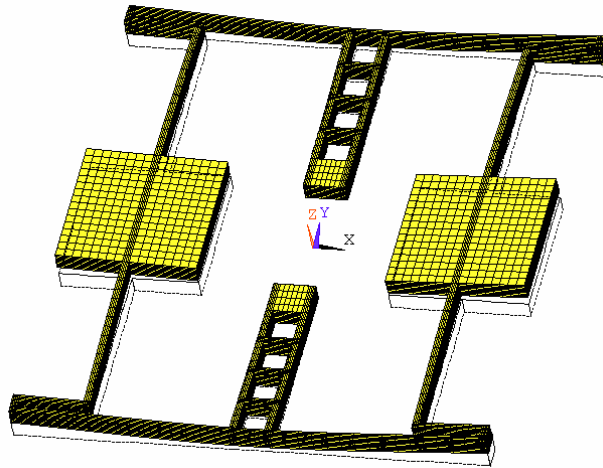
Figure 4.5: Out-of-plane flexural resonant mode
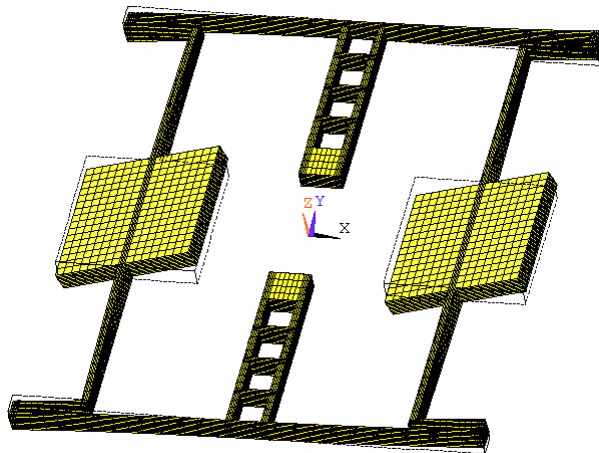
Figure 4.6: Out-of-plane proof-mass tilting resonant mode

As observed in Table 4.1, the out-of-plane resonant modes of the M^2-TFG are isolated from the regular in-plane operating modes through design. Moreover elimination of the ground plane under the comb-drive electrodes through the fabrication process prevents the excitation of these modes in any case (as illustrated in the following section) [60].

4.2 Fabrication of Prototype SOI M^2-TFG

The prototype M^2-TFGs are implemented on low-resistivity SOI substrate with a device layer thickness of approximately 40-60μm. The outline of the fabrication process flow is shown in Figure 4.7. The moving sections of the structure and the area under the comb drives are first released from the rear by etching the handle silicon layer through to the buried oxide layer using the Bosch process. The handle layer silicon is typically between 300-500μm in thickness and a 2-3μm thick oxide mask (thermally grown wet oxide at 1100˚C) is usually the mask of choice. The buried oxide is then removed in a reactive ion etching (RIE) system. Finally the device layer is patterned all the way through; leaving behind a suspended structure whose anchor is supported to the substrate via support posts (as observed in Figure 4.9). SEM images of fabricated M^2-TFG are shown in Figures. 4.8-4.10. The device-layer silicon etching was performed using the Advanced Silicon Etch (ASE^{TM}) process developed by Surface Technology Systems (STS). At high plasma densities, the silicon etch profile tends to have high lateral etch rate at the Si-SiO$_2$ interface, an effect commonly referred to as notching. Eliminating the buried-oxide layer underneath the M^2-TFG area prevents structural damage via notching (as seen in Figure 4.10).

1. Low-resistivity (100) SOI substrate

2. Handle-layer silicon etching

3. Buried oxide-layer etching

4. Device-layer silicon etching
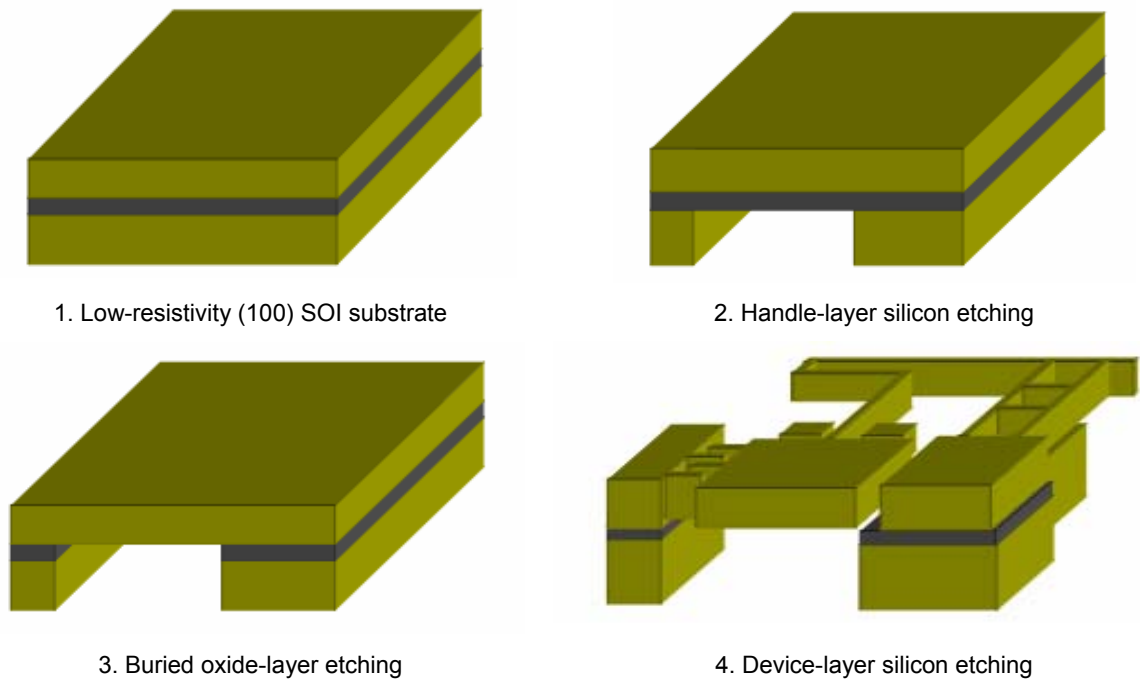
Figure 4.7: Outline of fabrication process flow for SOI M^2-TFG prototypes

Drive Monitor Electrode

1.5mm

1.4mm

Proof Mass

Central Drive Electrode

Sense Electrode

Quadrature Nulling Electrode

Z

Y

X
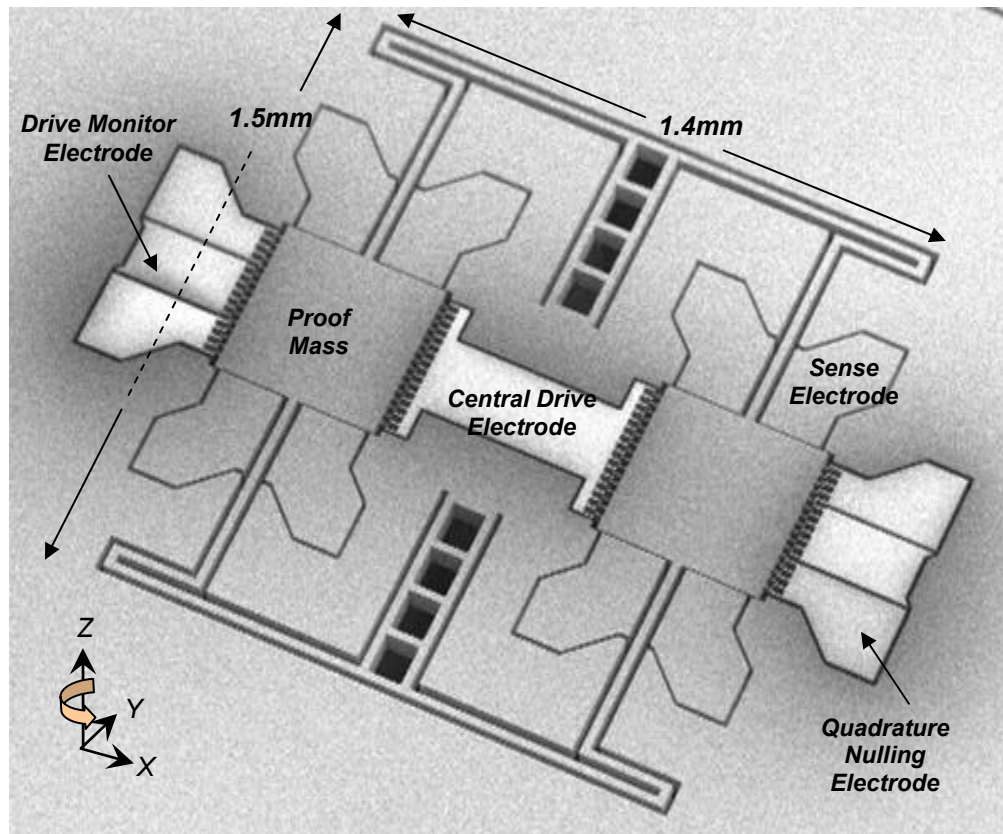
Figure 4.8: SEM overview of the Mode-Matched Tuning Fork Gyroscope.
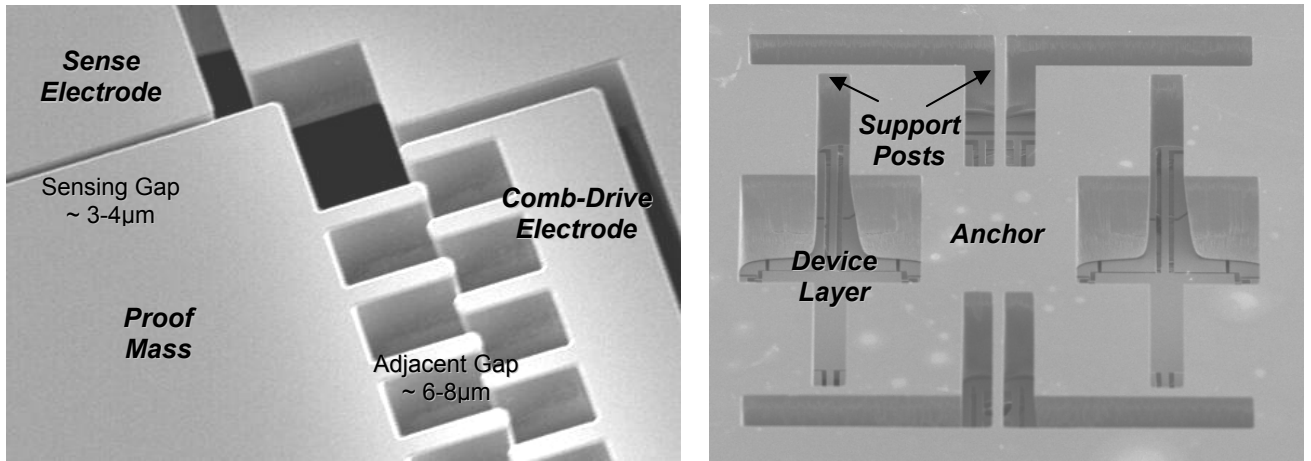
Figure 4.9 (Left) View of the comb-drive and sensing electrode gaps. (Right) View of the support posts of M2-TFG (as viewed from the handle layer).
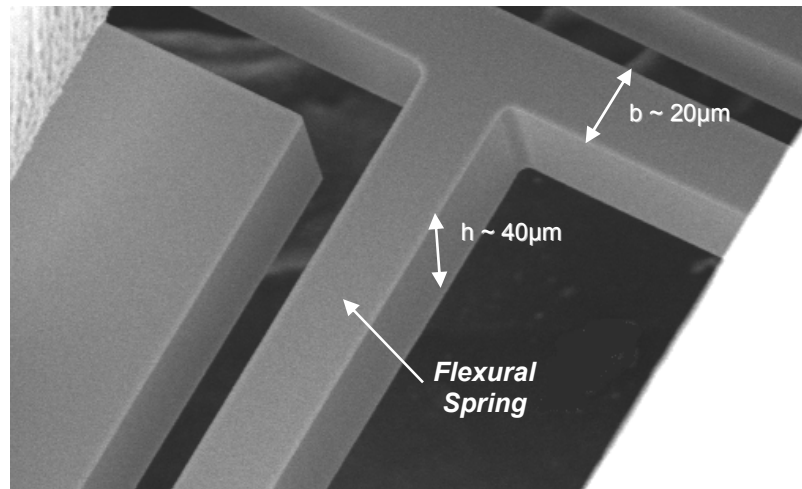
Figure 4.10: View of the flexural springs as observed from handle-layer openings.

However it does not prevent notching from occurring at the oxide interface in the electrode boundaries. The resultant accumulation of silicon debris compromises electrical isolation. Notching arises as a result of deflection of incoming ions onto the sidewalls due to charge build-up at the surface of the buried oxide. By reducing the operating RF frequency from 13.56 MHz to 380 kHz, it is possible to generate a surplus of low-energy ions. These low energy ions are able to neutralize the excess charge build-up resulting in debris-free electrode

trenches [61]. A short HF etch was performed to release areas under the anchor support posts. The fabrication process steps are summarized in Appendix A.

The fabrication process is simple and precludes the requirement of any perforations in the proof mass, resulting in a larger mass per unit area. The simultaneous elimination of the ground plane under the comb drives prevents the excitation of the out of plane modes and detrimental effects associated with comb-levitation. The fact that all the electrodes and the structure are defined using a single mask ensures that there are no horizontal misalignment errors of actuation/sense gaps.

4.3 Energy Loss Mechanisms in M²-TFG

A key performance parameter of vibratory gyroscopes is the mechanical quality factor (Q) of its operating modes. In order to achieve higher sensitivity and better rate-resolution and drift, the design of gyroscopes with large sense-mode Q is pursued. A large drive-mode Q is also necessary for improved bias stability as well as ensuring large drive amplitudes using small drive voltages - a desirable feature required in low-power CMOS interfacing [62, 63]. The energy dissipation mechanisms associated with the M²-TFG design are air damping, support loss, thermo-elastic damping (TED), surface loss, and the intrinsic loss of silicon. Hence the overall mechanical Q for an operating mode is expressed as the sum of all these contributions.

$$\frac{1}{Q} = \frac{1}{Q_{Air-Damping}} + \frac{1}{Q_{TED}} + \frac{1}{Q_{Support}} + \frac{1}{Q_{Surface}} + \frac{1}{Q_{Intrinsic}} \qquad (4.1)$$

Among them, the effect of air damping may be eliminated by operating the microgyroscope in vacuum, while the contribution of surface loss can be made negligible through optimized processing. With $Q_{Intrinsic}$ being very high in silicon, this leaves TED and support loss as the primary loss mechanisms in the M^2-TFG design. By simplifying the structure, one may identify basic trends required to operate in a region of high-Q.

4.3.1 Simplification of the M^2-TFG Structure

As illustrated in Figure 4.2, during the flexural vibrations in the operating resonant modes, the proof masses only undergo translational motion. The spring structures unlike the proof-masses experience structural deformation. Half the tuning fork structure in each operating mode may be viewed as a beam-like resonator with an added proof-mass symmetric with respect to the center-line [64]. The governing equations for the flexural-mode vibrations of the tuning fork structure will be explored by analyzing a clamped-clamped (C-C) beam resonator with a proof-mass attached at its center (as illustrated in Figure 4.11).
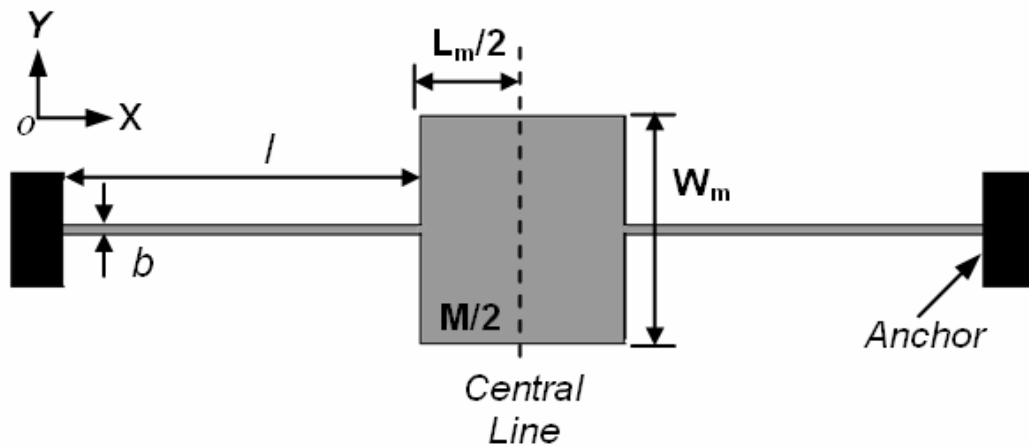
Figure 4.11: Schematic view of a clamped-clamped resonator with added proof-mass.

The width and thickness of the C-C beam are denoted by *b* and *h* respectively. The C-C beam is symmetric about the central line of the proof mass and half of its length is denoted by *l*. Since its cross-section ($W_m \times h$) is much larger than that ($b \times h$) of the beam, the proof mass does not experience deformation but translation motion during its vibrations. Therefore, the governing equation for the flexural-mode vibrations in such resonators can be expressed as Eq. 4.2:

$$EI\frac{\partial^4 Y}{\partial x^4} + \rho A\frac{\partial^2 Y}{\partial x^2} = 0 \tag{4.2}$$

where $I = (b^3h)/12$ and $A = bh$, denote the moment of inertia and the cross-section area of the beam respectively. The time-harmonic vibrations in the resonator will take the form:

$$Y(x,t) = Y_0(x)e^{i\omega_0 t} \tag{4.3}$$

In Eq. 4.3, ω_0 denotes the natural angular resonant frequency. By using the boundary condition at *x = 0*, requiring that both the displacement and the slope be zero, the solution to Eq. 4.2 is expressed as:

$$Y_0(x) = \frac{U}{2}\left\{\cosh\left(\beta\pi\frac{x}{l}\right) - \cos\left(\beta\pi\frac{x}{l}\right) + \chi\left(\sinh\left(\beta\pi\frac{x}{l}\right) - \sin\left(\beta\pi\frac{x}{l}\right)\right)\right\} \tag{4.4}$$

In Eq. 4.4, *β* and *χ* denote the mode constant and the mode shape factor, respectively. Both *β* and *χ* can be determined by the boundary condition at the other end of the beam. For a C-C beam resonator with a proof mass *M* at its center, only half of its symmetric structure is considered. The symmetric boundary condition at *x = l* requires that the slope be zero and the shear force be equal to the acceleration of half of the proof mass:

$$x = l: \quad \frac{\partial Y_0}{\partial x} = 0, \quad -EI\frac{\partial^3 Y}{\partial x} = \frac{M}{2}\omega^2 Y_0 \tag{4.5}$$

For arbitrary values of the proof mass M, there exist multiple Eigen-frequencies at which Eq. 4.5 is satisfied, and can be solved numerically to determine β and χ for a given proof mass M. Then, the natural angular resonant frequency is expressed in Eq. 4.6

$$\omega_0 = \left(\frac{\beta\pi}{l}\right)^2 \sqrt{\frac{EI}{\rho A}} \tag{4.6}$$

A micromechanical tuning fork gyroscope holds the same salient vibration features as a beam-like resonator with a proof mass: (1) deformation in the beam and (2) translation in the proof mass. Therefore, the theoretical derivations presented in this section are directly applicable to a tuning fork structure, serving as the core to analyze energy loss mechanisms of the mode-matched tuning fork gyroscope.

4.3.2 Estimation of Q$_{TED}$ in M²-TFG

From the previous subsection, the governing equation expressed in Eq. 4.3, for thermoelastic-uncoupled flexural-mode vibrations in a beam-like resonator with a proof mass is the same as the one for a simple beam resonator [65], except that the addition of a proof mass modifies the resonant frequency and mode shape. Based upon the theory of linear thermoelasticity, the equation for thermoelastic-coupled vibrations in this type of resonators is expressed as follows:

$$\rho A\frac{\partial^2 Y}{\partial t^2} + \frac{\partial^2}{\partial x^2}\left(EI\frac{\partial^2 Y}{\partial x^2} + E\alpha_T I_T\right) = 0 \tag{4.7}$$

In Eq. 4.7 I_T is the thermal contributions to the moment of inertia. This equation is exactly the same as the coupled one for a simple beam resonator. Therefore, following the same derivation in [65] gives rise to the exact solution to TED in a beam-like resonator with a proof mass:

$$Q_{TED}^{-1} = \Delta_E \left(\frac{6}{\xi^2} - \frac{6}{\xi^3} \frac{\sinh(\xi) + \sin(\xi)}{\cosh(\xi) + \cos(\xi)} \right)$$

(4.8)

In Eq. 4.8, ξ = b $\sqrt{(\omega_0/2\chi)}$; ΔE and χ denote the thermal relaxation strength and thermal diffusivity of the structure's material, respectively. The behavior of TED in a beam-like resonator with a proof mass versus resonant frequency is illustrated in Figure 4.12, where TED in a C-C beam resonator of length $2l$ (and same beam width) *is used* for comparison.
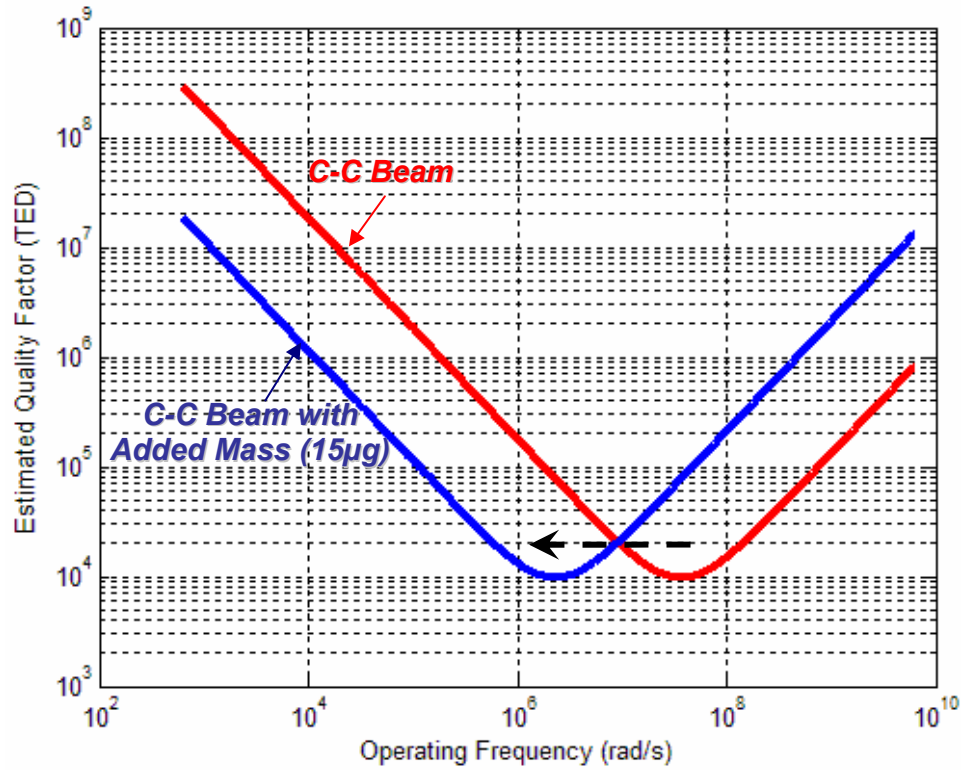
Figure 4.12: Effective Q-factor comparison of a clamped-clamped resonant structure with (blue) and without (red) an added proof-mass.

It is noticeable that the proof mass shifts the Debye peak of a simple beam resonator to lower resonant frequency. This can be explained by the fact that the proof mass does not suffer any TED because it does not undergo any volume change. However it does affect the value of ξ (which has an effect on TED according to Eq. 4.8). The Q_{TED} is a function of the flexural spring width (b) and the operating frequency (ω_0). In the current M^2-TFG design, the flexural spring dimensions and operating frequency regime were tactically selected to operate in a region away from the Debye peak of the Q_{TED} curve.

4.3.3 Estimation of $Q_{Support}$ in M^2-TFG

During resonant flexural vibrations, the proof-masses exert a time-harmonic load on the support structure. Acting as an excitation source, this time-harmonic load excites elastic waves propagating through the support. The vibration energy dissipated through elastic wave propagation in the support media represents the support loss. The complexity of the anchor geometry and composition prevented an accurate analysis of the support loss. However since the governing equation of a beam-like resonator with a proof mass is the same as its counterpart of a simple beam, it is reasonable to conclude that support loss in a beam-like resonator with a proof mass is similar to that in a beam resonator and thus is proportional to the cubic power of the ratio of the beam length to the beam width as expressed in Eq. 4.9 [66].

$$Q_{Support} \propto \left(\frac{l}{b}\right)^3 \tag{4.9}$$

The flexural beams of the M²-TFG were designed with high-aspect ratio to minimize support loss and ensure it would not be the dominating loss-mechanism in the structure.

4.4 M²-TFG Parallel Plate Sensing

A rotation signal along the normal axis (z-axis) of the M²-TFG results in a Coriolis induced acceleration on the individual proof-masses along the sensitive axis (y-axis). The magnitude of the Coriolis acceleration is given by the vector cross product of the input rotation rate vector and the velocity of the proof mass as measured in the rotating reference frame (Eq. 2.5). Considering that the proof-masses are oscillating in a sinusoidal fashion at the drive-mode resonance, the expression for the Coriolis acceleration along the sense-axis is given by:

$$a_{Coriolis-y} = 2\Omega_z(t)v_{Drive-x}(t) = 2\Omega_z(t)x_{Drive}\omega_{Drive}\cos(\omega_{Drive}t) \qquad (4.10)$$

In Eq. 4.10, 'Ω_z is the input rotation rate, '$v_{Drive-x}$' is the velocity of the drive resonant mode, 'x_{Drive}' is the amplitude of drive-mode oscillation and 'ω_{Drive}' is the drive-mode resonant frequency. This expression shows that the Coriolis acceleration generated in the M²-TFG is an amplitude modulated (AM) sinusoidal signal, which, in the frequency domain, appears as a dual sideband signal centered at the resonant frequency. The rotation-induced proof-mass displacements along the y-axis causes the gap between the parallel plate sense electrode and the proof-mass to change. This change in capacitive gap is proportional to the input rotation rate, and is detected by means of transimpedance front-end electronics as described in Chapter V.

4.5 Drive-Mode Actuation Mechanism of M^2-TFG

As discussed in Chapter II, a key parameter that determines both the resolution and the sensitivity of a micromachined vibratory gyroscope is the drive amplitude. Stable drive amplitudes approaching 5μm is essential in order to achieve the sub-deg/hr noise performance targeted by the M^2-TFG design. For this reason, comb-drive electrodes were chosen ahead of parallel-plate electrodes as the choice of actuation for the drive resonant mode. Comb-drive actuation offers greater linear range of operation as well as larger drive displacement before pull-in [67, 68]. However, voltage-controlled comb-drive actuation scheme as employed by the M^2-TFG is susceptible to snap-down along the transversal direction. The M^2-TFG is not a de-coupled design (i.e. proof-mass undergoes sense and drive mode deflections) and since it operates at mode-matched operation, the relative stiffness along the operating modes is the same (i.e. $k_x = k_y$)

Figure 4.13 shows the comb-drive architecture deployed by the M^2-TFG. To analyze the stability of comb-drive electrode, it is necessary to determine the expression for the potential energy of the overall actuation system. The overall capacitance of the comb-drive electrode is expressed as:

$$C_{comb-drive} = N\varepsilon_0 h\left(x + w_0\right)\left(\frac{1}{g-y} + \frac{1}{g+y}\right) \qquad (4.11)$$
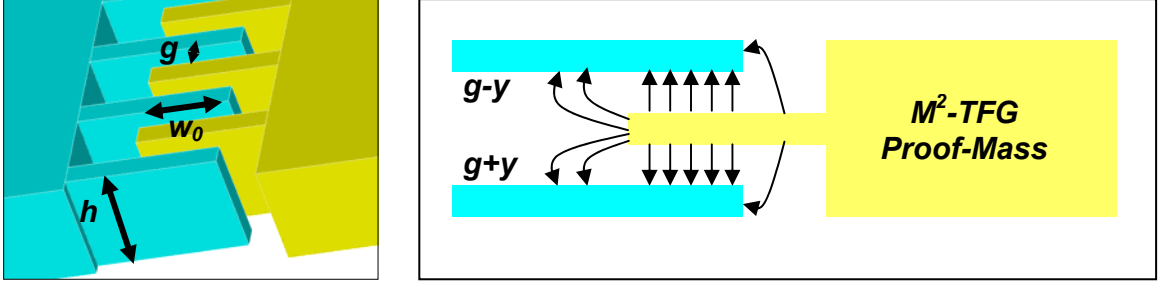
Figure 4.13: Salient feature of the comb-drive actuation scheme deployed in the M2-TFG.

In Eq. 4.11, 'N' indicates the number of combs, 'h' refers to the comb-thickness, 'w_0' is the initial overlap, 'g' is the adjacent gap size, 'x' is the lateral displacement amplitude along the drive axis (x-axis) and 'y' represents the transversal displacement along the sense axis (y-axis) which may be caused either by Coriolis or quadrature errors.

The total potential energy of the M^2-TFG actuator system is expressed by the sum of the electrostatic energy stored inside the comb-drive capacitance and the energy stored inside the restoring springs (along the operating axes)

$$P.E. = \frac{1}{2}k_x x^2 + \frac{1}{2}k_x x^2 - \frac{1}{2}C_{comb-drive}V^2 \qquad (4.12)$$

The stability of the comb-drive electrode scheme along the drive axis (i.e. x-axis) is first investigated as follows.

$$\frac{\delta P.E.}{\delta x} = k_x x - \frac{1}{2}N\varepsilon_0 h\left(\frac{1}{g-y} + \frac{1}{g+y}\right)V^2 \qquad (4.13)$$

$$\frac{\partial^2 P.E.}{\partial x^2} = k_x \qquad (4.14)$$

From Eq. 4.14, it is evident that $\delta^2 P.E./\delta x^2 > 0$ for all displacements along the x-axis. Hence the comb-drive induced displacement of the proof-masses along the x-axis is stable. However, the expression for stability along the sense axis (y-axis) is not as straightforward.

$$\frac{\delta P.E.}{\delta y} = k_y y - \frac{1}{2} N\varepsilon_0 h(x + w_0)\left(\frac{1}{(g-y)^2} - \frac{1}{(g+y)^2}\right)V^2 \qquad (4.15)$$

$$\frac{\partial^2 P.E.}{\partial y^2} = k_y - \frac{1}{2} N\varepsilon_0 h(x + w_0)\left(\frac{1}{(g-y)^3} - \frac{1}{(g+y)^3}\right)V^2 \qquad (4.16)$$

The force re-balance equation along the x-axis may be expressed as Eq. 4.17. The relationship between applied voltage 'V' and the individual components of the comb-drive geometry is expressed in Eq. 4.19.

$$F_x = \frac{1}{2}V^2 \frac{\delta C_{comb-drive}}{\delta x} = k_x x \qquad (4.17)$$

$$\frac{1}{2}V^2 N\varepsilon_0 h\left(\frac{1}{g-y} + \frac{1}{g+y}\right) = k_x x \qquad (4.18)$$

$$V^2 = \frac{2k_x \Delta x}{Nh\varepsilon_0}\frac{1}{\left(\dfrac{1}{g-y} + \dfrac{1}{g+y}\right)} \qquad (4.19)$$

Hence Eq. 4.16 may be re-written in the following form:

$$\frac{\partial^2 P.E.}{\partial y^2} = k_y - \left(\frac{1}{(g-y)^3} - \frac{1}{(g+y)^3}\right)\frac{2k_x x(x+w_0)}{\left(\dfrac{1}{g-y} + \dfrac{1}{g+y}\right)} \qquad (4.20)$$

$$\frac{\partial^2 P.E.}{\partial y^2} = k_y - 2k_x x(x+w_0)\frac{g^2 + 3y^2}{(g^2 - y^2)^2} \qquad (4.21)$$

Hence the condition $\delta^2 P.E./\delta x^2 > 0$ may be satisfied with Eq. 4.22, which is an expression that relates all the important components of comb-drive actuator stability for transversal pull-in. For the case of the M^2-TFG, $k_x = k_y$ for operation under mode-matched conditions.

$$k_y - 2k_x x\left(x + w_0\right)\frac{g^2 + 3y^2}{\left(g^2 - y^2\right)^2} > 0 \qquad (4.22)$$

$$x_{max} < \frac{-w_0 + \sqrt{w_0^2 + 2g^2}}{2} \qquad (y \ll g) \qquad (4.23)$$

The comb-drive actuator scheme employed in the M^2-TFG prototype has initial comb overlap and adjacent gap sizes designed to accommodate drive amplitudes approaching 5μm while staying in the stable operating regime while undergoing deflections as large as 1/5th of the sense gap.

4.6 M²-TFG System Modeling

The M^2-TFG can be conceptualized as a coupled resonator system, with the rotation induced Coriolis force being the coupling agent between the two resonant operating modes [23]. The dynamics of the device are governed by Newton's second law of motion. The ordinary differential equation (ODE) that relates the proof-mass displacement along the drive axis (x-axis for reference) to the applied forcing voltage 'v_{drive}' (at the drive resonance frequency) for an M^2-TFG is expressed as:

$$\frac{d^2 x}{dt^2} + \frac{D_x}{M}\frac{dx}{dt} + \frac{K_x}{M}x = -\frac{V_P v_{drive}}{M}\frac{\delta C_{comb-drive}}{\delta x} \qquad (4.24)$$

$$\frac{\delta C_{comb-drive}}{\delta x} = \frac{\varepsilon_0 Nh}{g} \tag{4.25}$$

'D_x' and 'K_x' represent the damping and mechanical stiffness terms of the drive-mode and are related to the M^2-TFG parameters similar to Eq. 2.12-2.13. Similarly the ODE for the sense-mode deflections (along the y-axis) in response to a rotation signal normal to the plane of operation of the M^2-TFG may be expressed as:

$$\frac{d^2 y}{dt^2} + \frac{D_y}{M}\frac{dy}{dt} + \frac{K_y}{M}y = 2\Omega_z \frac{dx}{dt} = 2\Omega_z q_{Drive}\omega_{Drive} \tag{4.26}$$

'D_y' and 'K_y' represent the damping and mechanical stiffness terms of the sense-mode and are related to the M^2-TFG parameters as follows:

$$D_y = \frac{\omega_y M}{Q_y} \tag{4.27}$$

$$K_y = \omega_y^2 M - K_{Electrostatic} \tag{4.28}$$

The stiffness term 'K_y' incorporates the effect of electrostatic spring-softening as expressed in Eq. 4.28. The stiffness along the sense-axis is a function of the applied polarization voltage and forms the basis of electrostatic spring softening (or frequency tuning of the sense-resonant mode) in the M^2-TFG. This concept will be explained in detail in Chapter V.

The ODE expressions in Eq. 4.24, 4.26 can be used to generate an equivalent electrical model which may be used for simulating the M^2-TFG structure in SPICE. Figure 4.14 shows the RLC equivalent circuit used to model the resonant operating-modes of the M^2-TFG. Since the M^2-TFG is a capacitive sensor, the

parallel feed-through capacitance 'C_{FT}', models the AC coupling path between the proof-mass and electrodes. The series RLC path models the sensor motional current, i.e., the current due to proof-mass motion.
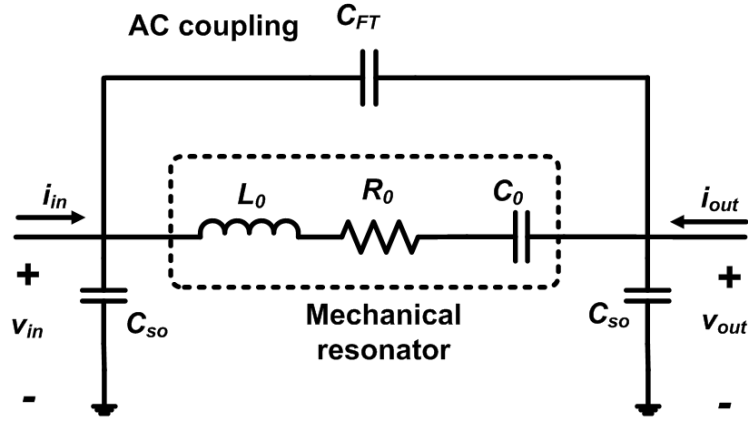
Figure 4.14: Equivalent RLC circuit representation of the M²-TFG.

Table 4.2: Approximate values of equivalent RLC parameters for the M²-TFG.

Circuit Parameter	Drive-Mode (Comb-Drive)	Sense-Mode (Parallel-Plate)
R - Motional Resistance	$\dfrac{\omega_0 M g^2}{Q\left(\varepsilon_0 N h V_P\right)^2}$	$\dfrac{\omega_0 M d_{s0}^2}{Q\left(n\varepsilon_0 l h V_P\right)^2}$
L - Motional Inductance	$\dfrac{M g^2}{\left(\varepsilon_0 N h V_P\right)^2}$	$\dfrac{M d_{s0}^4}{\left(n\varepsilon_0 l h V_P\right)^2}$
C - Motional Capacitance	$\dfrac{\left(\varepsilon_0 N h V_P\right)^2}{\omega_0^2 M g^2}$	$\dfrac{\left(\varepsilon_0 n l h d_{s0} V_P\right)^2}{\omega_0^2 M d_{s0}^3 - 2\varepsilon_0 n l h V_P^2}$

The M²-TFG uses comb-drive electrodes for actuating the drive mode, while parallel plate electrodes are used for sensing proof-mass motion along the y-axis. Hence, expressions for the equivalent motional elements along these axes differ and have been summarized in Table 4.2.

CHAPTER V

OPERATING SYSTEM OVERVIEW OF THE M²-TFG

In this chapter, the major control blocks of the M²-TFG interface system are identified and discussed. The entire system of the M²-TFG may be broadly classified under three parts: (1) the drive loop – which oscillates the proof-masses at the drive-mode resonant frequency with a constant displacement amplitude, (2) the sense channel – which extracts the input rotation signal information from the AM modulated Coriolis response, and (3) the quadrature nulling and frequency tuning branch – which operated in tandem ensures quadrature signal nulling and consequent compensation of the frequency mismatch between the operating modes of the M²-TFG.

5.1 Two-Chip MEMS Capacitive Interfaces

The minimum detectable rotation rate in the gyroscope depends on the noise floor of the entire system and is given by the TNEΩ expression (Eq. 2.20). The objective of designing interface electronics for high-precision microgyroscopes is to ensure that the circuit noise is not the limiting factor in system performance (i.e. ENEΩ < MNEΩ). Since a fixed DC potential 'V_P' has been maintained across the sense gap 'd_{s0}', Coriolis-induced displacement of the proof-mass in response to input rotation about the normal axis 'Ω_z' changes the sense rest capacitance 'C_{s0}', generating a motional current I_{SENSE}, expressed as [62]:

$$I_{SENSE} = \frac{2V_P C_{s0} Q_{EFF} q_{drive}}{d_{s0}} \Omega_z \qquad (5.1)$$

The ENEΩ of a capacitive-based vibratory gyroscope depends on the minimum detectable capacitance 'ΔC_{MIN}' of the sense channel interface electronics and the rate scale factor (SF) expressed in F/deg/hr.

$$ENE\Omega = \frac{\Delta C_{MIN}}{SF} \tag{5.2}$$

For a parallel plate detection scheme, ΔC_{MIN} is proportional to the input referred current noise of the interface electronics integrated over the bandwidth of interest as seen in Eq. 5.3 [62]:

$$\Delta C_{MIN} = \frac{I_{noise}\sqrt{BW}}{\omega_0 V_P} \tag{5.3}$$

The theoretical MNEΩ of the M^2-TFG prototypes approach 0.1deg/hr/√Hz. Hence the electronic front-end must be able to detect a proof-mass displacement as small as 0.1Å, which corresponds to a capacitance change of approximately 0.02aF/√Hz at the sensor operating frequency (10-15 kHz).
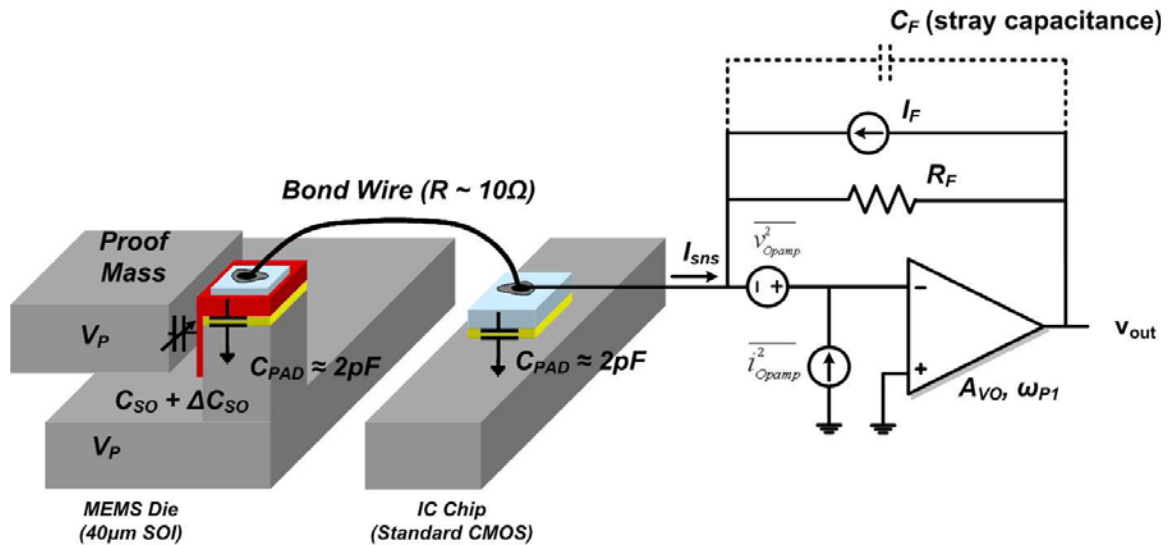
Figure 5.1: Schematic representation of the transimpedance amplifier (with noise sources) interfaced with the SOI M^2-TFG prototype [62].

M^2-TFG prototypes are fabricated using SOI bulk-micromachining technology, which facilitates large resonant mass and high-aspect ratio capacitive sensing gaps. The sensor is fabricated on a different substrate and is interfaced to front-end electronics via wire-bonds, as shown in Figure 5.1. A two-chip implementation allows for the decoupling of the MEMS design and fabrication from the design of the interface electronics. As a result the sensor performance can be improved considerably, unlike existing commercial MEMS gyroscope such as Analog Devices ADXRS150 [69], by leveraging the benefits of high aspect-ratio silicon processing (highlighted in Chapters VII). In [69], the microgyroscope is implemented using surface micromachining techniques, to ensure compatibility with the 3µm BiCMOS foundry used for the manufacture of the interface electronics. Figures 2.4-2.6 highlighted the impact of a large resonant mass on mechanical noise floor. In addition, standard CMOS processes can be used which significantly lowers cost and allows the electronics to be optimized for low power dissipation, speed, and reliability. However, the front-end interface must be strategically chosen to ensure that the sub-pA motional currents can be detected even in the presence of increased parasitics. This work has been presented in [21], but is included in this dissertation for completeness.

5.1.1 Transimpedance-Based Front-Ends

Figure 5.1 shows a schematic of a continuous-time transimpedance amplifier (CT-TIA) interfaced with a microgyroscope. R_F is the feed-back resistance, C_F is the associated stray capacitance, and C_{TOT} is the lumped parasitic capacitance at the inverting terminal of the op-amp. C_{TOT} is composed of the electrode-to-

substrate capacitance on the MEMS die ($C_{PAD-MEMS}$ = 1.5pF), the interface IC pad capacitance ($C_{PAD-ASIC}$ = 1.5pF), and the gate capacitance of the input differential pair transistors (C_{GS-IN} = 0.5pF) in the op-amp. The high open loop DC gain of the op-amp ensures a good virtual ground at the inverting terminal, while the shunt-shunt feedback presents low input impedance to the high-impedance sensor pick-off node. This makes the signal path relatively insensitive to the total parasitic capacitance (C_{TOT} = $C_{PAD-MEMS}$ + $C_{PAD-ASIC}$ + C_{GS-IN}), preventing significant signal loss. The low input impedance provided by the shunt-shunt feed-back helps reduce the loading that the sustaining electronics will have on the quality factor of the gyroscope drive-mode. When locked into electromechanical oscillations, the loaded drive mode quality factor (Q_L) is lower than its unloaded value (Q_{UL}) [62]:

$$Q_L = \frac{R_{Motional-Drive}}{R_{Motional-Drive} + R_{IN-AMP} + R_{OUT-AMP}} Q_{UL} \tag{5.4}$$

In Eq. 5.4, R_{IN-AMP} and $R_{OUT-AMP}$ are the input and output impedances seen by the sensor from the sustaining electronics. By applying the appropriate loading conditions at the input and the output for the TIA front-end, R_{IN-AMP} can be approximated as:

$$R_{IN-AMP} \approx \frac{R_F}{A_{V0}} \tag{5.5}$$

In Eq. 5.5, A_{V0} is the open-loop DC gain of the core op-amp. Typical values for R_F in the case of MEMS gyroscope interfaces are in the MΩ range, and the DC gain is typically between 80 - 100dB. Hence R_{IN-AMP} is as low as $10 - 100$. Since the TIA

front-end provides low R_{IN-AMP}, there is generally minimal Q-loading (which enhances the M^2-TFG device performance).

The TIA interface permits the proof-masses to be maintained at a constant DC potential unlike [70, 71]. By maintaining the proof-mass at a constant DC potential, any spurious signal coupling into the sensing electrodes is eliminated and the number of demodulation and filtering stages required are minimized. This plays a significant role in power reduction. In Figure 5.1, v^2_{op-amp} and i^2_{op-amp} are the input referred voltage and current noise of the op-amp respectively, and represent the main noise contributors in TIA front-end interface. The quantity $I_F = 4k_BT/R_F$ represents the thermal noise power of the feedback resistor (R_F). Since the sensor output is a current proportional to proof-mass displacement, it is the total input referred current noise of the TIA front-end that ultimately determines the minimum detectable capacitance (Eq. 5.3), and hence resolution of the M^2-TFG. In a bandwidth of 10Hz about the sensor operating frequency, the equivalent input noise spectrum is assumed white, and thermal noise of the feedback resistor forms the dominant noise contributor. The electronic noise floor (ENEΩ) for the M^2-TFG interfaced with a TIA is given by [62]:

$$ENE\Omega = \frac{d_{s0}}{2V_P C_{s0} Q_{EFF} q_{rive}} I_{N-Total} \sqrt{BW} \tag{5.6}$$

The advantage of using a TIA front-end becomes clear when the expression for signal to noise ratio (SNR) of the front-end interface is explored. A TIA with transimpedance gain R_F yields an output signal voltage of $I_{SENSE} \times R_F$ (for input motional current I_{SENSE}), and output noise voltage of $\sqrt{4k_BTR_F}$. The amount of displacement current $i_{Brownian}$ due to the random Brownian motion of the proof-

mass along the sense axis is derived by applying the equipartition theorem to the M^2-TFG at resonance and computing the noise displacement x_n [20].

$$\overline{x}_n^2 = \frac{4k_B T Q_{EFF}}{M\omega_0^3} \tag{5.7}$$

The sense resonant mode of the M^2-TFG can be modeled as a second-order system with an equivalent series RLC representation, similar to that presented for the drive mode in Chapter IV. The Brownian noise displacement is related to the mechanical motional resistance of the sense mode '$R_{Motional-Sense}$', and the equivalent Brownian noise current is derived:

$$\overline{i}_{BROWNIAN}^2 = \omega_0^2 V_P^2 \left(\frac{\delta C_{s0}}{\delta x}\right) \overline{x}_n^2 = \frac{4k_B T}{R_{Motional-Sense}} \tag{5.8}$$

By using $I_{SENSE} = i_{Brownian}$, the overall SNR is derived as:

$$SNR = \sqrt{\frac{R_F}{R_{MOTIONAL-SENSE}}} \tag{5.9}$$

Therefore, increasing R_F improves the total SNR of a M^2-TFG sensor interface. From Eq. 5.5-5.9, it is evident that a large R_F for capacitive detection is beneficial not only for obtaining increased transimpedance gain, but also a better SNR and lower input current noise. In [62], a continuous time, programmable T-network TIA that provides state-of-the-art capacitive resolution was designed and interfaced with an SOI M^2-TFG prototype.

4.2 Drive Loop Electronics

The drive loop uses an off-chip HC4046 digital PLL to lock to the drive resonant frequency, and supplies the actuation voltage to the drive comb electrodes

[72]. On start-up, the PLL locks on to the output of the front-end I-V converter, which is implemented using a discrete TIA front-end. The output of the PLL, after down-conversion, is a rail-to-rail digital signal at the drive-mode resonant frequency. This digital output signal is then attenuated to achieve the desired voltage amplitude and used to drive the proof-masses of the M^2-TFG. The discrete implementation of the drive-loop has been shown in Appendix B.
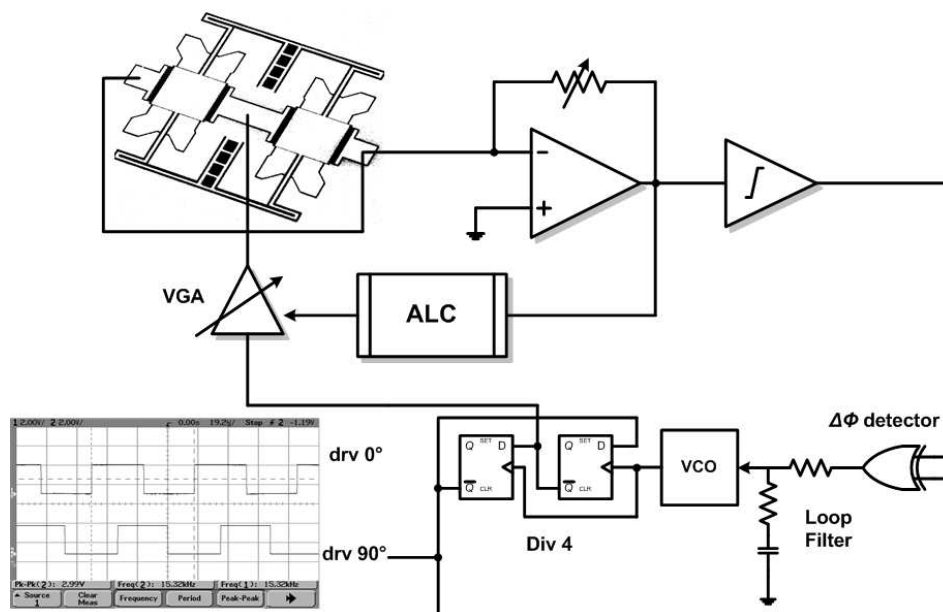
Figure 5.2: Schematic diagram of the PLL-based drive loop of the M^2-TFG.

The drive-electrode configuration ensures that the PLL does not lock into the pseudo-drive vibration mode of the M^2-TFG. Figure 5.2 shows the circuit schematic of the PLL-based drive oscillator loop and the oscilloscope waveforms of the 90° phase shifted signals (implemented using two D flip-flops).

5.2.1 Drive Amplitude Measurement

The drive-mode displacement amplitude of the proof-masses x_{Drive} is a key parameter that determines the sensor Brownian noise floor and Coriolis sensitivity.

Hence it is important to verify the amplitude of the drive-mode displacement as well characterize its linearity. As discussed in Chapter IV, the displacement amplitude of an electrostatic comb-drive actuation mechanism is limited by the lateral snap-down, and is proportional to the square of the gap between adjacent combs (g). The expression for the output motional current at drive-mode resonance is expressed as [73]:

$$i_{OUT}(RMS) = \frac{\delta C}{\delta x} V_P \frac{dx}{dt} = \frac{\varepsilon_0 N h V_P}{g} \frac{dx}{dt}$$

(5.10)

In Eq. 5.10, 'dx/dt' represents the velocity of the proof-mass displacement along the x-axis, 'N' is the number of combs, 'h' is the structural height, and 'V_P' is the DC polarization voltage. From the measured motional current at resonance, the value of '$x_{DRIVE}(MAX)$' can therefore be expressed as:

$$x_{DRIVE}(MAX) = \frac{i_{OUT} g}{2 \varepsilon_0 N h V_P \omega_0}$$

(5.11)

In Eq. 5.11, 'i_{out}' is the measured peak-to-peak value of the motional current. The sensor is driven to oscillate using the PLL-based drive oscillator, and the variation of the drive amplitude with input excitation voltage is measured. The drive amplitude was computed from the measured output voltage waveform by compensating the effects of the 2pF parasitic capacitance (present at the interface between the MEMS and the electronic front-end). Figure 5.3 shows the drive amplitude as a function of input peak-to-peak drive voltage and the least-squares curve fit demonstrates the linearly.
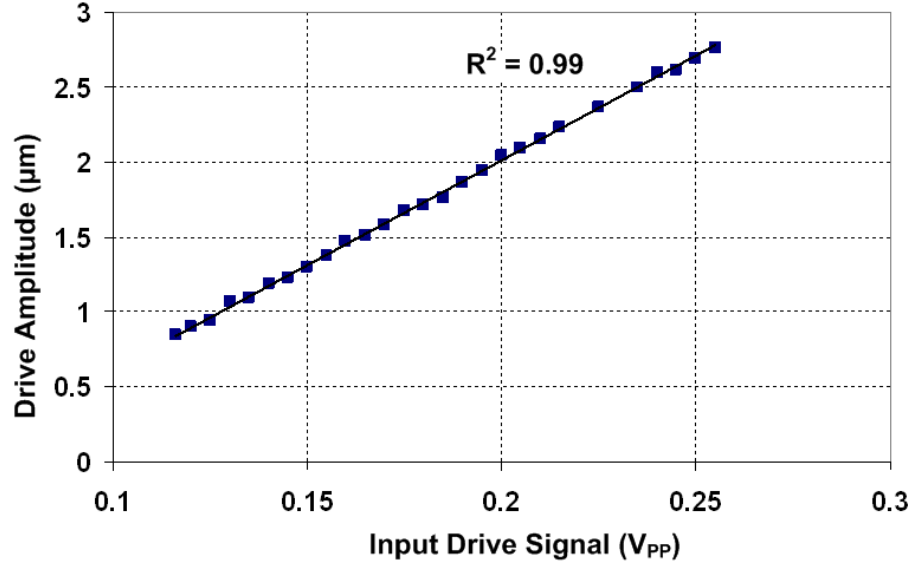
Figure 5.3: Measured variation of drive amplitude as a function of the input drive signal.

It must be mentioned that commercial microgyroscope systems use drive voltages approaching $12V_{P-P}$ to achieve displacements in the range of 5-10µm [69]. In the M^2-TFG owing to high-Q resonant operation, it utilizes only $0.25V_{P-P}$ to achieve displacement amplitudes approaching 3µm.

5.3 Sense Channel Electronics

The front-end of the M^2-TFG sense-channel is comprised of two discrete transimpedance amplifier chains that process signal from a pair of differential sense electrodes as shown in Figure 5.4. Any offset that manifests itself on each signal chain is cancelled before being fed into the instrumentation amplifier. The sense channel further consists of a synchronous demodulator to extract the rate signal from the sensor output. The drive-loop PLL generates the 90° phase-shifted signals that are proportional to the drive velocity and drive displacement. This square wave is used in a synchronous demodulator to chop the incoming signal

from the sense-channel and subsequently low-pass filtered to obtain the rate signal. Proof-mass displacements, due to both Coriolis acceleration and quadrature error take place at the sense-mode resonant frequency.
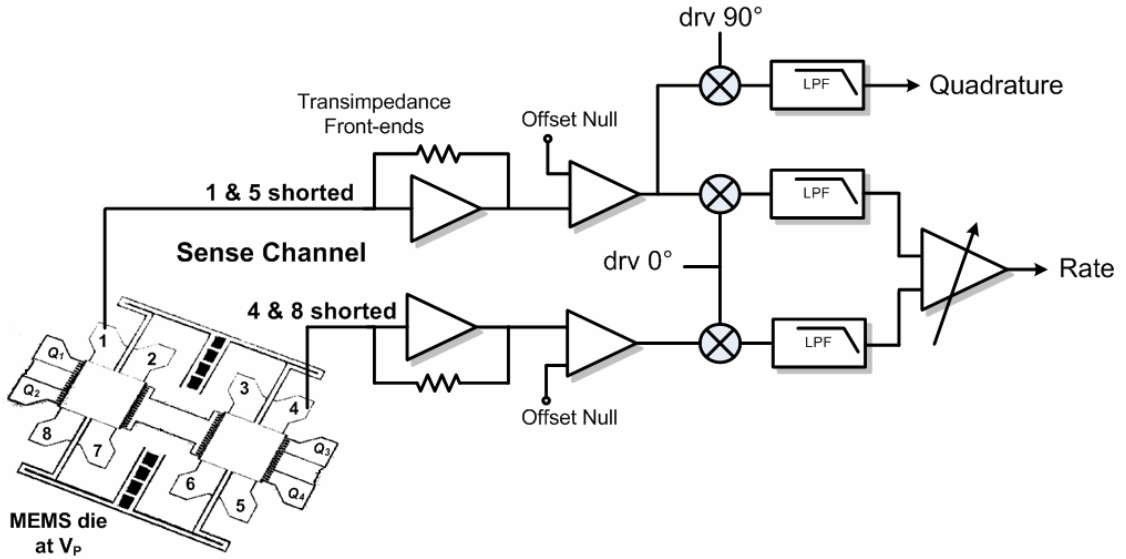
Figure 5.4: Schematic diagram of the TIA-based sense channel interface of the M^2-TFG.

A synchronous demodulator maintains inherent phase information while demodulating the AM signal. This phase relationship is used to distinguish between the rotation rate and quadrature signal (and will be explained further in the following section). Therefore, the sense channel uses a phase sensitive synchronous I-Q demodulation scheme to extract the rotation rate, rather than a simple envelope detection scheme. Finally, the M^2-TFG electrode configuration illustrated in Figure 5.4 allows for a fully differential sensing topology, which automatically rejects linear acceleration as common-mode. An overview of the discrete implementation of the sense-channel is given in Appendix B.

5.4 Mode-Matching Scheme

The primary motivation for mode-matching is to leverage the mechanical signal amplification provided by the effective quality factor (Q_{EFF}) of the vibratory gyroscope at mode-matched operation. Typical mechanical quality factors are in the range of 10,000 - 50,000 [27]. Q_{EFF} depends on the inherent mechanical quality factors of the structure, as well as on the frequency split between the drive and sense resonant modes. For a given mechanical structure, Q_{EFF} is maximum when the drive and sense resonant mode frequencies are equal. A higher Q_{EFF} lowers both the Brownian noise floor as well as the electronic noise floor (via improved capacitive sensitivity), as expressed in Chapter II. Finally, empirical studies (and observations recorded in Chapter VI) have shown that a high Q_{EFF} contributes directly to a low bias drift. Therefore, for a given form-factor, a microgyroscope performance can be enhanced by orders of magnitude through mode-matching. A high Q_{EFF} also alleviates the constraints on the interface circuit design in terms of operating frequency, gain, and power.

5.4.1 Concept of Quadrature Error in M²-TFG

Quadrature error is common in all micromachined vibratory gyroscopes [23, 74] and manifests itself as imbalances in the mechanical elements due to fabrication imperfections. For the purposes of this dissertation, the quadrature error in an M2-TFG structure is modeled in a simplified single proof-mass example illustrated in Figure 5.5. Flexural springs permit the proof-mass to move along both the drive and sense axes (x-axis and y-axis respectively). Ideally, the motion of the proof-mass during drive-mode resonance is restricted exclusively along the x-

axis. Motion along the sense-axis (y-axis) only occurs when the proof-mass undergoes rotation-induced Coriolis acceleration (Eq. 2.10-2.11).
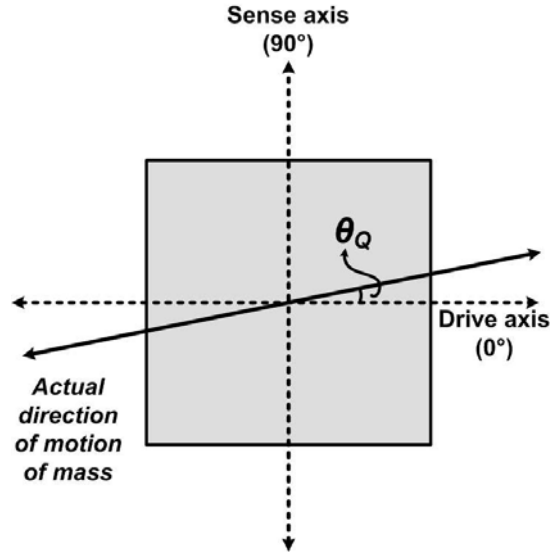
Figure 5.5: Demonstration of quadrature error in the M²-TFG proof-mass.

However, imbalances present in the mechanical structure cause the proof-mass to oscillate at an angle 'θ_Q' from the actual drive-axis (as shown in Figure 5.5). This off-axis proof-mass displacement results in mechanical coupling of the drive motion along the sensitive y-axis, and an oscillatory deflection that will be measured along the sense axis with the Coriolis induced deflections. This spurious mechanical coupling is quadrature error. The mechanical coupling results in an output signal in the absence of any input rotation. The proof-mass is driven into resonant sinusoidal motion along the drive axis with a maximum drive displacement 'x_{drive}'.

$$x(t) = x_{drive} \sin(\omega_{drive} t) \tag{5.12}$$

The misalignment of the proof-mass by angle 'θ_Q' results in a displacement component along the sense axis '$y_{QUADRATURE}$' expressed as:

$$y_{QUADRATURE}(t) = \sin(\theta_Q) x_{drive} \sin(\omega_{drive} t) \cong \theta_Q x_{drive} \sin(\omega_{drive} t) \tag{5.13}$$

In Eq. 5.13, the small angle approximation allows $\sin(\theta_Q) \approx \theta_Q$. The Coriolis induced acceleration is expressed as Eq. 5.14, and the proof-mass velocity along the drive-axis is represented in Eq. 5.15.

$$a_{CORIOLIS} = 2v_{drive} \times \Omega_Z \tag{5.14}$$

$$v_{drive}(t) = x_{drive} \omega_{drive} \cos(\omega_{drive} t) \tag{5.15}$$

Hence, Coriolis induced proof-mass displacement along the sense axis (y-axis) is expressed as:

$$y_{CORIOLIS}(t) = \frac{2\Omega_z(t) x_{drive} \omega_{drive} \cos(\omega_{drive} t)}{\omega_{sense}^2} \tag{5.16}$$

When the device is operated at mode-matched condition (i.e. $\omega_{drive} = \omega_{sense}$), the Coriolis expression reduces to as follows:

$$y_{CORIOLIS}(t) = \frac{2\Omega_z(t) x_{drive} Q_{EFF} \cos(\omega_{drive} t)}{\omega_{drive}} \tag{5.17}$$

A comparison of Eq. 5.13 and 5.17, demonstrates that while both the quadrature error and Coriolis deflection are amplitude modulated signals centered at the drive-mode resonant frequency they have an inherent relative phase of 90° (hence the term quadrature error). This phase difference originates from the fact that the Coriolis acceleration is sensitive to proof-mass velocity (Eq. 5.14), while the quadrature error is proportional to the proof-mass position (Eq. 5.13).

Additionally, the level of the quadrature displacement may be of significant concern (as observed in Eq. 5.18).

$$\frac{y_{QUADRATURE}}{y_{CORIOLIS}} \cong \frac{\omega_{drive}\theta_Q}{2Q_{EFF}\Omega_z} \qquad (5.18)$$

A small misalignment angle θ_Q may cause significant overwhelming of the Coriolis-induced displacement with the quadrature error (under low-Q_{EFF} operation). While the quadrature component of the sense-signal may be identified using the phase-sensitive I-Q demodulation scheme highlighted earlier, its role in preventing perfect mode-matching (i.e. zero Hz frequency split between operating modes) must be addressed. The impact of quadrature error on the microgyroscope system dynamics can be modeled effectively by adding cross-coupling coefficients in the 2-DOF spring stiffness matrix K [74].

$$K = \begin{pmatrix} k_{xx} & k_{xy} \\ k_{yx} & k_{yy} \end{pmatrix} \qquad (5.19)$$

In Eq. 5.19, 'k_{xx}' and 'k_{yy}' represent the mechanical spring stiffness along the drive (x) and sense(y) axes respectively. 'k_{xy}' and 'k_{yx}' represent the cross-diagonal spring stiffness terms that model the quadrature induced mechanical coupling. Reducing the quadrature error is best achieved by ensuring that the spring matrix is diagonalized by the application of specific quadrature nulling techniques. Further, these cross-diagonal terms cause the non-degeneracy of the 2-DOF system which represents the greatest obstacle for mode-matching.

5.4.2 Quadrature-Minimization Mechanism in M²-TFG

Quadrature error remains a significant issue, despite the best efforts in robust mechanical design and fabrication optimization of gyroscope structures. All vibratory microgyroscopes reported in literature use some form of quadrature compensation that involves electronic or mechanical compensation of the quadrature signal. For a robust design, the quadrature minimization scheme must be repeatable and be able to provide the required spatial re-orientation of the mechanical structure over several batches of devices. The M²-TFG uses a custom electrode configuration that is employed to efficiently reduce the quadrature error. Dedicated quadrature minimization electrodes were added at the corners, two for each proof-mass, as shown in Figure 5.6. Each electrode contains a set of parallel-plate fingers to apply an electrostatic force at the corner of the proof-mass. The technique implemented uses an effective-torque to rotate the proof-masses and thereby correct for any spatial misalignment.
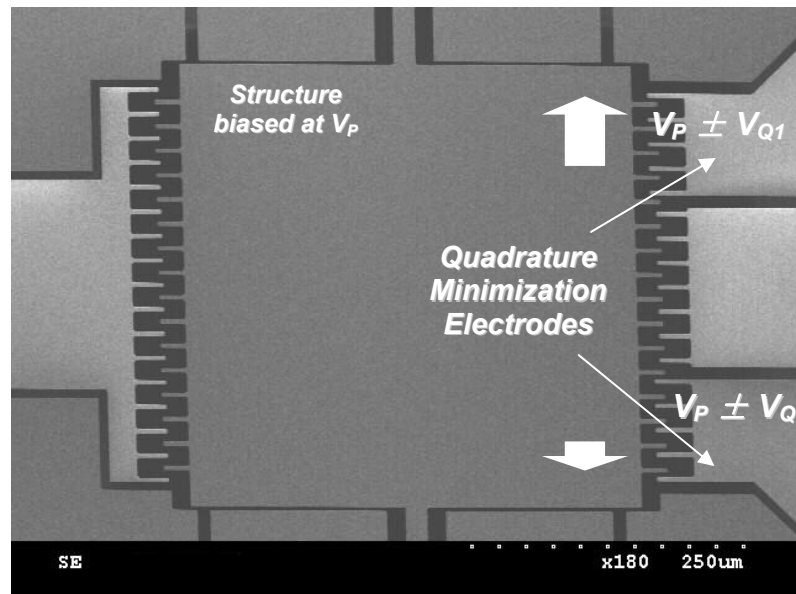
Figure 5.6: Dedicated quadrature minimization electrodes in M²-TFG.

An illustration of the technique is shown in Figure 5.7. Application of appropriate torques on each proof-mass enables clockwise or counter-clockwise rotation, correcting misalignment of the drive axis and thereby suppressing the quadrature signal.
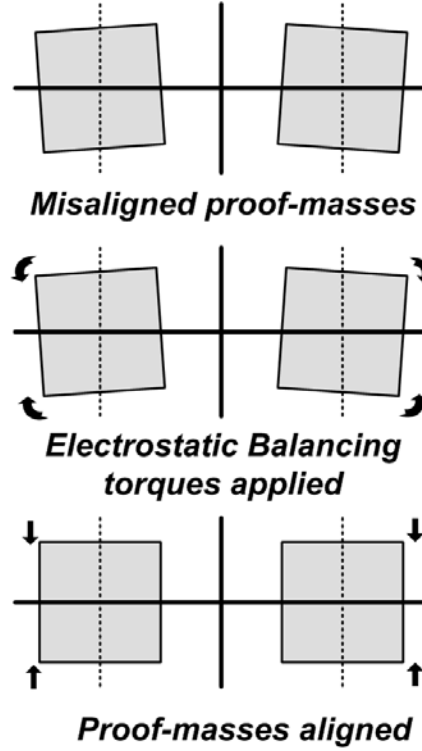
Figure 5.7: Illustration of quadrature minimization in M²-TFG using effective torque.

Mathematically, quadrature nulling can be represented as applying appropriate voltages to eliminate the cross-diagonal terms in the spring stiffness matrix:

$$K(QM) = \begin{pmatrix} k_{xx} & k_{xy} \\ k_{yx} & k_{yy} \end{pmatrix} + \begin{pmatrix} 0 & -k_{xy-Electrostatic} \\ -k_{yx-Electrostatic} & 0 \end{pmatrix} = \lim_{\Delta \to 0} \begin{pmatrix} k_{xx} & \Delta k_{xy} \\ \Delta k_{yx} & k_{yy} \end{pmatrix} \quad (5.20)$$

In Eq. 5.20, '$k_{xy-Electrostatic}$' and '$k_{yx-Electrostatic}$' are stiffness coefficients that result from the electrostatic torques applied to the dedicated quadrature minimization electrodes, resulting in the electromechanical matrix K(QM). A mode-matched

gyroscope is one in which the drive and sense modes are Eigen-modes, i.e., they are degenerate. A 2-DOF microgyroscope system (such as the M^2-TFG) can be considered degenerate only when its mass and spring stiffness matrices are diagonal [23, 74]. The quadrature induced off-diagonal terms in the spring-stiffness matrices prevents degeneracy of the Eigen-modes consequently leading to a mismatch in the resonant frequencies. In order to achieve mode degeneracy, it is necessary that these terms are electronically eliminated, and the spring-stiffness matrix be diagonalized. Hence quadrature minimization becomes the first step to achieve perfect mode-matching. Once the quadrature error has been sufficiently reduced, the drive and sense stiffness coefficients can be equalized to ensure that the drive and sense frequencies are made equal. This is achieved though electrostatic spring softening and will be addressed in the following section.

5.4.3 Electrostatic Frequency Tuning in M^2-TFG

In the M^2-TFG design, the flexural sense-mode resonant frequency is designed to occur at a higher frequency in comparison to the flexural drive-mode resonant frequency. Upon quadrature minimization, electrostatic spring softening is used to compensate this frequency variation. Selective electrostatic tuning of the sense mode resonant frequency is an attractive feature of the M^2-TFG. Due to the parallel plate electrodes along the sense direction, an increase of the DC polarization voltage 'V_P' causes a lowering of the sense resonant frequency. The drive oscillations however are excited using comb-drive electrodes, making the

drive frequency relatively immune to the changes in polarization voltage [75]. The sense mode resonant frequency is expressed as:

$$\omega_{sense} = \sqrt{\frac{k_{sense-mechanical} - \sum_{i=1}^{N}\left(\frac{\varepsilon_0 A_i}{d_{s0}} V_P^2\right)}{M_{EFF}}} \quad (5.21)$$

In Eq. 5.21, 'N' is the number of parallel plate electrodes with a DC voltage difference of V_P across them, 'A' and 'd_{s0}' are the area and capacitive gap of the sensing electrode respectively, and 'M_{EFF}' is the effective mass of the structure. The variation of the sense mode frequency as a function of V_P is predicted to be parabolic according to Eq. 5.21. This has been experimentally verified in Chapter VI, where a 150Hz frequency split between the drive and sense resonant modes of a 40µm-thick SOI prototype are compensated. This selective electrostatic tuning of the sense mode resonant frequency is key to mode-matching. Minimizing the quadrature induced cross-coupling terms in the matrix 'K' alone is not sufficient to make the system degenerate. Electrostatic tuning complements quadrature nulling by ensuring the remaining diagonal elements are equalized electronically, thereby resulting in a diagonal matrix. This is represented mathematically as:

$$K(V_P) = \begin{pmatrix} k_{xx} & \Delta k_{xy} \\ \Delta k_{yx} & k_{yy} \end{pmatrix} + \begin{pmatrix} 0 & 0 \\ 0 & -\sum_{i=1}^{N}\left(\frac{\varepsilon_0 A_i}{d_{so}} V_P^2\right) \end{pmatrix} = \lim_{\Delta \to 0} \begin{pmatrix} k_{xx} & \Delta k_{xy} \\ \Delta k_{yx} & k_{xx} \end{pmatrix} \quad (5.22)$$

Electrostatic spring softening can only be used to lower the mechanical resonant frequency due to the negative nature of the electrostatic spring softening.

Mode-matching is achieved by increasing V_P until the sense mode frequency decreases, and becomes equal to that of the drive mode.

Quadrature error in earlier prototypes of the M^2-TFG could not effectively minimized due to the lack of dedicated quadrature electrodes. Hence, the minimum frequency separation that could be achieved was 12Hz [76]. The combination of electronic quadrature nulling and electrostatic tuning results in the previously non-degenerate modes of the M^2-TFG to become Eigen-modes and thereby permit perfect mode-matched operation.

5.4.4 Automatic Mode-Matching Scheme in M^2-TFG

An automatic mode-matching scheme was developed in [63] for the M^2-TFG structure and has been discussed in depth in [21]. The concept of the automatic mode-matching scheme in M^2-TFG is based upon the residual quadrature error. When the operating modes are matched, the M^2-TFG is sensitive to any displacement along the y-axis, whether quadrature-induced or Coriolis-induced. Hence, the amplitude of the residual ZRO serves as an accurate indicator of mode-matching. Once matched, synchronous I-Q demodulation is used to distinguish between the quadrature error and the Coriolis signal. Figure 5.8 shows the block-diagram of the automatic mode-matching system implemented in [21]. The scheme exploits the unique characteristics of the sensor in the time domain, to achieve and maintain zero or finite frequency split between the two modes in a fraction of the time and hardware as compared to [77].
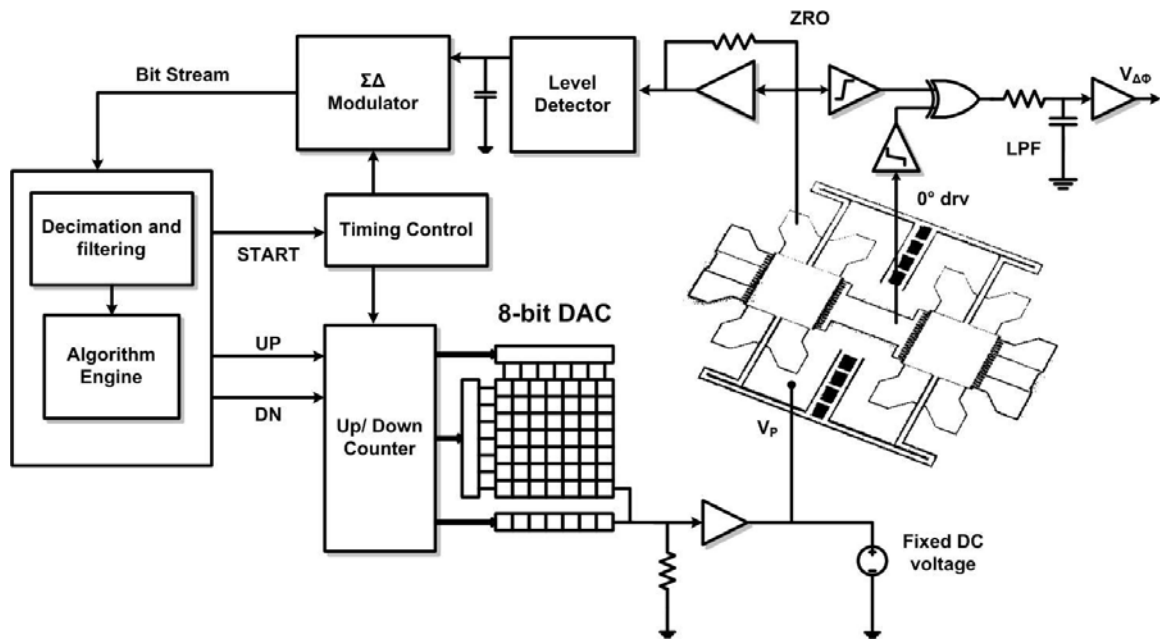
Figure 5.8: Schematic of the automatic mode-matching system implemented in [21].

The ZRO level is extracted at the sense electrodes with a level detector and converted into a bit stream for processing in an external software (in this case MATLAB). The control algorithm compares the ZRO value with the initial value and increases the polarization voltage supplied to the structure at quantized DC values. Once the maximum ZRO is detected the polarization voltage is set fixed at the particular constant value (which ensures perfect mode-matching).

CHAPTER VI

PERFORMANCE CHARACTERIZATION OF THE M²-TFG

This chapter examines the performance parameters of prototype SOI M²-TFGs. The M²-TFG represents the first Class-I vibratory microgyroscope, reported in literature, to demonstrate perfect mode-matching (i.e. 0Hz frequency split between high-Q operating resonant modes). This allows for unprecedented improvements in device sensitivity, resolution and overall bias stability of the system. This chapter highlights results from various characterization experiments of the M²-TFG system.

6.1 Quality Factor Characterization

Preliminary open-loop characterization of the M²-TFG is performed using dedicated analog front-end electronics (AFE) implemented by means of discrete amplifiers. The M²-TFG die is mounted on the AFE board and wire-bonded to pads that interface them to transimpedance amplifiers. This AFE board is then placed in the vacuum chamber and the device characterization is performed. The devices were characterized in 1mTorr vacuum and an Agilent 4395A network analyzer was used to measure the frequency response. The measured drive and sense resonant modes for a prototype 40μm thick M²-TFG are shown in Figures 6.1 respectively. In this particular device the drive and sense-mode Qs were measured to be 78,000 and 45,000 respectively.
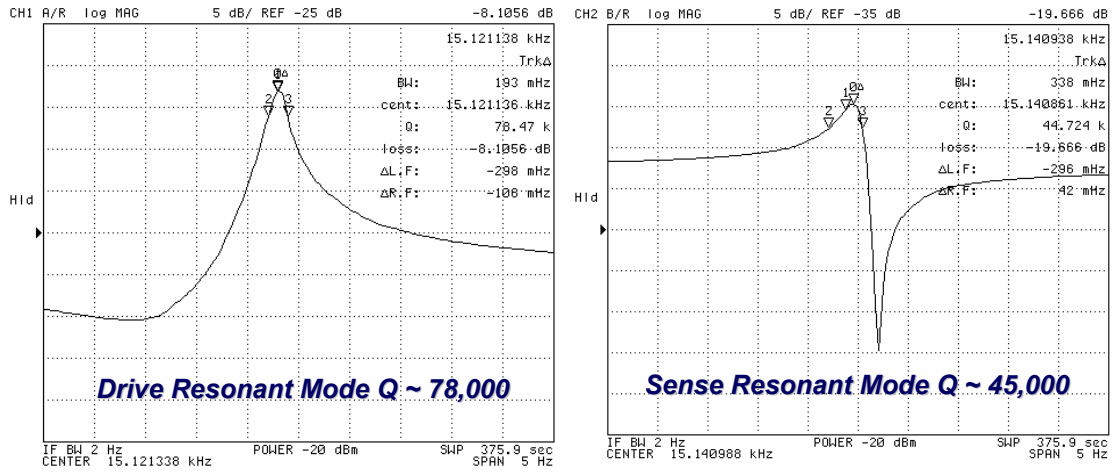
Figure 6.1: (Left) Measured drive resonant mode Q of 78,000. (Right) Measured sense resonant mode Q of 45,000.

As observed in Figure 6.2, the vibrations in the drive resonant mode effectively ensure force cancellation at the anchor. However, the vibrations in the sense resonant mode (as seen in Figure 6.3) introduce forces to the anchor regions. These forces are off-center and lead to a net torque along the support structure.
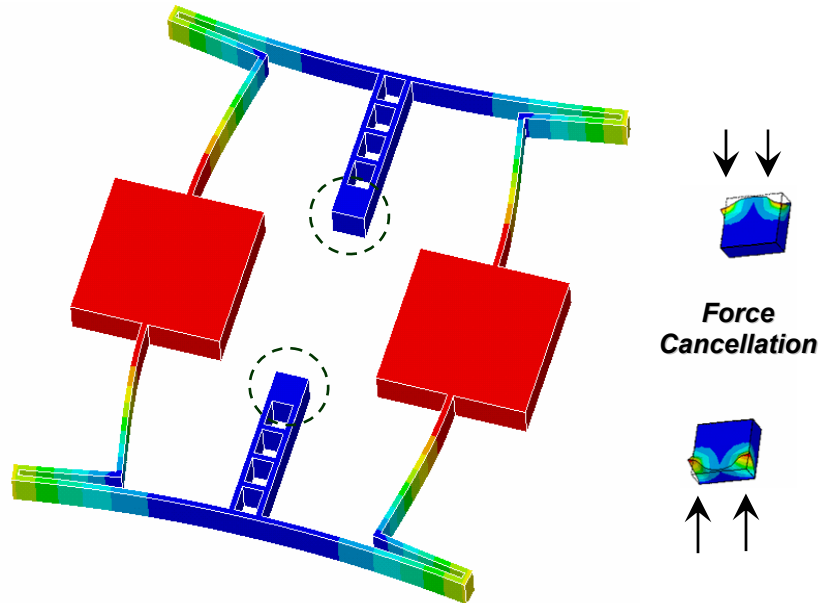
Figure 6.2: Resonant drive flexural mode and forces at the support anchor.
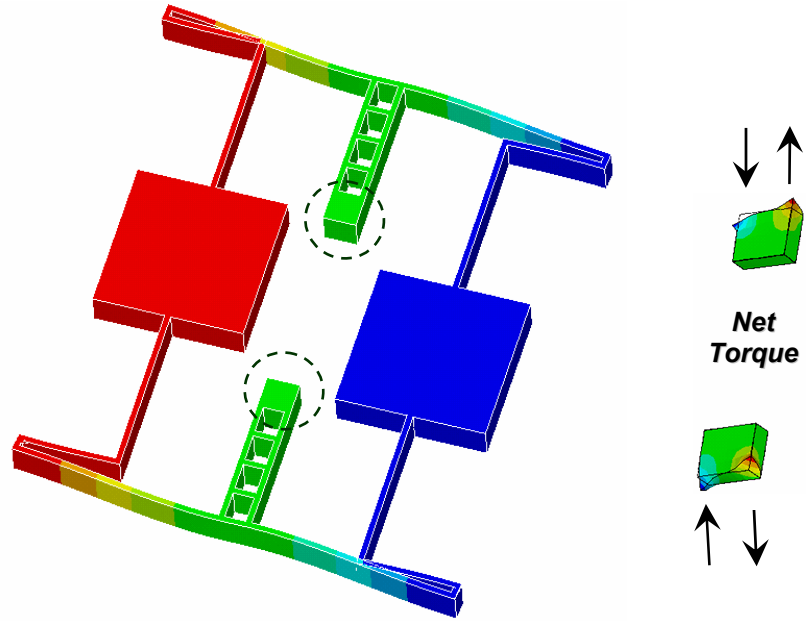
Figure 6.3: Resonant sense flexural mode and forces at the support anchor.

As a result, the drive-mode Q is expected to be higher than the sense-mode Q due to effective torque cancellation. This fact has been verified in Table 6.1 which tabulates the average Q values recorded over five samples in two batches of 40μm-thick M^2-TFGs. Also as predicted from Eq. 4.8, a device with larger beam width displays lower Q-factor operating modes.

Table 6.1: Measured frequencies and Q-factors of two batches of M^2-TFG

	Drive		Sense	
	Frequency (Hz)	**Q**	**Frequency (Hz)**	**Q**
Batch # 1 (Beam Width ~ 20μm)				
Mean (5)	17040	68183	17210	49160
ANSYS	17413		17458	
Batch # 2 (Beam Width ~ 18μm)				
Mean (5)	14950	84098	15076	58331
ANSYS	14833		14955	

6.2 Mode-Matching Demonstration in M²-TFG

The preceding chapters of this dissertation have discussed the motivation and methodology of mode-matching as means of improving the drift, resolution, and noise floor of the M²-TFG system. Mode-matching is performed by increasing the DC polarization voltage (V_P) on the MEMS structure until electrostatic spring softening decreases the sense-mode frequency to become equal to the drive-mode frequency. The capacitive clearance between the drive-mode flexures and the sense electrodes (see Figure 5.6) are large enough to ensure that drive-mode remains relatively constant as illustrated by the collection of frequency response plots displayed in Figure 6.4. The M²-TFG was the first reported high-Q perfectly matched implementation (i.e. zero-Hz frequency split) of a class-I vibratory microgyroscope [27]. A sample tuning curve of a prototype 40μm thick SOI M²-TFG is displayed in Figure 6.5 (utilizing four-sense electrodes).
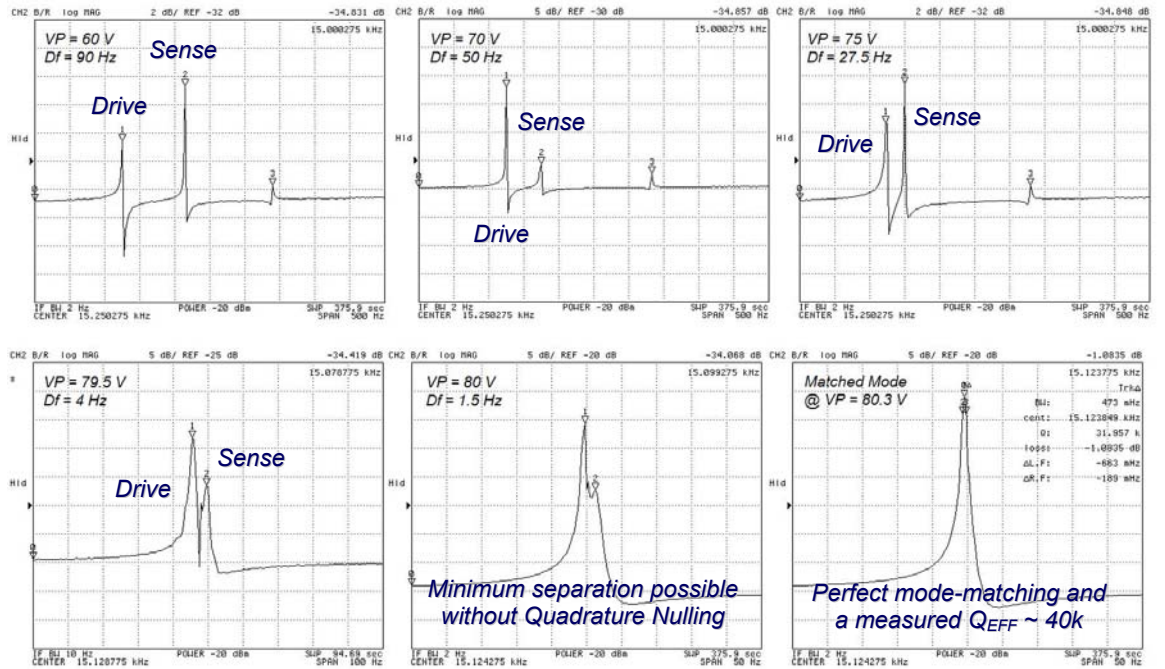
Figure 6.4: Illustration of mode-matching of M²-TFG.
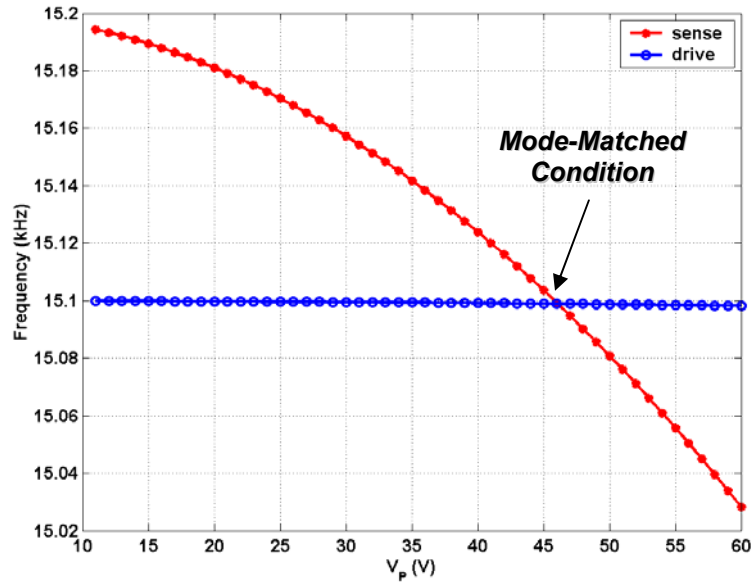
Figure 6.5: Tuning characteristics of the sense and drive modes of the M²-TFG. Note that frequency split of 100Hz is compensated with a V_P of approximately 46V.

Despite an optimized flexural design, in practice, fabrication imperfections lead to quadrature error – an introduction of non-zero off-diagonal elements in the spring stiffness and damping coefficient matrices as expressed in Eq. 5.19. Only through the minimization of this quadrature error is the perfect matching of the drive and sense resonant modes possible. Unlike Coriolis acceleration, which is proportional to the proof-mass velocity, quadrature errors are accelerations attributed to the proof-mass position. Quadrature minimization electrodes are situated at the corners of each proof-mass (as described in Chapter V). Nullifying quadrature error requires electrostatic forces which are in phase with the motion of the proof-mass while in drive-mode resonance. The forcing function can be accomplished by slightly unbalancing the bias voltages applied to the structure for mode-matching (as seen in Figure 5.6). This force is directly proportional to the proof-mass displacement (i.e. a time varying force). By adjusting V_Q it is possible

to align the proof-masses by eliminating the off-diagonal components of the stiffness matrix of the system (refer to Eq. 5.20).

6.2.1 Automatic Mode-Matching in M²-TFG

As discussed in Chapter V, the automatic mode-matching scheme developed for the M²-TFG utilizes the residual quadrature signal is to determine the mode separation. When the modes are matched, the M²-TFG is sensitive to any displacement along the y-axis, whether is be quadrature-induced or Coriolis-induced. Hence the amplitude of the residual ZRO serves as an accurate indicator of sensor sensitivity.
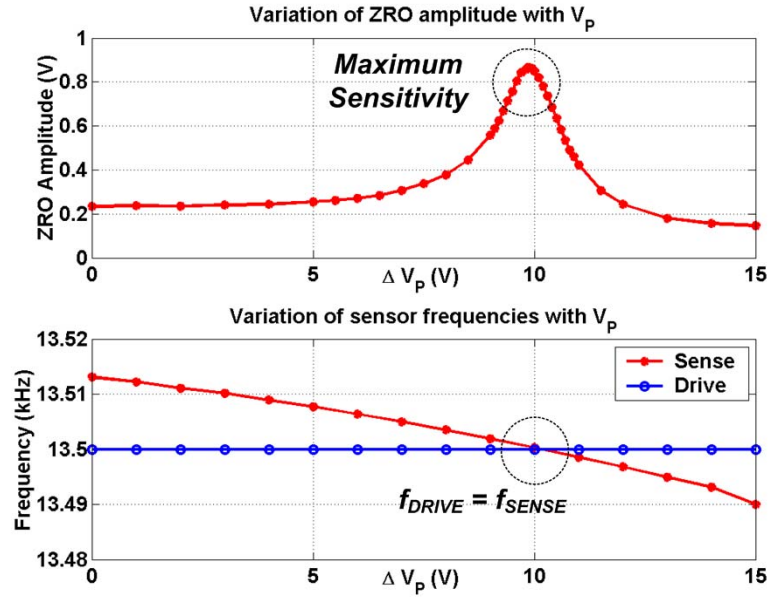
Figure 6.6: Measured ZRO as a function of frequency separation for a prototype M²-TFG.

Figure 6.6 shows the measured amplitude of the ZRO as a function of applied polarization voltage. It is evident that the maximum ZRO amplitude occurs when frequency separation between the drive and sense resonant modes is nullified.

Figure 6.7 illustrates the time-domain results of interfacing the M²-TFG with the mode-matching ASIC and control algorithm [63].
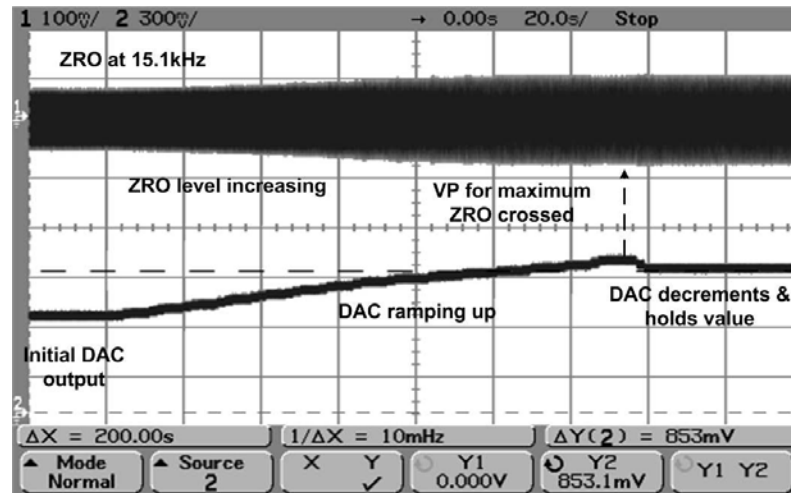
Figure 6.7: Time domain plot of M²-TFG ZRO with increasing V$_P$ [63].

The unique 90° phase difference that exists between the drive output and the ZRO at mode-matched condition (Figure 6.8) is monitored for mode-matching stability. Once matched, synchronous I-Q demodulation is used to distinguish between the quadrature error and the Coriolis signal.
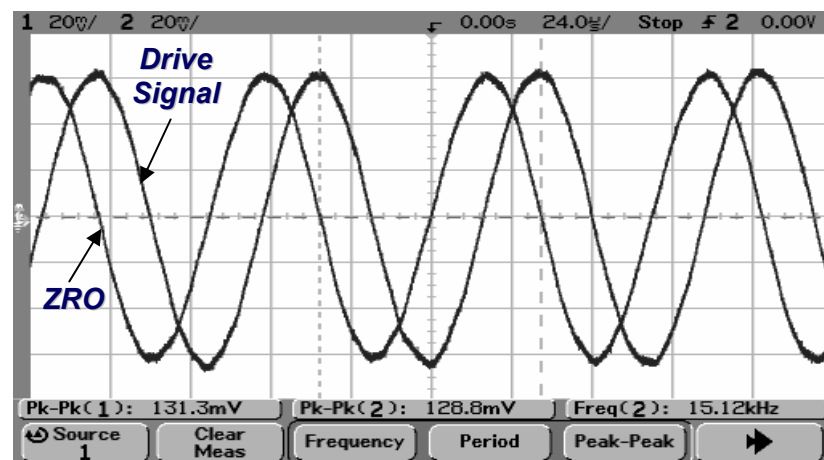
Figure 6.8: Unique 90° phase shift between the drive-signal and ZRO of the M²-TFG (at matched-mode condition).

6.2.2 Long-Term Mode-Matching Stability

Long-term M^2-TFG performance was characterized to analyze the stability of mode-matching over time. Any mismatch of the operating modes over time translates to a reduction in the Q_{EFF} from the mode-matched value, consequently affecting the M^2-TFG performance. While environmental effects like temperature fluctuations can be compensated for, random mismatch of the modes can only be corrected by performing periodic checks (and re-calibration as required). To test for any random mismatch of the operating-modes after mode-matching, the M^2-TFG was operated at rest (locked into drive resonance) continuously for a period of 30 hours at a constant 25°C. The drive oscillator signals and ZRO were recorded at 10s intervals during the specified time-span. The analysis of the data collected determines whether periodic calibration of the M^2-TFG is necessary, and if so, how often it must be performed.
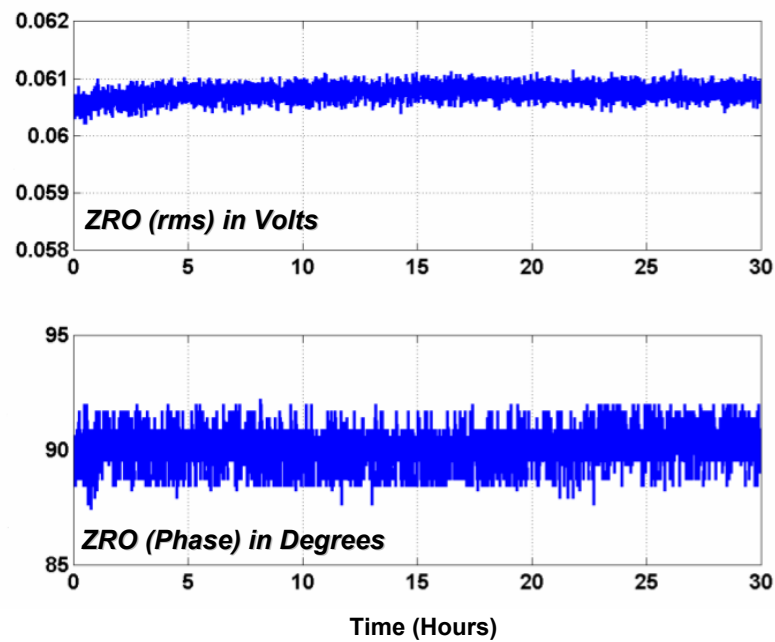
Figure 6.9: Long-term ZRO of the M^2-TFG (under mode-matched condition).

125

Figure 6.9 shows the recorded ZRO rms value and phase difference. It shows that once the operating modes are perfectly matched, they remain mode-matched (under constant temperature and pressure condition). Any mode separation due to fluctuations in interface circuit parameters or M^2-TFG structural instability would manifest itself as a change in either the phase or amplitude of the ZRO. This validates that the mode-matching of the M^2-TFG modes is extremely stable over time. Hence, no continuous-time monitoring or periodic calibration of the modes is essential to maintain the M^2-TFG performance.

6.3 Temperature Characterization

In order to ensure high-performance, it is essential that mode-matching is maintained over temperature. The M^2-TFG was tested under both matched and split-mode conditions to accurately determine the effects of temperature on the individual operating modes. Figure 6.10 shows the measured frequency variation of the individual unmatched resonant modes of a prototype 40µm-thick SOI M^2-TFG (with operating modes of 18.4 kHz) as a function of temperature.
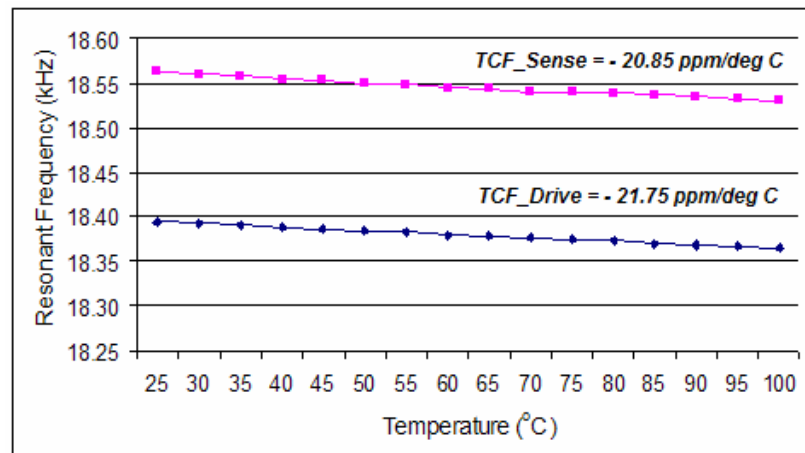
Figure 6.10: Temperature variation of operating resonant mode frequencies.

Such frequency variation is attributed to the temperature dependency of Young's modulus, thermal expansion, and thermally induced stresses in the single crystalline silicon substrate [78]. The drive mode temperature coefficient of frequency (TC_f) is measured to be – 21.75 ppm/°C. The TC_f of the drive and sense resonant modes vary by less than 1ppm/°C. Table 6.2 highlights Q-factor degradation in individual operating resonant modes at increased temperatures for a second prototype 40µm thick SOI M^2-TFG device. This observation is attributed to increased TED losses at elevated temperatures [79].

Table 6.2: Measured operating mode Q-factors with temperature.

Temperature (˚C)	Drive Mode		Sense Mode	
	Frequency (Hz)	Measured Q	Frequency(Hz)	Measured Q
-20	17469	88884	17567	72705
5	17458	72502	17555	51729
25	17449	64794	17547	45182
50	17435	54457	17533	33881
75	17422	45906	17519	32512

A separate M^2-TFG device under mode-matched condition was also subjected to the TC_f measurement test (Figure 6.11). Perfect mode-matching is maintained over the temperature range of 25 – 100 ˚C (without requiring any external quadrature compensation and frequency tuning). Hence a single temperature compensation circuit will suffice to maintain mode-matching over temperature. A mode-matched Q-factor degradation was observed at elevated temperature similar to the split-mode characterization (seen in Figure 6.12).
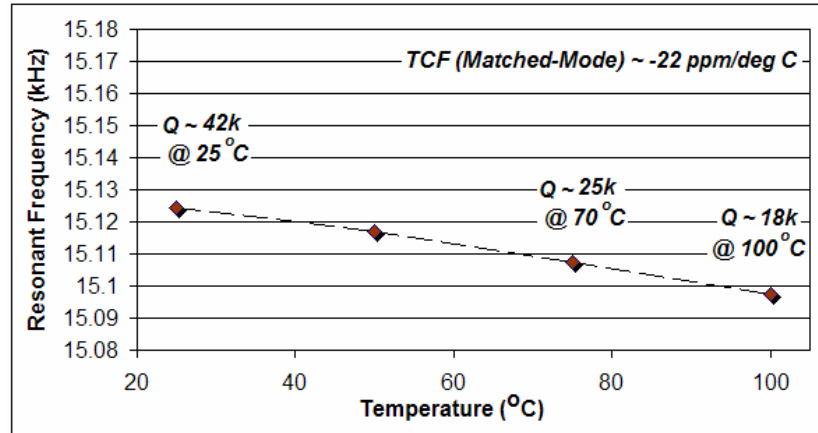
Figure 6.11: Temperature variation of mode-matched frequency and Q-Factor.

Table 6.3: Measured mode-matched Q-factor with temperature.

Temperature (˚C)	Mode-Matched Peak	
	Frequency (Hz)	Measured Q
25	15124	42547
70	15107	25240
100	15097	18301
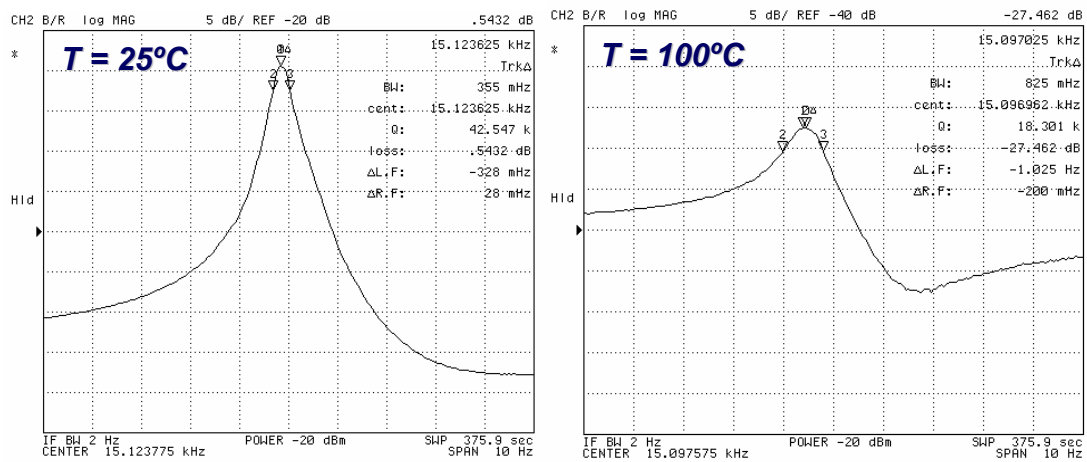
Figure 6.12: (Left) Measured mode-matched Q-factor of 42,000 at 25ºC. (Right) Measured mode-matched Q of 18,000 at 100ºC.

6.4 Scale-Factor Measurements

The set-up used to measure the rotation rate sensitivity of the prototype M^2-TFG devices is shown in Figure 5.13. An Ideal Aerosmith single-axis rate table (Model 1291 BR) was used to generate rotation signals at various rates [80].
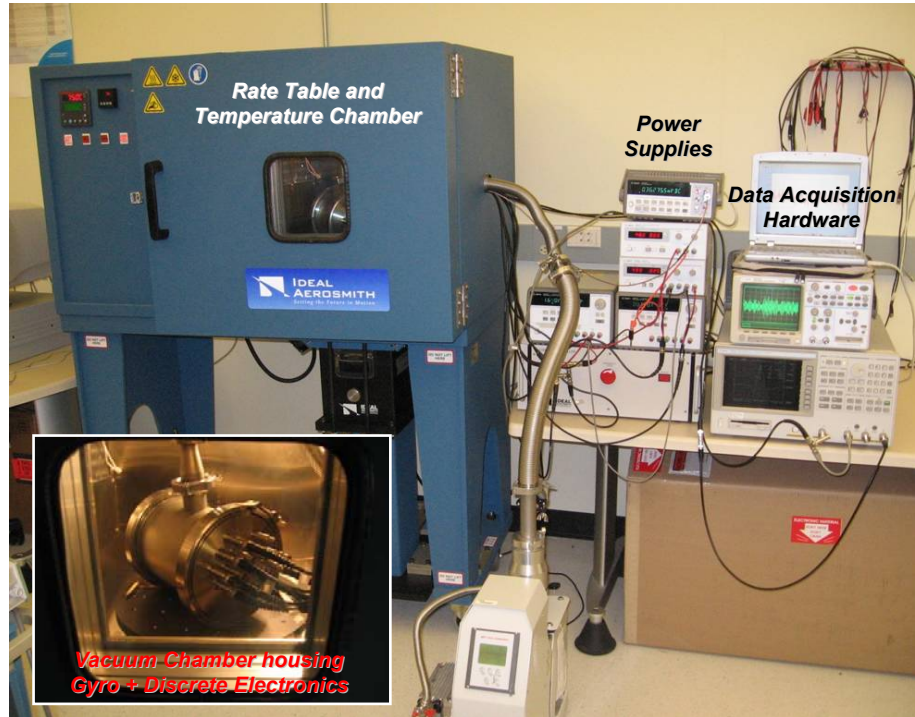
Figure 6.13: Experimental set-up for measuring the scale-factor of the M^2-TFG

The rotation rate sensitivity response of a 40µm-thick M^2-TFG under mode-matched operation and a fully differential configuration (using four sense electrodes) is presented in Figure 6.14. The perfectly matched-mode device with Q_{EFF} of 42,000 (Figure 6.12) exhibits a rate sensitivity of 20mV/deg/s. Figure 6.15 shows the signal observed at one sense electrode for a 1°/s step input signal and Figure 6.16 shows the response of the M^2-TFG to a sinusoidal input rotation signal. The settling time of 2s is consistent with high-Q second-order system dynamics.
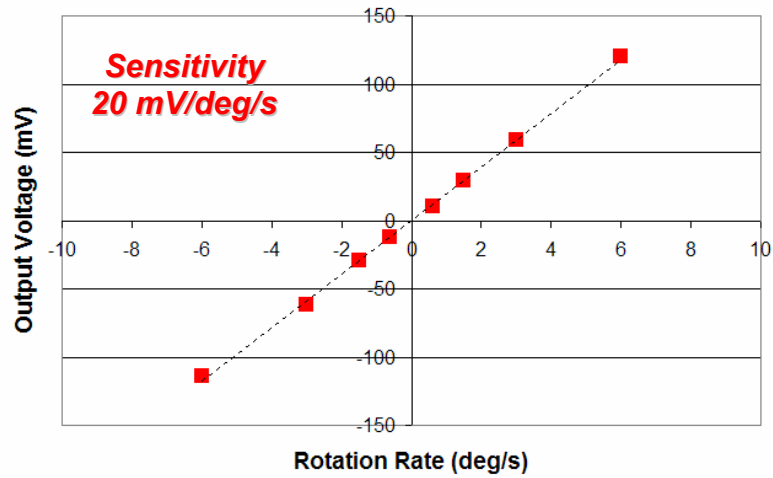
Figure 6.14: Scale-factor plot of a 40μm-thick SOI M²-TFG prototype with an effective mode-matched Q-factor of 40,000.
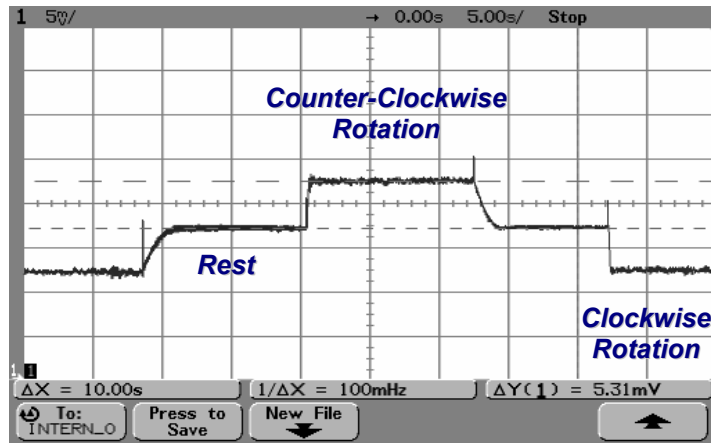
Figure 6.15: Response to a 1 deg/s rotation step input (observed at one sense electrode)
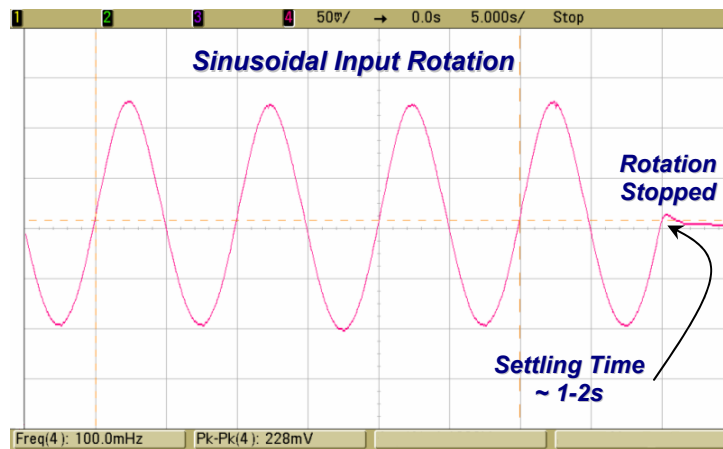
Figure 6.16: Response to a sinusoidal input rotation signal

130

6.4.1 Dynamic Linear Operating Range of M²-TFG

The linear dynamic range of the M²-TFG is restricted by the limitations of the capacitive sense gaps. Only rotation rates that induce a displacement of 1/10th of the gap size will result in a linear response at the output. While operating open-loop, the 40µm SOI M²-TFG prototype operating under perfect mode-matched operation (Q~40,000) has a linear dynamic range of ±20 deg/s for the drive-mode amplitude of 3µm. The effective sensor bandwidth is 0.5Hz.

The advantage of the M²-TFG mode-matching scheme is that the high gain that is achieved by leveraging the Q_{EFF}, can be traded off for increased linear dynamic range and sensor bandwidth. With other parameters such as polarization voltage, initial rest gap, and operating frequency kept constant; the scale factor can be controlled by varying the Q_{EFF}. Figure 6.17 shows the frequency response of a second 40µm-thick SOI M²-TFG with similar resonant mode Q's but operated with a 2Hz mode-mismatch (i.e. Δf ~ 2Hz).
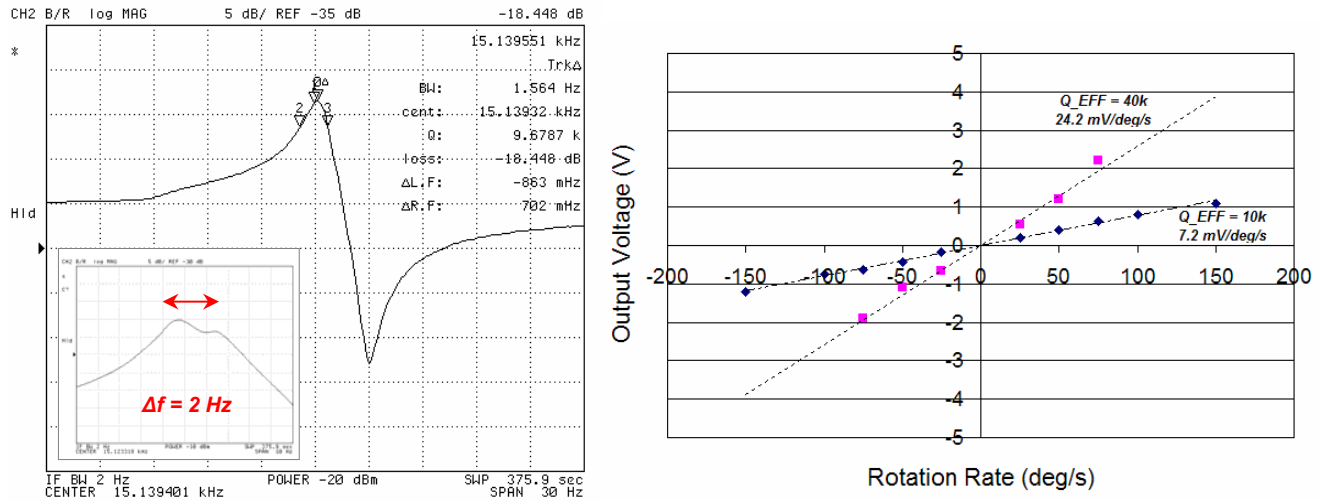
Figure 6.17: (Left) Induced mode-splitting of 2Hz resulting in a reduced Q_{EFF} of 10,000. (Right) Scale-factor comparison under two different matched conditions.

A scale factor comparison for the sensor with a bandwidth of 2Hz and the mode-matched case reveals that while the rate sensitivity has decreased from 24mV/deg/s to 7.2mV/deg/s, mode-mismatch allows for an improvement in the linear dynamic region of the device. While the linear operating range for the mode-matched case is limited to ±50deg/s, it is increased to ±150deg/s when there is a 2-Hz mode-split. Both scale-factor measurements were performed at drive displacement amplitude of 1μm.

6.5 Bias Drift Measurements

The output of a gyroscope in the absence of an input rotation rate is referred to as the gyroscope bias. Expressed in terms of angular rate (deg/hr or deg/s), the bias is an accurate measure of the long-term stability of a gyroscope. The drift in the gyroscope bias has systematic and random components. The systematic component of the bias drift is related to environmental conditions such as temperature, pressure, voltage fluctuations, and mechanical vibration. Often, these may be calibrated and compensated for in a system. The other components, by virtue of being random cannot be compensated and is therefore of concern. The random variation in the gyroscope bias, computed over specified finite sample time and averaging time intervals, is referred to as the bias instability, and is related to the noise build up in the sensor.

Bias instability of a gyroscope forms the fundamental limit that determines if the sensor is capable of navigation grade performance [2-4, 6]. The lower the gyroscope bias instability, the smaller the angular error over time, and better the overall heading accuracy of the inertial navigation system. Typically, the

accumulated error over time is corrected in the system by periodic calibration with an external reference, such as GPS [2]. However it is desirable to limit communications with external references to prevent electronic jamming/spoofing and reduce computational complexity. A gyroscope with low bias instability allows for longer time between calibrations. The analysis of the bias drift of a micromachined gyroscope offers insights into the inherent noise mechanisms in the sensor.

6.5.1 Allan Variance Technique

Bias drift is a function of the long-term average of the ZRO data and hence is a statistical phenomenon, and stochastic methods are used to model it (as opposed to a singular data point). Bias drift had been previously specified as a single root-mean-square (RMS) number over time. However, this was a very conservative estimate, and did not offer any particular insight into the actual noise mechanisms. Subsequently, since bias drift is related to random noise in a system, the power spectral density (PSD) was used to characterize gyroscope drift. The output of the gyroscope in the absence of any rotation input is recorded in the time domain, and Fourier analysis yields the two-sided PSD ($S_\Omega(f)$). A time-domain method that determines the angular error characteristics over time offers more insight for navigation applications, to determine the long-term stability of a gyroscope. One such method is the Allan Variance technique, which has been used extensively in recent times to study drift, both in fiber-optic gyroscopes and Coriolis-based vibratory gyroscopes. This technique, developed in the 1960's by David Allan, is a time-domain (TD) analysis, which was initially

introduced to study frequency stability of oscillators [7]. It aids in understanding the underlying random processes that give rise to data noise, and also enables identification of each noise term in the collected data. The Allan variance method relies on the principle that each noise component has its own characteristic PSD, and thereby is able to correlate each random component based on a specific averaging time. The IEEE is undertaking several initiatives to standardize the specification and test procedures for CVGs. Currently, the Allan variance technique is used as the standard for drift characterization in MEMS gyroscopes [81].

6.5.2 Computing the Allan Variance

The Allan Variance is defined as follows: the quantity expressed by one half the mean value of the square of the difference of adjacent time averages from a time series as a function of averaging time and is expressed mathematically as:

$$\sigma^2(\tau) = \frac{1}{2(n-1)} \sum_i \left(y(\tau)_{i+1} - y(\tau)_i \right)^2 \qquad (6.1)$$

In Eq. 6.1, '$\sigma(\tau)$' is the root Allan variance as a function of averaging time 'τ', 'n' is the total number of data clusters, and 'y_i' is the average value of the measurement in cluster i. The procedure to compute the root Allan variance consists of repeatedly averaging the data over varying clustering/bin times. The iterative procedure to compute Allan variance can be summarized as follows:

I. Data Collection: The ZRO is sampled from the micromachined vibratory gyroscope prototype at a specified sampling interval (τ_0) for a given period of time (typically between 3-12 hours at constant temperature).

II. Data Clustering: The long sequence of data is subsequently divided into finite clusters based on an averaging time, τ (an integer multiple of the initial sampling interval τ_0).

III. Data Averaging: The sum of all the data points in each cluster is calculated and the average over the length of cluster is evaluated.

IV. Variance Computation: The difference of the averages in successive clusters is evaluated and squared. The values are then summed up and divided by the rescaling factor. The square root of the result of the previous operation is then computed. This provides a quantitative measure of how much the average has changed at that particular value (of averaging time). This term is referred to as the Allan Deviation or Root Allan Variance.

V. Repeated Averaging: The final step of the calculation involves revisiting the ZRO data and increasing the τ, and repeating steps I-V. The process is repeated cluster lengths.

Allan Variance and the PSD of the collected data shares a unique relationship, as expressed in Equation (6.2)

$$\sigma_\Omega^2(\tau) = 4\int_0^\infty S_\Omega(f)\frac{\sin\theta^4(\pi f\tau)}{(\pi f\tau)^2} \qquad (6.2)$$

This can be interpreted as the Allan variance being directly proportional to the output noise power of the gyroscope when the output is passed through a filter with a transfer function $\sin^4(\pi f\tau)/(\pi f\tau)^2$. This particular transfer function arises due to the nature of the process used for computing the Allan Variance, i.e. the data clustering and averaging. The filter bandwidth depends on the sampling time τ.

Therefore, by varying τ, different types of random processes, and therefore different properties associated with the noise, can be evaluated.

6.5.3 Noise Components in Coriolis-Based Vibratory Gyroscopes

The values of the root Allan variance of ZRO data are plotted as a function of averaging time. Figure 6.18 has been adapted from [81] and plots the typical Allan variance curve of a vibratory gyroscope. The time domain data from the gyroscope contains contributions from various noise terms. It has been observed and verified that each noise term is correlated with different averaging times (τ), and hence correspond to different portions on the Allan Variance curve. The Allan Variance curve allows for easy identification of the various random processes that exist in the gyroscope output, and therefore forms a powerful tool of vibratory gyroscope drift analysis.
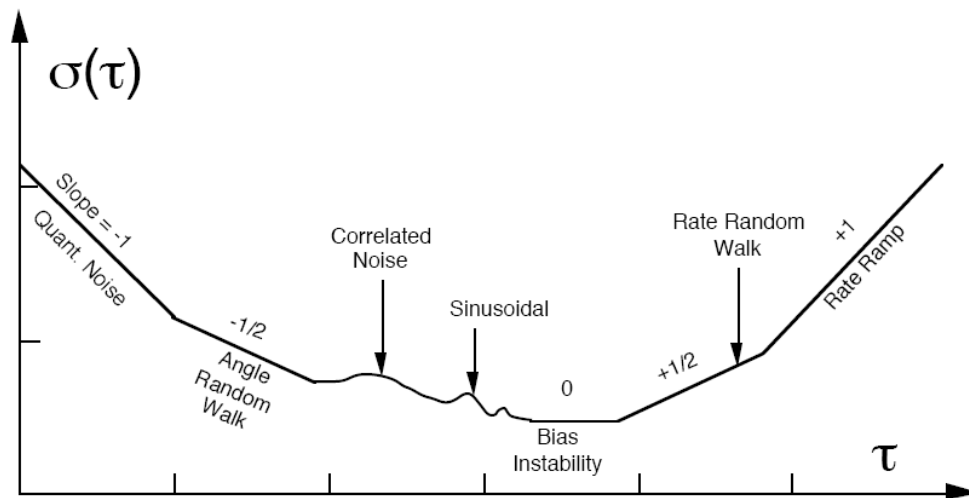
Figure 6.18: Sample plot of Allan variance analysis highlighting sections of the graph corresponding to various noise sources (after IEEE 952-1997) [81]

It is observed in Figure 6.18, that there are four distinct regions along the Allan Variance curve, which correspond to the following noise terms:

1. Quantization Noise

2. Angle Random Walk (ARW)

3. Bias Instability

4. Rate Random Walk (RRW)

The random processes that contribute to these noise terms can be assumed to be uncorrelated (i.e., statistically independent). The total Allan variance at a given sampling time τ can be obtained by the RMS sum of the magnitude of each of these components at that τ, as:

$$\sigma_{TOTAL}^2(\tau) = \sigma_{QUANTIZATION}^2(\tau) + \sigma_{ARW}^2(\tau) + \sigma_{BIAS\ INSTABILITY}^2(\tau) + \sigma_{RRW}^2(\tau) \tag{6.3}$$

6.5.4 Quantization Noise

This noise is the error introduced during the conversion of analog signal to a digital bit-stream. Quantization noise is caused by small differences in the actual amplitude of the points being samples and the resolution of the analog-to-digital converter. The angle PSD for such a process is expressed in [82].

$$S_\theta(f) = \tau Q^2 \left(\frac{\sin(\pi f \tau)}{\pi f \tau} \right)^2 \tag{6.4}$$

In Eq. 6.4, 'Q' is the quantization noise coefficient. Its theoretical limit is set to S/√12, where 'S' is the gyroscope scale-factor. The rate PSD is related to the angle PSD (by differentiation process) through the following:

$$S_\Omega(f) = (2\pi f)^2 S_\theta(f) = \frac{4Q^2}{\tau} \sin^2(\pi f \tau) \tag{6.5}$$

Substituting Eq. 6.5 in Eq. 6.2 and performing the necessary integration yields:

$$\sigma^2_{QUANTIZATION}(\tau) = \frac{3Q^2}{\tau^2}$$

(6.6)

Therefore the root Allan variance of the quantization noise when plotted in the log-log scale is represented by a slope of -1. The quantization noise has a short correlation time (i.e. wide bandwidth). Because the wideband noise can usually be filtered out because of low bandwidth of the vehicular motion in most application, it is not considered a major source of error/concern [83].

6.5.5 Angle Random Walk

ARW is a result of integrating a wideband rate PSD noise. Angle random walk is typified by a small varying angular drift with increasing variance as a function of time (and is a function of the white noise in the system). Angle random walk noise typically has a bandwidth less than 10Hz and is therefore within the bandwidth of most IMU systems. Hence unlike quantization noise, if angle random walk is not modeled accurately, it will result in significant errors in an IMU [83]. The associated PSD for wideband rate noise can be represented as follows:

$$S_\Omega(f) = N^2$$

(6.7)

In Eq. 6.7, 'N' is the angle random walk coefficient usually expressed in deg/hr/√Hz. Substituting Eq. 6.7 in Eq. 6.2 and performing the appropriate integration yields:

$$\sigma^2_{ARW}(\tau) = \frac{N^2}{\tau}$$

(6.8)

Therefore the root Allan variance of the angle random walk when plotted in the log-log scale is represented by a slope of -1/2. The numerical value of N can be evaluated directly on the root Allan variance plot at slope line (τ-$^{1/2}$) at τ = 1s. Being a measure of short term system stability, the ARW is significant at start-up, as it can prevent the initial biases of the system from being measured accurately. ARW is expressed in deg/√hr, and may be converted to noise density (expressed in deg/hr/√Hz) by multiplying its value with 60. The noise density refers to the TNEΩ of the vibratory gyroscope system and is commonly expressed in datasheets.

6.5.6 Bias Instability

The origin of this noise is electronics, or other components susceptible to random flickering. Because of its low-frequency nature it shows as the bias fluctuations in the data. The rate PSD associated with this noise, also known as 1/f noise is:

$$S_{\Omega}(f) = \begin{cases} \left(\dfrac{B^2}{2\pi}\right)\left(\dfrac{1}{f}\right) & f \leq f_0 \\ 0 & f > f_0 \end{cases} \qquad (6.9)$$

In Eq. 6.9, 'B' is the bias instability coefficient and 'f_0' is the 3-dB cutoff frequency. Similarly substituting Eq. 6.9 in Eq. 6.2 and performing appropriate integration yields [83]:

$$\sigma^2_{BIAS\ INSTABILITY}(\tau) = \frac{2B^2}{\pi}\left[\ln 2 - \frac{\sin^3(\pi f_0 \tau)}{2(\pi f_0 \tau)^2}\sin(\pi f_0 \tau) + 4\pi f_0 \tau \cos(\pi f_0 \tau) + \int\limits_{2\pi f_0 \tau}^{\infty}\frac{\cos t}{t}dt - \int\limits_{4\pi f_0 \tau}^{\infty}\frac{\cos t}{t}dt\right] \quad (6.10)$$

Therefore as seen in Eq. 6.10, the bias instability value can be read off the root Allan variance at the region where the slope is 0. The numerical value is the minimum value on the Allan deviation curve.

$$\sigma^2_{BIAS\ INSTABILITY}(\tau) = B^2 \left(\frac{2\ln 2}{\pi} \right) \tag{6.11}$$

Bias instability represents the minimum attainable bias drift of the vibratory gyroscope system (when sampled at the averaging time corresponding to the minima of the root Allan variance curve).

6.5.7 Rate Random Walk

This is a random process with uncertain origin and is the result of integrating a wideband acceleration PSD. The rate PSD associated with this noise is [83]:

$$S_\Omega(f) = \left(\frac{K}{2\pi} \right)^2 \frac{1}{f^2} \tag{6.12}$$

In Eq. 6.12, 'K' is the rate random walk coefficient. Substituting Eq. 6.12 in Eq. 6.2 and performing the appropriate integration yields:

$$\sigma^2_{RRW}(\tau) = \left(\frac{K^2}{3} \right) \tau \tag{6.13}$$

Therefore as seen in Eq. 6.13, the rate random walk value can be read off the root Allan variance at the region where the slope is +1/2. The RRW represents the drift-rate error build-up with time that is due to the white noise of the angular acceleration component in the vibratory gyroscope.

6.5.8 Evaluation of Bias Drift in 40µm-thick SOI M²-TFG Prototype

The ZRO of the perfectly matched 40µm-thick SOI M²-TFG prototype (presented in Sections 6.2-6.4) was sampled every 100ms for a period of 12 hours. The normalized bias value of the gyroscope is shown in Figure 6.19. The initial one hour of data was rejected to allow the system to stabilize at the set temperature.

The remaining data was used for Allan Variance analysis to characterize the long-term stability of the matched-mode device (interfaced with the discrete electronics). The root Allan variance plot of the M^2-TFG is shown in Figure 6.20. From this graph, the estimated angle random walk (ARW) is determined to be 0.045deg/√hr. This corresponds to a measured noise floor of 15μV/√Hz over the signal bandwidth (1-10Hz) for the entire gyroscope sensor system. The output-referred total equivalent noise density (M^2-TFG + Electronics) is therefore 2.7deg/hr/√Hz. The minima point on the Allan variance curve represents the bias instability of the M^2-TFG system, which is recorded at 0.96deg/hr.
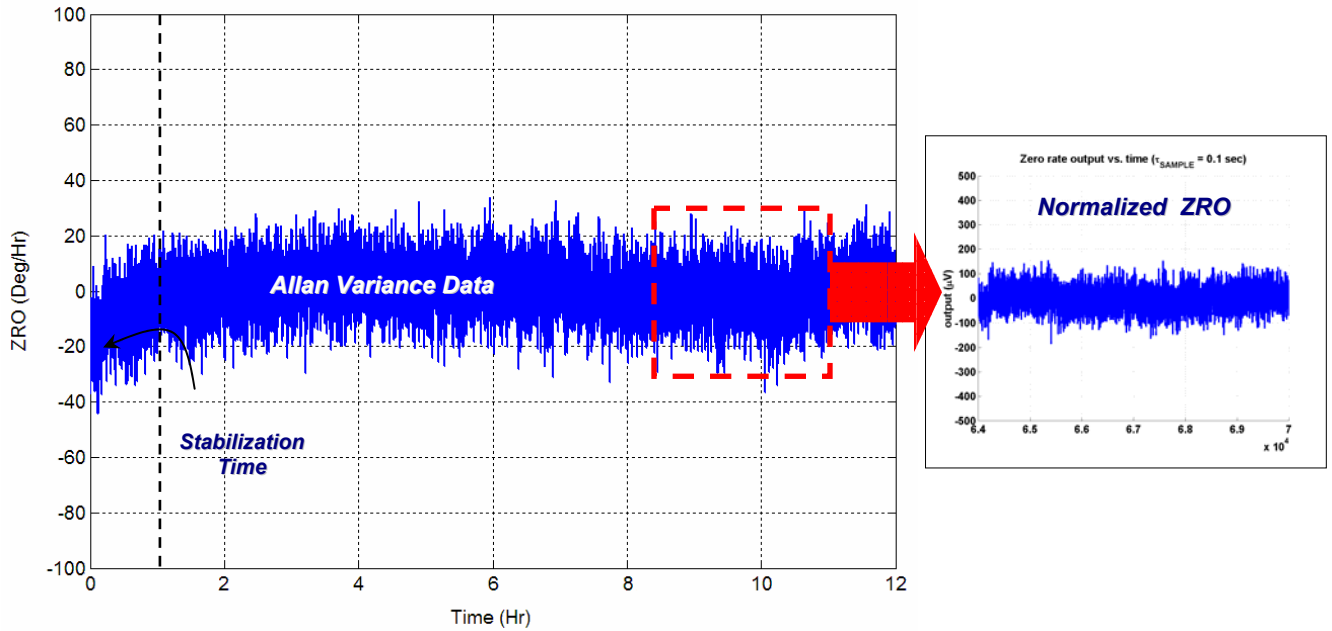
Figure 6.19: Time domain plot of the ZRO (recorded at 25˚C)
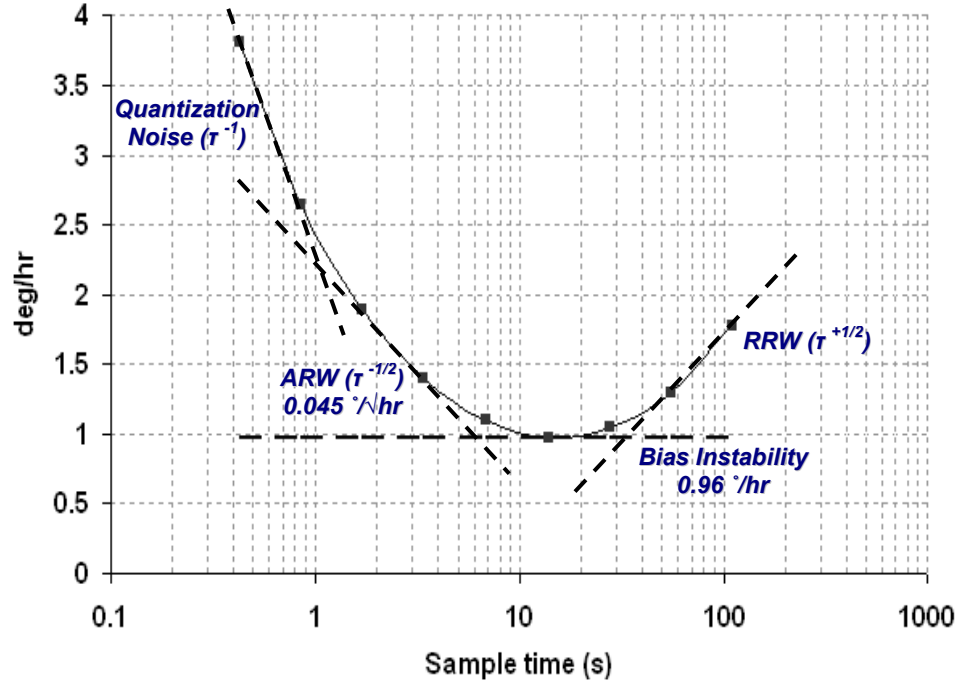
Figure 6.20: Root Allan Variance plot of the 40µm M^2-TFG prototype.

6.6 Device Enhancements

Several avenues of device performance enhancement exist in the 40µm-thick SOI M^2-TFG prototypes. By ensuring a larger proof-mass, drive amplitude, improved sense gap aspect ratio it is possible to improve the device Brownian noise floor, sensitivity and reduce the operating voltage requirements. The 40µm-thick SOI M^2-TFG represents the first Class-I vibratory gyroscope reported in literature that operates under mode-matched operation with a 0Hz frequency split between the drive and sense resonant modes. A high-Q$_{EFF}$ enabled large device sensitivity and Allan variance bias instability values approaching sub-1deg/hr. However, the prototype design did not utilize the full-potential of the structure. Device substrate thickness and proof-mass dimensions were limited to

142

40µm and 400µm² respectively. The stable region of drive-axis displacements were restricted by the initial overlap and comb-thickness. The sense electrodes did not fully utilize the real-estate efficiently, and the aspect ratio of the sense gaps was limited to 8:1 (5µm wide sensing gaps). This resulted in large operating voltage requirements as displayed in Figure 6.4.

Table 6.4: Parameter comparison of the M²-TFG improvements

Device Parameter	40µm M²-TFG	60µm M²-TFG
Proof-Mass dimensions (µm²)	400	550
Measured Sense Gap (µm)	4.8	3.6
Approximate Resonant mass (µg)	30	85
Aspect Ratio	~ 8.33	~ 16.67
Maximum drive amplitude (µm)	3	5

A critical aspect of the new M²-TFG prototypes was the sense capacitance enhancements as shown in Figure 6.21. To address these inadequacies, a new optimized version of the M²-TFG was designed. A list of device optimizations made to the M²-TFG design (implemented on a 60µm-thick SOI substrate) is summarized in Table 6.4. By increasing the sense electrode area and optimizing device-layer silicon etching to yield aspect ratio approaching 20:1 (see Appendix A), it will be possible to reduce operating voltage requirements and improve scale-factor of the device. By optimizing the flexural dimensions based upon the design rules discussed in Chapter III, it is possible to maintain the same operating frequency regime thereby ensuring high-Q mode-matched operation demonstrated in the 40µm-thick SOI M²-TFG predecessors. The mode-matched resonant peak of the 60µm-thick SOI M²-TFG is displayed in Figure 6.22.
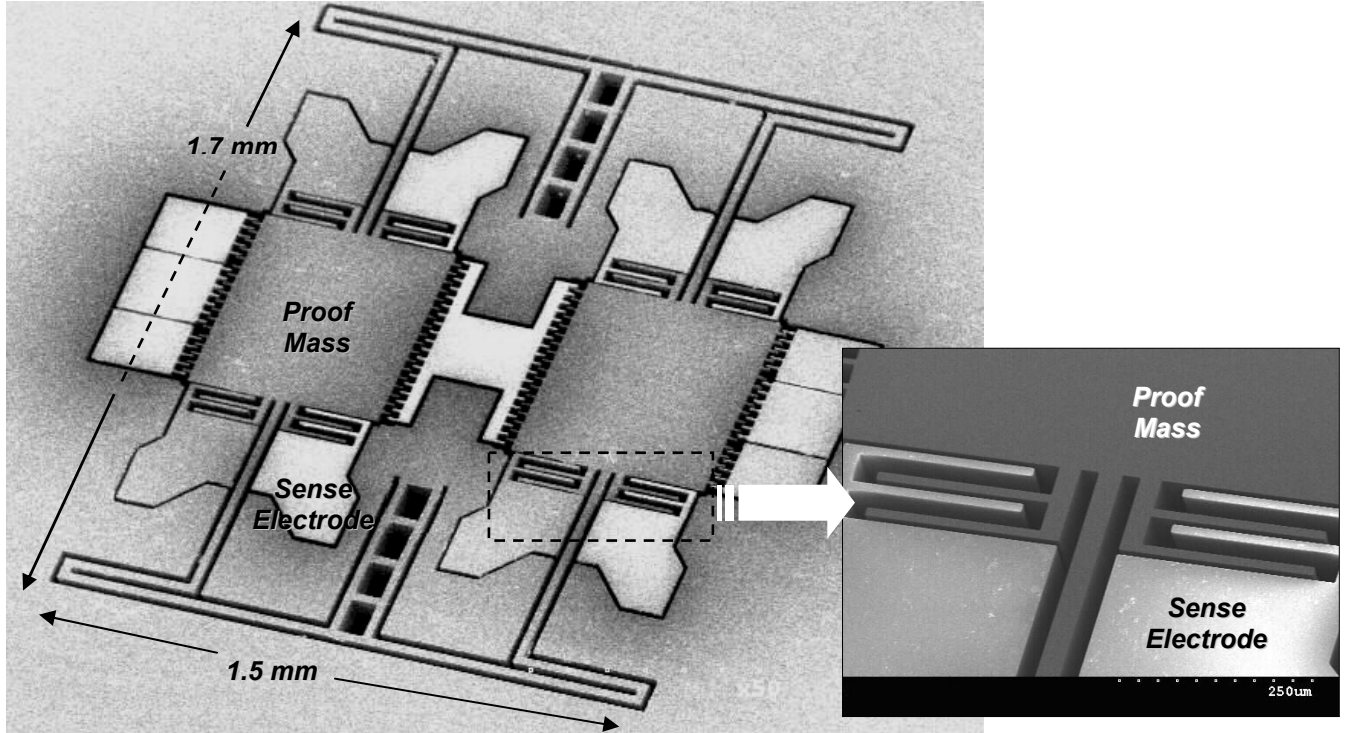
Figure 6.21: SEM overview of the optimized M^2-TFG device implemented on 60µm thick SOI substrate. (Inset) A close-up view of the sense electrodes.
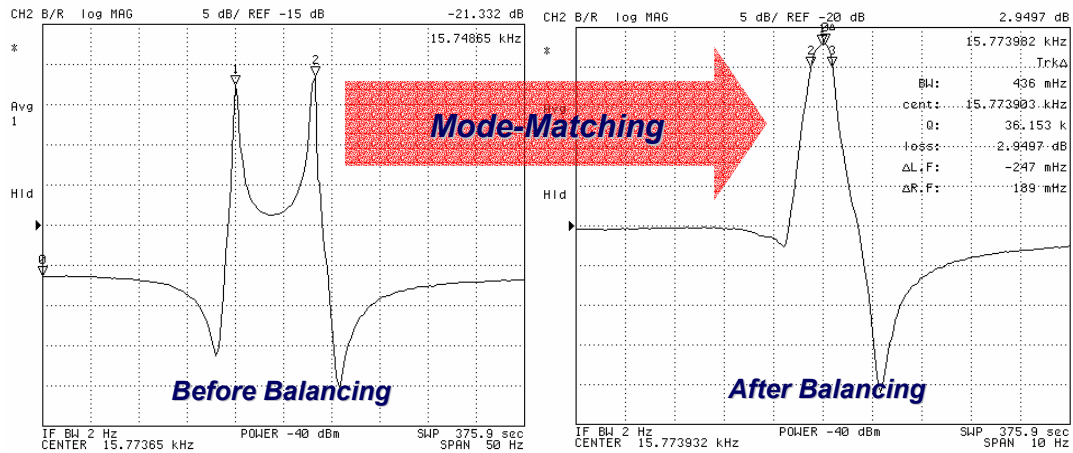
Figure 6.22: (Left) Minimum possible mode-separation possible before quadrature nulling (Right) Mode-matched resonant peak of device with Q$_{EFF}$ of 36,000.

6.6.1 Scale-Factor Enhancements of the M^2-TFG

Result of the sensitivity measurements from the device is displayed in the scale-factor plot shown in Figure 6.23. The scale-factor plot of the device (under mode-matched operation) is approximately 83mV/deg/s.

144
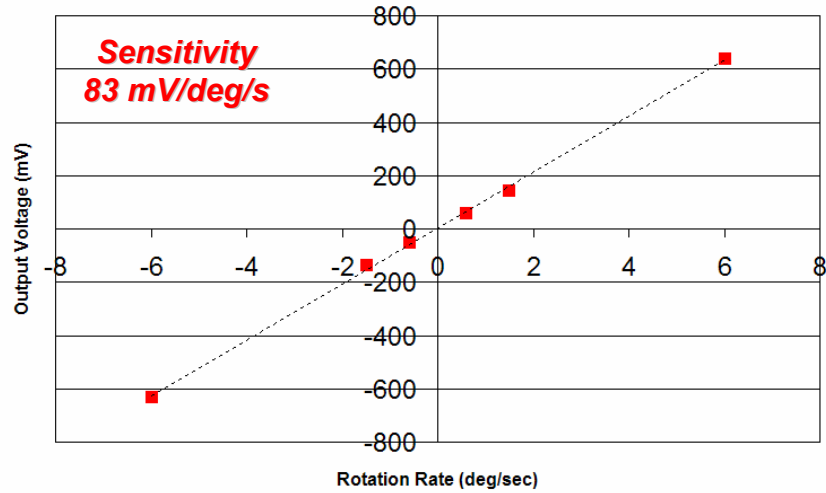
Figure 6.23: Scale-factor plot of a 60μm-thick SOI M²-TFG prototype with an effective mode-matched Q-factor of 36,000 (Drive amplitude = 5μm).

Owing to the increased drive amplitude, high-Q_{EFF}, and larger aspect ratio sensing gaps; the sense-channel output displays non-linearity at rates approaching ±5deg/s. The dynamic range of the M²-TFG is enhanced by reducing the drive amplitude to 1μm. Figure 6.24 shows the device with reduced drive amplitude displaying an enhanced linear dynamic range of ±35 deg/s. The scale factor has been electronically enhanced.
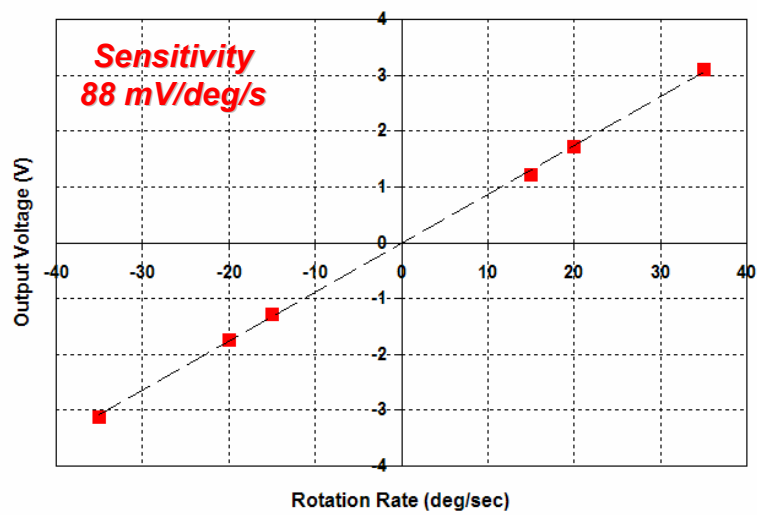
Figure 6.24: Scale-factor plot of a 60μm-thick SOI M²-TFG prototype with an effective mode-matched Q-factor of 36,000 (Drive amplitude = 1μm).

6.7 Improvement in Bias Stability

Several design optimization techniques that lower the total system noise floor and consequently result in superior gyroscope bias drift had been specified in [21]. In order to improve the bias drift of the M^2-TFG, a sufficiently low system noise floor design must be adopted. Increased mass, implemented in the optimized version of the M^2-TFG, helps lower the Brownian noise floor thereby improving bias drift. The gyroscope bias drift has also been shown to depend significantly on the Q_{EFF}. The high-Q operating modes supplied by the optimized M^2-TFG ensure this enhancement is preserved. The noise considerations imply that a low-bias drift M^2-TFG must have ultralow noise interface circuits. While low-noise front-ends are necessary to ensure a low minimum detectable capacitance, the flicker noise of subsequent stages is of primary concern. The bias drift of the gyroscope is determined by the flat portion of the Allan variance curve, and quantifies the flicker noise in the system. Large flicker noise due to electronics therefore results in a direct increase in bias drift. Decreasing the flicker noise corner frequency of the interface electronics can significantly improve bias stability. JFETs exhibit significantly lower flicker noise corner frequencies, and for this reason discrete JFTE op-amps have been used at the final output stage (which demonstrate very low current and voltage noise performances) [84]. The final criterion for ensuring better bias stability is enhancement in the capacitive sensitivity as demonstrated by the 60μm-thick SOI M^2-TFG prototype.

6.7.1 Allan Variance Analysis of the 60μm-thick SOI M^2-TFG

Allan variance analysis was performed with ZRO data collected over a period of 3-6 hours, and at three constant temperature settings. In each case, the 60μm-

thick SOI M²-TFG prototype was operated under mode-matched operation with drive amplitude of 5µm. As observed in Figure 6.25, the device has a bias instability of 0.31 deg/hr at 25˚C, which is by far the best reported for a MEMS vibratory gyroscope to date. The bias instability degraded at 50ºC, which is primarily caused by the sensitivity of the device quality factor to temperature variations. However at 5ºC, the M²-TFG prototype displayed an enhanced bias instability of only 0.16 deg/hr. Sub-0.1 deg/hr bias drift allows integration of MEMS gyroscopes into high-precision applications such as gyrocompassing (within 10mrad precision) – something that has been very challenging in the past due to performance limitations.

Temp (˚C)	ARW (deg/√hr)	Bias Drift (deg/hr)
5	0.005	0.16
25	0.0083	0.32
50	0.015	0.76
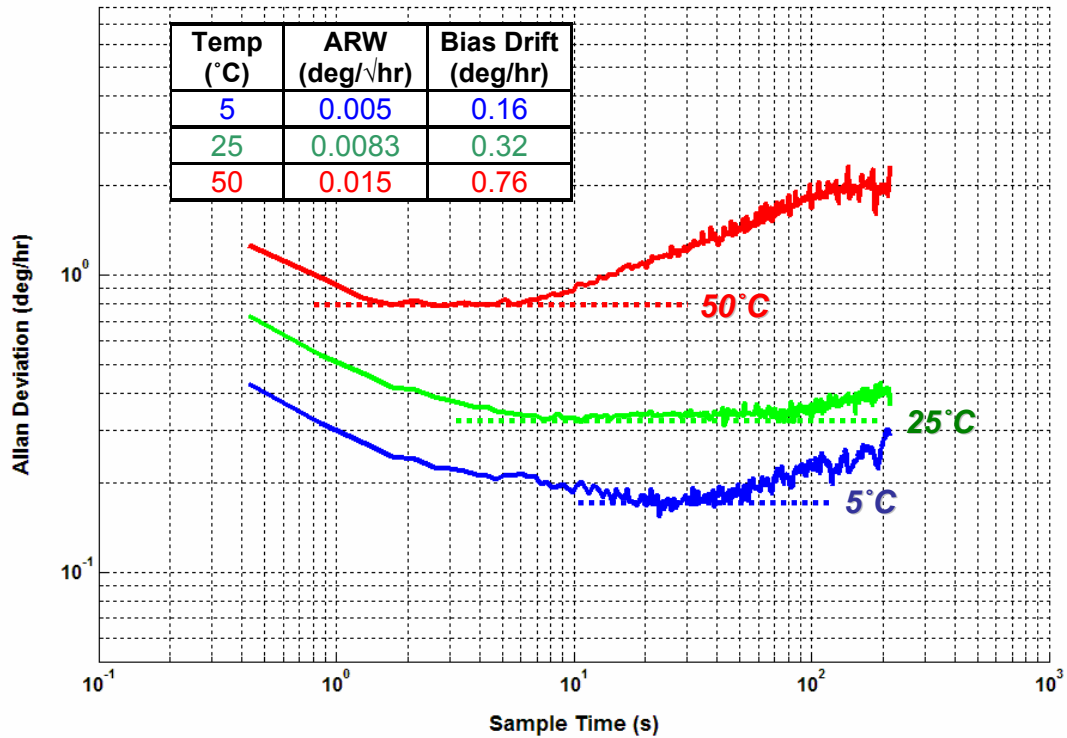
Figure 6.25: Root Allan Variance plot of the optimized 60µm M²-TFG prototype.

CHAPTER VII

FABRICATION TECHNOLOGY OPTIMIZATION AND PACKAGING

Enhancement in sense gap aspect ratio and resonant mass provides significant improvements in the device sensitivity and Brownian noise floor respectively and consequently the bias drift of the M^2-TFG structure. In order to further enhance the device performance, a migration towards thicker SOI substrate is desired. A thicker SOI device layer enables larger mass. However the sensing gaps cannot be scaled accordingly. The aspect ratio of the sensing gaps is pre-dominantly a function of the Silicon etching tool. Aspect ratio of silicon trenches (that are reliably repeatable) in the SOI low-frequency module are restricted to 10:1 (i.e. 8μm sensing gaps for device thickness of 80μm). In an effort to address the limitations of the sensing gaps defined by the silicon deep-reactive ion etching tools, doped-polysilicon was investigated as means of reducing the gap and enhancing the aspect ratio.

7.1 Blanket Polysilicon Deposition

The first approach taken to address the sense-gap aspect ratio was an optimized version of the blanket doped-polysilicon deposition technique described in [85]. In this two-mask approach similar to the process flow described in Chapter III, the M^2-TFG geometry is defined by the device layer deep-reactive ion silicon etching. LPCVD Polysilicon is deposited in a conformal fashion at 588ºC to reduce the capacitive gap openings (thereby enhancing aspect ratio). The handle layer silicon and buried oxide (BOX) etching is then performed in a similar

fashion as [27, 86] to release the structure. Finally the electrode isolation is achieved by a combination of device and handle-layer silicon etching.
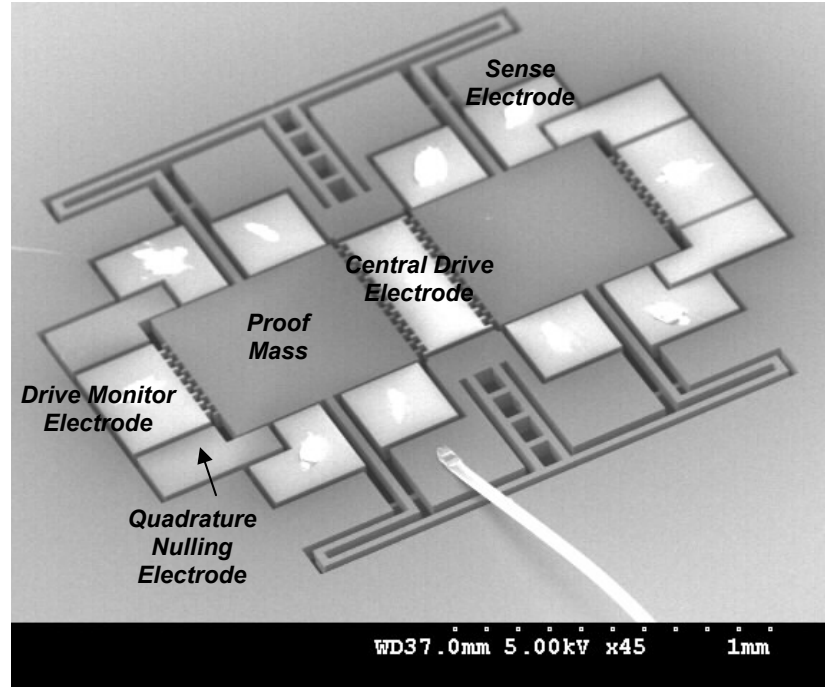
Figure 7.1: SEM overview of a M²-TFG device with (600μm)² proof-masses implemented using the blanket-polysilicon deposition process outlined in [85]

Figure 7.1 demonstrates a prototype M²-TFG (on 70μm thick SOI substrate) with 600μm² proof-masses implemented using this process flow. Figures 7.2-7.3 show a comparison of the device features of two M²-TFG prototypes before and after the deposition of 1.5μm thick polysilicon. It is observed that polysilicon is deposited indiscriminately. This means that polysilicon exists not only between the sensing gaps where it is desirable, but also along the device flexures and actuation comb-electrodes. The drawbacks of this process flow will be evident in the characterization results.

149
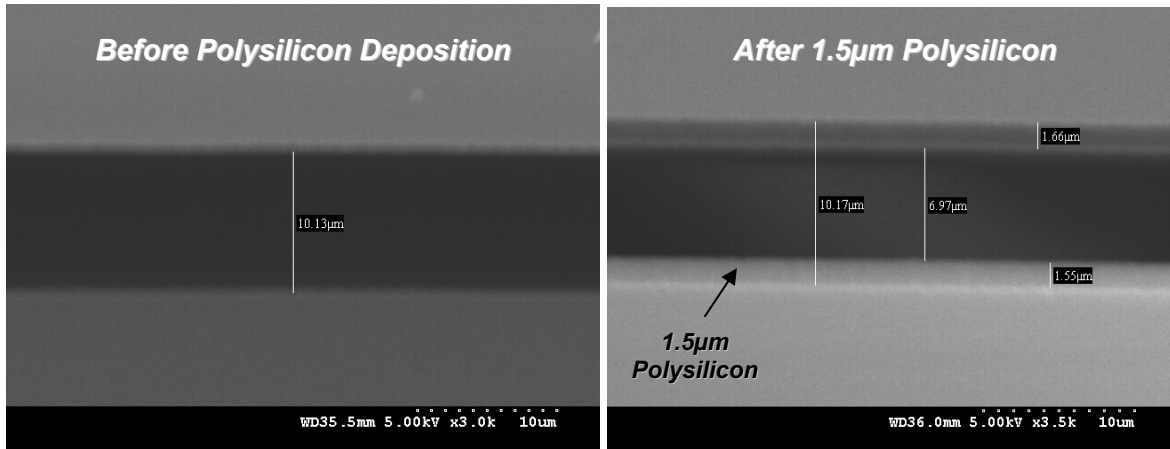
Figure 7.2: View of the device sensing gaps before and after deposition of 1.5μm p-doped LPCVD polysilicon.
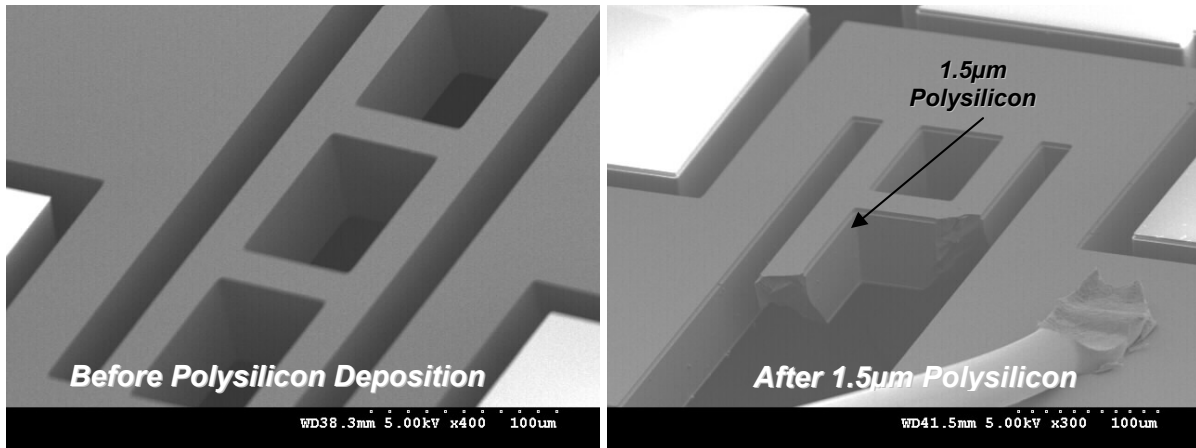
Figure 7.3: View of the device anchor region before and after deposition of 1.5μm p-doped LPCVD polysilicon.

Polysilicon on the flexural springs affects the resonant frequencies of the operating modes as well as the operating mode Q-factors. A comparison of the drive-mode Q-factor of a M^2-TFG before and after the deposition of 1.5μm-thick polysilicon is shown in Figure 7.4. Table 7.1 summarizes a comparison of the measured operating-mode frequencies and Q-factors between the device with polysilicon on the flexural springs, and without. It is evident that the resonant operating mode-frequencies do not correspond to the values simulated in ANSYS. This may be attributed to the stress in polysilicon.

150
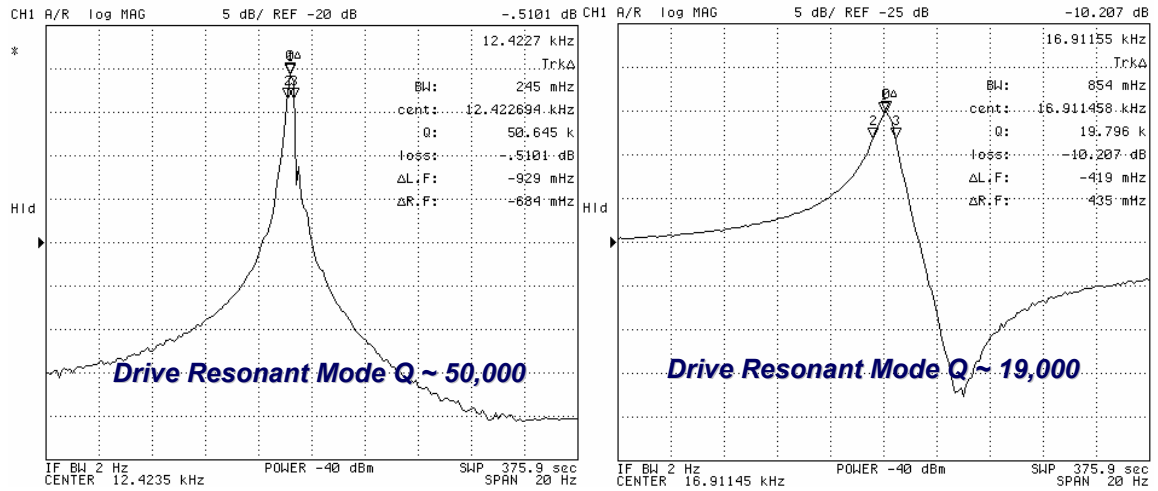
Figure 7.4: (Left) Measured drive-mode Q of 50,000 before polysilicon deposition. (Right) Measured drive-mode Q of 19,000 after 1.5μm polysilicon deposition.

Table 7.1: Measured frequency response and Q-factor of two batches of M^2-TFG

	Drive		Sense	
	Frequency (Hz)	**Q**	**Frequency (Hz)**	**Q**
Device without Polysilicon on Flexural Springs				
Measured	12.422	50,640	13.189	26,280
ANSYS	12.663		13.203	
Device with 1.5μm-thick Polysilicon on Flexural Springs				
Measured	16.911	19,800	17.713	9,100
ANSYS	17.112		17.362	

7.2 Aspect-Ratio Enhancement using Selective Polysilicon Deposition

Owing to the shortcomings of the blanket-polysilicon approach described in the previous section, a new fabrication technology was developed – The Selective Polysilicon Deposition (SPD) process. The salient processing steps of this new approach are outlined in Figure 7.5 (and discussed further in Appendix A).

Oxide

Device Layer

BOX

Handle Layer

II.   The device and handle layer mask of the low-resistivity SOI wafer is constructed using patterned wet oxide.

I.   The capacitive sense gaps are etched using DRIE.

Doped Polysilicon

III.   3-4μm of LPCVD polysilicon is deposited and doped (handle layer polysilicon is not shown).

PECVD Oxide

IV.   Handle-layer silicon and BOX layer are successively etched. The polysilicon bridges are eliminated.

VI.   Device-layer silicon is etched to release the structures.

Enhanced Sense Gap

Electrode

Proof Mass

SCS Flexure

V.   The residual polysilicon is etched away and area under support-posts released in HF solution.

Figure 7.5: Outline of SPD fabrication process flow for SOI M²-TFG prototypes

In this process flow, the aspect ratio of the sense gaps is significantly improved through the deposition of doped-LPCVD polysilicon. However, the structural integrity of the single-crystalline silicon flexural springs is preserved. The prototype M^2-TFGs are implemented on low-resistivity (100) SOI substrate with a device layer thickness of approximately 80-100μm. Thermally grown wet oxide (at 1100°C) serves as the masking layer for the device and handle-layer silicon etching. The initial device layer lithography process patterns the oxide mask to define the M^2-TFG geometry. The second device-layer lithography process generates the openings for silicon DRIE. Self-aligned sense gaps are formed in this processing step as highlighted in Figure 7.6.
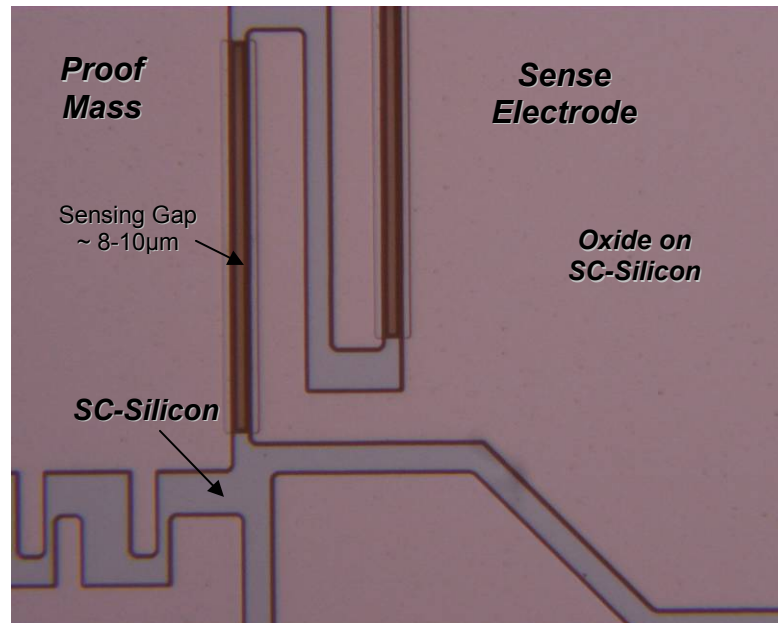
Figure 7.6: Generation of self-aligned sense gaps in the M^2-TFG prototype.

LPCVD polysilicon is consequently deposited in a conformal manner at 588°C to reduce the capacitive gaps at the sense electrodes. The polysilicon is then doped and annealed using Boron-diffusion doping at 1000°C. The final

153

lithography process in the device-layer generates the mask for the device-layer DRIE which defines the electrodes, comb-drive actuators and the general structure of the device. A 4-5μm thick PECVD oxide layer was utilized to generate a bridge over the sensing gaps, thereby preserving the integrity of the sensing gaps. This has been illustrated in Figure 7.7.
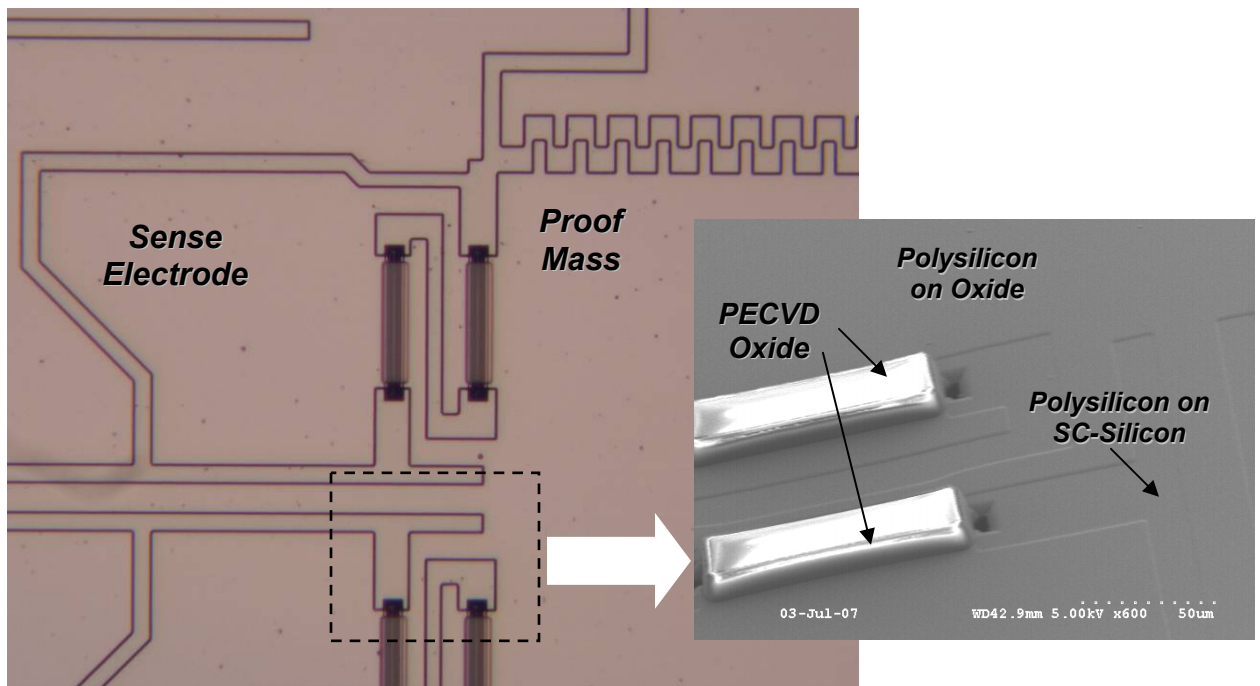
Figure 7.7: Microscope image of PECVD oxide bridges that preserve the enhanced sense-gap aspect ratio. (Inset) SEM image of PECVD oxide bridging the sense gaps.

The focus of the processing now switches to the handle-layer silicon etching. Handle-layer silicon etching through to the buried oxide layer is performed using the Bosch process [87]. The handle layer silicon is typically between 300-500μm in thickness and a 2-3μm thick oxide mask (thermally grown wet oxide at 1100°C) is usually the mask of choice. The buried oxide is then removed in a reactive ion

etching (RIE) system. The polysilicon bridges that connect the sense gaps are consequently etched as shown in Figure 7.8.
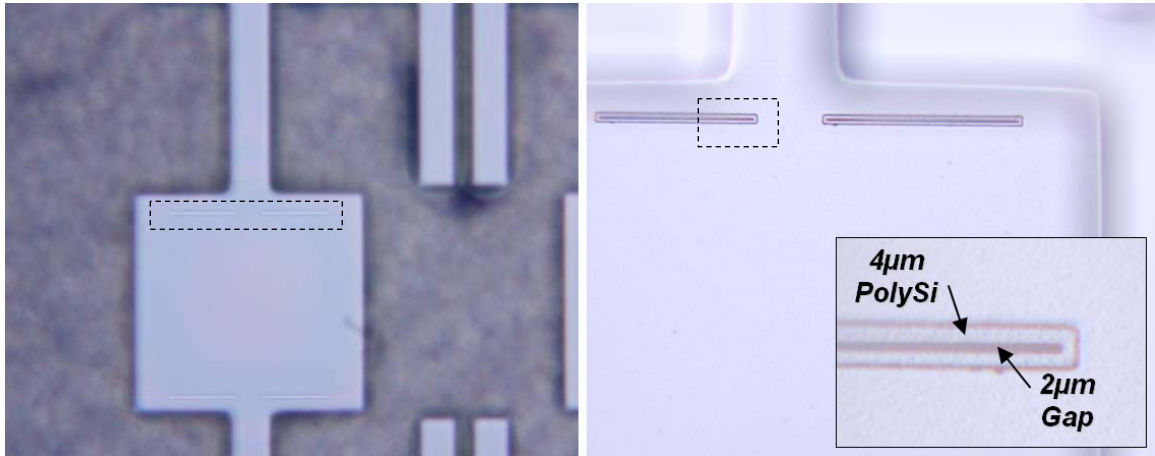
Figure 7.8: (Left) Prototype M^2-TFG as viewed from the handle layer after silicon etching. (Right) Microscope image of sense gaps after BOX and polysilicon are eliminated.

The final processing stage involves anisotropic device-layer silicon etching. This is performed using the ASE process developed by the Surface Technology Systems [61]. In this silicon etching step, the entire device geometry (including the flexural springs and actuation and quadrature comb-electrodes) is defined and sense electrode isolation is performed as illustrated in Figure 7.9.

The polysilicon overhangs seen in Figure 7.9 are the result of the PECVD mask that protects the polysilicon inside the capacitive trenches during device-layer silicon etching. Since the PECVD masking process is susceptible to alignment errors during photolithography, the polysilicon causes mass asymmetries on the individual proof-masses. This will manifest itself as increased quadrature error in the overall M^2-TFG system. The final plasma-etching step involves the elimination of the polysilicon bridges as shown in Figure 7.10.
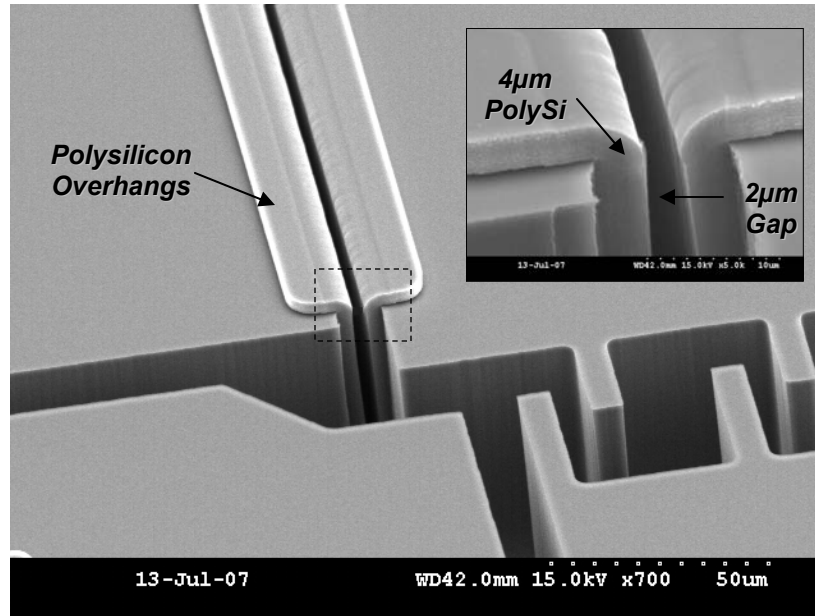
Figure 7.9: View of the M²-TFG sense area after device-layer silicon etching showing the polysilicon overhangs. (Inset) Close-up view of the high-aspect ratio sense gaps.
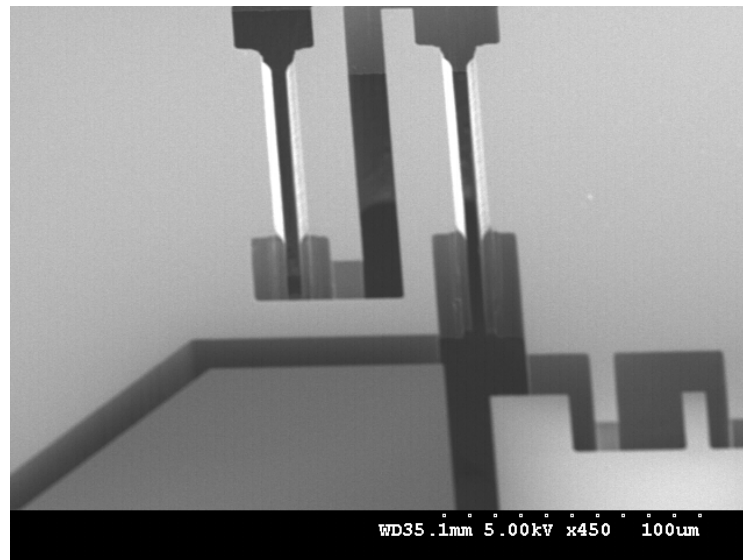
Figure 7.10: View of the single-crystalline silicon M²-TFG sense area after the elimination of the polysilicon overhangs.

Figure 7.11 displays a view of the single crystalline silicon structural geometry of

the M²-TFG. The inset displays finite amount of surface roughness on the flexural

springs. Figure 7.12 demonstrates a prototype M²-TFG (on 80μm thick SOI substrate) with 500μm² proof-masses implemented using the new process flow.
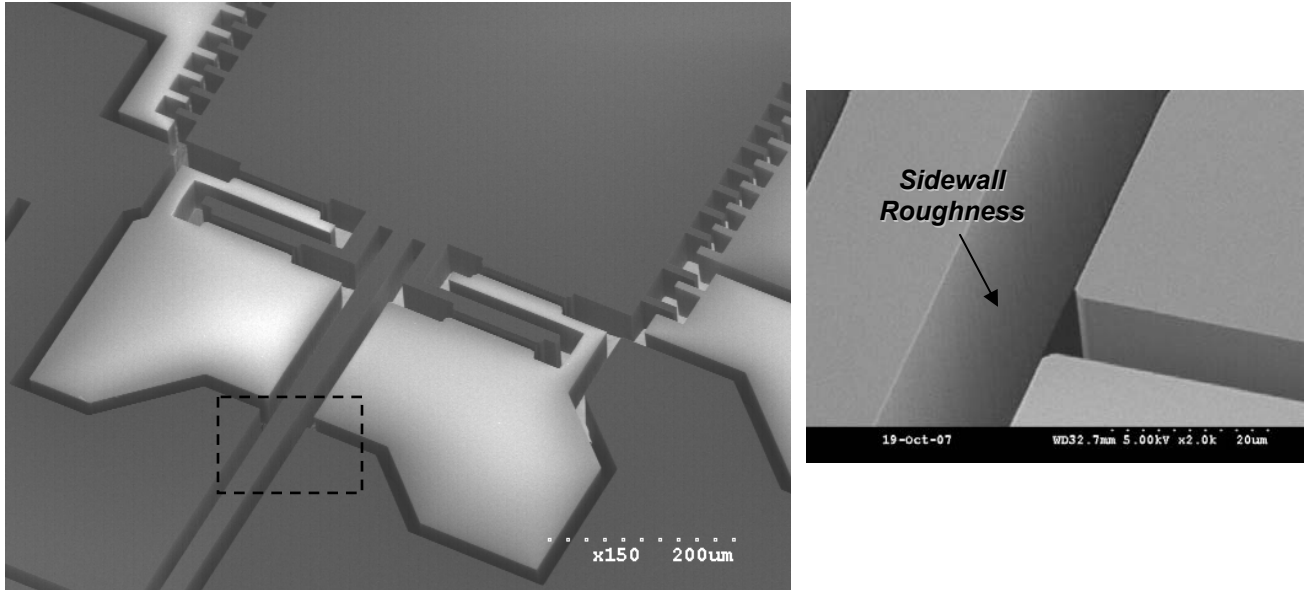
Figure 7.11: View of the single-crystalline silicon flexural springs of the M²-TFG. (Inset) Close-up view of the sidewall surface roughness.
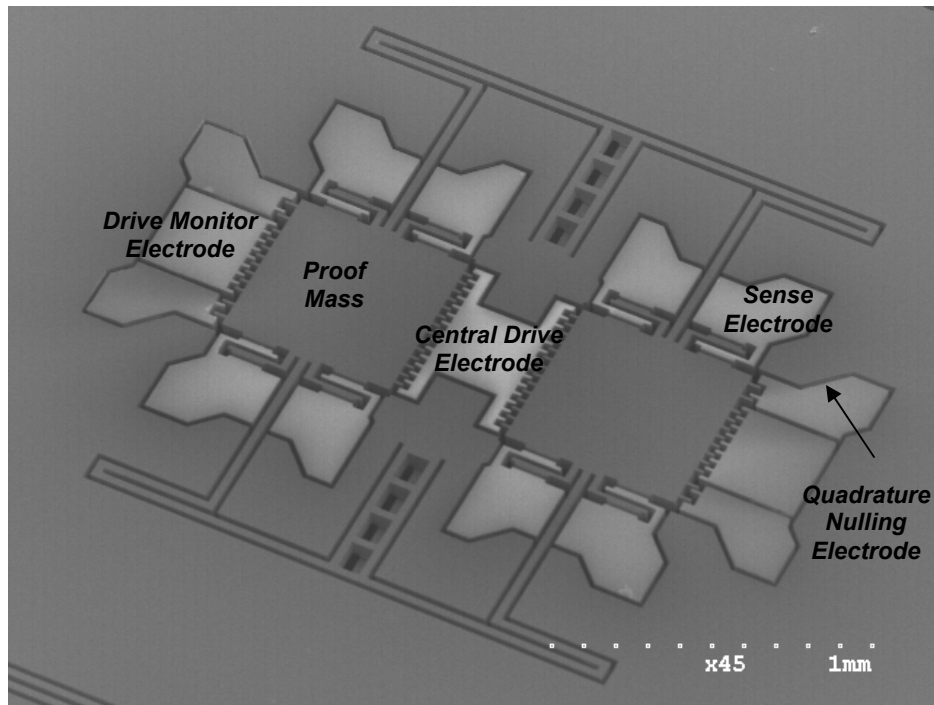
Figure 7.12: SEM overview of an 80μm-thick SPD M²-TFG prototype.

The SPD process flow is also compatible with the fabrication of high-precision inertial sensors such as micro-g accelerometers [88]. Figure 7.13 illustrates the capability of this process, whereby aspect ratio of 50:1 was demonstrated during the realization of shock-stops in the accelerometer prototypes. By implementing the support tethers using exclusively single-crystalline structural material, it was possible to accurately predict stiffness (and sensitivity). This had proved challenging in [85], where stress induced during polysilicon deposition manifests itself in increased stiffness (and reduced sensitivity).
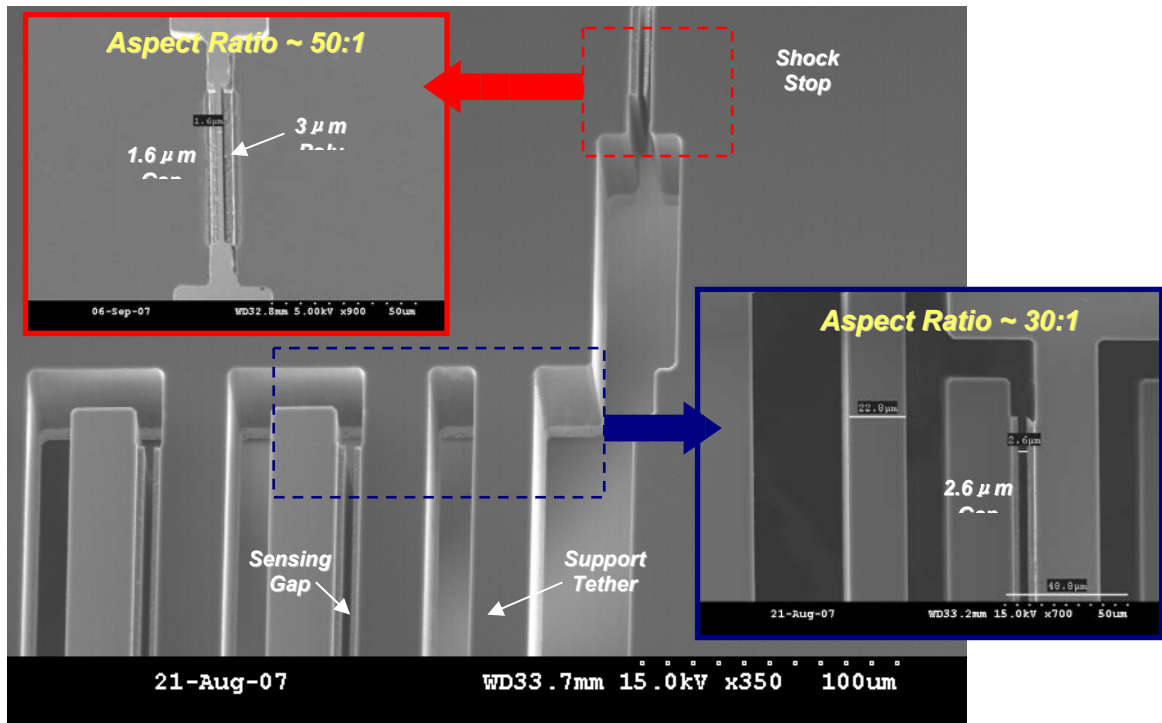
Figure 7.13: View of salient features of a micro-g accelerometer sample implemented using the SPD process flow.

7.2.1 Device Characterization and Performance Evaluation

The M^2-TFG prototypes, implemented on 80μm thick SOI device layer using the optimized fabrication technology were characterized in vacuum. Figure 7.14 displays a collection of the frequency response plots highlighting the effect of

improved aspect-ratio on the sense-mode tuning. In contrast to 80.3V required to compensate 120Hz of frequency split (in Figure 6.4), the M^2-TFG implemented using the advanced fabrication process flow manages to compensate 180Hz of initial frequency split with 38V. In an effort to increase device bandwidth, the device was operated at controlled mode-mismatch to simulate 5Hz bandwidth.
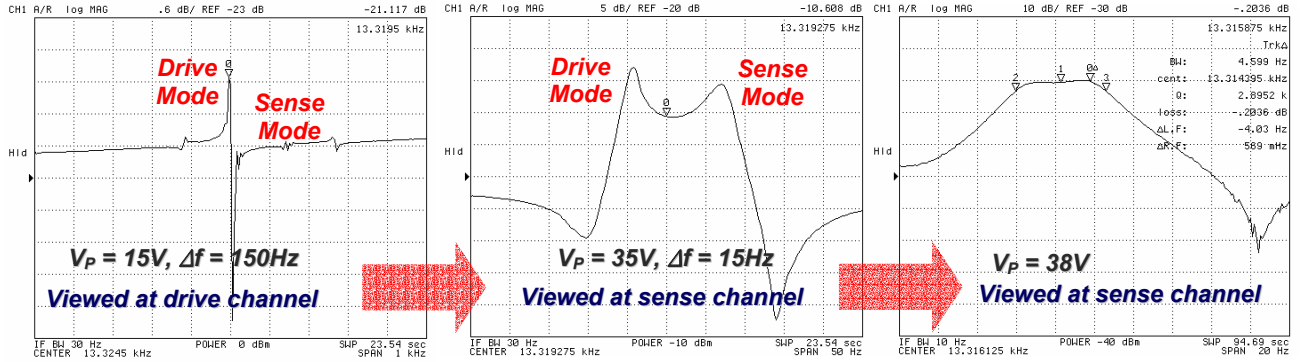
Figure 7.14: Illustration of finite mode-matching in M^2-TFG to simulate larger bandwidth.

The rotation rate sensitivity response of the M^2-TFG under mode-matched operation (with intentional 5Hz split) and one differential pair of sensing electrodes is presented in Figure 7.15. The device with Q_{EFF} of 4,000 exhibits a rate sensitivity of 12mV/deg/s. Figure 7.16 shows the response of the M^2-TFG to a sinusoidal input rotation signal. Unlike the response of a high-Q mode-matched M^2-TFG device (shown in Figure 6.16), bandwidth enhancement improves the response time of the device to less than 200ms. The improved sense-gap aspect ratio is able to compensate the device sensitivity in the absence of high-Q_{EFF}.
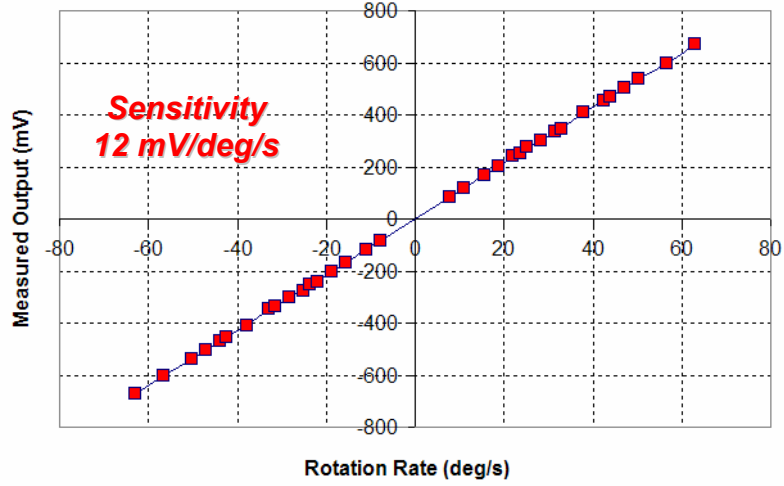
Figure 7.15: Scale-factor plot of 80μm-thick SOI M²-TFG prototype with an effective mode-matched Q-factor of 4,000.
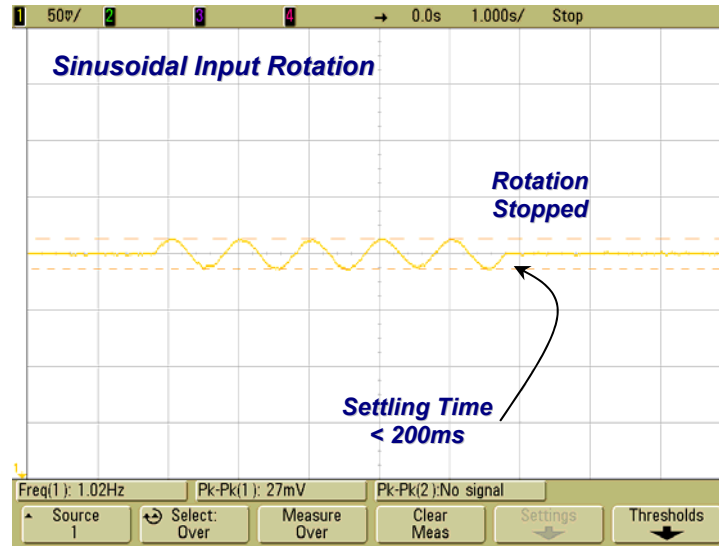
Figure 7.16: Response to a sinusoidal input rotation signal

The ZRO of the M²-TFG prototype was sampled every 100ms for a period of 3 hours (at constant temperature of 23°C). The root Allan variance plot of the M²-TFG is shown in Figure 7.16. From this graph, the estimated angle random walk (ARW) is determined to be 0.15deg/√hr and the bias instability of the M²-TFG system is recorded at 1.82deg/hr. The summary of the device performance

parameters of a prototype 80μm-thick SOI M^2-TFG device, implemented using the SPD process flow, are listed in Table 7.2.
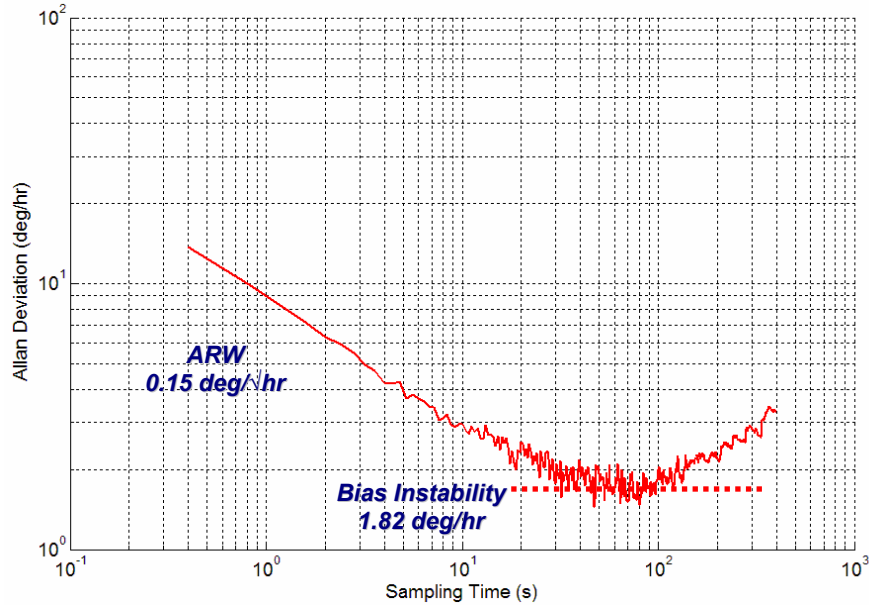
Figure 7.17: Root Allan Variance plot of the SPD M^2-TFG prototype.

Table 7.2: Device parameter summary of the SPD M^2-TFG prototype.

Device Parameter	Value
Effective Sense Quality Factor	4,000
Drive Amplitude	6 μm
Aspect Ratio of Sense Gaps	~ 20:1
Drive Resonant Mode (Measurement at V_P = 15V)	Measured : 13.671 kHz ANSYS : 13.324 kHz
Sense Resonant Mode (Measurement at V_P = 15V)	Measured : 13.720 kHz ANSYS : 13.464 kHz
Rate Sensitivity	12 mV/°/s
Angle Random Walk	0.15 °/√hr
Bias Instability	1.82 °/hr

7.3 Characterization of Packaged M^2-TFG Devices

Silicon-on-glass processing technology was used to fabricate 100μm-thick M^2-TFG prototypes [44]. The devices were successfully vacuum-packaged at University of

Michigan using the process summarized in Appendix C. In this section, the characterization results from the packaged devices will be presented.

7.3.1 Frequency Response Characterization

The first experiment performed on the vacuum-packaged M^2-TFG prototypes was to measure the drive-mode resonant frequency and Q-factor in an effort to identify the level of vacuum inside the packages. Figure 7.18 compares the Q-factor of a device tested inside a vacuum chamber (under 1mTorr vacuum) and a packaged device. It is evident that the Q-factor is similar suggesting pressure levels in the order of sub-5mTorr inside the packages.
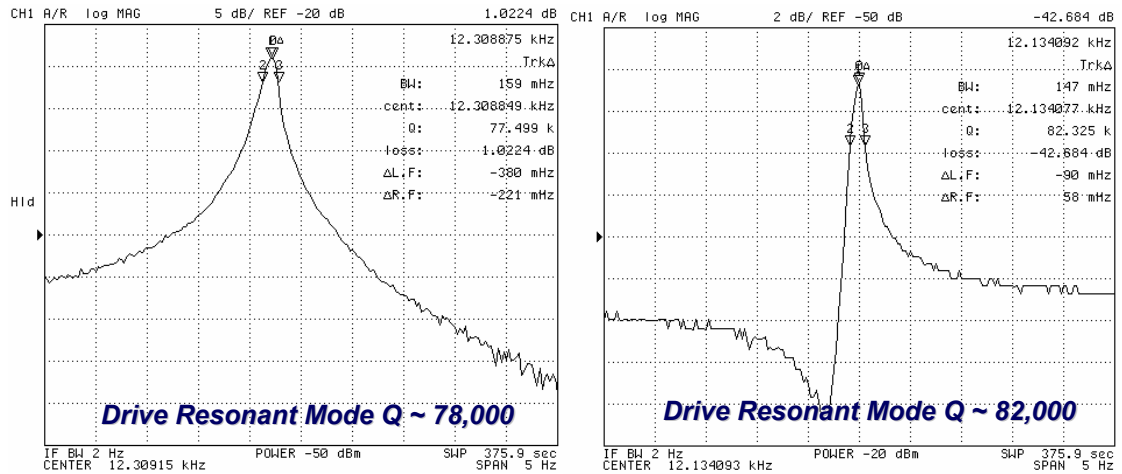
Figure 7.18: (Left) Measured drive-mode Q of 78,000 inside a vacuum chamber. (Right) Measured drive-mode Q of 82,000 of vacuum-packaged M^2-TFG prototypes.

Figure 7.19 shows a collection of plots illustrating mode-matching of a vacuum-packaged M^2-TFG prototype. The Q_{EFF} of a perfectly mode-matched device was measured to be 51,000 at 23°C. This has been the highest reported Q_{EFF} achieved at normal room temperature.
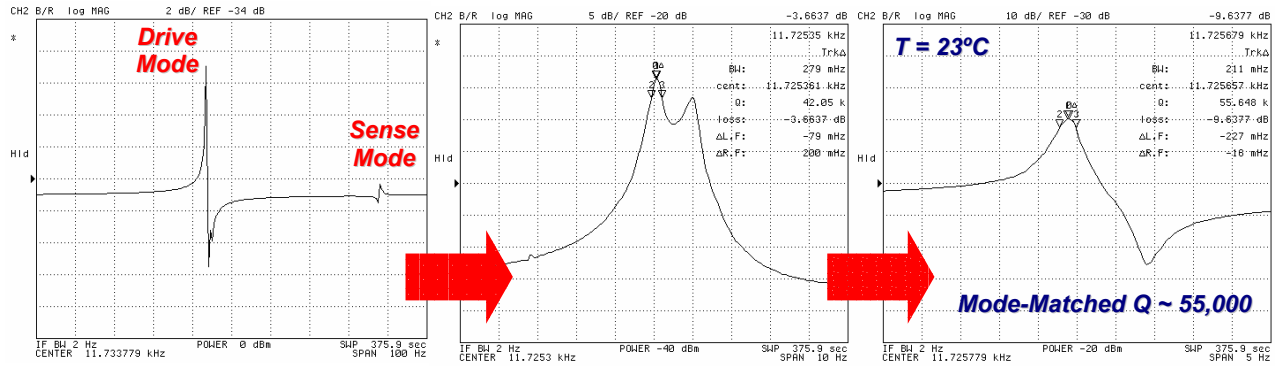
Figure 7.19: Illustration of mode-matching in vacuum-packaged M²-TFG sample.

The thermal stability of the operating modes is important. To examine the frequency stability of a packaged sample, temperature cycling of the drive-mode resonant peak was performed between -25°C to 75°C. Table 7.3 tabulates the measurement points taken over the period of three days, and Figure 7.20 demonstrates the overall stability of the drive-mode over temperature. Two important observations were made in Figure 7.20. Firstly, the temperature coefficient of frequency (TC$_f$) for the drive-mode resonant frequency has decreased from -22ppm/°C to -17ppm/°C. This may be attributed to the packaging scheme and requires further investigation.

Table 7.3: List of the data points for drive-mode temperature characterization.

Data Point	Date	Time	Temp (°C)	v_d = -20dBm, V_P =25V	
				Freq. (kHz)	Q-Factor
1	2/16/2008	12:50 AM	50	12.127578	57338
2	2/16/2008	7:40 AM	75	12.121007	35512
3	2/16/2008	3:40 PM	50	12.127576	53930
4	2/16/2008	10:20 PM	25	12.133617	86340
5	2/17/2008	8:30 AM	0	12.138870	106890
6	2/17/2008	2:00 PM	-25	12.143434	124020
7	2/17/2008	7:50 PM	0	12.138862	105650
8	2/18/2008	8:50 AM	25	12.133618	85098
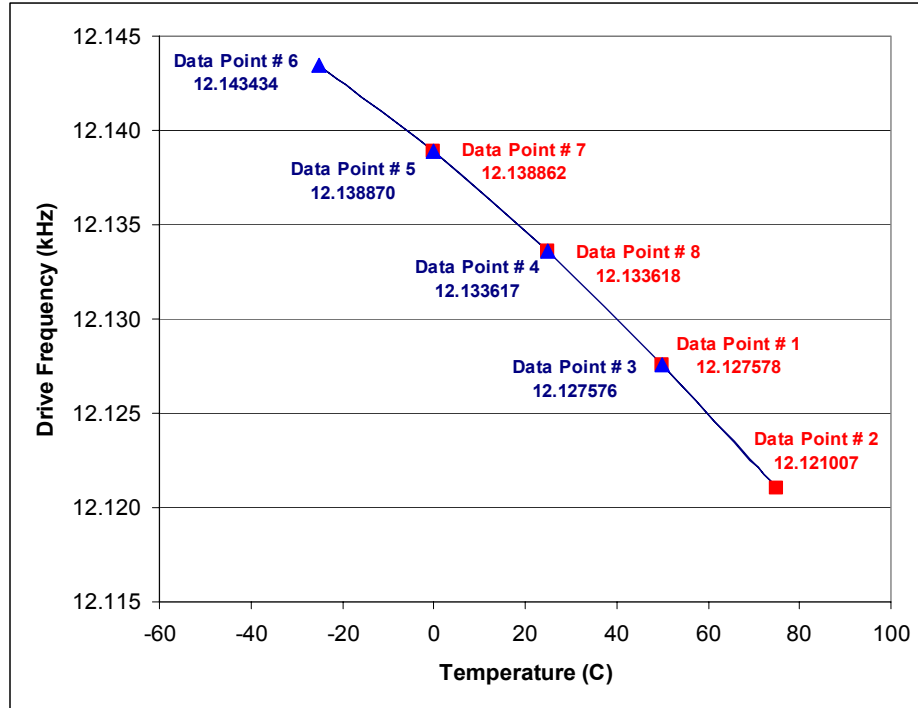
Figure 7.20: Examination of drive-mode frequency stability over temperature.

The second important observation is the relative thermal stability of the modes at various fixed operating temperatures. The observed variation at fixed measurement temperatures was less than 1ppm.

7.3.2 Device Performance Evaluation

The rotation rate sensitivity response of the M^2-TFG at 23ºC under mode-matched operation and one differential pair of sensing electrodes is presented in Figure 7.21. The device with Q_{EFF} of 51,000 exhibits a rate sensitivity of 92mV/deg/s. Figure 7.22 shows the response of the M^2-TFG to a 1 deg/s sinusoidal input rotation signal. The high-Q_{EFF} is reflected by the longer settling time.

164
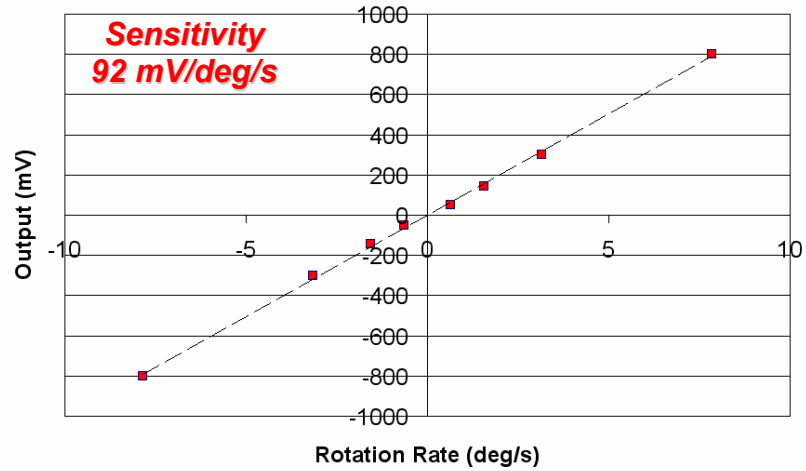
Figure 7.21: Scale-factor plot of 100µm-thick vacuum-packaged M^2-TFG prototype with an effective mode-matched Q-factor of 51,000.
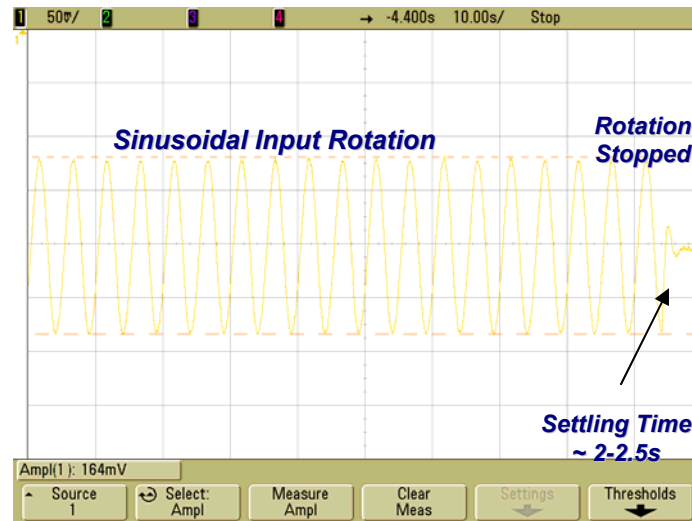
Figure 7.22: Response to 1deg/s sinusoidal input rotation signal

In an effort to enhance device sensitivity and overall resolution, the device was operated at 0°C. Figure 7.22 shows the mode-matched Q$_{EFF}$ at 0°C was 65,000.
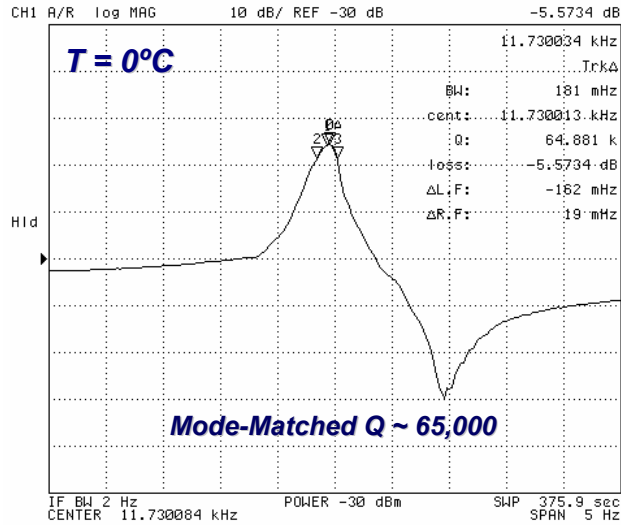
Figure 7.23: Mode-matched resonant peak of device with Q_{EFF} of 65,000 at 0ºC.

Figure 7.24 illustrates the response of the device to a 36 deg/hr (or 0.01 deg/s) sinusoidal rotation at 0 °C. In this set-up, the device undergoes ±1.6 degrees of sinusoidal rotation at 1mHz (time-period = 1000s). It is evident from Figure 7.24 that rotation rates below earth-rate (~12-15deg/hr) can be measured using the vacuum-packaged M^2-TFG, making it compatible for navigation-grade applications such as gyrocompassing.
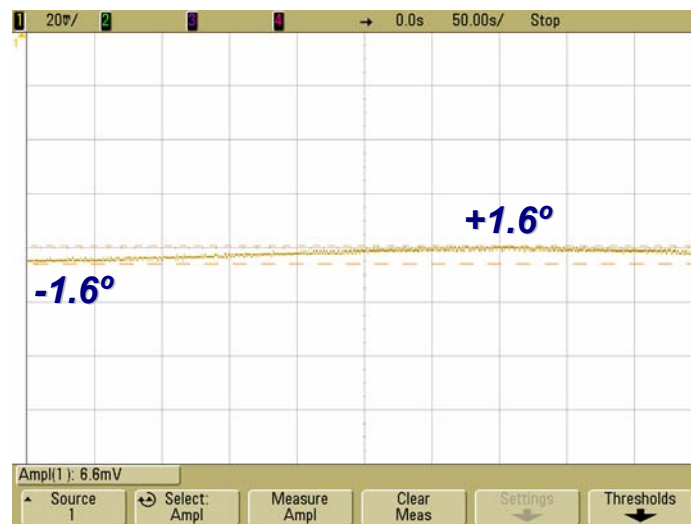
Figure 7.24: Response to 0.01deg/s(36deg/hr) sinusoidal input rotation signal. This measurement was made at 0ºC.

Finally an Allan variance analysis for the ZRO collected over a period of 3 hours was performed and the results at two temperatures are shown in Figure 7.25. A summary of the salient device parameters of the vacuum-packaged M²-TFG at 23ºC have been summarized in Table 7.4.

Temp (˚C)	ARW (deg/√hr)	Bias Drift (deg/hr)
5	0.012	0.55
25	0.025	0.72
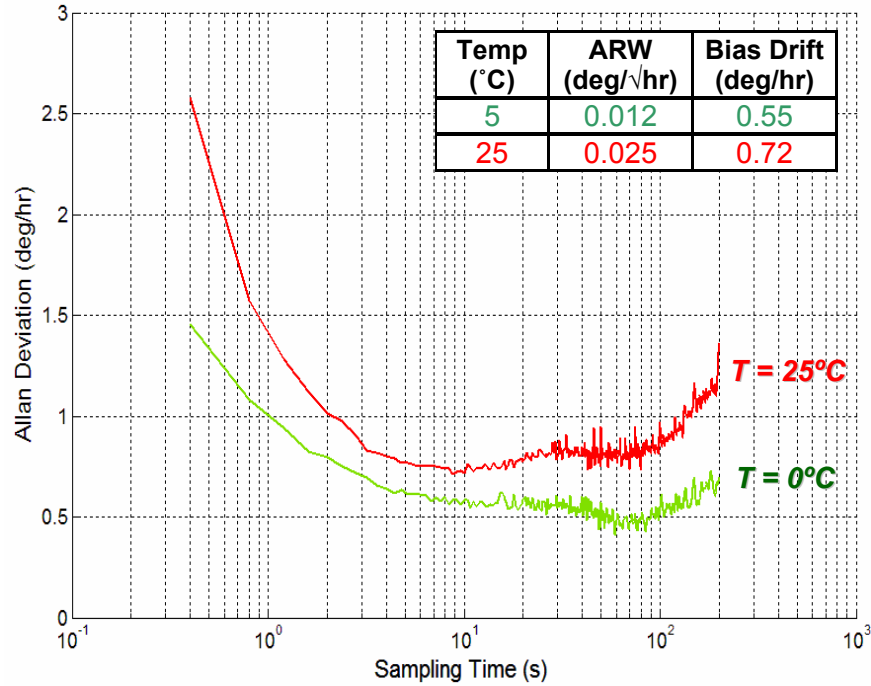
Figure 7.25: Root Allan Variance plot of the vacuum-packaged M²-TFG prototype.

Table 7.4: Device summary of the vacuum-packaged M²-TFG (at T=23ºC).

Device Parameter	RSG Value
Proof-Mass Dimensions	500µm x 500µm x 100µm
Drive Amplitude	3-4 µm
Operating Frequency	11.7 kHz
Mode-Matched Q_{EFF}	51,000
Sense Gaps (Aspect Ratio)	5.5µm (18:1)
Polarization Voltage)	42 V
Rate Sensitivity (2-Electrodes)	92 mV/˚/s
Angle Random Walk	0.012 ˚/√hr
Bias Instability	0.72 ˚/hr

CHAPTER VIII

CONCLUSIONS AND FUTURE DIRECTIONS

This dissertation presented the research performed on two prototype micromachined silicon vibratory gyroscopes – the Mode-Matched Tuning Fork Gyroscope (M^2-TFG) and the Resonating Star Gyroscope (RSG). The design concept of the M^2-TFG and RSG originated at the IMEMS Laboratory at Georgia Institute of Technology [100, 101]. Funding for the consequent development work of the M^2-TFG and RSG was provided by the DARPA HERMIT program (Contract # W31P4Q-0-1-R001) [99]. This project, a joint collaboration between the IMEMS Laboratory at the Georgia Institute of Technology (Atlanta, GA) and the WIMS Center at the University of Michigan (Ann Arbor, MI), was aimed at the demonstration of a vacuum-packaged sub-deg/hr micromachined silicon gyroscope mounted on a temperature controlled vibration isolation platform. The IMEMS Laboratory was in charge of the microgyroscope design, fabrication, and integrated interface electronics, while the WIMS center was responsible for the implementation of a vacuum-packaging scheme incorporating a thermal and vibration isolation platform.

8.1 Summary of Research Project

This dissertation has focused on the design, fabrication, and performance evaluation of high-precision micromachined Silicon vibratory gyroscopes which operate under mode-matched operation. A list of the technical contributions made through the course of this work has been summarized as follows:

(1) Design and Development of the Mode-Matched Tuning Fork Gyroscope (M^2-TFG): The M^2-TFG structure is a Class-I vibratory microgyroscope which relies on the Coriolis-induced transfer of energy between two in-plane, temperature-tracking, operating vibratory modes to sense yaw-rate. The M^2-TFG design has all the necessary attributes required to achieve sub-deg/hr noise performance. Operated under vacuum, it offers very high-Q operating modes (facilitated by TED analysis of flexural-suspension springs). The simple two-mask fabrication process used to generate prototypes on (100) 40-60µm thick SOI substrate enables maximum mass-per-unit area and facilitates large device capacitance. Large stable drive-mode deflections are achieved through an optimal comb-drive actuation mechanism.

(2) Demonstration of Performance Enhancement in M^2-TFG using Perfect Mode-Matching: The M^2-TFG represents the first reported perfectly mode-matched operation in Class-I high-Q vibratory microgyroscope. This implementation has been made possible by the development of quadrature minimization electrode scheme. 0-Hz mode-split enables a Q-factor enhancement in the device sensitivity, bias stability and the overall resolution of the device. Experimental results of SOI M^2-TFG prototypes, demonstrate effective mode-matched quality factor (Q_{EFF}) approaching 50,000, one of the highest Q-factors reported to-date for silicon vibratory gyroscopes, with a measured scale-factor approaching 100mV/deg/s (in vacuum). An extensive analysis of Allan variance technique and its role in identifying the various noise components of the microgyroscope was

169

performed. SOI M^2-TFG prototype (implemented on 60µm-thick SOI substrate) under high-Q mode-matched operation displayed a measured ARW and bias drift of 0.0083deg/hr and 0.32 deg/hr respectively (recorded at 25ºC). This represents almost two-orders of magnitude improvement over current commercial microgyroscopes [47, 50].

(3) Development of High-Aspect Ratio Fabrication Processing Technology: The more popular avenue of reducing Brownian noise floor and enhancing device capacitance is to implement M^2-TFG samples on increasingly thicker SOI substrate. The aspect ratio of the sensing gaps however is limited by the Silicon etching tool. In an effort to increase capacitive aspect ratio, a new fabrication technology was developed that involved the selective deposition of doped-polysilicon inside the capacitive sensing gaps (SPD Process). By preserving the structural composition integrity of the flexural springs, it is possible to generate operating-modes at the correct frequencies while maintaining high-Q operation. The M^2-TFG devices implemented on 80µm-thick SOI substrate with 3µm sensing gaps demonstrated mode-matched operation (Q_{EFF} = 4,000) with enhanced bandwidth. The device displayed a rate sensitivity of approximately 12mV/deg/s and a measured Allan deviation bias instability of 1.8deg/hr at 23ºC. The SPD process was also used to implement micro-g accelerometer samples, with demonstrated aspect ratio exceeding 50:1 (at the shock-stops).

(4) Characterization of Vacuum-Packaged Samples: 100µm-thick M^2-TFG devices, fabricated using the Silicon-on-Glass fabrication technology,

were successfully vacuum-packaged at the University of Michigan (as part of the DARPA HERMIT Program). The vacuum-packaged M^2-TFG prototypes demonstrated high-Q mode-matched operation (Q_{EFF} = 55,000) and excellent temperature stability. The device displayed a rate sensitivity of approximately 92mV/deg/s and a measured Allan deviation bias instability of 0.7deg/hr at 23°C.

(5) Design and Development of the Resonating Star Gyroscope (RSG): The final contribution of this dissertation was the implementation of a novel class-II shell-type microgyroscope. The RSG offers improved mass and capacitance area over its circular analogue of similar dimensions. 1mm RSG prototypes were implemented with the HARPSS process using trench-refilled polysilicon as the structural material. Thermoelastic damping was experimentally verified as the dominant loss-mechanism in the structures. An optimized version of the RSG with 2.7mm radial diameter was implemented using a multiple-shell approach on 40µm-thick (111) SOI substrate. The device displayed a rate sensitivity of approximately 16mV/deg/s (with Q_{EFF} = 30,000) and a measured Allan deviation bias instability of 3.47deg/hr at 23°C.

8.2 Future Work

Several avenues for improvements exist in both the M^2-TFG and the RSG concerning device performance and system design before feasible implementation into commercial products. In this section, some of the more immediate tasks are outlined and briefly discussed.

Improvement in Dynamic Range

In the current implementation, both the M^2-TFG and the RSG are operated open-loop. While the current configuration offers the highest mechanical gain and lowest noise floor (via Q-factor enhancements), the dynamic range is limited. The stable dynamic range for the M^2-TFG is limited to ±50deg/s while in the RSG it is limited to ±500deg/s (when operating under the optimal sensitivity and noise setting). This is insufficient for several high-performance applications. To address the dynamic range limitations, the M^2-TFG and the RSG may be operated closed-loop (for rotation sensing). Closed-loop sensing in MEMS has already been demonstrated in accelerometers [86] and gyroscopes [22, 90]. Figure 8.1 shows a possible closed-loop solution for the M^2-TFG outlined in [65].
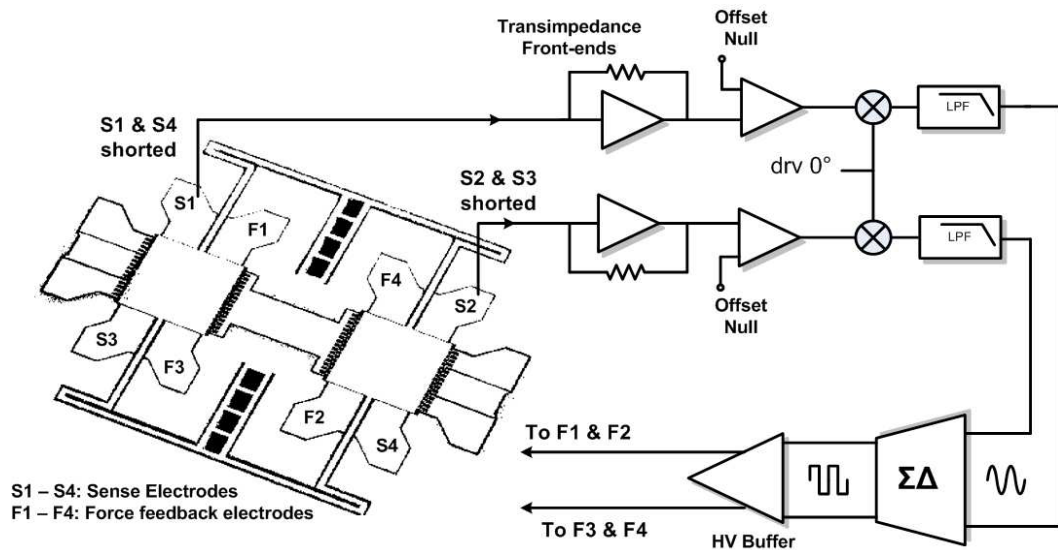
Figure 8.1: Block-diagram of proposed closed-loop operation of the M^2-TFG [23].

Closed-loop operation involves force-balancing the proof-masses along the sense-axis. This may be accomplished by placing the proof-mass in a negative feedback loop. The feedback loop measures the Coriolis-induced sense-mode

deflections, and then applies the necessary force along the opposite direction to keep the proof-masses stationary (along the sense-axis). By preventing proof-mass deflections, it is possible to increase the dynamic range by limiting the non-linearity of the sensing electrodes, and the mechanical springs.

Device Bandwidth Enhancement

The bandwidth of the gyroscope is a function of the effective Q-factor of the sense mode. Bandwidth enhancements have been made through complicated network of coupled-structures as reported in [91]. Controlled mode-splitting has also been demonstrated as means of improving device bandwidth [92]. However, it involves a lengthy pre-calibration scheme to determine device sensitivity as a function of bandwidth. The preferred means of enhancing device sensitivity (in open-loop configuration) is Q-loading. Q-factor of the operating modes may be reduced in one of two ways. In the first method, Q-factor is electronically loaded. Q-loading decreases the Q_{EFF} while maintained the gyroscope in mode-matched condition. Q_{EFF} is lowered with no change in frequency, and therefore the bandwidth is increased. Electronic Q-loading can be achieved by varying the input impedance viewed by the M^2-TFG at the transimpedance front-end stage as expressed in Eq. 5.4 [21]. The second method of Q-loading can be accomplished by mechanical design, as formulated in Section 4.3. By varying flexural beam widths along the operating axes, it is possible to operate the sense-mode in a region of low Q_{TED}, while preserving the high-Q_{TED} operation of the drive mode.

Automatic Quadrature-Minimization Scheme

The quadrature-minimization stage of the M^2-TFG and RSG operation is currently performed using manual voltage manipulation. In order to be viable commercially, an automatic calibration scheme must be developed. In a possible solution, an iterative means of gauging each quadrature electrode's response to V_P tuning may be derived. A singular value decomposition technique can consequently be utilized to determine general trends and an optimization routine may be implemented that adjusts the appropriate quadrature voltages

Temperature Compensation Scheme

The Q-factor of the operating modes of the M^2-TFG and the RSG are a strong function of temperature (as highlighted by observations made in Chapters III, VI-VII). At mode-matched operation, Q_{EFF} has a direct impact on device sensitivity (and overall bias stability of the device). Hence detecting temperature fluctuations becomes critical for compensating any loss in device sensitivity attributed to Q_{EFF} degradation. Two potential solutions to address the temperature problem are: (1) dynamically detect temperature changes and correct for the loss in sensitivity by adjusting the drive-mode amplitude, and (2) operate the device at a constant temperature (preferably elevated from the ambient room temperature).

Long-Term Device Characterization

A battery of experiments must be performed to examine the viability of the vacuum-packaged M^2-TFG samples for commercial applications. The reliability

and the operating lifetimes of these devices must be determined and involves understanding how failures that affect MEMS devices behave at both operating and extreme conditions (i.e. at high temperature, under shock-signals). Accelerated testing protocols may be developed once the relationship between the failure times at standard and extreme conditions are known [93].

Furthermore, a series of performance parameter characterization have yet to be completed for either the M^2-TFG or the RSG. This includes the examination of (1) Measured off-axis sensitivity, and (2) Scale-Factor Stability. Finally, a practical measurement set-up to detect earth-rate rotation must be assembled similar to [94] to demonstrate gyrocompassing accuracy of the M^2-TFG device.

Examination of Surface Roughness on Quality Factors

The M^2-TFG flexural geometry is defined by Silicon DRIE. This process generates a surface damaged layer along the sidewalls of the flexural springs. The mechanical structure may now be considered as a combination of two parts – (1) The mechanical structure defined by the bulk SCS material, and (2) The ion-damaged surface layer (conforming to the mechanical structure). The M^2-TFG implemented in the SPD process demonstrated low-Q operating modes, despite single-crystalline silicon structural composition of the flexural springs. As viewed in Figure 7.11, excessive surface roughness was observed owing to the existing limitations of the STS-ICP tool. The expressions for surface loss in flexural resonant structures have been investigated in [95]. A study co-relating these expressions with the measured surface profile observed in the SPD M^2-TFG prototypes would

175

be useful in determining the minimum surface roughness threshold before $Q_{Surface}$ dominates Q_{TED}.

8.3 Concluding Remarks

Since its conception in 1991 [32], the performance of MEMS gyroscopes, indicated by the ARW, has improved by an order of magnitude every two years as shown in Figure 8.2. The work performed in the development of the M^2-TFG as a part of this dissertation has successfully continued this trend. It is anticipated that a continuing improvement in the various performance metrics of micromachined gyroscopes (resolution, bias stability, dynamic range, scale-factor stability etc.) will be seen over the next decade.
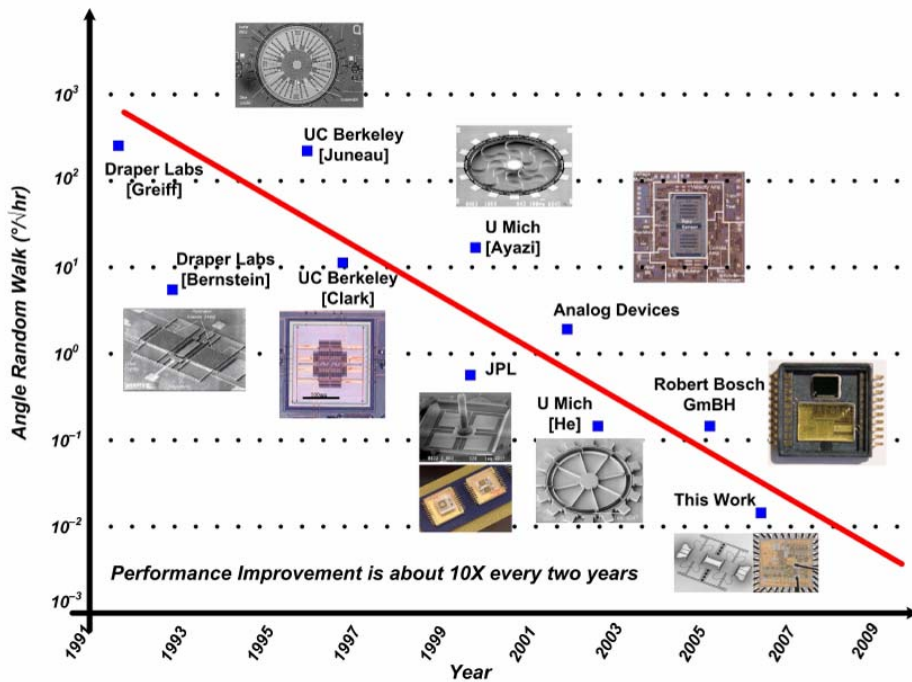
Figure 8.2: An illustration of resolution enhancement of micromachined gyroscopes over a period of two decades.

It is forecasted in [1], that as the technology becomes more mature with new packaging and fabrication technology integrated with sophisticated control

electronics, MEMS gyroscopes will slowly replace fiber-optic and mechanical gyroscopes in the lower-range of navigation applications (as shown in Figure 8.3). In the same report, the authors speculate that by the year 2020, the entire application space for navigation-grade applications will be dominated by MEMS gyroscopes.
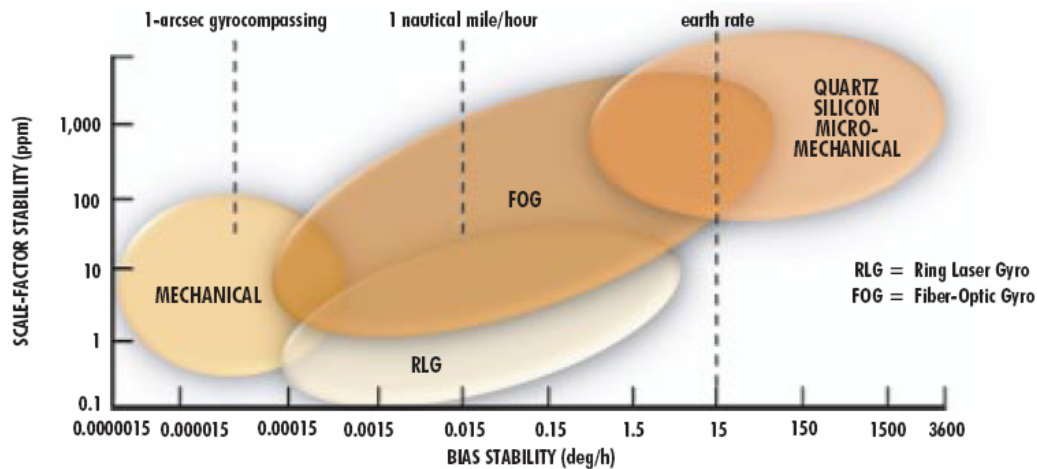
Figure 8.3: Projected application space of gyroscope technology by year 2010 [1].
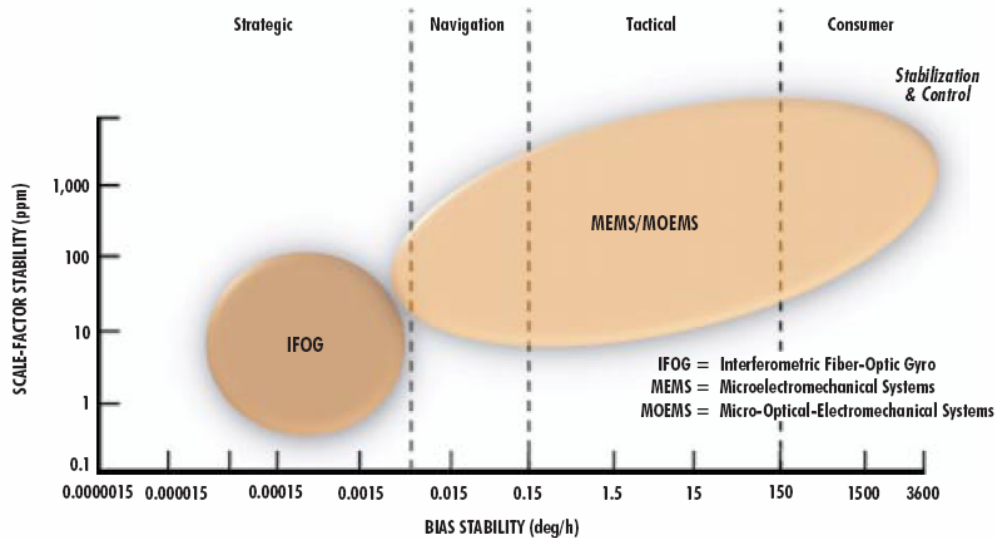
Figure 8.4: Projected application space of gyroscope technology by year 2020[1].

APPENDIX A

FABRICATION PROCESS PARAMETER SUMMARY

Fabrication process flows were developed and adopted to fabricate the various implementations of the M^2-TFG and RSG. In Appendix A, the key processing parameters utilized to execute the salient micromachining steps are presented.

Silicon Etching Process Parameters

Silicon etching was carried out exclusively in the STS-ICP tool in MiRC Cleanroom. In the following sections, the starting points of several silicon etching steps are highlighted. It must be noted that the process parameters were frequently calibrated to obtain the desired trench profile and sidewall roughness. Two masks were utilized, positive photoresist (SC-1827, SPR220) and silicon dioxide (of varying thickness). The mask selectivity is a function of the process parameters.

[1] Anisotropic Silicon Etching for Defining RSG Geometry

Table A.1: Starting point for anisotropic silicon etching to define RSG geometry.

Parameter	Etching Cycle	Passivation Cycle
Pressure Setting	APC Manual Mode (Setting 68.4%)	
C_4F_8 Flow Rate	0 sccm	100 sccm
SF_6 Flow Rate	130 sccm	0 sccm
O_2 Flow Rate	13 sccm	0 sccm
Generator Power (Connected to 13.56MHz source)	600W	600W
Platen Power (Connected to 13.56MHz source)	10W	0W
Cycle Time	10s	8s

[2] Anisotropic Silicon Etching for SOI M²-TFG Handle-Layer

Table A.2: Starting point for anisotropic silicon etching of SOI M²-TFG handle-layer.

Parameter	Etching Cycle	Passivation Cycle
Pressure Setting	APC Manual Mode (Setting 68.4%)	
C_4F_8 Flow Rate	0 sccm	100 sccm
SF_6 Flow Rate	130 sccm	0 sccm
O_2 Flow Rate	13 sccm	0 sccm
Generator Power (Connected to 13.56MHz source)	600W	600W
Platen Power (Connected to 13.56MHz source)	12W	0W
Cycle Time	11s	8s

[3] Anisotropic Silicon Etching for SOI M²-TFG Device-Layer

Table A.3: Starting point for anisotropic silicon etching of SOI M²-TFG device-layer.

Parameter	Etching Cycle	Passivation Cycle
Pressure Setting	APC Automatic Mode (15 mTorr)	
C_4F_8 Flow Rate	0 sccm	100 sccm
SF_6 Flow Rate	130 sccm	0 sccm
O_2 Flow Rate	13 sccm	0 sccm
Generator Power (Connected to 13.56MHz source)	600W	600W
Platen Power (Connected to 380kHz source)	14W	0W
Cycle Time	7s	5s

[4] Anisotropic Silicon Etching for SOI M²-TFG Device-Layer (SPD Process)

Table A.4: Starting point for anisotropic silicon etching of SPD M²-TFG device-layer.

Parameter	Etching Cycle	Passivation Cycle
Pressure Setting	APC Manual Mode (70%)	
C_4F_8 Flow Rate	0 sccm	85 sccm
SF_6 Flow Rate	130 sccm	0 sccm
O_2 Flow Rate	13 sccm	0 sccm
Generator Power (Connected to 13.56MHz source)	800W	600W
Platen Power (Connected to 380kHz source)	14W (+0.1W/min)	0W
Cycle Time	8s	5s

[5] Anisotropic Silicon Etching for Polysilicon Etch-Back

Polysilicon etch-back is performed in the HARPSS implementation of RSG during the opening of oxide windows. In M^2-TFG polysilicon process implementation, polysilicon etch-back was utilized to eliminate polysilicon bridges through handle layer (as seen in Figure 7.8) and polysilicon overhangs (as seen in Figure 7.9).

Table A.5: Starting point for polysilicon etch-back.

Parameter	Etching Cycle	Passivation Cycle
Pressure Setting	APC Automatic Mode (10mTorr)	
C_4F_8 Flow Rate	0 sccm	85 sccm
SF_6 Flow Rate	130 sccm	0 sccm
O_2 Flow Rate	13 sccm	0 sccm
Generator Power (Connected to 13.56MHz source)	600W	600W
Platen Power (Connected to 380kHz source)	35W	0W
Cycle Time	5s	3s

[6] Isotropic Silicon Etching

Isotropic silicon etching is used primarily in the fabrication of the RSG devices. In the HARPSS implementation, the polysilicon structure (protected by sacrificial oxide) is released from the silicon substrate using isotropic silicon etch []. In (111) SCS SOI multiple-shell RSG, the oxide islands between the flexural springs are eliminated using isotropic silicon etching.

Table A.6: Starting point for isotropic silicon etching.

Parameter	Value
Pressure Setting	APC Manual Mode (68.4%)
SF_6 Flow Rate	130 sccm
O_2 Flow Rate	13 sccm
Generator Power (Connected to 13.56MHz source)	600W
Platen Power (Connected to 13.56MHz source)	35W

SiO$_2$ Etching Process Parameters

Oxide etching defines the following process parameters:

(1) Pad geometry in the HARPSS implementation of RSG.

(2) Openings for isotropic silicon etching in HARPSS RSG and (111) SOI RSG.

(3) Device geometry in SOI implementation of M^2-TFG.

(4) Elimination of buried-oxide layer (during dry release of SOI M^2-TFG)

The process parameters of silicon dioxide etching inside the Plasma-Therm ICP tool in the MiRC cleanroom are enclosed below.

Table A.7: Starting point for SiO$_2$ etching in Plasma-Therm ICP.

Parameter	Value
Pressure	5 mTorr
Ar Flow Rate	15 sccm
O$_2$ Flow Rate	3 sccm
CF$_4$ Flow Rate	40 sccm
C$_4$F$_6$ Flow Rate	20 sccm
RF1 Coil Power	350 W
Typical Etch Rate	1100Å/min

Si$_3$N$_4$ Etching Process Parameters

Nitride etching defines the pad geometry in the HARPSS implementation of the RSG. The process parameters of silicon nitride etching inside the Plasma-Therm ICP tool in the MiRC cleanroom are enclosed below.

Table A.8: Starting point for Si$_3$N$_4$ etching in Plasma-Therm ICP.

Parameter	Value
Pressure	5 mTorr
CF$_4$ Flow Rate	20 sccm
RF1 Coil Power	50 W
RF2 Plasma Power	400 W
Typical Etch Rate	800Å/min

LPCVD Polysilicon Deposition Parameters

Polysilicon defines the structural component of the HARPSS RSG. In the advanced fabrication implementation of the M^2-TFG, polysilicon is used to improve the aspect ratio of the sensing gaps. Polysilicon deposition is carried out using the LPCVD Tystar-Furnace inside the MiRC cleanroom. The process condition of the polysilicon deposition is tabulated below:

Table A.9: LPCVD polysilicon deposition process parameters.

Parameter	Value
Operating Temperature	588 °C
Pressure	250 mTorr
SiH_4 Flow Rate	100 sccm
Deposition Rate	60 Å/min
Typical Tensile Stress	30 – 280 MPa

LPCVD Oxide Deposition Parameters

LPCVD oxide performs the role of sacrificial layer that defines the high-aspect ratio sensing gaps in the HARPSS implementation of RSG. Oxide deposition is carried out using the LPCVD Tystar-Furnace inside the MiRC cleanroom. The process condition of the LPCVD oxide deposition is tabulated below:

Table A.10: LPCVD oxide deposition process parameters.

Parameter	Value
Operating Temperature	825 °C
Pressure	100 mTorr
$SiCl_2H_2$ Flow Rate	60 sccm
N_2O Flow Rate	120 sccm
Deposition Rate	800 Å/hr

LPCVD Nitride Deposition Parameters

LPCVD nitride offers pad isolation for the HARPSS RSG implementation. The nitride layer protects pad peel-off during the extended HF release step in the HARPSS process. Nitride deposition is carried out using the LPCVD Tystar-Furnace inside the MiRC cleanroom. The process condition of the LPCVD nitride deposition is tabulated below:

Table A.11: LPCVD nitride deposition process parameters.

Parameter	Value
Operating Temperature	850 °C
Pressure	150 mTorr
$SiCl_2H_2$ Flow Rate	100 sccm
NH_3 Flow Rate	15 sccm
Deposition Rate	50 Å/min

P-Type Boron Doping and Annealing Parameters

The MiRC cleanroom facility does not have the capability for deposition of in-situ doped polysilicon. Polysilicon is p-doped (to make the structure conductive) using solid Boron-doping sources in the diffusion furnaces. Annealing is performed in the same Tystar furnace tube. The process parameters for p-type doping and consequent annealing have been summarized in Table A.11-A.12. The measured

Table A.12: Boron doping process parameters.

Parameter	Value
Operating Temperature	1050 °C
Process Time	1 hrs
O_2 Flow Rate	200 sccm
N_2 Flow Rate	5000 sccm

Table A.13: Annealing process parameters.

Parameter	Value
Operating Temperature	1050 °C
Process Time	1 hrs
O_2 Flow Rate	200 sccm
N_2 Flow Rate	5000 sccm
Measured Resistivity	0.02 Ω-cm

Thermal Oxidation Process Parameters

Oxide mask forms an integral part in several stages of the fabrication process flow for both the RSG and the M^2-TFG. Thermal oxidation is performed inside the Tystar furnaces in the MiRC cleanroom using the following process parameters:

Table A.14: Thermal oxidation process parameters.

Parameter	Value
Operating Temperature	900-1100 °C
O_2 Flow Rate	1000 sccm
H_2/O_2 Flow Rate	185 sccm

PECVD Oxide Deposition

PECVD oxide is deposited during the optimized M^2-TFG fabrication process to protect the polysilicon inside the trenches (as observed in Figure 7.7). The Unaxis-PECVD tool inside the MiRC cleanroom was utilized for the deposition of this oxide layer, and the process parameters have been summarized as follows:

Table A.15: PECVD oxide deposition process parameters.

Parameter	Value
Operating Temperature	250 °C
SiH_4 Flow Rate	400 sccm
N_2O Flow Rate	900 sccm
RF Power	25W

Photolithography Processing Parameters

Photolithography is exclusively performed using one of two positive photoresist products: SC 1827, and SPR 220. Organic solvent hexamethyldisilizane (HMDS) is frequently utilized as an adhesion promoting agent during photoresist spinning. The key process parameters for photolithography are summarized as:

Table A.16: HMDS dispensing parameter.

Parameter	Value
Spin Speed	3000rpm @ 500rpm/s
Soft Baking Time (Temperature)	30s (115ºC)

Table A.17: SC 1827 photolithography parameters.

Parameter	Value
Spin Speed (Thickness)	3000rpm @ 500rpm/s (2.5µm) 2000rpm @ 500rpm/s (3.1µm)
Soft Baking Time (Temperature)	1-2 min (115ºC)
Exposure Wavelength	405 nm (Hard Contact)
Exposure Intensity (Time)	20mW/cm^2 (20s)
Developer	MF-319

Table A.18: SPR 220 photolithography parameters

Parameter	Value
Spin Speed (Thickness)	3000rpm @ 500rpm/s (3.8µm) 2000rpm @ 500rpm/s (4.6µm)
Soft Baking Time	2-4 min (115ºC)
Exposure Wavelength	405 nm (Hard Contact)
Exposure Intensity (Time)	20mW/cm^2 (50s)
Developer	MF-319

Photoresist and Passivation Layer Removal

After the completion of $Si/SiO_2/Si_3N_4$ etching, the process wafer is typically left with a combination of the residual photoresist mask on the surface and in most cases a collection of passivation layer on the sidewalls of the high-aspect ratio

trenches. In an effort to eliminate both, the following steps are taken in sequence:

Photoresist removal using liquid stripper solution:

For the case of SPR220, or SC1827 positive photoresist elimination, the process wafer is initially treated to a bath of 1112-A at 80°C, for a period of 20 minutes. The wafer is then rinsed in DI water and dried before plasma-treatment

Photoresist and Passivation layer removal using Oxygen plasma

Oxygen plasma treatment is performed inside the Plasma-Therm RIE system inside the MiRC cleanroom using the following process parameters.

Table A.19: Process parameters for O_2 plasma treatment

Parameter	Value
Pressure	300 mTorr
O_2 Flow Rate	100 sccm
RF Power	400 W

APPENDIX B

GYROSCOPE DISCRETE-LEVEL EVALUATION BOARD

This appendix summarizes the block diagrams of the discrete gyroscope control electronics. The gyroscope die is mounted and the electrode connections wire-bonded to the pads on the evaluation board. The evaluation board, as seen in Figure B.1, rests on the mobile-platform of the single-axis rate table. In the case of unpackaged devices, the evaluation board is mounted inside a vacuum chamber (as seen in Figure 6.13).
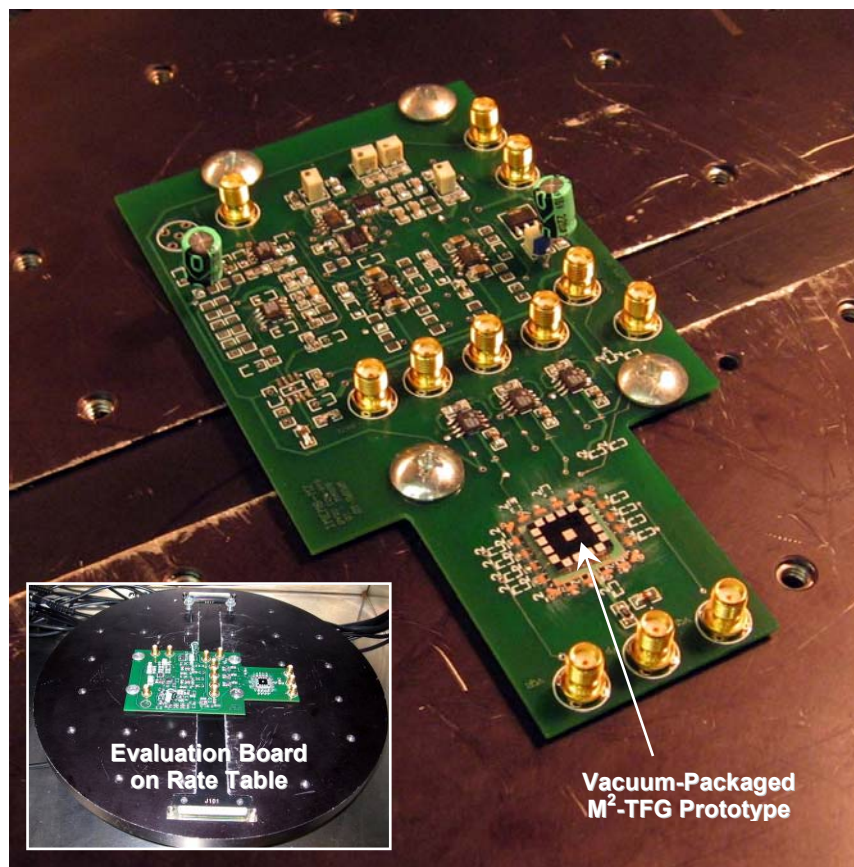
Figure B.1: Discrete evaluation board for M^2-TFG and RSG performance evaluation.

Figure B.2 shows the discrete implementations of the drive-loop and the sense-loop (beyond the initial transimpedance front-end stage).
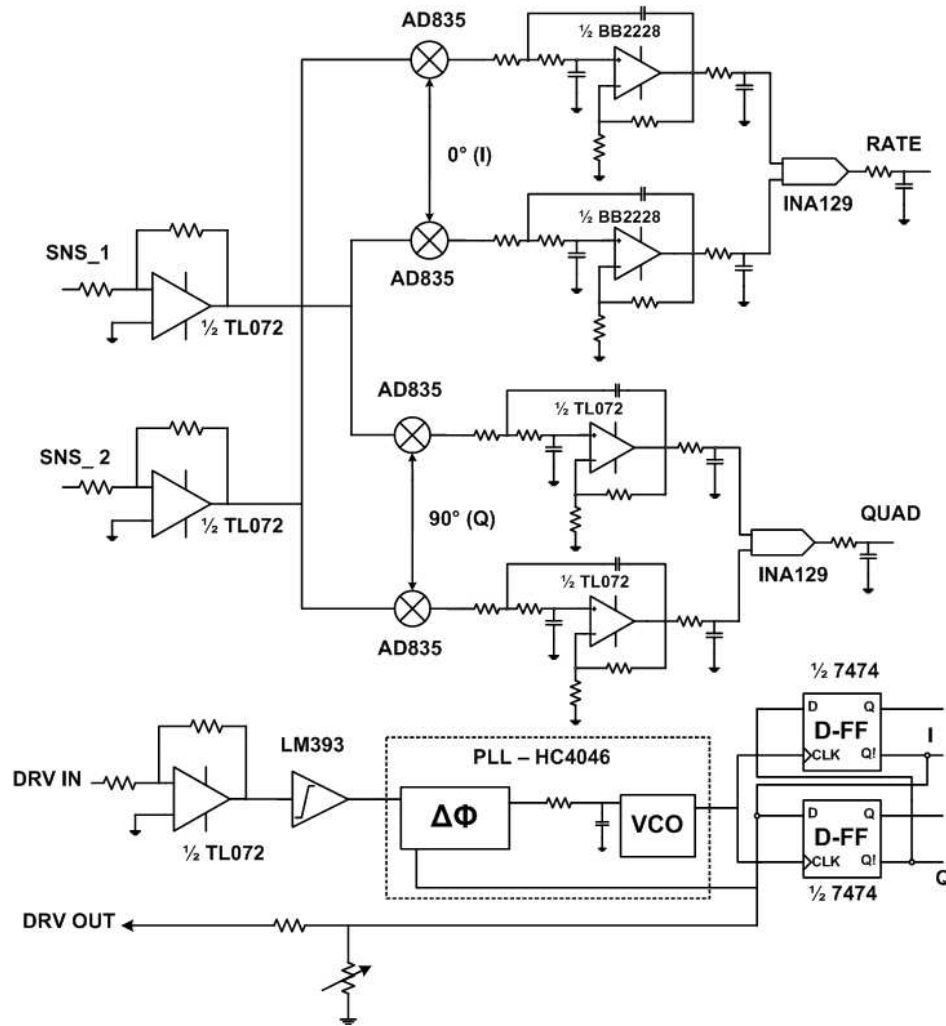
Figure B.2: Discrete implementation of control electronics interface [21].

The drive loop is implemented using the PLL-based drive oscillator described in Chapter V. Figure B.3 shows the schematic of the PLL circuit that uses a discrete HC4046 digital PLL [72]. The phase detector used is the simple XOR phase detector and 7474 D-Flip Flops are utilized to generate the 0°/90° phase-shifted signals at the drive-mode frequency [96].

Figure B.3: Discrete implementation of drive-loop PLL electronics [21].
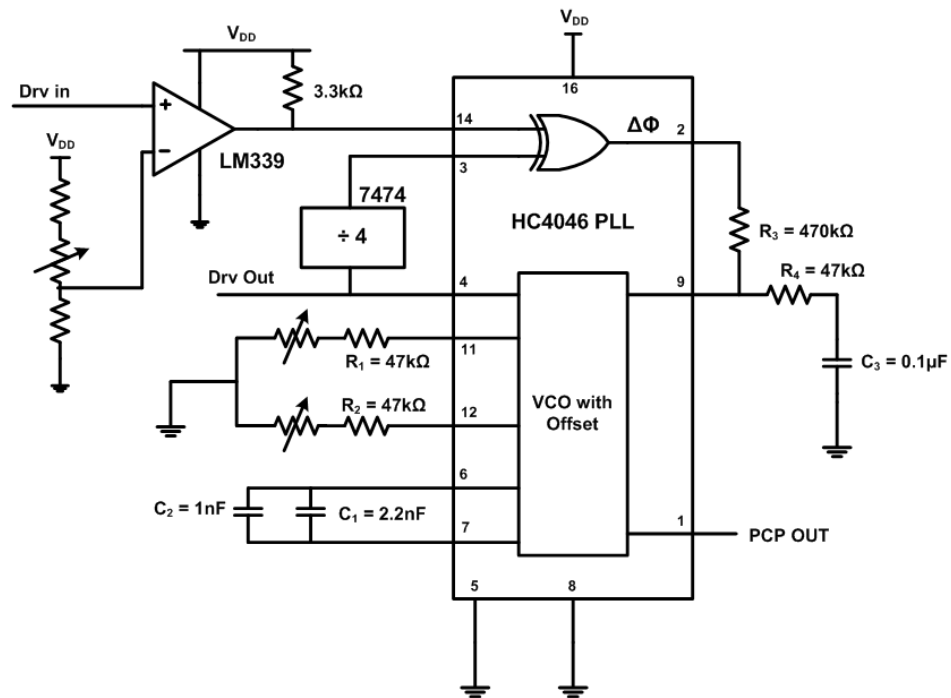
Synchronous demodulators for obtaining the rate and quadrature signals are implemented using multipliers and low-pass filters. The multipliers used in the evaluation board are AD835 [97]. The low-pass Sallen-Key filter is implemented using either a TL072 [98] dual op-amp as shown in Figure B.4.

Figure B.4: Discrete implementation of second-order Sallen-Key low-pass filter [21].
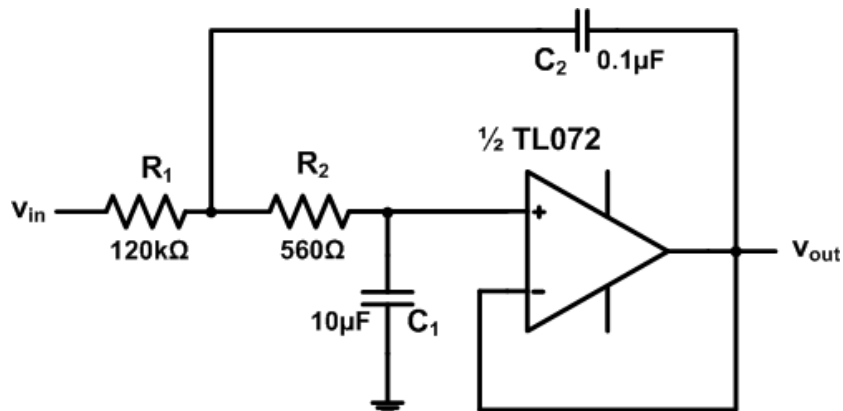
APPENDIX C

OVERVIEW OF THE VACUUM-PACKAGED M²-TFG DEVICE

The M²-TFG prototypes were vacuum-packaged at the University of Michigan as part of the HERMIT program initiative to develop a temperature controlled vibration isolation platform [99]. The schematic cross-section of the package highlighting the various package components is shown in Figure C.1.
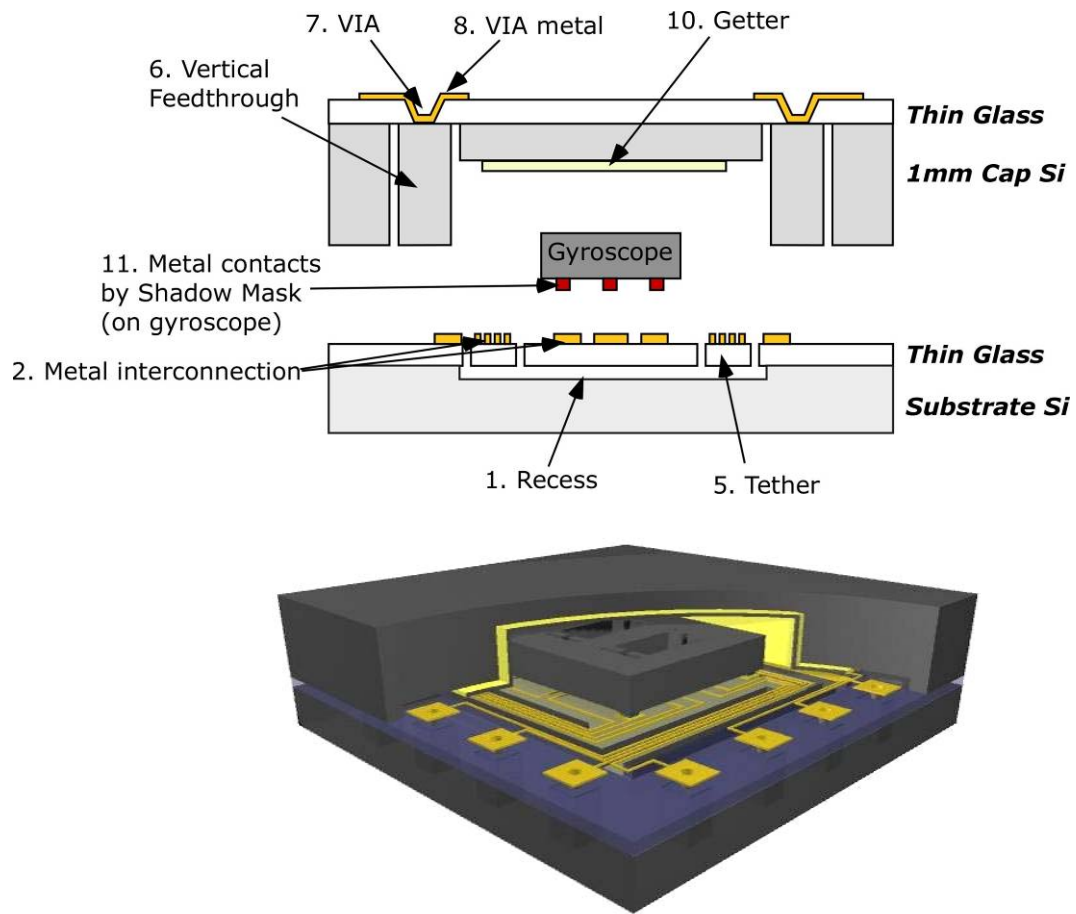
Figure C.1: Schematic cross-section of the vacuum-packaged M²-TFG resting on a temperature-controlled vibration-isolation platform.
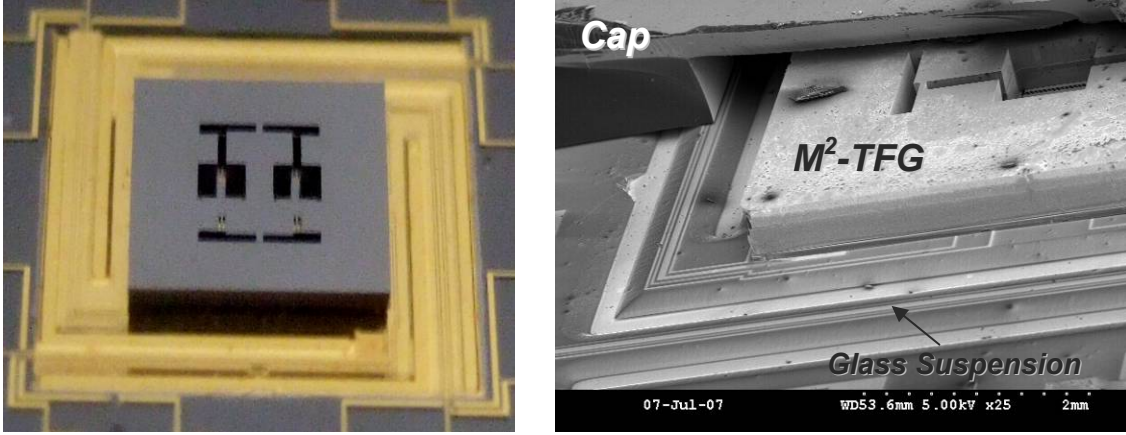
Figure C.2: (Left) SEM image of the M²-TFG die resting on the vibration isolation platform. (Right) SEM image of the cross-section of a vacuum-packaged M²-TFG device.

A schematic view of the connections of the M²-TFG is shown in Figure C.3. The characterization results of this M²-TFG prototype are presented in Section 7.3.
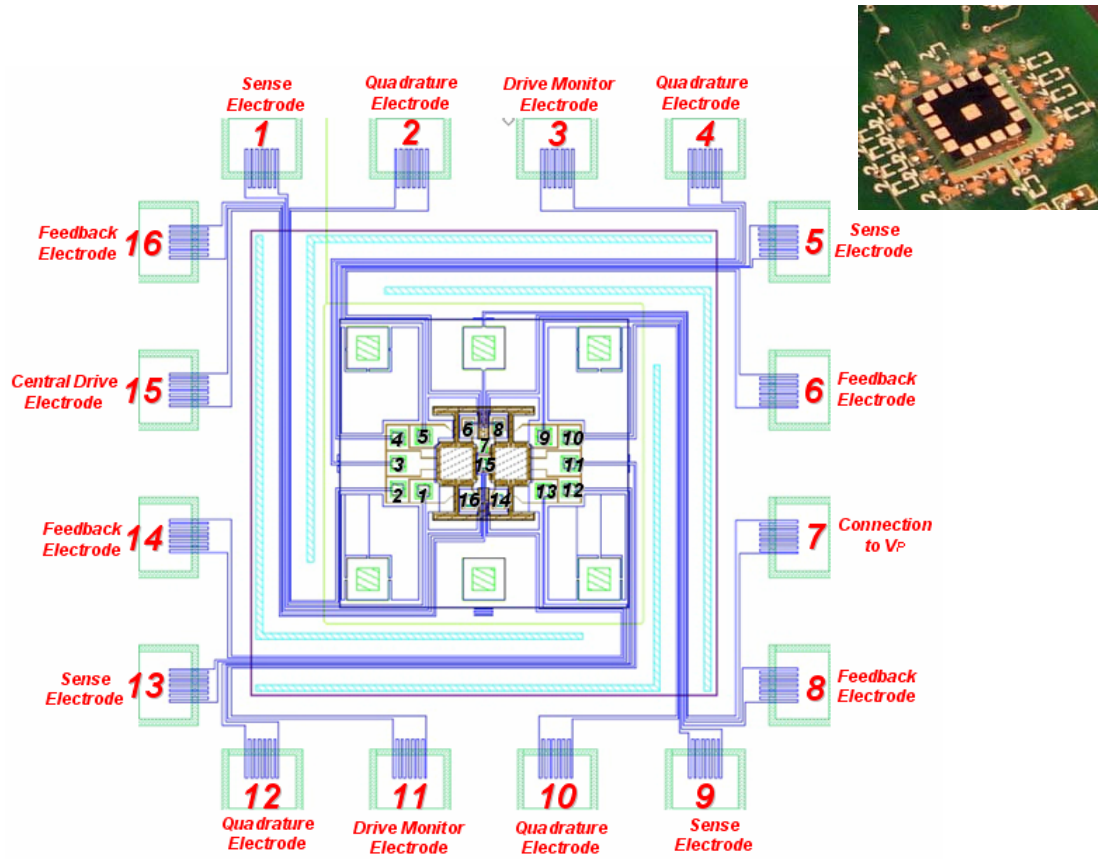
Figure C.3: Overview of the connections to the M²-TFG device (Inset) View of a 15mm x 15mm vacuum-packaged die housing a 1.7mm x 1.5mm M²-TFG prototype.

REFERENCES

[1] N. Barbour, and G. Schmidt, "Inertial sensor technology trends," in Proceedings of IEEE Workshop on Autonomous Underwater Vehicles, pp. 55-62, August 1998.

[2] B. Hofmann-Wellenhof, K. Legat, and M. Wieser, "Navigation, principles of positioning and guidance," Springer, 2003.

[3] G. Beck, "Navigation systems", Van Nostrand Reinhold, 1979.

[4] C. Lin, "Modern navigation, guidance, and control processing," Prentice-Hall, 1991.

[5] D. Hoag, "Apollo guidance and navigation consideration of Apollo IMU gimbal lock," MIT Instrumentation Laboratory Document E-1344, 1963.

[6] O. Woodman, "An introduction to inertial navigation," University of Cambridge Technical Report UCAM-CL-TR-696, August 2007.

[7] D. Allen, "Statistics of atomic frequency standards," Proceedings of IEEE, Vol. 54, No.2, pp. 221-230, February 1966.

[8] W. Wrigley, M. Hollister, W. Denhard, "Gyroscopic theory, design, and instrumentation," M.I.T. Press, 1969.

[9] A. Lawrence, "Modern inertial technology," Springer-Verlag, 1993.

[10] "HG 9900 navigation-grade inertial measurement unit," in Honeywell Data Sheet, 2007.

[11] "LN-260 advanced embedded INS/GPS," in Northrop-Grumman Data Sheet, 2006.

[12] R. R. Ragan and D. D. Lynch, "Inertial technology for the future, part x: Hemispherical resonator gyro," IEEE Transactions on Aerospace Electronic Systems, vol. AES-20, p. 432, July 1984.

[13] "Scalable SIRU," in Northrop-Grumman Data Sheet, 2007.

[14] "GG1320AN ring laser gyroscope," in Honeywell Data Sheet, 2007.

[15] "GG5300 three-axis MEMS rate gyroscope package," in Honeywell Data Sheet, 2007.

[16] G. Coriolis, "On the principle of kinetic energy in relative movement of machines," Journal Ecole Polytechnique, Vol. 13, pp. 268-302, 1832.

[17] B. Haim, "Analytical dynamics," McGraw-Hill, 1998.

[18] L. Meirovitch, "Analytical methods in vibrations," McMillan Publishing, 1967.

[19] Gyroscope and Accelerometer Panel, IEEE Aerospace and Electronics Systems Technology, "IEEE standard for inertial sensor terminology," IEEE 2001.

[20] T.B. Gabrielson, "Mechanical-thermal noise in micromachined acoustic and vibration sensors," *IEEE Trans. Electron Devices*, vol. ED-40, no. 5, pp. 903-909, May 1993.

[21] A. Sharma, "CMOS circuits and systems for sub-degree/hour MEMS gyroscopes," Ph.D. dissertation, Georgia Institute of Technology, December 2007.

[22] C. Ezekwe, and B. Boser, "A mode-matching signma-delta closed-loop vibratory-gyroscope readout interface with a 0.004 deg/s/√Hz noise floor over a 50Hz bandwidth," in Proceedings ISCCC'08.

[23] M.W. Putty, "A high aspect-ratio high performance polysilicon vibrating ring gyroscope," Ph.D. dissertation, University of Michigan, Dec. 2000.

[24] J. Bernstein et al., "A micromachined comb-drive tuning fork rate gyroscope," in Proceedings IEEE MEMS'93, pp. 143-148.

[25] H. Xie, and G. Fedder, "A DRIE CMOS-MEMS gyroscope," in Proceedings IEEE Sensors'04, pp. 1413-1416.

[26] S. Bhave et al., "An integrated, vertical-drive, in-plane-sense microgyroscope," in Proceedings IEEE Transducers'03, pp. 171-174.

[27] M. F. Zaman, A. Sharma, and F. Ayazi, "High performance matched-mode tuning fork gyroscope," in Proc. of IEEE International Conference on Micro-Electro Mechanical Systems, (MEMS'06)., Istanbul, Turkey, 2006, pp. 66–69.

[28] O. Schwarzelbach et al., "New approach for resonant frequency matching of tuning fork gyroscopes by using a non-linear drive concept," in Proceedings IEEE Transducers'01, pp.464-467.

[29] Y. Mochida, M. Tamura, and K. Ohwada, "A micromachined vibrating rate gyroscope with independent beams for the drive and detection modes," in Proceedings of IEEE MEMS'99, pp. 618-623.

[30] F. Ayazi, and K. Najafi, "A HARPSS polysilicon vibrating ring gyroscope," in IEEE Journal of Microelectromechanical Systems, Vol. 10, 2001, pp. 161-179.

[31] M. F. Zaman et al., "The resonating star gyroscope," in Proceedings IEEE MEMS'05, pp. 355-358.

[32] P. Greiff, B. Boxenhorn, T. King, and Niles, "Silicon monolithic micromechanical gyroscope," Technical Digest of the 6th International Conference on Solid-State Sensors and Actuators (Transducers '91) , pp. 966-968

[33] Y. Gianchandani, and K. Najafi, "A bulk silicon dissolved wafer process for microelectromechanical systems" in IEEE Journal of Microelectromechanical Systems, 1992, pp. 77-85.

[34] M.W. Putty and K. Najafi, "A micromachined vibrating ring gyroscope," in Technical Digest Solid-State Sensor and Actuator Workshop, Hilton Head Island, SC, USA, 1994, pp. 213-20.

[35] W. A. Clark, R. T. Howe and R. Horowitz, "Surface micromachined Z-axis vibratory rate gyroscope," in Technical Digest, Solid-State Sensor and Actuator Workshop, Hilton Head Island, SC, USA, 1996, pp. 283-7.

[36] I. D. Hopkin, C. P. Fell, K. Townsend and T. R. Mason, Vibrating Structure Gyroscope, United States Patent Number 5,932,804, issued August 3, 1999.

[37] T. Juneau, A. P. Pisano, and J. H. Smith, "Dual axis operation of a micromachined rate gyroscope," in Proc. International Conference on Solid-State Sensors and Actuators, Transducers '97, Chicago, IL, USA, 1997, pp. 883-886.

[38] M. Lutz, W. Golderer, J. Gerstenmeier, J. Marek, B. Maihofer, S. Mahler, H. Munzel and U. Bischof, "A precision yaw rate sensor in silicon micromachining," in Proc. Ninth International Conference on Solid-State Sensors and Actuators, Transducers 1997, pp. 847-850.

[39] A. Kourepenis, J. Borenstein, J. Connelly, R. Elliott, P.Ward, and M.Weinberg, "Performance of MEMS inertial sensors," in Proc. IEEE Position Location and Navigation Symposium, 1998. pp. 1-8.

[40] Y. Mochida, M. Tamura, and K. Ohwada, "A micromachined vibrating rate gyroscope with independent beams for the drive and detection modes," Sensors and Actuators A (Physical), vol. A80, no.2, Mar., pp. 170-8, 2000.

[41] H. Song, et al., "Wafer level vacuum packaged de-coupled vertical gyroscope by a new fabrication process," in Proceedings IEEE Thirteenth International Conference on Micro Electro Mechanical Systems, Miyazaki, Japan, 2000, pp. 520-524.

[42] W. Geiger, et al., "Decoupled microgyroscopes and the design principle DAVED," Sensors and Actuators A (Physical), vol. A95, nos. 2-3, Jan., pp. 239-49, 2002.

[43] S. Bae, K. Hayworth, K. Shcheglov, K. Yee, and D. Wiberg, "JPL's MEMS gyroscope fabrication, 8-electrode tuning and performance results," Digest, Solid-State Sensors and Actuators Workshop 2002.

[44] G. He, and K. Najafi, "A single-crystal silicon vibrating ring gyroscope," in Proc. Fifteenth IEEE International Conference on Micro Electro Mechanical Systems, Las Vegas, NV, USA, Jan., 2002, pp. 718-21.

[45] H. Xie, and G. Fedder, "A CMOS-MEMS lateral-axis gyroscope," Proc. of IEEE Int. Micro Electro Mechanical Systems 2001, pp. 162-165.

[46] R. Neul, et al., "Micromachined angular rate sensors for automotive applications," in IEEE Sensors Journal, Vol. 7, 2007, pp. 302-309.

[47] "ADXRS614 Yaw rate gyroscope ," in Analog Devices Data Sheet, 2007.

[48] "SMG061 Angular rate sensor," in Bosch Data Sheet, 2007.

[49] "SiRRS01 Angular Rate Sensor," in Silicon Sensing Systems Data Sheet, 2007.

[50] "IDG-1004 Integrated dual-axis gyroscope," in Invensense Data Sheet, 2007.

[51] "MAG-16 MEMS single axis gyroscope," in Northrop-Grumman Data Sheet, 2006.

[52] F. Ayazi, and K. Najafi, "High aspect-ratio combined poly and single-crystal silicon (HARPSS) MEMS technology," in IEEE Journal of Microelectromechanical Systems, Vol. 9, 2000, pp. 288-294.

[53] R. Abdolvand et al., "Quality factor in trench-refilled polysilicon beam resonator," in IEEE Journal of Microelectromechanical Systems, Vol. 15, 2006, pp. 471-478.

[54] D. Galayko et al., "Clamped-clamped beam micro-mechanical resonators in thick-film epitaxial polysilicon technology," in Proceedings of 32nd European Solid-State Device Research Conference 2002, pp. 447-450.

[55] J. Kim, D. Cho, and R. Muller, "Why is (111) Si a better mechanical material for MEMS?," in Proceedings IEEE Transducers'01, pp.662-665.

[56] R. Eley, C. Fox, S. McWilliam, "Anisotropy effects on the vibration of circular rings made from single crystalline silicon," in Journal of Sound and Vibration, Vol. 228, pp. 11-35, 1998.

[57] S. Wong et al., "A preliminary investigation of thermo-elastic damping in silicon rings," in IOP Journal of Micromechanics and Microengineering, Vol. 14, pp. 108-113, 2004

[58] Surface Technology Systems: http://www.stsystems.com/ (Last accessed: March 2008)

[59] K. Park et al., "Laterally oscillated and force-balanced micro vibratory rate gyroscope supported by fish-hook-shaped springs," in Journal Sensors and Actuators A, Vol. 64, Dec. 1998, pp. 69-76.

[60] W. Tang, M. Lim, and R. Howe, "Electrostatic comb drive levitation and control method," in IEEE Journal of Microelectromechanical Systems, Vol. 1, pp. 170-178, 1992.

[61] S. McAuley et al., "Silicon micromachining using a high-density plasma source", Journal Physics D: Applied Physics, 34 (2001) 2769-2774.

[62] A. Sharma, M.F. Zaman, and F. Ayazi, "A 104-dB dynamic range transimpedance-based CMOS ASIC for tuning fork microgyroscopes," in IEEE Journal of Solid-State Circuits, Vol. 42, Aug. 2007, pp. 1790-1802.

[63] A. Sharma, M.F. Zaman, and F. Ayazi, "A 0.2 deg/hr microgyroscope with automatic CMOS mode matching," in Proceedings ISCCC'07, pp. 386-387.

[64] Z. Hao et al., "Energy loss mechanisms in bulk-micromachined tuning fork gyroscopes," in Proceedings IEEE Sensors'06, pp. 1333-1336.

[65] Ron Lifshitz, and M. L. Roukes, "Thermoelastic damping in micro-and nanomechanical systems", Physical Review B, Vol. 61, 2000, pp.5600-5609.

[66] Z. Hao, A. Erbil, and F. Ayazi, "An analytical model for support loss in micromachined beam resonators with in-plane flexural vibrations," Journal Sensors and Actuators A, Vol. 109, Dec. 2003, pp. 156-164.

[67] J.D. Grade, "A Large-deflection, high-speed, electrostatic actuators for optical switching applications," Ph.D. dissertation, Stanford University, Sept. 2003.

[68] R. Legtenberg, A. Groeneveld, and M. Elwenspoek, "Comb-drive actuators for large displacements," in IOP Journal of Micromechanics and Microengineering, Vol. 12, pp. 320-329, 1996.

[69] J. A. Geen, S. J. Sherman, J. F. Chang, and S. R. Lewis, "Single-chip surface micromachined integrated gyroscope with 50 deg/hr Allan deviation," IEEE Journal of Solid-State Circuits, vol. 37, no. 12, pp. 1860–1866, Dec. 2002.

[70] V. P. Petkov and B. E. Boser, "A fourth-order sigma-delta interface for micromachined inertial sensors," IEEE Journal of Solid-State Circuits, vol. 40, no. 8, pp. 1602– 1609, Aug. 2005.

[71] J. Wu, G. K. Fedder, and L. R. Carley, "A low-noise low-offset capacitive sensing amplifier for a 50µg/pHz monolithic CMOS MEMS accelerometer," IEEE Journal of Solid-State Circuits, vol. 39, no. 5, pp. 722–730, May 2004.

[72] "HC4046 phase locked loop," in Phillips Semiconductors Data Sheet, 2001.

[73] C. T. C. Nguyen and R. T. Howe, "An integrated CMOS micromechanical resonator high-q oscillator," IEEE Journal of Solid-State Circuits, vol. 34, no. 4, pp. 440–455, Apr. 1999.

[74] W. A. Clark, "Micromachined vibratory rate gyroscopes," Ph.D. dissertation, University of California, Berkeley, May 1997.

[75] W. C. Tang, M. G. Lim, and R. T. Howe, "Electrostatically balanced comb drive for controlled levitation," in Tech. Digest of Solid-State Sensors, Actuators and Microsystems Workshop, 1990., Hilton Head Island, SC, USA, June 4–7, 1990, pp. 23–27.

[76] M. Zaman, A. Sharma, B. V. Amini, and F. Ayazi, "Towards inertial grade vibratory microgyros: A high-q in-plane silicon-on-insulator tuning fork device," in Tech. Digest of Solid-State Sensors, Actuators and Microsystems Workshop, 2004., Hilton Head Island, SC, USA, June4–7 2004, pp. 384–385.

[77] D. Keymeulen, W. Fink, M. I. Ferguson, C. Peay, B. Oks, R. Terrile, and K. Yee, "Tuning of MEMS devices using evolutionary computation and open-loop frequency response," in IEEE Aerospace Conference 2005, Mar. 2005, pp. 1–8.

[78] T. Remtema, and L. Lin, "Active frequency tuning for microresonators by localized thermal stressing effects," in Tech. Digest of Solid-State Sensors, Actuators and Microsystems Workshop, 2000., Hilton Head Island, SC, USA, 2000, pp. 363-366.

[79] N. Kim et al., "Temperature dependence of quality factor in MEMS resonators," in Proceedings of IEEE MEMS'06, pp. 590-593.

[80] "1291-BR single-axis rotation rate table," in Ideal Aerosmith Data Sheet, 2006.

[81] IEEE Standards 1431 – 2004, IEEE standard specification format guide and test procedure for Coriolis vibratory gyros.

[82] J. Papoulis, "Probability, random variables, and stochastic processes," McGraw-Hill, 1991.

[83] H. Hou, "Modelling inertial sensors errors using Allan variance," Masters Dissertation, University of Calgary, September 2004.

[84] "OPA656 JFET amp data sheet," in Texas Instruments Data Sheet, 2000.

[85] R. Abdolvand, B. Amini, and F. Ayazi, "Sub-micro-gravity in-plane accelerometers with reduced capacitive gaps and extra seismic mass," in IEEE Journal of Microelectromechanical Systems, Vol. 16, 2007, pp. 1036-1043.

[86] B. Amini, R. Abdolvand, and F. Ayazi, "A 4.5mW closed-loop sigma-delta micro-gravity CMOS SOI accelerometer," in IEEE Journal of Solid-State Circuits, Vol. 41, Dec. 2006, pp. 2983-2991.

[87] D. Manos, "Plasma-etching – An introduction," Academic Press Inc, 1989

[88] D. Zhao, M. Zaman, and F. Ayazi, "An ultra-low chopper stabilized lateral BJT interface circuit in 0.6µm CMOS for capacitive accelerometers," in IEEE International Solid-State Circuits Conference, February 2008.

[90] V. Petkov, and B. Boser, "A fourth-order sigma-delta interface for micromachined inertial sensors," IEEE journal of Solid-State Circuits, Vol. 40, no. 8, pp. 1602-1609, August 2005

[91] C. Acar,"Robust micromachined vibratory gyroscopes," Ph.D. dissertation, University of California, Irvine, December 2004.

[92] A. Sharma, M. F. Zaman, and F. Ayazi, "A 0.1 deg/hr bias drift electronically matched tuning fork microgyroscope," in Proc. of IEEE International Conference on Micro-Electro Mechanical Systems, (MEMS'08), Tucson, AR, 2008, pp. 6–9.

[93] D. Tanner et al., "Science-based MEMS reliability methodology," in Journal of Microelectronics Reliability, Vol. 47, Issue 9, pp. 1806-1811, November 2007.

[94] R. Arnaudov, and Y. Angelov, "Earth rotation measurement with micromechanical yaw-rate gyro," in IOP Journal of Measurement Science and Technology, Vol. 16, pp. 2300-2306, 2005.

[95] K. Yasutnura et al., "Quality factors in micron- and submicron-thick cantilevers," in IEEE Journal or Microelectromechanical Systems, Vol. 9, pp. 117-125, March 2000.

[96] 7474 Dual positive-edge-triggered D flip-flops, in Fairchild Semiconductor Data Sheet, 1998

[97] AD835 250Mhz, voltage output 4-quadrant multiplier, in Analog Devices Data Sheet, 2003

[98] "TL072 Dual low-noise JFET-input general-purpose operational amplifier," in Texas Instruments Data Sheet, 2005

[99] DARPA HERMIT Program: http://darpa.mil/mto/programs/hermit/ (Last accessed: March 2008)

[100] F. Ayazi et al., "A high-resolution in-plane tuning fork gyroscope and methods of fabrication," United States Patent No. 7,043,985

[101] F. Ayazi et al., "The resonating star gyroscope and fabrication methods," United States Patent Application No. 20060225504

VITA

Mohammad Faisal Zaman was born in Dhaka, Bangladesh. He received his Bachelor of Science degree in Electrical Engineering from the Georgia Institute of Technology in December 2001. He received his Doctor of Philosophy degree in Electrical and Computer Engineering from the Georgia Institute of Technology in April 2008. His Ph.D. dissertation was titled "Degree-Per-Hour Mode-Matched Silicon Micromachined Gyroscopes".